Multiscale modelling of damage in ductile heterogeneous materials

Jurčević, Ante

University of Zagreb
Faculty of Mechanical Engineering and Naval Architecture

Ante Jurčević

Multiscale Modelling of Damage in Ductile Heterogeneous Materials

DOCTORAL THESIS

Zagreb, 2024.

University of Zagreb
Faculty of Mechanical Engineering and Naval Architecture

Ante Jurčević

Multiscale Modelling of Damage in Ductile Heterogeneous Materials

DOCTORAL THESIS

Supervisor: prof. Zdenko Tonković, PhD

Zagreb, 2024.

Sveučilište u Zagrebu
Fakultet strojarstva i brodogradnje

Ante Jurčević

Višerazinsko modeliranje oštećenja u duktilnim heterogenim materijalima

DOKTORSKI RAD

Mentor: Prof. dr. sc. Zdenko Tonković

Zagreb, 2024.

Acknowledgments

I wish to express my sincere gratitude and respect to my supervisor, Prof. Zdenko Tonković, for his unwavering support and for providing me with the opportunity to explore my research interests under his guidance. I am also extremely thankful to Academician Jurica Sorić for many useful discussions and valuable advice he gave me during my research phase.

Deep appreciation goes to Committee members: Academician Jurica Sorić, Assoc. Prof. Tomislav Lesičar and Prof. Marko Čanađija for dedicating their time to review my thesis, and to provide me with insightful comments and constructive suggestions.

Special thanks goes to Assoc. Prof. Tomislav Lesičar, who has been nothing short of a second advisor to me. His practical knowledge and willingness to devote his time have been crucial in the early stages of my research.

I extend my sincere gratitude to Dr. sc. Karlo Seleš for sharing with me his research and ideas during my freshman year. His findings and accomplishments were the basis for my PhD thesis.

I also would like to thank Krešimir Jukić. His remarkable knowledge of numerical algorithms and coding in general has both inspired and motivated me to explore the world of computer science and algorithms in a more detailed way.

Sincere thanks goes to Assoc. Prof. Zvonimir Tomičević for many interesting polemics both related and unrelated to science. In that sense, I would also like to thank Assoc. Prof. Ivica Skozrit, Prof. Igor Karšaj, Assoc. Prof. Tomislav Jarak, Prof. Damir Semenski and Prof. Janoš Kodvanj.

Although the landscape of my department has changed significantly over the past 6 years, I express gratitude to all my past and present colleagues (in no preferred order): Assist. Prof. Lana Virag, Ivan Trapić, Joško Frančeski, Matija Novak, Dr. sc. Filip

Putar, Assist. Prof. Boris Jalušić, Dr. sc. Damjan Čakmak, Dr. sc. Bruno Dogančić, Dr. sc. Frane Pamuković, Petra Adamović, Tomislav Polančec, Matej Stanić, Toni Škugor, Andrija Zaplatić, Ana Mandić, Ana Lisac, Marin Vukovojac, Luka Labar, Daria Ćurko, Dr. sc. Zoran Tomić, Josip Živić, Jurica Rožić, Marko Čeredar, Ana Marija Šegon, Jelena Pankretić and to our Head of Office Tina Pintar. Simple and brief but always meaningful conversations I had with them were enough to bring me relief and shift my mind away from negative thoughts.

I especially want to thank my friend Ivana Jovanović for her support and friendship that started many years ago.

I would also like to thank Ms. Izidora Herold and Mr. Damir Kačer for providing administrative support during my PhD studies.

My deepest gratitude and appreciation goes to my family. Without my parents, my father Stipan and mother Marija, I definitely would not be here. Their support, love and many sacrifices they endured are the cornerstone of my existence. I am extremely thankful to my sister Iva for her unwavering support, numerous conversations and words of encouragement that helped me to finish this dissertation. To my nephews, Marija and Matej, who bring immeasurable joy and laughter into my life, enriching every moment — my thanks for the endless happiness you provide.

Finally, I reserve my profound gratitude to God, whose grace and guidance have been my constant companions on this journey. It is with a heart full of thanks that I acknowledge the strength, wisdom, and peace bestowed upon me, carrying me through challenges and leading me towards fulfillment and purpose.

Ante Jurčević
Zagreb, September 2024.

Abstract

In modern times, the use of advanced manufacturing techniques such as 3D printing or sintering allows for the creation of specific heterogeneous structures at the nano, i.e. microlevel, which can eventually lead to advantageous thermal, electrical or mechanical properties at the macrolevel. Since the behaviour of modern engineering materials is directly influenced by the behaviour of their microstructure, the use of classical phenomenological constitutive relations is insufficient when considering highly localized effects such as plasticity or damage. Therefore, the discovery of accurate and efficient numerical procedures for the description of material behaviour that take into account the contribution of each individual microconstituent is becoming increasingly important.

Concurrent multiscale methods are able to overcome the limitations of classical continuum mechanics by establishing a direct link between the microscale and the response of the material at the macroscale through the process of homogenization. This computational approach is based on the solution of two boundary value problems, one at each scale. Homogenized results obtained by the simulation of a statistically representative sample of material, named Representative Volume Element (RVE), are used as input data at the macrolevel. Direct numerical simulation (DNS), performed by the finite element method (FEM) or the fast Fourier transformation (FFT), is the most accurate and flexible method for solving the RVE boundary value problem. However, due to the significant number of degrees of freedom (DOF), DNS can be very consuming in terms of time and computational resources.

Concurrent multiscale methods have become a valuable tool in the numerical modelling of material failure since the highly localized phenomena, such as damage, occur at the lower levels first and cannot be captured appropriately using classical continuum mechanics. Today, multiscale modelling of damage in heterogeneous materials represents a particularly interesting and demanding topic in the field of computational mechanics. On the one hand, by modelling small domains of a material, concurrent multiscale methods which employ DNS for solving RVE boundary value problem can improve the accuracy and predict material failure. On the other hand, high computational costs that come along with concurrent multiscale methods are a

major obstacle in the analysis of realistic macrostructures. Moreover, incorporating damage into the concurrent multiscale procedure is a significant challenge in itself. The simple homogenization scheme that can be used for acquiring macroscopic stress-strain response will encounter stability issues when the material experiences strain softening. Also, studies have shown that the macroscopic value of material damage cannot be well captured by applying direct homogenization of the damage parameter at the lower levels, as it will eventually lead to non-physical results. In addition to that, the use of either discrete or continuum damage models at the macroscale exhibits certain challenges. For the continuum damage model at the macroscale, pathological mesh dependency will occur if the nonlocal damage model is not applied. Discrete damage models on the other hand require additional fracture criteria to address the questions about the macro crack trajectory, but also suffer from mesh dependency since the macroscopic crack propagates along element's edges.

In this research, a novel multiscale procedure capable of describing static fracture processes in both brittle and ductile heterogeneous materials for both two- and three-dimensional problems is developed. The novel procedure includes the use of a reduced-order homogenization method called self-consistent clustering analysis (SCA) and a nonlocal continuum damage theory called phase-field. SCA and phase-field fracture formulations are implemented at the microlevel and macrolevel, respectively. The issue of high computational costs, that comes with the use of concurrent multiscale methods that employ DNS at the microlevel, is circumvented by the utilization of the SCA. On the other hand, nonlocal continuum damage formulation, such as phase-field, at the macrolevel ensures objectivity and mesh independence of the final results. In this way, the calculation of the material degradation at the macrolevel does not include any kind of damage analysis at the microlevel, which provides additional stability of the concurrent approach.

The developed concurrent procedure is implemented into commercial finite element software Abaqus through UEL and UMAT user subroutines, and is exhaustively tested on a large number of different geometrical specimens. Presented examples include multiscale analysis with simple unit cell/sphere microstructures, but also complex ones which were obtained from experimental metalography of nodular cast iron. Since special attention is given to the computational efficiency, a detailed discussions regarding the proposed implementation's CPU time usage are also provided.

Keywords: microlevel, macrolevel, concurrent multiscale methods, heterogeneous material, RVE, homogenization, self-consistent clustering analysis, phase-field, Abaqus, k-means clustering, Lippmann-Schwinger equation, Green's function, material cluster

Prošireni sažetak

Uvod

U moderno vrijeme težnja za pouzdanim, trajnim i učinkovitim konstrukcijskim komponentama u konstantnom je porastu. S ciljem postizanja što viših stupnjeva učinkovitosti te što nižih troškova proizvodnje nužno je poznavanje specifičnih fizikalnih svojstava modernih inženjerskih materijala, kojih je u današnje vrijeme sve više i više. Korištenjem naprednih tehnologija proizvodnje kao što su 3D printanje i sinteriranje omogućeno je stvaranje heterogenih struktura odgovarajuće geometrije na nano, tj. mikrorazini, koje u konačnici mogu dovesti do povoljnih mehaničkih, toplinskih i električnih svojstava na makrorazini. Mehanička svojstva modernih heterogenih materijala na makrorazini izravna su posljedica međusobne interakcije materijalnih konstituenata na nano, tj. mikrorazini. Višerazinska priroda heterogenih materijala od izuzetne je važnosti i do danas predstavlja veliku prepreku u njihovom numeričkom modeliranju. Klasična mehanika kontinuuma opisuje uprosječeno ponašanje materijala, odnosno ne uzima u obzir pojedinačne doprinose svakog pojedinog mikrokonstituenta koji tvori materijal. Pri pojavi visokolokaliziranih fenomena, kao što su plastičnost i oštećenje, upotreba klasičnih fenomenoloških relacija ne dovodi do kvalitetnih rezultata. Stoga je razvoj točnih i učinkovitih numeričkih postupaka za opisivanje ponašanja heterogenih materijala, koji u obzir uzimaju doprinos od svakog pojedinačnog mikrokonstituenta, u fokusu brojnih znanstvenih istraživanja i projekata.

Numeričko modeliranje heterogenih materijala

Jedan od brojnih načina numeričkog modeliranja heterogenosti predstavlja upotreba izravnih, tj. direktnih numeričkih simulacija (eng. *direct numerical simulation*, DNS) pri čemu se heterogena mikrostruktura modelira izravno - bez pojednostavljenja. Ovo

predstavlja najprecizniju, ali i ujedno računalno najzahtjevniju metodu modeliranja heterogenih materijala, budući da ukupan broj stupnjeva slobode vrlo brzo može dosegnuti iznimne vrijednosti - prevelike za bilo koje moderno računalo.

Poopćena mehanika kontinuuma, poznata i kao teorija gradijenata višeg reda, predstavlja jedan od prikladnijih načina opisivanja mehaničkog ponašanja heterogenih materijala. Proširivanjem tenzora malih deformacija ili tenzora gradijenta deformiranja s gradijentima višeg reda, osigurava se kvalitetno opisivanje nelinearnog i visokolokaliziranog ponašanja kao što je plastičnost ili oštećenje. Na ovaj način, informacije s nižih razina su izravno ugrađene u numerički proračun bez potrebe za analizom same mikrostrukture. U ovom trenutku, dva najveća izazova koja se javljaju prilikom korištenja poopćene mehanike kontinuuma su visoki računalni troškovi te pojava velikog broja materijalnih parametara, čije eksperimentalno određivanje u većini slučajeva nije moguće.

S druge strane, višerazinske (eng. *multiscale*) metode predstavljaju skup numeričkih postupaka s mogućnošću analiziranja mehaničkog ponašanja heterogenog materijala na više razina. Izravna posljedica kod korištenja ovih metoda jest ovisnost između različitih razina, gdje rješenje s jedne razine izravno utječe na rješenja druge razine. Iako postoji značajan broj višerazinskih metoda, one se općenito dijele na konkurentne, sekvencijalne, homogenizacijske, paralelne, hibridne i hijerarhijske.

Konkurentne višerazinske metode predstavljaju najpopularniju i najčešće korištenu klasu višerazinskih metoda. Ove metode karakterizira izravna veza između niže razine i odziva materijala na višoj razini, koja se ostvaruje korištenjem procesa homogenizacije. Niža razina je najčešće vezana za mikrostrukturu materijala, dok se viša (makro) razina odnosi na konstrukcijsku komponentu koja se proračunava. Tijekom analize, svojstva materijala kao i njegovo ponašanje u svakoj materijalnoj točki se dobiva izravno iz svojstava i ponašanja njegove mikrostrukture, koja je određena preko reprezentativnog volumenskog elementa (eng. *representative volume element*, RVE). Nakon rješavanja problema rubnih vrijednosti na mikrorazini, rezultate analize je potrebno homogenizirati, tj. uprosječiti. Uprosječeni rezultati se nakon toga šalju na makrorazinu gdje se upotrebljavaju kao ulazni podaci za rješavanje problema rubnih vrijednosti na makrorazini. Direktna numerička simulacija predstavlja najtočniji i najfleksibilniji način rješavanja problema rubnih vrijednosti na mikrorazini. Metoda konačnih elemenata (MKE) i brza Fourierova transformacija (BFT) su jedni od načina putem kojih je moguće provesti direktnu numeričku simulaciju. Međutim, zbog velikog broja stupnjeva slobode, provođenje konkurentne višerazinske analize za sobom nosi potrebu za značajnim računalnim resursima i dugotrajnim vremenom računanja. Razlog tome jest činjenica da se problem rubnih vrijednosti na mikrorazini mora riješiti

za svaku materijalnu točku na makrorazini i za svaki inkrement cjelokupne analize.

Budući da je glavni (i osnovni) cilj rješavanja problema rubnih vrijednosti na nižoj razini određivanje prosječnog (homogeniziranog) ponašanja RVEa, dobivanje "finih" (detaljnih) raspodjela polja deformacije i naprezanja nije nužno. S relativno malim brojem stupnjeva slobode na nižoj razini nije moguće na ispravan način opisati raspodjelu polja deformacije i naprezanja, ali je moguće doći do njihovih prosječnih vrijednosti. Zbog toga se pribjegava upotrebi takozvanih reduciranih metoda (eng. *reduced-order homogenization methods*), koje uz odgovarajući gubitak na točnosti homogeniziranih rezultata osiguravaju značajno smanjenje vremena računanja višerazinskog konkurentnog postupka. Ubrzanje se postiže prvenstveno zbog smanjenja složenosti proračuna na mikrorazini, a danas se u tu svrhu sve češće koriste velike baze podataka.

Višerazinsko modeliranje heterogenih materijala putem velikih baza podataka

Značajnim rastom računalnih resursa, numeričkom modeliranju mehaničkog ponašanja heterogenih materijala sve češće se pristupa sa stajališta velikih baza podataka. Analizom "sirovih podataka" moguće je doći do prethodno nepoznatih materijalnih zakona i regularnosti, koje se kasnije mogu koristiti za značajno smanjivanje računalne zahtjevnosti konkurentnog višerazinskog postupka. Proces "učenja" i analiziranja "sirovih podataka" se odvija u takozvanom "*offline* koraku", kojeg je potrebno provesti samo jednom. Do "sirovih podataka" moguće je doći ili eksperimentalnim putem ili upotrebom numeričkih simulacija, a s gledišta njihove upotrebe razlikuju se dva pristupa: makroskopski i mikroskopski.

U makroskopskom pristupu, analizom "sirovih podataka" dolazi se do regularnosti koje služe za izravno predviđanje mehaničkog ponašanja heterogenog materijala pri odgovarajućem opterećenju. Točnije, uključivanje makroskopskog pristupa u konkurentnu višerazinsku proceduru znači da se homogenizirana (uprosječena) vrijednost bilo koje veličine može dobiti izravno iz vrijednosti makroskopske deformacije, tj. makroskopskog gradijenta deformiranja. Budući da je rješavanje problema rubnih vrijednosti na mikrorazini u potpunosti isključeno, makroskopski pristup osigurava najviši stupanj računalne učinkovitosti.

Iako računalno izuzetno učinkovit i prilagodljiv, makroskopski pristup je uvelike uvjetovan kvalitetom i količinom "sirovih podataka". Opisivanje i modeliranje visokolokaliziranih fenomena kao što su plastičnost i oštećenje zahtijeva stvaranje

ogromnih baza podataka, što u nekim slučajevima nije moguće. Također, zbog manjka informacija s mikrorazine, točnost predviđanja koju makroskopski pristup nudi je često ograničena. To je pogotovo izraženo u prijelaznim slučajevima, tj. trenutcima gdje heterogeni materijal značajno mijenja svoju krutost uslijed akumulacije oštećenja ili prijelaza iz elastičnog u elastoplastično područje.

S druge strane, mikroskopski pristup se služi direktnom numeričkom simulacijom kako bi u *offline* koraku prikupio podatke iz svake materijalne točke razmatrane mikrostrukture (RVEa) koji se zatim koriste za stvaranje velike baze "sirovih podataka". Analizom tih podataka dolazi se do odgovarajućih regularnosti koje se kasnije koriste za smanjenje složenosti i ubrzavanje računanja problema rubnih vrijednosti na mikrorazini. Budući da rješavanje problema rubnih vrijednosti nije isključeno (kao u makroskopskom pristupu), mikroskopski pristup se nalazi na nižem stupnju računalne učinkovitosti, ali s druge strane nudi veću količinu informacija u odnosu na makroskopski pristup. U neke od najpoznatijih mikroskopskih pristupa spadaju pravilna ortogonalna dekompozicija (eng. proper orthogonal decomposition), analiza putem transformacijskih polja (eng. transformation field analysis), analiza putem neuniformnih transformacijskih polja (eng. nonuniform transformation field analysis) te metoda homogenizacije s reduciranim brojem stupnjeva slobode temeljena na analizi klastera (eng. reduced order homogenization: self-consistent clustering analysis).

Metoda homogenizacije s reduciranim brojem stupnjeva slobode

Metoda homogenizacije s reduciranim brojem stupnjeva slobode predstavlja jednu od procedura, u području mikroskopskih pristupa, za analizu mehaničkog ponašanja heterogenih materijala. Temeljena je na dvije inovacije: (1) upotreba algoritma strojnog učenja za dekompoziciju RVEa u odgovarajući broj potpodručja, tj. klastera i (2) upotreba Lippmann-Schwingerove jednadžbe za rješavanje problema rubnih vrijednosti na RVEu koji je diskretiziran odgovarajućim brojem klastera.

Prva inovacija iskorištava svojstvo *k-means* algoritma, ili bilo kojeg drugog algoritma za klasteriranje podataka, kako bi se broj stupnjeva slobode (koji su prisutni na mikrorazini) značajno smanjio. Redukcija se postiže grupiranjem točaka (konačnih elemenata u slučaju MKEa) u odgovarajuće materijalne klastere. Pojam "materijalni klaster" označava područje konačnog volumena u kojem je vrijednost bilo koje varijable konstantna. Točnije, svaka varijabla unutar jednog klastera ima isključivo jednu vrijednost. Dekompozicijom složene mikrostrukture u materijalne klastere, broj stupnjeva

slobode se može smanjiti i za nekoliko stotina puta. Broj materijalnih klastera kojima se diskretizira mikrostruktura je proizvoljan, s pravilom da ne može biti manji od broja mikrokonstituenata koji tvore mikrostrukturu, niti veći od broja točaka (konačnih elemenata u slučaju MKEa) kojima je inicijalno diskretizirana mikrostruktura. Proces klasteriranja, tj. grupiranja točaka (konačnih elemenata u slučaju MKEa) u odgovarajuće materijalne klastere provodi se u *offline* koraku, i potrebno ga je izvršiti samo jednom. Dobivena diskretizacija se kasnije može koristiti za bilo koju vrstu opterećivanja kao i za bilo koji konstitutivni materijalni zakon.

Druga inovacija je nešto složenija i odnosi se na korištenje Lippmann-Schwingerove jednadžbe s ciljem modeliranja i analize mehaničkog ponašanja svakog pojedinog klastera kao i cjelokupnog RVEa. Iako je inicijalno izvedena za potrebe opisivanja sudara čestica u problemima kvantne mehanike, Lippmann-Schwingerova jednadžba pronašla je svoje mjesto i u području mehanike deformabilnih tijela. Prvi radovi koji razmatraju modifikaciju i primjenu Lippmann-Schwingerove jednadžbe za rješavanje problema heterogenih mikrostruktura pojavili su se početkom 70-ih godina prošlog stoljeća. U njima je jednadžba korištena za dobivanje prosječne (homogene) vrijednosti modula elastičnosti i modula smičnosti odgovarajućeg heterogenog materijala. U slučaju metode homogenizacije s reduciranim brojem stupnjeva slobode, Lippmann-Schwingerova jednadžba se može smatrati jednadžbom ravnoteže klastera.

Usprkos vrlo gruboj diskretizaciji, metoda homogenizacije s reduciranim brojem stupnjeva slobode osigurava visok stupanj točnosti, tj. malu grešku kada se usporede vrijednosti dobivene nekom od numeričkih metoda kao što su MKE i BFT. Osim računalne učinkovitosti, metodu karakterizira i značajna fleksibilnost. Točnije, Lipmann-Schwingerova jednadžba, koja je diskretizirana po klasterima, valjana je za bilo koji konstitutivni zakon u određenom materijalnom klasteru, a također osigurava relativno jednostavan prelazak s malih na velike deformacije. Međutim, visoka razina točnosti nije uvijek zagarantirana, te je ovisna o vrsti opterećenja, ali i samoj materijalnoj kao i geometrijskoj konfiguraciji razmatrane mikrostrukture.

Numeričko modeliranje oštećenja i loma

Numeričke metode modeliranja oštećenja i loma najčešće se razvijaju u sklopu metode konačnih elemenata, a općenito se mogu podijeliti na diskretne (diskontinuumske) i difuzne (kontinuumske). Ovo je ujedno i osnovna podjela numeričkih metoda za modeliranje oštećenja i loma koja je ustanovljena s gledišta način prikaza i modeliranja pukotina unutar materijala.

Diskretne metode pukotinu opisuju kao oštar geometrijski diskontinuitet u polju pomaka. Danas, dvije najpoznatije teorije koje stoje iza diskretnih metoda su linearno elastična mehanika loma (eng. *linear elastic fracture mechanics* LEFM) i metoda modeliranja kohezivnih zona (eng. *cohesive zone modelling* CZM). Za razliku od linearno elastične mehanike loma, čija primjena je moguća samo kada je nelinearna zona ispred vrška pukotine zanemarivo mala, metoda modeliranja kohezivnih zona je doživjela značajno veću primjenu. S mogućnošću potpunog isključivanja singularnosti naprezanja ispred vrška pukotine, metoda modeliranja kohezivnih zona našla je svoju primjenu u problemima krhkog i duktilnog loma, pri malim i velikim deformacijama. S gledišta numeričke analize, uvođenje i modeliranje geometrijskih diskontinuiteta predstavlja značajan izazov, pogotovo u slučaju metoda temeljenih na prostornoj diskretizaciji (eng. *mesh-based methods*) kao što je MKE. Budući da pukotina raste duž rubova elemenata, linearno elastična mehanika loma kao i metoda modeliranja kohezivnih zona podliježu problemima vezanim uz ovisnost rezultata o veličini mreže (eng. *mesh dependency*), ali i problemima vezanim uz ovisnost rasta pukotine o usmjerenosti konačnih elemenata (eng. *bias dependency*). S druge strane, odgovarajućim modifikacijama konačnih elemenata, geometrijski diskontinuitet se može pratiti ne po rubu elementa već po samom elementu. Takva modifikacija se naziva obogaćivanje (eng. *enrichment*), a elementi se samim time nazivaju obogaćeni elementi. Proširena metoda konačnih elemenata (eng. *extended finite element method*) predstavlja najpoznatiju i najpopularniju metodu ove vrste. U njoj, topologija pukotine je opisana implicitno, pomoću Heavisideovih polinoma i asimptotskih funkcija, što osigurava neovisnost rasta pukotine o mreži konačnih elemenata i time isključuje potrebu za promrežavanjem. Međutim, upotreba proširene metode konačnih elemenata za sobom dovodi do potrebe za visokim računalnim resursima, ali i problema vezanih za numeričku implementaciju. Povrh toga, gore navedene diskretne metode nisu samodostatne, tj. zahtijevaju dodatne kriterije za određivanje trenutka i mjesta nastanka kao i samog rasta pukotina.

Za razliku od diskretnih (diskontinuumskih) pristupa, informacije o oštećenju se u kontinuumskim (difuznim) modelima dobivaju kao dio rješenja matričnog sustava jednadžbi. Uvođenjem dodatne varijable koja kontrolira stupanj oštećenja, degradacija naprezanja, koja je povezana s nastankom i rastom pukotine, je izravno uključena u konstitutivni model. Vrijednost varijable oštećenja se kreće između 0 i 1, pri čemu 0 označava neoštećen materijal, dok 1 predstavlja potpuno degradiran materijal koji ne posjeduje krutost. S gledišta načina razvoja oštećenja, kontinuumski modeli oštećenja se mogu podijeliti na izotropne, ortotropne i anizotropne. U izotropnim modelima varijabla oštećenja je skalar, dok je u ortotropnim, tj. anizotropnim modelima ona tenzor višeg reda.

Kontinuumski modeli oštećenja, bazirani na lokalnom (standardnom) kontinuumu predstavljaju skup lokalnih kontinuumskih modela oštećenja. U tim modelima, ponašanje materijala u svakoj materijalnoj točki je opisano određenim konstitutivnim zakonom, a varijabla oštećenja ovisi isključivo o deformaciji u promatranoj točki. Točnije, uzimaju se u obzir samo lokalni efekti. To u konačnici uzrokuje lokalizaciju oštećenja koja dovodi do lokalnog gubitka eliptičnosti sustava parcijalnih diferencijalnih jednadžbi, zbog čega numeričko rješenje ne konvergira ka fizikalno smislenoj vrijednosti. Uz to, lokalni kontinuumski modeli nisu u stanju opisati efekt veličine uzorka (eng. *size effect*), koji se javlja u eksperimentalnim analizama.

Navedeni problemi mogu se riješiti uvođenjem nelokalnih kontinuumskih modela u kojima za razliku od lokalnih kontinuumskih modela, varijabla oštećenja u promatranoj točki ovisi i o deformaciji u točkama koje ju okružuju - nelokalni efekti se uzimaju u obzir. Iako postoji pozamašan broj nelokalnih kontinuumksih modela oštećenja, sve ih karakterizira uvođenje parametra duljine (eng. *length parameter*). Njime se omogućava regularizacija problema rubnih vrijednosti čime je osigurana eliptičnost parcijalnih diferencijalnih jednadžbi i omogućeno dobivanje objektivnih i fizikalnih rezultata. Također, nelokalni kontinuumski modeli imaju mogućnost opisivanja efekta veličine uzorka, upravo zbog činjenice da prilikom određivanja vrijednosti oštećenja uzimaju u obzir i nelokalne efekte.

Jedan od glavnih nedostataka kontinuumskih modela jest nemogućnost opisivanja stvarnog diskontinuiteta, što pukotina u konačnici i jest. Ova činjenica je dovela do razvoja takozvanih kontinuumskih-diskontinuumskih modela u kojima je kontinuumski način opisivanja oštećenja aktivan sve dok se ne pojavi pukotina, koja se kasnije modelira putem diskretnog principa. Povrh toga, upotreba nelokalnih kontinuumskih metoda za opisivanje oštećenja može, pri nekim uvjetima opterećivanja, dovesti do neispravnih rezultata u smislu krive topologije, ali i mjesta nastanka pukotine.

Metoda faznog polja

Metoda faznog polja (eng. *phase-field method*) predstavlja općeniti pristup modeliranju fizikalnih sustava s dvije ili više faza koje su razdijeljene nekom vrstom oštrog diskontinuiteta. Ova se metoda temelji na kontinuiranoj varijabli polja koja stvara razliku između fizikalnih faza preko "glatke" i kontinuirane tranzicije. U kontekstu mehanike oštećenja i loma, ova "glatka" tranzicija odnosi se na prijelaz iz neoštećenog u potpuno oštećeni dio materijala i obrnuto. Na taj način, oštar diskontinuitet, kojeg pukotina predstavlja, je zamijenjen kontinuiranom varijablom faznog polja (eng. *phase-field*

variable) koja u suštini tvori difuzni pojas.

Ono što ovu metodu čini izuzetno atraktivnom u području numeričkog modeliranja oštećenja i loma jest njena mogućnost da na elegantan i učinkovit način modelira složene procese koji se javljaju pri pojavi i rastu pukotina. Pukotine koje rastu bivaju automatski praćene preko varijable faznog polja koja se izračunava kao dio ukupnog rješenja matričnog sustava jednadžbi. Numerička vrijednost te varijable izravno utječe na razinu oštećenja u difuznom pojasu, čija je širina kontrolirana preko parametra duljine. Budući da metoda faznog polja spada u grupu nelokalnih kontinuumskih metoda, ovisnost konačnih rezultata o veličini mreže konačnih elemenata kao i problem opisivanja efekta veličine uzorka su izbjegnuti. Povrh toga, implementacija metode faznog polja u metodu konačnih elemenata predstavlja relativno jednostavan zadatak, bez obzira radi li se o problemu opisanom u dvije ili tri dimenzije.

Formulacija metode faznog polja, koja je prisutna u ovoj disertaciji, potječe od varijacijskog pristupa krhkom lomu gdje je osnovna Griffithova teorija krhkog loma pretvorena u problem minimizacije ukupne potencijalne energije. Unutarnji dio potencijalne energije ukupnog funkcionala se u tom slučaju sastoji od energije unutarnjih sila i energije oslobođene (disipirane) uslijed nastanka i rasta pukotine. Na taj način, varijacija ukupne potencijalne energije dobiva se minimiziranjem funkcionala po dvije varijable - pomaku i samoj pukotini. Varijacijski princip nalaže da se tijelo deformira, a pukotina raste na onaj način koji osigurava minimum ukupne potencijalne energije. Naći analitičko rješenje, tj. odrediti vrijednost pomaka i topologiju diskretne pukotine koji zadovoljavaju princip minimuma ukupne potencijalne energije je moguće samo u ograničenom broju slučajeva. Stoga je, nedugo nakon uvođenja varijacijskog principa krhkog loma, napravljena regularizacija izvedenog funkcionala. Pri tome je korištena eliptična regularizacija problema koji je karakteriziran Mumford-Shah funkcionalom. Posljedica regularizacije bilo je stvaranje sustava eliptičnih parcijalnih diferencijalnih jednadžbi koje preko varijable faznog polja u potpunosti opisuju nastanak i rast pukotine. Sam izvod metode faznog polja spada u još jednu od njenih pozitivnih karakteristika. Razlog tome jest činjenica da rubni uvjeti i međuovisnost varijabli slijede "prirodno" iz jednog izvoda - što nije slučaj s ostalim nelokalnim kontinuumskim metodama.

U zadnjem desetljeću popularnost metode faznog polja je značajno porasla, što potvrđuju brojni radovi na temu krhkog i duktilnog loma, ali i loma pri malim, tj. velikim deformacijama. Nadalje, metoda faznog polja uspješno je primijenjena za opisivanje nastanaka i rasta pukotina uzrokovanim termomehaničkim, elektromehaničkim, ali i hidrauličkim opterećenjem. Uz to, problemi zamora materijala, dinamičkog oštećenja kao i višerazinsko modeliranje heterogenih materijala također su

opisani metodom faznog polja.

Iako učinkovita i fleksibilna, metoda faznog polja ima odgovarajuće nedostatke i probleme koji se javljaju prilikom njene numeričke implementacije. Trenutno, dva najveća problema su nekonveksnost funkcionala ukupne potencijalne energije te potreba za gustim mrežama u području nastanka i rasta pukotina.

Prva poteškoća proizlazi iz činjenice da izvedeni funkcional nije strogo konveksan, već u sebi posjeduje nekoliko ekstrema. Točnije, mala promjena (diferencijal) ukupne potencijalne energije poprima vrijednost 0 u više različitih točaka, što otežava jednostavno određivanje globalnog minimuma. Sa stajališta metode konačnih elemenata to predstavlja veliki nedostatak, budući da nekonveksnost remeti konvergenciju i stabilnost simulacije, a to je pogotovo izraženo prilikom nastanka i rasta pukotine. Drugi problem vezan je za visoke računalne resurse koji proizlaze iz potrebe za vrlo gustim i finim mrežama konačnih elemenata. Veličina konačnog elementa je u izravnoj vezi s vrijednošću parametra duljine koji kontrolira debljinu difuznog sloja, a u problemima u kojima je topologija pukotine unaprijed poznata, ovo ne predstavlja značajan problem. U suprotnom, ovo može uvelike povećati računalne troškove, budući da se unaprijed progušćena mreža ne može jasno odrediti.

Višerazinsko modeliranje oštećenja i loma

Otpornost materijala na pojavu i razvoj pukotina u velikoj je mjeri uvjetovano njegovom mikrostrukturom. Male promjene oblika, prostorne raspodjele, volumenskog udjela ili mehaničkih svojstava svakog individualnog mikrokonstituenta mogu značajno izmijeniti lomne karakteristike materijala, te ga učiniti više ili manje otpornim na pojavu oštećenja. Prostorna i materijalna konfiguracija mikrostrukture materijala će u konačnici dovesti do nejednolične raspodjele polja deformacije i naprezanja što će u konačnici stvoriti područja pogodna za nastanak i razvoj oštećenja. Višerazinsko modeliranje materijala ima mogućnost povezivanja ponašanja mikrostrukture i odziva materijala na makrorazini, stoga predstavlja vrijedan alat za numeričko modeliranje oštećenja u heterogenim materijalima. Međutim, provođenje konkurentnih višerazinskih analiza koje u sebi uključuju neki od algoritama za modeliranje oštećenja predstavlja velik izazov.

Za početak, određivanje prosječne (homogene) vrijednosti parametra oštećenja unutar RVEa nije moguće klasičnom primjenom računalne homogenizacije prvog reda, budući da takav način u konačnici rezultira nefizikalnim vrijednostima. Također, takav pristup ne može odgovoriti na pitanje upitne reprezentativnosti RVEa prilikom

pojave oštećenja i loma kao i utjecaja njegove veličine na konačne rezultate. Druga prepreka očituje se u samoj zahtjevnosti sa strane računalnih resursa, budući da konkurentni pristup temeljen na primjeni direktne numeričke simulacije za rješavanje problema rubnih vrijednosti na mikrorazini, i bez algoritma oštećenja zahtjeva značajne računalne resurse. Još jedan problem koji zahtjeva pažnju jest neovisnost konačnih rezultata o veličini i orijentiranosti elemenata na makrorazini - bez obzira da li je u pitanju diskretni ili difuzni model oštećenja. U slučaju korištenja diskretnog pristupa modeliranju oštećenja i loma, potrebno je uvesti odgovarajući algoritam promrežavanja kao i dodatne kriterije za kontrolu razvoja i rasta pukotine. S druge strane, izostanak nelokalne teorije u slučaju difuznog modela oštećenja na makrorazini, rezultirat će ovisnošću konačnih rezultata o veličini mreže konačnih elemenata.

Ciljevi i hipoteze istraživanja

Cilj ovog istraživanja je razviti i implementirati novi višerazinski postupak za modeliranje oštećenja i loma u duktilnim heterogenim materijalima uslijed statičkog opterećenja. Postupak bi trebao zadovoljiti sljedeće zahtjeve:

- povezati svojstva heterogene mikrostrukture sa svakom materijalnom točkom na makrorazini,
- osigurati reprezentativnost mikrostrukturnog uzorka, tj. RVEa tijekom pojave i razvoja oštećenja,
- osigurati neovisnost konačnih rezultata o veličini i usmjerenosti konačnih elemenata,
- postići računalnu učinkovitost,
- omogućiti jednostavno proširenje sa problema krhkog loma pri malim deformacijama, na probleme duktilnog loma pri velikim deformacijama.

Također, metodologija bi trebala biti općenita i stabilna, tj. u stanju provesti višerazinsku analizu sa složenim mikrostrukturama na nižoj razini, s proizvoljnim brojem mikrokonstituenata različitog oblika, volumenskog udjela, prostorne raspodjele i mehaničkih svojstava. Hipoteza ovog rada je mogućnost razvoja takve metode kombiniranjem metode faznog polja na makrorazini i metode homogenizacije s reduciranim brojem stupnjeva slobode na mikrorazini.

Prisutnost nelokalnog kontinuumskog modela oštećenja, kao što je metoda faznog polja, na makrorazini će osigurati objektivnost i neovisnost konačnih rezultata o

mreži konačnih elemenata. Također, implementacija metode faznog polja u numeričku metodu kao što je MKE nije složen postupak, što je također dodatna prednost. Uz to, izostanak algoritma za modeliranje oštećenja na mikrorazini imat će pozitivan učinak na osiguravanje reprezentativnosti RVEa tijekom pojave i razvoja oštećenja.

S druge strane, funkcija metode homogenizacije s reduciranim brojem stupnjeva slobode bit će rješavanje problema rubnih vrijednosti na mikrorazini i određivanje prosječnih (homogeniziranih) materijalnih svojstava mikrostrukture kroz upotrebu računalne homogenizacije prvog reda. Valjanost i primjenjivost metode homogenizacije s reduciranim brojem stupnjeva slobode za bilo koji konstitutivni zakon od iznimne je važnosti jer pridonosi općoj primjenjivosti cjelokupne višerazinske procedure.

U sklopu ovog rada razvijena je višerazinska konkurentna metoda za modeliranje nastanka i razvoja oštećenja u krhkim i duktilnim materijalima, pri statičkom opterećivanju za dvodimenzijske i trodimenzijske probleme. Metoda je ugrađena u komercijalni MKE programski paket Abaqus, primjenom korisničkih rutina *UEL* i *UMAT*. Pomoću više različitih geometrijskih uzoraka te nekoliko različitih mikrostruktura, provedena je detaljna i temeljita verifikacija razvijene metode. Velika pozornost posvećena je računalnoj učinkovitosti, stoga je prva faza testiranja orijentirana isključivo na nju. Ostale faze testiranja usmjerene su na ispitivanje stabilnosti i učinkovitosti novorazvijenog višerazinskog postupka u određivanju nastanka i razvoja oštećenja u slučaju složenih mikrostruktura.

Zaključak i doprinos rada

Glavni doprinosi ovog rada i istraživanja odnose se na područje višerazinskog modeliranja oštećenja u krhkim i duktilnim heterogenim materijalima. Ključni doprinosi rada su:

1. Implementacija algoritma metode homogenizacije s reduciranim brojem stupnjeva slobode u komercijalni MKE programski paket Abaqus

    - Algoritam homogenizacije s reduciranim brojem stupnjeva slobode je inicijalno razvijen i testiran u komercijalnom programskom paketu Matlab. Međutim, s ciljem provođenja konkurentnog višerazinskog postupka, algoritam je naknadno implementiran u komercijalni MKE programski paket Abaqus.
    - Brojni testovi na različitim 2D i 3D mikrostrukturama pokazali su zamjetan nivo računalne učinkovitosti i točnosti što je ključno u višerazinskom

postupku. Također je uočeno da pojedine vrste makro-opterećenja, pri određenim materijalnim konfiguracijama na mikrorazini, treba izbjegavati.

2. Spajanje metode faznog polja i metode homogenizacije s reduciranim brojem stupnjeva slobode u jedan jedinstveni višerazinski postupak

   - Razvijeni konkurentni višerazinski postupak je dokazano ispravan i računalno učinkovit, što pokazuju testovi provedeni na nekoliko geometrijskih uzoraka pri čemu je razmatran krhki i duktilni lom.
   - Postupak je također stabilan, što je dokazano ponovo na nekoliko geometrijskih uzoraka pri čemu je na mikrorazini bila prisutna složena mikrostruktura.
   - U konačnici, postupak je općenit i fleksibilan. Točnije, proširenje na ostale tipove materijala, npr. hiperelastični materijal, i druge modele plastičnosti kao što je Drucker-Prager ili Mohr-Coloumb kriterij tečenja, predstavlja relativno jednostavan postupak.

Ključne riječi: mikrorazina, konkurentne višerazinske metode, heterogeni materijal, RVE, homogenizacija, metoda homogenizacije s reduciranim brojem stupnjeva slobode temeljena na analizi klastera, metoda faznog polja, Abaqus, k-means klasteriranje, Lippmann-Schwingerova jednadžba, Greenova funkcija, materijalni klaster

Contents

List of Figures

List of Tables

Nomenclature

Calligraphy letters

$\mathcal{H}$	Heaviside function
∇	gradient operator
∇^2	Laplace operator

Greek letters

α	geometric crack function
β^I	homogeneous variable in the domain of the I-th material cluster
$\boldsymbol{\Phi}$	vector of global phase-field degrees of freedom
$\boldsymbol{\phi}$	vector of local phase-field degrees of freedom
$\boldsymbol{\sigma}$	Cauchy stress tensor
$\boldsymbol{\sigma}^{\pm}$	tensile/compressive part of the Cauchy stress tensor
$\boldsymbol{\varepsilon}$	small strain tensor
$\boldsymbol{\varepsilon}^0$	far-field small strain tensor
$\boldsymbol{\varepsilon}^{\mathrm{e}}$	elastic part of the small strain tensor
$\boldsymbol{\varepsilon}^{\mathrm{p}}$	plastic part of the small strain tensor
$\boldsymbol{\varepsilon}^{\pm}$	tensile/compressive part of the small strain tensor
$\boldsymbol{\varepsilon}_{\mathrm{dev}}$	deviatoric part of the small strain tensor
$\boldsymbol{\Xi}$	position vector in the Fourier coordinate system for the reference configuration

$\boldsymbol{\xi}$	position vector in the Fourier coordinate system for the current configuration
χ^I	characteristic function in the domain of the I-th material cluster
$\delta\boldsymbol{\phi}$	variation of the vector of local phase-field degrees of freedom
$\Delta\boldsymbol{\sigma}$	incremental Cauchy stress tensor
$\Delta\boldsymbol{\varepsilon}$	incremental small strain tensor
$\Delta\boldsymbol{\varepsilon}^0$	incremental far-field small strain tensor
$\delta\Gamma$	variation of the crack surface
$\Delta\mathbf{F}$	incremental deformation gradient tensor
$\Delta\mathbf{F}^0$	incremental far-field deformation gradient tensor
$\Delta\mathbf{P}$	incremental first Piola-Kirchhoff stress tensor
$\delta\mathbf{u}$	variation of the displacement field
$\delta\mathbf{v}$	variation of the vector of local displacement degrees of freedom
$\Delta\overline{\boldsymbol{\sigma}}$	incremental value of the homogenized (macroscopic) Cauchy stress tensor
$\Delta\overline{\boldsymbol{\varepsilon}}$	incremental value of the homogenized (macroscopic) small strain tensor
$\Delta\overline{\boldsymbol{\varepsilon}}_{\mathrm{dev}}$	incremental value of the homogenized (macroscopic) deviatoric part of the small strain tensor
$\Delta\overline{\varepsilon}_{\mathrm{h}}$	incremental value of the homogenized (macroscopic) hydrostatic part of the small strain tensor
$\Delta\overline{\mathbf{F}}$	incremental value of the homogenized (macroscopic) deformation gradient tensor
$\Delta\overline{\mathbf{F}}_{\mathrm{dev}}$	incremental value of the homogenized (macroscopic) deviatoric part of the deformation gradient tensor

$\Delta\overline{\mathbf{P}}$	incremental value of the homogenized (macroscopic) first Piola-Kirchhoff stress tensor
$\delta\phi$	variation of the phase-field parameter
$\delta\Pi$	variation of the total (free) energy functional
$\delta\Pi^{\text{ext}}$	variation of the external part of the total (free) energy functional
$\delta\Pi^{\text{int}}$	variation of the internal part of the total (free) energy functional
δ	Dirac delta function
$\delta\boldsymbol{\varepsilon}$	correction of the incremental small strain tensor, variation of the small strain tensor
δ_{ij}	Kronecker delta symbol
$\mathbb{\Phi}^0$	Green's function in the Cartesian coordinate system- fourth-order tensor
Γ	crack surface
γ	crack surface density function
$\hat{\boldsymbol{\sigma}}$	Cauchy stress tensor in the Fourier coordinate system
$\hat{\boldsymbol{\varepsilon}}$	small strain tensor in the Fourier coordinate system
$\hat{\mathbb{\Phi}}^0$	Green's function in the Fourier coordinate system- fourth-order tensor
κ	Lamé constant (bulk modulus)
κ^0	Lamé constant (bulk modulus) of the reference material
λ	Lamé constant
λ^0	Lamé constant of the reference material
λ_a	a-th eigenvalue
μ	Lamé constant (shear modulus)

Nomenclature

μ^0	Lamé constant (shear modulus) of the reference material
ν	Poisson ratio
Ω	volume of the n-dimensional body
Ω^I	volume of the I-th material cluster
$\overline{\boldsymbol{\varepsilon}}$	homogenized (macroscopic) small strain tensor
$\overline{\nu}$	homogenized (macroscopic) Poisson ratio
$\overline{\psi}$	homogenized (macroscopic) strain energy density
$\overline{\psi}_{\mathrm{e}}$	homogenized (macroscopic) elastic part of the strain energy density
$\overline{\psi}_{\mathrm{p}}$	homogenized (macroscopic) plastic part of the strain energy density
$\overline{\sigma}_{\mathrm{eq}}$	homogenized (macroscopic) von Mises stress
$\overline{\sigma}_{\mathrm{h}}$	homogenized (macroscopic) value of the hydrostatic part of the Cauchy stress tensor
$\overline{\sigma}_{\mathrm{y}}^0$	homogenized (macroscopic) initial yield strength
$\overline{\varepsilon}_{\mathrm{eq}}^p$	homogenized (macroscopic) equivalent plastic strain
$\overline{\varepsilon}_{\mathrm{h}}$	homogenized (macroscopic) value of the hydrostatic part of the small strain tensor
$\partial\Omega$	surface of the n-dimensional body
$\partial\Omega_{\mathrm{h}}$	surface of the n-dimensional body on which traction load is applied
Φ	Green's function in the Cartesian coordinate system-scalar function
ϕ	crack phase-field parameter
Π	total (free) energy functional
Π^{b}	body's bulk energy

Π^{ext}	external part of the total (free) energy functional
Π^{int}	internal part of the total (free) energy functional
Π^{s}	fracture-induced dissipating potential energy
ψ	strain energy density
$\psi^{\pm}$	tensile/compressive part of the strain energy density
$\psi_{\text{e}}^{\pm}$	tensile/compressive part of the elastic strain energy density
ψ_{e}	elastic part of the strain energy density
ψ_{p}	plastic part of the strain energy density
ρ	density of the n-dimensional body
σ_{y}	hardening function
σ_{y}^{0}	initial yield strength
ε	scalar value of tolerance
$\varepsilon_{\text{eq}}^{\text{p}}$	equivalent plastic strain
ξ	scalar parameter in the geometric crack function

Latin letters

$\hat{\mathbf{q}}$	polarization stress tensor (in the small strains configuration) in the Fourier coordinate system
$\hat{\mathbf{u}}$	vector of displacement in the Fourier coordinate system
$\mathbb{A}$	strain/deformation gradient concentration tensor
$\mathbb{C}$	material stiffness tensor
$\mathbb{C}^{0}$	material stiffness tensor of the reference material
$\mathbb{D}^{IJ}$	interaction tensor
$\mathbb{I}$	fourth-order identity tensor
$\mathbb{I}_{\text{s}}$	symmetric part of the fourth-order identity tensor

Nomenclature

$\mathbb{M}$	system Jacobian matrix of the discretized Lippmann-Schwinger equation
$\ddot{\mathbf{u}}$	vector of the acceleration
$\mathbf{b}$	volume force vector
$\mathbf{B}_{\mathbf{v}}, \mathbf{B}_{\phi}$	matrices of shape functions derivatives
$\mathbf{C}$	material stiffness tensor in Voigt notation, right Cauchy–Green deformation tensor
$\mathbf{F}$	deformation gradient tensor
$\mathbf{F}^0$	far-field deformation gradient tensor
$\mathbf{f}_{\mathbf{v}}^{\text{ext}}, \mathbf{f}_{\phi}^{\text{ext}}$	local external force vectors
$\mathbf{f}_{\mathbf{v}}^{\text{int}}, \mathbf{f}_{\phi}^{\text{int}}$	local internal force vectors
$\mathbf{h}$	surface traction vector
$\mathbf{I}$	second-order identity tensor
$\mathbf{K}_{\mathbf{v}\,\mathbf{v}}, \mathbf{K}_{\mathbf{v}\,\phi}, \mathbf{K}_{\phi\,\mathbf{v}}, \mathbf{K}_{\phi\,\phi}$	global stiffness matrices
$\mathbf{k}_{\mathbf{v}\,\mathbf{v}}, \mathbf{k}_{\mathbf{v}\,\phi}, \mathbf{k}_{\phi\,\mathbf{v}}, \mathbf{k}_{\phi\,\phi}$	local stiffness matrices
$\mathbf{M}_a$	a-th projection matrix
$\mathbf{n}$	unit outward-pointing normal
$\mathbf{N}_{\mathbf{v}}, \mathbf{N}_{\phi}$	matrices of shape functions
$\mathbf{n}_a$	a-th eigenvector
$\mathbf{P}$	first Piola-Kirchhoff stress tensor
$\mathbf{Q}$	polarization stress tensor in the finite strains configuration
$\mathbf{q}$	polarization stress tensor in the small strains configuration
$\mathbf{r}$	residual vector of the discretized Lippmann-Schwinger equation

$\mathbf{R}_{\mathbf{v}}, \mathbf{R}_{\phi}$	global residual vectors
$\mathbf{r}_{\mathbf{v}}, \mathbf{r}_{\phi}$	local residual vectors
$\mathbf{S}$	deviatoric part of the Cauchy stress tensor, second Piola-Kirchhoff stress tensor
$\mathbf{S}^*$	effective (non-degraded) deviatoric part of the Cauchy stress tensor
$\mathbf{u}$	vector of displacement
$\mathbf{V}$	vector of global displacement degrees of freedom
$\mathbf{v}$	vector of local displacement degrees of freedom
$\mathbf{X}$	position vector in the Cartesian coordinate system for the reference configuration
$\mathbf{x}$	position vector in the Cartesian coordinate system for the current configuration
$\overline{\mathbb{C}}$	homogenized (macroscopic) material stiffness tensor
$\overline{\mathbf{C}}$	homogenized (macroscopic) material stiffness tensor in Voigt notation
$\overline{E}$	homogenized (macroscopic) modulus of elasticity
$\overline{G}_{\mathrm{c}}$	homogenized (macroscopic) critical value of the strain energy release rate
$\overline{k}$	homogenized (macroscopic) material parameter of Swift's non-linear hardening law
$\overline{l}$	homogenized (macroscopic) length-scale parameter
$\overline{r}$	homogenized (macroscopic) material parameter of Swift's non-linear hardening law
c^I	volume fraction of the I-th material cluster
E	modulus of elasticity
f	von Mises yield surface

g	degradation function
g^p	plastic degradation function
G_c	critical value of the strain energy release rate
i	complex number, current iteration number
k	total number of material clusters, material parameter of Swift's non-linear hardening law
l	length-scale parameter
n	number of dimensions, current increment number
r	material parameter of Swift's non-linear hardening law
s	scalar value that controls the slope of the cubic degradation function
t	time
w, w_1, w_2	cost functions

Other letters

$\mathscr{F}$	Fourier transform operator
$\mathscr{F}^{-1}$	inverse Fourier transform operator
$\mathscr{H}$	strain energy density history field parameter
$\mathscr{L}$	linear differential operator

1. Introduction

1.1. Background and motivation

Mechanical properties of modern engineering materials are in a direct link with their hierarchical nature. This hierarchy arises from the interaction of simple, small-scale constituents, that together form a compound that can spam multiple time- but also length-scales. At their lower scales, heterogeneous materials often exhibit a significant level of heterogeneity. This heterogeneity manifests itself in the form of several different microconstituents (material phases) with arbitrary shape, volume fraction, spatial distribution and mechanical properties - **Figure 1.1**.

Therefore, the overall mechanical behaviour of the material will be the result of the mutual interaction and contribution of each of its material phases. Advanced manufacturing techniques such as 3D printing [1–3] and sintering [4–6] allow for the creation of a specific nano and microstructures, which can eventually lead to advantageous thermal, electrical or mechanical properties at the macroscale. This multiscale nature of heterogeneous materials has become the subject of intensive research in the field of material science, but it also poses a continuing challenge in the computational modelling of macroscopic structures.

Traditional phenomenological constitutive relations [7] characterize the average behaviour of material, i.e. the contributions from all the material phases are not accounted for as an individual interaction of separate constituents. The main disadvantage of this approach lies in its inability to span microstructural mechanisms essential for understanding the general behaviour of the material. Besides mathematical limitations, practical numerical problems also involve mesh dependency of the results. In addition, highly localized processes such as plasticity, fatigue and damage always occur at the lower scales first, and they cannot be captured appropriately using classical continuum mechanics.

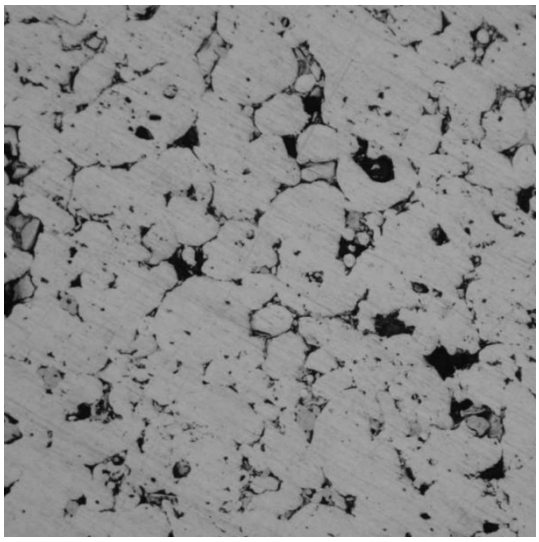

(a) Al-Mg-Si-Cu-Fe alloy [8]

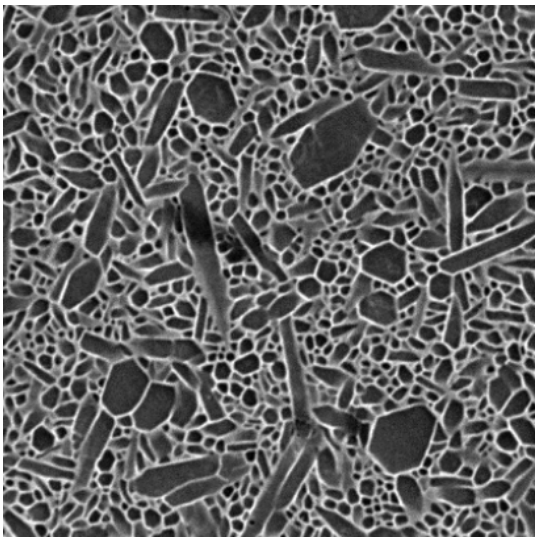

(b) Sintered silicon nitride ceramics [9]

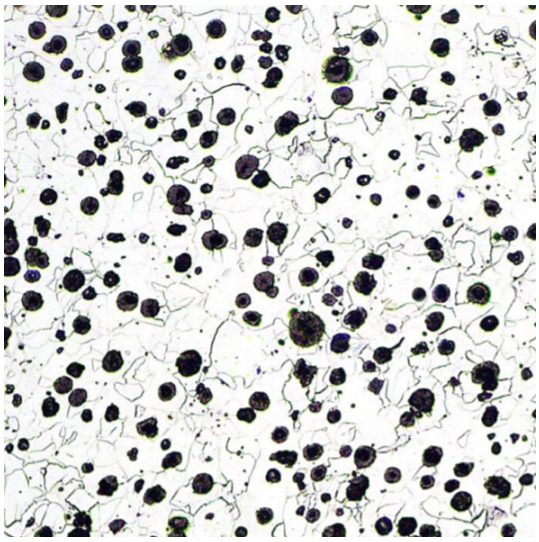

(c) Nodular graphite cast iron [10]

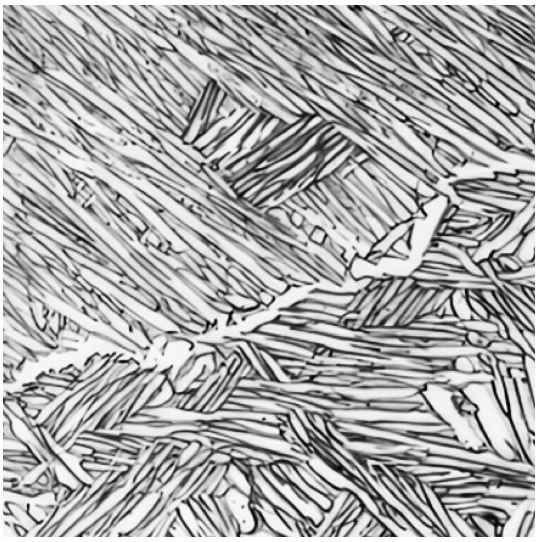

(d) Ti-5Al-1.5Mo-1.8Fe alloy [11]

Figure 1.1: Microstructure of modern heterogeneous materials

Although with flaws, the classical phenomenological approach is still widely used in numerical simulations for a wide variety of physical problems. Its robustness, stability and overall simplicity are the main reasons for its strong presence in the industry. With the further increase in computational resources, more and more effort will be invested into the development of new numerical procedures that take into account material behaviour at lower scales. However, the classical phenomenological approach will certainly be in use for some time to come.

1.2. Numerical modelling of heterogeneous materials

Generalized continuum mechanics, also known as higher-gradient theories, represents one of the ways in which it is possible to consider structural phenomena at the lower scales. By introducing a higher-order gradient of deformation, microscopic information can be incorporated into the numerical analysis. The first known work in extension to the higher-order continuum theory was done by the Coserrat brothers at the beginning of the 20th century [12]. In their work, they introduced additional rotational degrees of freedom (DOF) at the microscale, along with a non-symmetric stress tensor and a higher-order couple stress tensor. The potential of this approach was recognized about half a century later, as evidenced by the works of Mindlin [13–16], Koiter [17], Toupin [18, 19] and Eringen [20]. With the introduction of double stress tensor as the work conjugate to the second derivative of the displacement, Mindlin [14, 21] further extended the original Cosserat theory in order to account for not only local rotations but also stretch gradients. Some approaches introduce material with microstructure [13, 22], where each point of the microstructure has its own DOF. In the last few decades, higher-order theories have become a valuable tool in the field of computational mechanics for modelling of not only simple linear elastic but also highly localized material responses such as plasticity and damage. Due to higher-order gradients, the description of localization phenomena is possible without loss of ellipticity of governing equations [23–28].

Currently, the major challenge in all higher-gradient theories lies in the relatively large number of coefficients that are associated with higher-order terms [29]. The experimental determination of these coefficients can be quite a complex and delicate task, since the gradient of strain is generally not directly informed by the microstructure. In addition to that, numerical implementation of higher-order theories often requires computationally expensive and demanding numerical algorithms, which are not suitable for practical use.

Multiscale methods, on the other hand, represent a class of numerical methods with the ability to analyze material behaviour at different levels, i.e. scales. These methods imply dependency between different scales, where the solution at one scale is transferred to the other scale in an appropriate way. Thereby, the response of the material at the macrolevel will be directly related to the microstructure geometry and the material properties of the microconstituents. Depending on the variable-passing hierarchy, we distinguish bottom-up and top-down approaches. In the bottom-up

approach, the solution is driven by the smaller scale, while in the top-down approach, lower scales are added until desired effects are captured [30]. Due to the rapid increase in computational power, and their ability to link material behaviour at different levels, multiscale methods have become a particularly attractive tool in the field of numerical modelling of heterogeneous materials. Although there exists a wide range of multiscale methods, generally speaking, they can be classified as hierarchical, concurrent, sequential, homogenization, parallel and hybrid [30]. For more details on the development and applications of the multiscale methods see [31–34].

1.2.1. Concurrent multiscale methods

Concurrent multiscale methods, which will be used in this dissertation, represent the most popular and widely used class of multiscale methods [35–38]. These methods avoid the calibration process in the phenomenological approach by directly establishing the link between the microstructure and the response of the material at the macrolevel, with the use of the homogenization method [30, 35, 36, 39–45]. Because of that, they do not require an explicit *a priori* constitutive relation at the macrolevel which opens up the possibility of modelling geometrical and material nonlinearities, as well as a description of a microstructural irregularity. In terms of variable-passing hierarchy, concurrent methods fall in the category of bottom-up approaches - since the solution is driven by the behaviour at a lower scale.

During the analysis, the material properties and its behaviour at each macroscopic point is obtained from the behaviour and properties of its microstructure, which is defined by *representative volume element* (RVE) [46–50]. After solving the RVE boundary value problem at the microlevel, homogenization (averaging) of stress and material tangent matrix needs to be performed. The averaged (homogenized) values are then transferred back to the macrolevel, where they are used as input parameters for the boundary value problem at the macrolevel - **Figure 1.2**. For a material with random microstructure, its true macroscopic properties are obtained as converged values only if the size of the RVE becomes sufficiently large, i.e. RVE should be a statistically representative sample of the material's microstructure [49, 50].

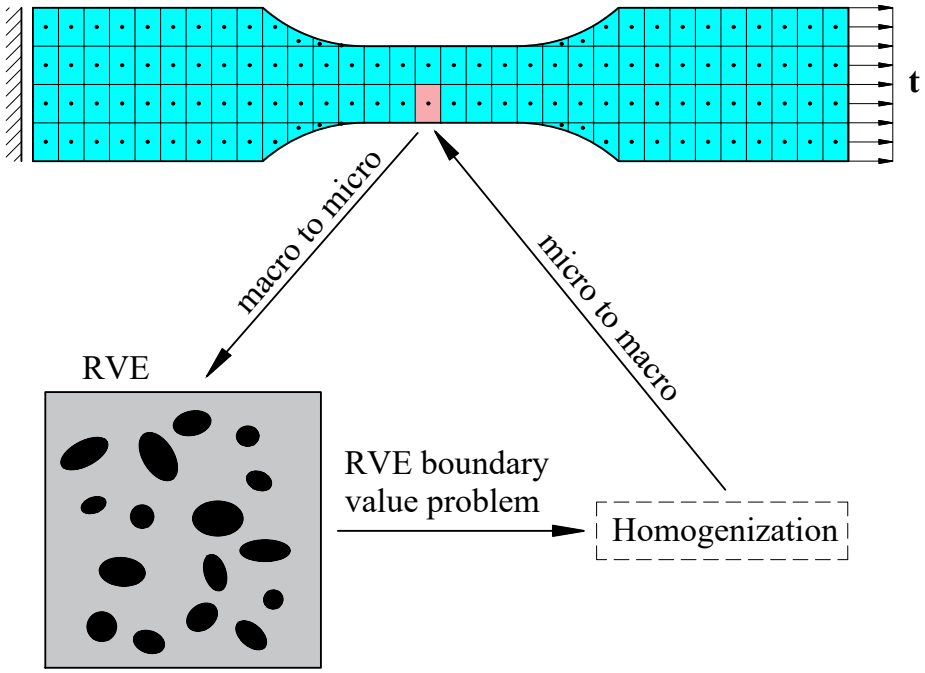

Figure 1.2: Schematic representation of the concurrent multiscale approach

First-order computational homogenization [39–43], which will be used in this dissertation, is the most flexible and accurate method through which one can obtain the macro response of the RVE. It can be defined by assuming scale separation and vanishing external body force inside the RVE, i.e. through the use of Hill-Mandel macro-homogeneity condition [51, 52]. This condition is equivalent to the statement that the volume average of the work variation done on the RVE must be equal to the work variation at the macrostructural material point. It also ensures that the homogenized stress and strain tensors are admissible variables in the macroscale constitutive relations.

In terms of boundary conditions, the solution of the RVE boundary value problem can be obtained using displacement boundary conditions (DBC), traction boundary conditions (TBC) or periodic boundary conditions (PBC). It has been shown that the use of DBC eventually leads to too stiff RVE behaviour, while the results obtained with TBC show too compliant behaviour. On the other hand, PBC [30] provide the best homogenization results and the fastest convergence properties by increasing the RVE size. As shown in [39, 40], the results obtained by PBC lie between the values obtained by the DBC (upper bound) and TBC (lower bound). For proper use, PBC require periodicity in the geometry of the RVE that is being analyzed, which is not the case in DBC or TBC. For more details on PBC and their application see [30].

Direct numerical simulation (DNS) represents the most accurate and flexible method with whom one can obtain the solution of the RVE boundary value problem. Finite element method (FEM) [53] and Fast Fourier transform (FFT)-based micromechanics methods [54, 55], are two basic ways in which DNS analysis can be performed. However, due to the large number of DOF, DNS can be very time-consuming. Since the RVE boundary value problem has to be solved for each material point at the macrolevel and for each increment of the analysis, the total computational cost of this approach is tremendous. For practical problems, the use of concurrent multiscale approach with either FEM or FFT-based solver at the microlevel is inefficient.

1.2.2. Reduced-order multiscale methods

Bearing in mind the fact that the goal of solving the RVE boundary value problem is to determine the average (homogenized) behaviour of the microstructure, one can easily conclude that the precise description of the strain and stress field inside the RVE is not crucial. This is because high concentrations of stress and strain in certain areas of the RVE do not have a significant influence on their average values.

With this information in mind, the complexity of the RVE boundary value problem can be reduced in various ways without significant loss of accuracy of the final results, which are needed at the macrolevel. Throughout decades, a significant number of homogenization methods have been developed with the goal of finding an appropriate balance between accuracy and computational complexity. These are generally referred to as reduced-order methods. Analytical micromechanical methods [52, 56–59], the Voronoi cell finite element method (VCFEM) [60], the generalized method of cells [61], the transformation field analysis (TFA) [62], the nonuniform transformation field analysis (NTFA) [63, 64] and the proper orthogonal decomposition (POD) [65], are some of the most successful methods of this kind. Although successful in the reduction and speed up of the calculation at the microlevel, the aforementioned methods are plagued by several issues.

Analytical micromechanical methods, which are based on analytical solutions and mean-field assumptions, aim to describe heterogeneous microstructure by employing several different microstructural descriptors. Although efficient, their usefulness drastically decreases when considering complex microstructure and localized phenomena such as plasticity and damage. Similarly, the generalized method of cells, which is simply a generalization of the original method of cells developed by Aboudi [66], also suffers from the inability to analyze arbitrary microstructure for the case of complex loading conditions. Its use is limited only to microstructure consisting of two material

phases, i.e. matrix and unidirectional fibers that all have uniform rectangular shape and are distributed in such a way, that they form an ordered rectangular array. On the other hand, the VCFEM attempts to overcome difficulties in the calculation at the lower level by using Dirichlet tessellation in order to decompose complex microstructure into relatively small numbers of Voronoi cells. This is particularly useful in the case of crystal plasticity, where the observed microstructure is made of a specific number of crystal grains. While successful in the reduction of DOF, the VCFEM mesh brings with it problems involving complex numerical implementation which is especially pronounced in the case of 3D analysis. The TFA, NTFA and POD approach the problem in a different way by first conducting DNS simulations on the RVE subjected to specific loading conditions. This process is called the *offline stage* [67]. POD uses the collected data from the DNS analysis to construct the reduced basis which are then used in the RVE boundary value problem during the concurrent analysis. As shown in [65], POD can lead to significant savings in computational time and resources. However, the approach is suitable only for history-independent problems where a relatively small number of DNS simulations in the offline stage are sufficient to obtain satisfactory results. The idea behind TFA and NTFA is to use data generated in the offline stage to define a set of reduced variables that are then subjected to evolution equations. Consequently, the computational cost of both TFA and NTFA is low, but the inclusion of empirical laws that require further calibration is a limitation. Furthermore, the RVEs need to be subjected to irreversible deformation to obtain the plastic modes which leads to an extensive exploration of the deformation space in the offline stage.

1.2.3. Data-driven multiscale methods

With the exponential growth of computational resources in the last decade, data-driven homogenization methods have attracted lots of attention. By sifting through the raw data in the database, previously unknown regularities or patterns can be extracted and generalized to make accurate predictions [67]. A raw dataset can be generated either by conducting a large number of numerical simulations or through experimental analysis. Regarding the type of raw dataset, data-driven methods in the field of multiscale analysis of heterogeneous materials are divided into two main approaches, i.e. microscopic and macroscopic.

The macroscopic approach uses the raw data in order to make predictions about the material behaviour and its properties based on the specific type of loading condition. In the case of a concurrent multiscale approach, this means that the value of the homogenized stress tensor and material tangent matrix is obtained directly from

the value of small strain or deformation gradient tensor at the macrolevel. Since solving the RVE boundary value problem is avoided, data-driven macroscopic approaches exhibit the highest efficiency regarding both computational time and resources.

One of the first attempts at the reduction of the concurrent multiscale analysis complexity employing a data-driven macroscopic approach was presented by Yvonnet et al. [68]. In it, the raw data, generated through a series of finite element simulations on the RVE subjected to different macroscopic loading conditions, was interpolated using multidimensional spline interpolation [69]. The result was an explicit relationship between macroscopic strain energy density and stress tensor of heterogeneous hyperelastic material undergoing small strains. The same procedure was later applied in [70] to model the behaviour of heterogeneous hyperelastic materials exhibiting large strains, while in [71], the influence of the microstructure was considered. Le et al. [72] followed the same procedure, but used neural networks to interpolate the data for the case of 3D analysis, where multidimensional spline interpolation would be computationally expensive task. A different approach, in which calculations are carried out directly on the pure (unprocessed) experimental data was presented by Kirchdoerfer and Ortiz [73]. The developed algorithm aims to assign to each material point the state from a prespecified data set while at the same time satisfying the conservation laws. Later, the approach was improved by the same group of authors in [74], with the use of clustering analysis. Specifically, to each data point from the raw data set a variable relevance was assigned depending on the distance to the solution and maximum-entropy estimation. Flaschel et al. [75] developed an unsupervised sparse regression approach that can determine constitutive law for heterogeneous hyperelastic materials from the data set that can come either from the experimental analysis or numerical simulations. The presented approach does not require stress data but only displacement and global force data, and it delivers interpretable models from a potentially very large library of candidate functions. Flaschel and his co-workers later extended the original procedure to model history-dependent problems, i.e. plasticity [76]. Along with their computational efficiency, the rapid development of deep neural networks [77] is another reason for the attractiveness and popularity of macroscopic approaches in the field of multiscale analysis of heterogeneous materials.

Although computationally efficient and quite versatile, the applicability of the macroscopic approaches is, to a large extent, dependent on the raw data that is available. Description of highly localized and history-dependent problems such as plasticity and damage requires the generation of enormous amounts of data, which in some cases is not a possibility. In addition, due to the lack of microscopic information, the accuracy and smoothness of the prediction obtained with macroscopic approaches is

often limited. This is especially pronounced when a significant change in heterogeneous material stiffness occurs due to the accumulation of damage or transition from elastic to elastoplastic region.

Microscopic approaches on the other hand collect data at each discretization point in the DNS analysis of the offline stage in order to reduce the complexity and speed up the calculation of the RVE boundary value problem that is present at each material point at the macrolevel. POD, TFA and NTFA fall in the category of microscopic approaches; however, with flaws listed in **subsection 1.2.2**.

To address the limitations of POD, TFA and NTFA, Liu developed a new microscopic approach for predicting the behaviour of general heterogeneous materials undergoing both elastic and inelastic deformations [78]. The proposed data-driven, two-scale approach included two major innovations: (1) the use of data compression algorithm, k-means clustering [79], during the offline stage in order to decompose the complex microstructure into a group of subdomains, i.e. clusters, and (2) a new method called *self-consistent clustering analysis* (SCA) used in the *online stage* that is valid for any constitutive law of each material phase, without the need for additional calibration. The first innovation makes use of k-means clustering, or any other clustering algorithm (for example self-organizing map [80]), to reduce the number of DOF at the microlevel. This is achieved by grouping the points that have similar behaviour into appropriate clusters, i.e. areas in which the field of stress and strain is constant. The second innovation on the other hand is more complex, and it involves the use of the Lippmann-Schwinger integral equation [67, 81] to analyze and model the behaviour of each cluster in the RVE.

As evident from [67, 78], the approach is characterized by a significant reduction in degrees of freedom, in some cases by several orders of magnitude, and a noticeable level of the accuracy of homogenized results. As a consequence, many ideas and problems in the field of concurrent multiscale approach that were previously too demanding from the point of both computational time and resources suddenly became a possible reality. Strain softening of heterogeneous materials, a particularly interesting and demanding topic in the field of multiscale analysis, found its place alongside self-consistent clustering analysis in [67, 82, 83]. Problems involving finite strains at both reversible and irreversible deformations weren't left behind either [84–87]. Moreover, the original approach [67] has been used in the multiscale analysis of fiber-reinforced composites [67], woven composites [88, 89], anisotropic crystal plasticity [67, 85, 86], thermoelasticity [90] and even microstructure with porosities [91]. Instead of the finite element method, which was used in [68], Bessa et al. [92] utilized SCA to speed up the generation of raw data, which was then interpolated in the same manner as in

[68]. A modification of SCA, called virtual clustering analysis [93] further improved the accuracy of homogenized results by taking into account boundary conditions of the Lippmann-Schwinger equation that were previously neglected. The mathematical investigation, which is necessary for a better understanding of the governing equations behind the self-consistent scheme during the online stage was conducted by Schneider [94]. However, only for material behaviour under small strains, which since then hasn't been extended to account for finite strains.

1.3. Numerical modelling of damage and fracture

Fracture is one of the most commonly encountered failure models in modern engineering materials and structures. Accurate prediction of damage accumulation, that eventually leads to cracking-induced failure is, therefore, a key ingredient in the design of reliable and safe products. Fracture mechanics, a sub-domain of solid mechanics in which the *a priori* presence of crack is assumed, was introduced in 1921, by Griffith [95]. His milestone work provided a quantitative connection between the fracture stress and crack size in ideally brittle materials and thus introduced the branch of fracture mechanics into the field of solid mechanics. According to the original approach [95], a crack becomes unstable and the fracture occurs when the strain energy change is sufficient to overcome the surface energy of the material [96]. Since this model assumes that the fracture energy comes exclusively from the surface energy of the material, it can only be applied in the case of ideally brittle solids.

Later development by Irwin [97, 98], who included the energy dissipated by plastic flow and developed the energy release rate concept, extended the original Griffith approach to a wider range of materials making it more useful for solving engineering problems. In 1961, Paris and his co-workers [99] applied fracture mechanics principles to the fatigue crack growth and thus introduced the idea that the rate of crack growth may depend on the stress intensity factor. Two years later, Paris law, i.e. equation that describes crack growth regarding the number of cycles was introduced. Since then, principles of fracture mechanics have been applied to a wide range of materials, exhibiting both small and finite deformations, subjected both static and dynamic loading.

Today, i.e. one century after the original Griffith theory, fracture mechanics has become a standard part of numerical methods, mostly FEM. Numerical modelling of damage and fracture in the 21st century represents a wide field of methods and

algorithms that all have two common goals: (1) predict the moment in which damage occurs, and (2) describe the strain softening phenomena from the moment the damage occurs to the moment of failure. Generally speaking, fracture can be numerically modelled using either a discontinuous approach (also referred to as a discrete approach) or a continuous (diffusive) one. This split into two major approaches arises from the manner in which the crack, present in the material, is treated - see **Figure 1.3**. In the former, the displacement field is allowed to be discontinuous across the fracture surfaces whereas in the latter the displacements are continuous everywhere but the stress values are gradually reduced to model the degradation process.

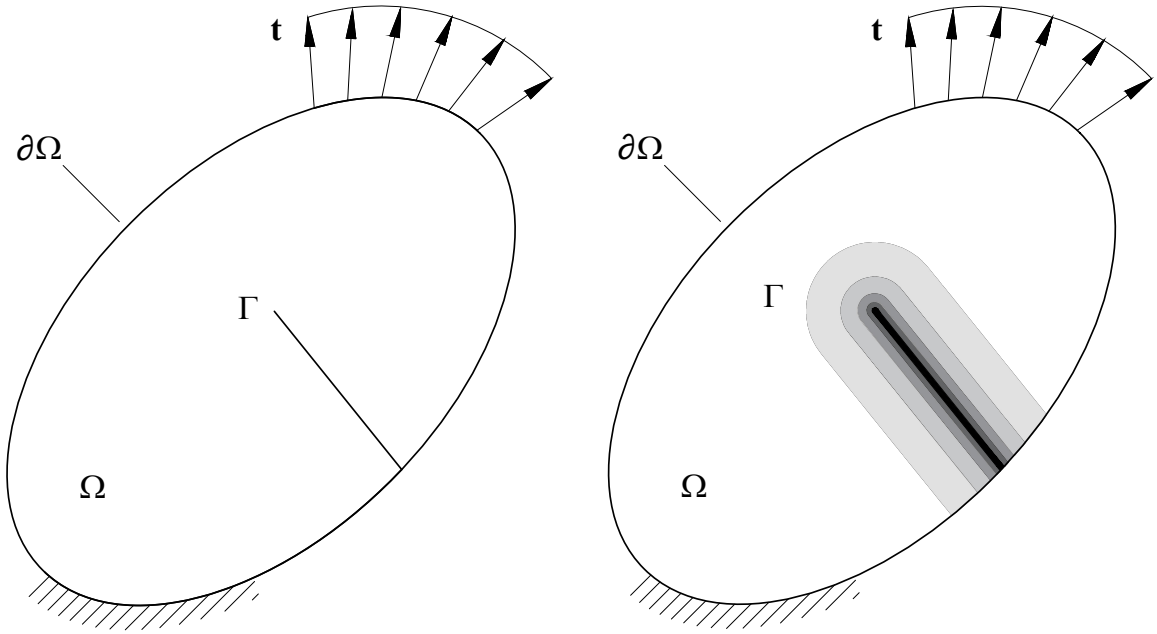

(a) Discrete crack modelling **(b)** Diffusive crack modelling

Figure 1.3: Schematic representation of the crack modelling approaches

1.3.1. Discrete crack modelling

Since they introduce the crack as a sharp geometrical discontinuity, as stated before, field of the displacement in the discrete crack approaches is discontinuous across the fracture surface. Today, two of the most well-known theories behind the discontinuous crack modelling approach are the linear elastic fracture mechanics (LEFM) [95, 97, 98] and the cohesive zone model (CZM) - firstly introduced in Barenblatt [100] and Dugdale [101].

Unlike LEFM, whose applicability is limited to problems in which the nonlinear zone ahead of the crack tip is negligible, CZM has experienced a significantly larger use in problems involving discrete crack propagation and failure. With its ability to

completely eliminate stress singularity at the crack tip, CZM has been applied to model fracture processes in both ductile and brittle solids [102–105], as well as for small and finite deformations [104–107]. It is implemented through interface or generalized contact elements which compose a narrow band ahead of the crack front called a cohesive zone [108]. At this zone, the material behaviour is governed by the constitutive law that describes the relationship between the stress and relative displacement of the cohesive surfaces. In order to be applied, CZM demands *a priori* knowledge about the crack path and the constitutive law, making a detailed experimental analysis a necessity. For more information on CZM and its advantages and limitations see [103].

From the perspective of numerical analysis, the introduction of the discontinuous displacement field poses a great challenge, especially in mesh-based numerical methods such as FEM. Since the crack propagates along the element edges, both standard LEFM and CZM can exhibit a significant dependence of the final result on the element's size and orientation. The only way to mitigate this problem is through the utilization of a proper remeshing algorithm [109, 110] that will track crack topologie as it propagates. Being only applicable to triangular (in the case of 2D analysis) and tetrahedral (in the case of 3D analysis) type elements, remeshing approach also exhibits significant implementation difficulties that arise due to the need for suitable transfer of the state variables from one mesh to another [111].

On the other hand, with the specific modification of the standard finite elements, discontinuity can be resolved not on the element's boundaries but on the element itself. This modification is usually called enrichment and the elements are therefore called enriched elements. Extended finite element method (XFEM), developed by Moes et al. [112], represents the most popular and widely used method of this kind. In the XFEM, crack topology is represented implicitly, through the use of finite elements that are enriched with the Heaviside function and asymptotic near-tip singularity functions. This enables cracks to propagate completely independent of the underlying mesh and thereby removes the need for mesh refinement. Since it was first proposed, XFEM has attracted lots of attention [113–118], and has even been successfully coupled with the CZM [119]. However, the computational complexity of the XFEM can quickly reach significant levels. The reason for this is the increase in the DOF, which occurs due to the increase in the number of level set functions that are required to describe each individual segment of the crack surface. Also, just like remeshing, XFEM is plagued with implementation issues that involve numerical integration, conditioning and data handling, which are especially pronounced in the case of 3D analysis.

It is also important to emphasize, that both LEFM and CZM, as well as the enriched finite element methods, from the fundamental point of view, are not

self-contained in the sense that they require additional criteria to address the following questions:

- When and where a crack initiates?
- How much it propagates and in which direction?

Some well-established fracture criteria that are commonly used are maximum circumferential stress criterion [120], minimum strain energy density criterion [121] and maximum strain energy release rate criterion [109]. A detailed overview and comparison of these criteria can be found in [109, 122].

To this end, the discontinuity surface has to be explicitly tracked, which is, sometimes, an intractable task for those problems with arbitrary and complex crack paths. Despite recent advances, numerical modelling of complex fracture problems using a discrete approach is still a challenging issue, especially in three dimensions [123, 124].

1.3.2. Diffusive crack modelling

In contrast to the discrete crack modelling approaches, crack topology in diffusive crack modelling approaches (often called continuum damage or smeared crack modelling approaches) is obtained as a part of the solution. With the introduction of the damage parameter at the material level that controls the stiffness of the material, degradation of stress associated with the crack formation is incorporated directly into the constitutive model. From the point of damage development, continuum damage models can be either isotropic, orthotropic or anisotropic [125]. In the isotropic damage modelling, which will be used in this dissertation, the damage parameter is a scalar variable that ranges between 0 (virgin material, with elastic stiffness) and 1 (completely damages material, with no stiffness). It is also assumed that this scalar variable depends on a state variable, which in turn depends on the strain. On the other hand, orthotropic and anisotropic damage models require the damage parameter to be a higher-order tensor, which is then able to capture different evolutions of damage in different directions.

Continuum damage models that are based on standard, also called local, continuum represent a class of local continuum damage models. The material behaviour in these models is characterized by the constitutive law at each material point, which does not exhibit the influence of the surrounding points. This is because the state variable depends only on strain at the point of consideration, i.e. only local effects are taken into account. As a consequence, this leads to a local loss of ellipticity of the governing differential equations, which in turn leads to physically meaningless solutions,

as discussed in de Borst et al. [126]. As evident from [127], local continuum damage models suffer from pathological mesh dependency, yielding physically unrealistic results. Moreover, they are unable to interpret size effects which are often observed in experimental analysis.

To overcome these drawbacks, various regularization techniques have been proposed, including nonlocal [128] and gradient-enhanced continuum approach [129], gradient damage model [130], phase-field fracture formulation [131], the crack band theory [132], micropolar [133] and later micromorphic continuum theory [134]. Among all these methods, the damage variable is made to depend on the strain state in a neighbourhood (associated with a characteristic length) of the point under consideration, i.e. nonlocal effects are taken into account. Essentially, through the use of material length parameter, the aforementioned approaches are able to regularize the original ill-posed boundary value problem, cure pathological mesh dependence and predict size effect. The material length parameter, which is related to both geometry and the material itself [135, 136], helps to diffuse (smear) the sharp crack topology over a finite domain region, thus allowing the objectivity of the numerical solution to be recovered.

The major drawback of continuous approaches is that the true discontinuity cannot be properly represented. This led to the development of so-called *continuous-discontinuous* approaches, where a continuous description of cracking is used until the final stage of failure, which is modelled by a discontinuous approach [137–140]. However, there is no consensus in defining the transition procedure between continuous and discontinuous approaches, especially when the cracking-induced anisotropy is important. Furthermore, the aforementioned techniques have been applied only to problems with the existing dominant propagating crack. On top of that, the use of nonlocal approaches [128, 129] for specific types of loading can lead to incorrect failure characterization in terms of damage initiation and propagation, as reported in Simone et al. [141]. From the author's own experience, this phenomenon may also occur in phase-field fracture formulation. The problem in question can be avoided by the introduction of material length parameter as a function of strain [142, 143]. However, the underlying assumption of these models might not have a microstructurally correct physical background as explained by Poh et al. [144].

1.3.3. Phase-field fracture approach

Phase-field modelling represents a general approach for the description of the behaviour of physical systems that consist of several phases that are divided by sharp interfaces.

It is based on the introduction of a continuous field variable (order parameter) which differentiates between multiple physical phases within a given system through a smooth transition. In the context of fracture, such an order parameter is used to describe the smooth transition between the fully broken and intact material phase, thus approximating the sharp crack discontinuity.

What makes this approach particularly attractive is its ability to elegantly simulate complicated fracture processes, including crack initiation, propagation, merging and branching - without the need for additional ad-hoc criteria. Propagating cracks are tracked automatically by the evolution of the smooth crack field on the fixed mesh, which leads to a significant advantage over the discrete fracture description methods outlined in **subsection 1.3.1**. In addition, numerical implementation of the phase-field fracture approach into the FEM represents a straightforward task, for both two- and three-dimensional problems.

The phase-field fracture formulation, which will be used in this dissertation, was conceived by Francfort and Marigo [131], who proposed a generalization of the original Griffith's approach by introducing the energy associated with the creation of new fracture surfaces into the total energy functional. As a consequence, the original Griffith's approach was transformed into an energy minimization problem, where the total energy functional can be minimized with respect to both displacement and the crack geometry. Energy functional derived in [131] was later regularized by Bourdin et al. [145, 146], who used Ambrosio and Tortorelli [147] elliptic regularization of the free-discontinuity problem characterized by the Mumford-Shah functional [148] to reformulate the problem into a system of elliptical partial differential equations that completely determine the crack evolution. Bourdin's formulation introduced a scalar variable (later termed the phase-field variable) that discriminates intact from the broken material and a small positive length scale parameter that controls the width of the localization band. Regularized phase-field fracture model [145] is, herein, referred to as *isotropic* since it does not distinguish between tensile and compressive fracture behaviour. In order to prevent the formation of cracks during compression, Amor et al. [135] presented an *anisotropic* phase-field model in which elastic strain energy density was additively decomposed into volumetric and deviatoric part. Another anisotropic model was proposed in Lancioni and Royer-Carfagni [149], to handle fracture for the case of shear loading, and was later applied to model the development of cracks in the masonry work of the French Panthéon, one of the most famous historical monuments in Paris.

Miehe et al. [150] achieved a major milestone in the development of the phase-field fracture model with the introduction of a spectral strain energy split and a new,

more intuitive, formulation that was more accessible to the engineering community. Since then, the popularity of the phase-field method in the field of numerical modelling of damage and fracture increased exponentially. Today, a considerable number of various phase-field brittle fracture formulations has been developed for both quasi-static [150–154] and dynamic [154–156] models. Furthermore, the framework has been extended to handle ductile fracture at small [157–159], but also finite strains [160–163]. Moreover, problems involving thermomechanical fracture [164–166], hydraulic fracture [167, 168], fatigue crack propagation [169–173], electromechanical fracture [174, 175], fracture in porous media [176–178] or biological tissues [179] and even multiscale damage modelling [180–182] were all tackled through the use of phase-field fracture approach. A majority of the aforementioned formulations have been thoroughly verified by the available numerical benchmark tests and qualitative experimental data comparing the predicted and observed crack paths. For quantitative experimental validations see Ambaty et al. [161], Nguyen et al. [136], Miehe et al. [162], Seleš et al. [172], Lesičar et al. [183], Dittmann et al. [160], Jukić et al. [173], and Nagaraja et al. [184].

However, the phase-field method is not without its disadvantages, with two main issues being: (1) non-convexity of the underlying free energy functional, and (2) the need for extremely fine mesh in the crack propagation zone.

The first flaw constitutes a major problem within the so-called *monolithic* treatment of the variational formulation where the system of partial differential equations is fully coupled. Therefore, both displacement and the crack phase-field are computed simultaneously as part of one solution vector. However, due to the non-convexity of the free energy functional, multiple extremes exist (schematically shown in **Figure 1.4**) thus creating issues with convergence and stability, which is especially pronounced during *brutal* crack evolution as well as in the post-peak loading regime.

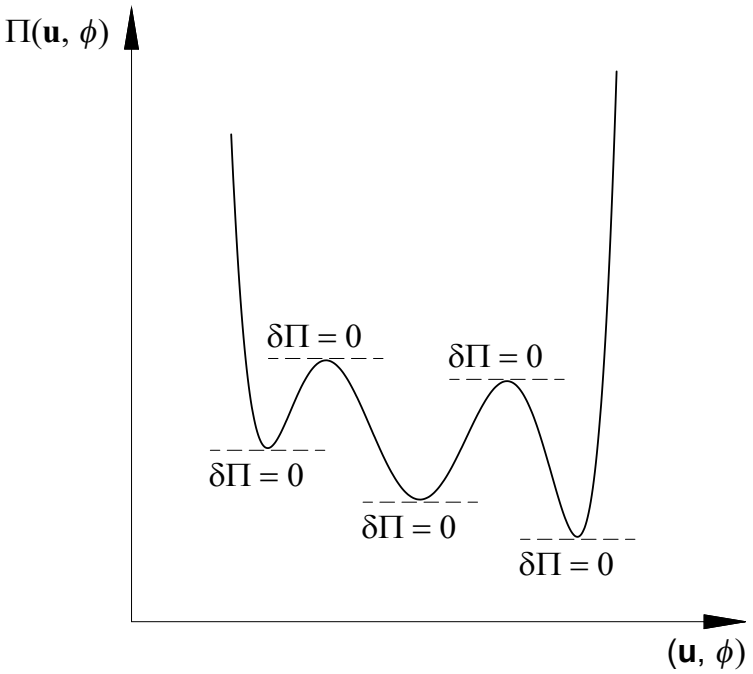

Figure 1.4: Schematic representation of non-convex energy functional

To mitigate this issue, different approaches have been proposed, most notably the modified line-search assisted monolithic solver [185], arc-length procedure [186], the modified Newton scheme with Jacobian modification [187] and a quasi-Newton algorithm [188]. A more robust and effective way of dealing with the problem of non-convexity is the utilization of a so-called *staggered* solution strategy, which is based on the observation that, while the free energy functional is generally non-convex, it is convex with respect to either displacement or the phase-field variable, if the other one is held constant [145]. Unlike monolithic procedure, the system of partial differential equations in a staggered solution scheme is fully decoupled, i.e. displacement and the crack phase-field are computed separately. This property was first exploited by Miehe et al. [151] where a staggered algorithm based on the single iteration procedure was presented. However, to be accurate with only one iteration the size of the loading increment has to be small, which is computationally inefficient for more complex problems. This led to the development of staggered schemes that allow for larger increment sizes by performing multiple iterations until the specific stopping criterion is met. In Duda et al. [189] and Bourdin et al. [146] the stopping criterion was the relative difference between solution variables in two consecutive iterations. A similar approach has been presented by Lesičar et al. [183]. In Ambati et al. [153], the status of the increment convergence has been determined based on the normalized change of the system's energy, while Seleš et al. [190, 191] developed a staggered solution scheme

with a stopping criterion based on the value of the residual norm.

The second issue that plagues the phase-field method is the need for fine meshes in the zone where the crack forms and propagates. The size of finite elements is directly related to the value of the length scale parameter controlling the width of the localization band, and in the cases where the crack topologies are known *a priori*, this does not represent a major problem. However, in the opposite case, this can increase computational cost significantly, since pre-refined meshes cannot be generated in an appropriate way. One antidote to this flaw is the utilization of the remeshing algorithm, which will track the crack topologies and refine the mesh depending on the specific criterion. Phase-field simulations with adaptive mesh refinement have been reported in e.g., Borden et al [192], Klinsmann et al. [193], Heister et al. [194], Jukić et al. [195], Wick et al. [187], Artina et al. [196]. Computational parallelization on the other hand is another remedy to the computational cost of phase-field fracture models, as presented in [154]. To this day, the high computational cost associated with fine meshes is one of the main reasons for the absence of a phase-field fracture approach in commercial use.

1.4. Multiscale modelling of damage and fracture

It is not unknown that the material fracture for any kind of loading is highly sensitive to the microstructure that forms it. Slight changes in the shape, spatial distribution and volume fraction of each individual microconstituent can alter material behaviour significantly, making it more or less resistant to the occurrence of damage and formation of cracks. In Čanžar et al. [197], an experimental analysis that was conducted on the nodular cast iron showed a high dependency of the fatigue crack initiation and propagation on the microstructure of the material. More precisely, the shape of the graphite nodules, which are one out of three microconstituents, proved to be a key factor in determining the material's resistance to fatigue-induced cracking. Spherically shaped graphite nodules had a positive impact on the values of stress by acting as stress concentration reductors, thus improving material's resistance to the formation of microcracks. On the other hand, the volume fraction of voids in the microstructure of sintered steel turned out to be a main enhancer/diminisher of its fracture properties [4]. Non-uniform stress and strain state inside the microstructure also arise due to the specific spatial distribution of the microconstituents, which can create areas suitable for the occurrence and development of damage. In the field of numerical modelling of damage and fracture in heterogeneous materials, multiscale analysis is a valuable tool

that couples the microstructural stress state with the macroscopic calculation in order to predict fracture processes at the macrolevel of material.

Over the past two decades, extensive studies on the numerical modelling of failure processes in heterogeneous materials have been performed. Unfortunately, the use of computational homogenization scheme described in **subsection 1.2.1** exhibits several issues. First of all, highly localized phenomena such as damage cannot be appropriately calculated at the macrolevel by simply performing averaging over the RVE domain, as it will lead to physically inaccurate and meaningless results [198]. Not only that, but due to the loss of statistical homogeneity, which occurs in strain softening, the representativeness of the RVE may come into question [50, 199]. Moreover, a distinction between scales is no longer clearly determined, resulting in another problem known as the lack of separation of scales [200, 201]. To tackle these issues, Gitmann et al. [202] developed a coupled-volume multiscale method in which the RVE is associated with a domain of finite volume (an element in a FEM context) rendering it objective to the size of the RVE; however, the approach did not experience any major extensions or improvements. Different procedures, all based on the Hill-Mandel homogenization scheme, that aim to describe material failure at the macrolevel by calculating homogenized traction-separation law (homogenized cohesive law) from the finite element analysis at the lower scales were developed for both adhesive [203, 204] and cohesive [205, 206] crack formations. By utilizing computational homogenization for adhesive type cracking, in [203] the existence of an RVE for strain softening materials (under tension and mixed-mode loading) which exhibits diffusive damage has been reported. The same result has been presented in [204] for fiber-epoxy material that undergoes discrete cracking. In [206] the authors have proved the existence of an RVE for softening materials, for both adhesive and cohesive cracks, by deriving a traction-separation law from the homogenized values of stress and strain. However, the method has been applied only to materials with a simple microstructure that exhibits discrete cracking. The question of the RVE representativeness during the strain softening was also the subject of work done by Nguyen et al. [207], where a modified averaging scheme was presented. More precisely, homogenization of the damage parameter was carried out only on the RVE domain that has experienced failure - failure averaging homogenization scheme. Unfortunately, the scheme is not suitable for any type of nonlocal continuum damage model since the failure zone is determined with respect to nonlocal equivalent deformation. Also, aditional criteria will be needed if one wishes to address strain softening in elastoplastic region. An approach that combines phase-field fracture formulation [131], multiscale finite element method based on multiscale basis functions [208, 209] and XFEM [112]

to model brittle fracture in heterogeneous materials can be found in [180–182]. In the mentioned works, the entire domain of interest was divided into two regions - with coarse and fine mesh discretization, which were modelled and computed individually. In the former, multiscale finite element method based on multiscale basis function was utilized to capture heterogeneous response, whereas in the latter phase-field was used to approximate sharp crack discontinuity while the XFEM was applied to model discontinuous displacement field. However, all numerical examples which were presented in [180–182] were conducted for cases of very simple 2D microstructures undergoing only brittle fracture.

One of the first approaches that deals with the problem of ductile softening in heterogeneous materials can be found in Ibrahimbegović et al. [210], where the solution method for the strong coupling of two scales, employing the implicit integration scheme at each scale, was utilized. Ductile heterogeneous material behaviour was captured by a two-phase microstructural model, where the nonlinear behaviour of one phase was described by the plasticity model undergoing small strains and the nonlinear behaviour of the other phase was represented by a damage model. Since the microstructure in question consisted of a phase that did not exhibit any kind of damage, the true failure of the microstructure and the material at the macrolevel couldn't be captured properly. Tchalla et al. [211] conducted a multiscale analysis of damage in fiber-reinforced elastoplastic composites by combining mean-field homogenization and incremental micromechanics scheme. The proposed approach; however, did not show good agreement with experimental analysis, which was especially pronounced in the case of high volume fraction of fibers. Also, due to the utilization of the mean-field homogenization method alongside the incremental micromechanics scheme, the intensive damage localization problem wasn't addressed. In order to bring stability and at the same time ensure clear separation of scales, Lesičar et al. [212] developed a two-scale approach in which first-order computational homogenization was performed on two microstructural samples, one without damage and another with embedded nonlocal gradient-enhanced damage model. The procedure also included a novel damage averaging scheme closely related to the failure averaging homogenization scheme presented in [207]. Herein, due to the presence of a local continuum at the macroscale, pathological mesh dependency of the final results at the macrolevel was unresolved. Approaches that deal with the problem of multiscale modelling of damage in ductile heterogeneous materials at finite strains were presented in e.g. Benedeti et al. [213] and Xiang et al. [214]. In [213], authors have developed a three-dimensional concurrent multiscale approach for describing failure in polycrystalline materials in which the intergranular degradation and failure at the microlevel were modelled with cohesive

and frictional contact laws. The macroscopic measure of degradation was obtained by the comparison of effective macro-stress for the damaged and undamaged RVE, while the pathological mesh dependence at the macrolevel was avoided through the use of integral nonlocal counterparts of the strains. However, the contribution [213] did not include any force-displacement diagrams, which calls into question the robustness and accuracy of the presented approach. As in [211], the mean-field homogenization method was also utilized in [214] to model the failure of aluminum and titanium alloy plates during impact loads. The evaluation of the damage variable was described by the nucleation-and-growth model [215], while the acceleration of the damage softening due to void coalescence was taken into account through the use of percolation theory [216]. Although more efficient than computational homogenization, mean-field homogenization does not provide a clear connection between the deformation gradient at two scales and therefore requires additional assumptions to create it. Contribution [82], already mentioned in **subsection 1.2.3**, represents a major milestone in the field of multiscale modelling of damage in ductile heterogeneous materials. It included a novel, three-step homogenization scheme, that was able to capture size effect and ensure RVE representativeness during the strain softening, but also a nonlocal formulation at the macrolevel that managed to completely eliminate mesh dependency. Since the RVE boundary value problem at each macroscopic point is resolved through the use of SCA, the computational efficiency of this approach is extremely high. However, the discretization of the microstructural domain into a relatively small number of clusters also led to the need for energy regularization, i.e. subsequent calibration of the damage parameters that are dependent on the different loading conditions. In addition, the multiscale damage formulation presented in [82] is not suitable for problems in which energy dissipated by plasticity is larger than that of elasticity.

1.5. Research hypothesis and objectives

The main objective of this study is to develop and implement a novel multiscale procedure for modelling damage and fracture processes in ductile heterogeneous materials for the static/quasi-static type of loading. The framework should be able to meet the following:

- link heterogeneous RVE properties with each macroscopic point,
- ensure RVE representativeness during strain softening,
- cure pathological mesh dependence at the macrolevel,

- provide computational efficiency,
- ensure straightforward extension from small strains brittle fracture, to the finite strains ductile fracture.

Also, the proposed multiscale framework should be general and robust, i.e. capable of dealing with complex microstructures, with an arbitrary number of microconstituents of different shape, volume fraction, spatial distribution and mechanical properties. The hypothesis is the possibility of the development of such a method by combining the phase-field fracture algorithm at the macrolevel and SCA at the microlevel.

The presence of a nonlocal continuum damage model, such as phase-field, at the macrolevel will ensure objectivity and mesh independence of the final results. In addition, phase-field implementation into FEM is a straightforward task (as stated in **subsection 1.3.3**), and any extension to different types of material behaviour is therefore easily doable. Also, the absence of a damage algorithm at the microlevel will be a beneficial factor in retaining a clear distinction between the two scales and ensuring the RVE representativeness during the strain softening process.

SCA will be used to solve the RVE boundary value problem and to obtain averaged (homogenized) properties of the microstructure through the use of a first-order computational homogenization. Utilization of the SCA at the microlevel will greatly increase computational efficiency, which is especially important for large-scale concurrent multiscale simulations. Moreover, as a method, SCA is valid for any constitutive law of each material phase (as stated in **subsection 1.2.3**), and therefore can be applied to any type of material/microstructure.

In contrast to many existing approaches, the calculation of the material degradation at the macrolevel will not include any kind of damage analysis at the microlevel. Generated RVE will serve exclusively for obtaining homogenized stress and tangent stiffness tensor, equivalent plastic deformation and strain energy density. By upscaling the homogenized values, the phase-field fracture algorithm will receive all the necessary input to perform its calculation and to determine the material degradation.

1.6. Thesis outline

The thesis is organized in five chapters. After the introductory lines described above, Chapter 2 includes a detailed derivation of all the necessary equations needed for the SCA, along with numerical validation, performed on two- and three-dimensional elastoplastic heterogeneous microstructure. Complete SCA analysis, which consists of the offline and online stage, is executed using commercial software Matlab. Chapter 3

gives a thorough description of the phase-field fracture formulation for both brittle and ductile materials as well as its numerical implementation into FEM. In Chapter 4, a novel concurrent multiscale procedure, based on SCA and phase-field fracture formulatino is presented. The proposed concurrent framework is implemented into commercial finite element software Abaqus, through the use of a user subroutine and is thoroughly tested on several geometrical samples. Finally, concluding remarks are given in Chapter 5 with suggestions for future work.

2. Data-driven homogenization: Self-consistent clustering analysis

2.1. Background

In the field of multiscale analysis of heterogeneous materials, the term "representative volume element", i.e. RVE represents a concept of crucial importance. There, unfortunately, is not a unique and exact definition of the RVE for an arbitrary heterogeneous material. However, in general, an RVE can be considered as a sample of a microstructure of an arbitrary size which fulfills the following three conditions: (1) an increase in the size of the sample does not lead to considerable differences in the homogenized properties, (2) the size of the sample is large enough so that the homogenized properties are independent of the microstructural randomness, and (3) the size of the sample is small enough so that the separation of scales principle is valid. In terms of geometry, RVE can be quite complex, and can consist of several different material phases of different shape, volume fraction and spatial distribution. Accurate description of the stress and strain field inside the RVE for a given load is not a trivial task, and it requires a significant number of finite elements (in the case of FEM), i.e. pixels/voxels (in the case of FFT-based solver).

Since the sole purpose of the RVE boundary value problem is to obtain homogenized values for a given load, the number of the DOF that are present at the microlevel does not need to be significant. However, although it is possible to drastically reduce the number of DOF at the microlevel, the concurrent multiscale approach that utilizes DNS for solving the RVE boundary value problem is, to this day, still too demanding from the point of computational time and resources. The main reason for this is the fact that the RVE boundary value problem has to be solved for every material point at the macrolevel, at every increment of the analysis. Of course, this does not represent an issue if the amount of macroscopic material points is in the range of single-digit numbers, but for practical problems, this number will be measured in thousands.

Reduced-order homogenization methods aim to further improve the efficiency of the concurrent multiscale simulations, by addressing the high costs associated with the calculation at the lower levels. However, the use of these methods comes at the cost of lower accuracy of the homogenized results that are upscaled to the macrolevel. The rule is simple: the more effort one puts into reducing the complexity of the RVE boundary value problem, the more accuracy will suffer. However, this dependence is not linear, and it is always beneficial to find the optimal balance between computational efficiency and overall accuracy. Also, reduced-order homogenization methods have their limits regarding RVE complexity, material behaviour, and the type of loading that the RVE is subjected to. This is also true for self-consistent clustering analysis [78] that is presented in detail in the following pages.

2.2. Offline stage

In the data-driven multiscale methods that fall in the category of microscopic approaches, the term "offline stage" stands for the part of the analysis that needs to be done only one time, but the quality of its execution can greatly affect the accuracy of homogenized results. The main goal in this stage is to gather as much information as possible about the behaviour of the microstructure subjected to different types of loading. This can be done by conducting multiple DNSes, in most cases by FEM, on the RVE which is discretized with a significant number of finite elements. This fine discretization will allow for an accurate description of the stress and strain field inside the RVE, which is a beneficial factor in any offline stage. Although conducting multiple finite element simulations with a large number DOF is not computationally efficient (especially in three-dimensional cases), the fact that it needs to be done only once makes it profitable in the long run.

In POD [65], the offline stage boils down to conducting several finite element analyses on the RVE subjected to different loading conditions. The goal is to collect the data from each integration point in order to construct the reduced basis which will then be used in the RVE boundary value problem during the concurrent multiscale approach. However, as stated in **subsection 1.2.2**, POD is only suitable for history-independent problems, where a relatively small number of finite element simulations are sufficient in order to obtain satisfactory results. The values and the type of macro-loading conditions that the RVE is subjected to in the offline stage are directly correlated with the problem of the macrostructure that is being analyzed. Therefore, it is important to choose offline macro-loading conditions that will include both minimum and maximum values

of the strain/deformation gradient present at the macrostructure under consideration. Otherwise, POD won't be able to provide accurate results, as the macro-loading conditions that have appeared during the analysis were not captured during the offline stage. The NTFA [63, 64], an extension of the TFA [62], uses data collected from the finite element analyses to define a set of internal variables that are then subjected to the evolutionary equations. Basically, the RVE boundary value problem is reduced through a decomposition of the microscopic inelastic strain field into a finite set of transformation fields. Again, as in the case of the POD, it is important to have general knowledge about the type of loading that the RVE will undergo during the concurrent analysis. This is because a relatively small number of plastic modes, obtained by the series of finite element simulations in the offline stage, will be used to describe complex inelastic strain field inside the RVE.

Unlike POD and NTFA, self-consistent clustering analysis [78], or simply SCA, is a reduced-order homogenization method that aims to improve computational efficiency at the microlevel by physically decomposing RVE into a finite number of large subdomains - **Figure 2.1**. These subdomains are designed as material clusters henceforth, and in each one of them the distribution of an arbitrary variable is constant, i.e. every local variable β within each material cluster is uniform [67]. This is equivalent to considering a piecewise uniform approximation to the local variables of interest in the RVE [67]

$$\beta\left(\mathbf{x}\right) = \sum_{I=1}^{k} \beta^{I} \chi^{I}\left(\mathbf{x}\right), \tag{2.1}$$

where β^I is the homogeneous variable in the I-th material cluster, $\mathbf{x}$ stands for position vector, k is the total number of material clusters, while χ^I represents a characteristic function in the domain of the I-th material cluster of the volume Ω^I, and is defined as

$$\chi^{I}\left(\mathbf{x}\right) = \begin{cases} 1, & \mathbf{x} \in \Omega^{I} \\ 0, & \mathbf{x} \notin \Omega^{I} \end{cases} \tag{2.2}$$

From (2.2), the following cluster averaging relationship is derived

$$\int_{\Omega} \chi^{I}\left(\mathbf{x}\right) \square \mathrm{d}\mathbf{x} = \int_{\Omega^{I}} \square \mathrm{d}\mathbf{x}, \tag{2.3}$$

where $\square$ signifies any quantity of interest to be averaged in the cluster domain Ω^I of the RVE with total volume Ω.

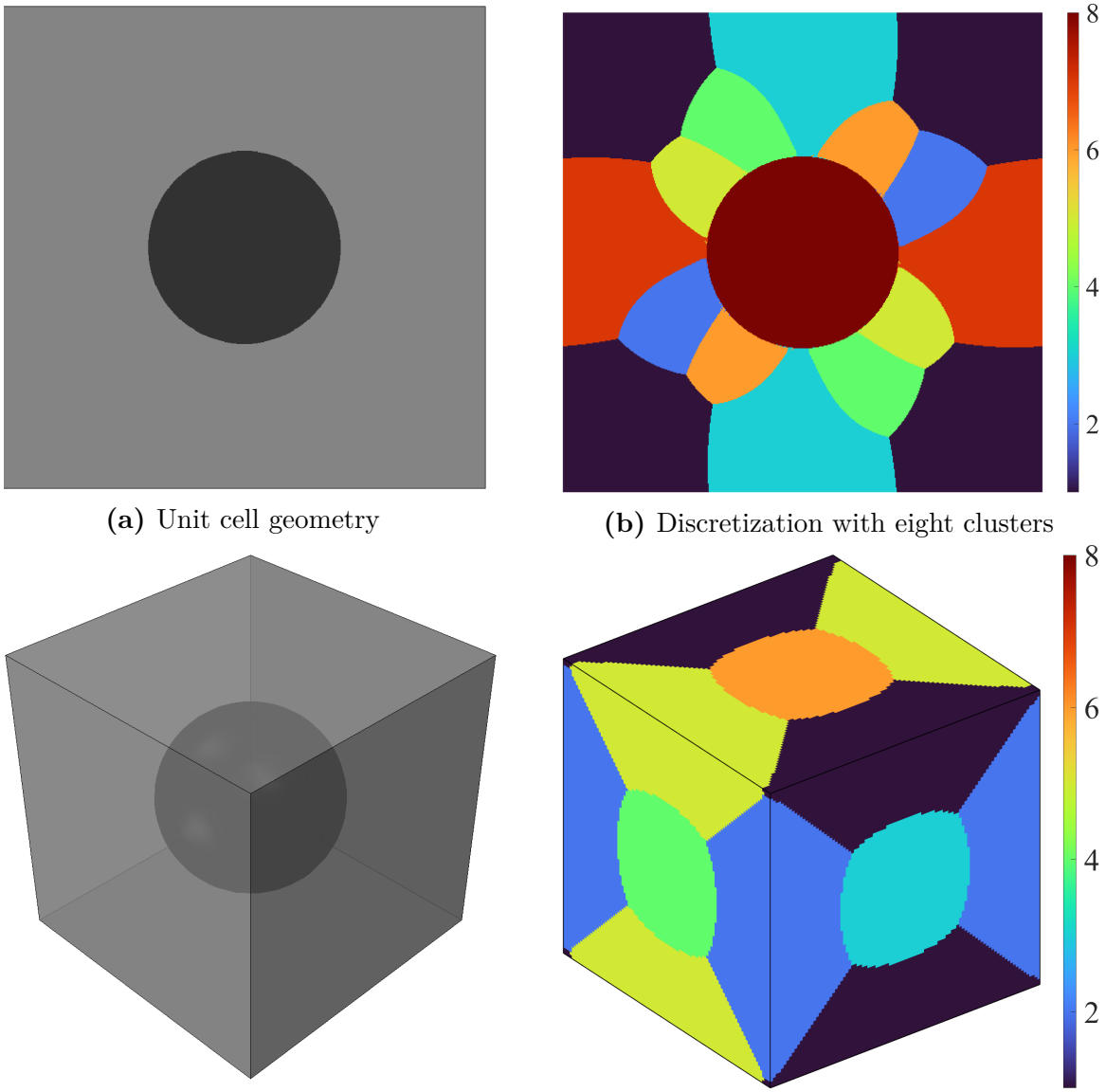

(a) Unit cell geometry

(b) Discretization with eight clusters

(c) Unit sphere geometry

(d) Discretization with eight clusters

Figure 2.1: Microstructure decomposition into an appropriate number of material clusters

The minimum number of material clusters inside the RVE must be equal to the total number of material phases. This is because each material phase can be decomposed with a minimum of one material cluster. Regarding the upper limit of the number of clusters, it is restricted by the total number of points used in each material phase. Of course, for practical use, the total number of clusters should be as small as possible in order to ensure maximum computational efficiency for a given problem.

2.2.1. Decomposition into k number of clusters

Clustering analysis by itself always involves grouping of points that have similar characteristics into one cluster. Points can be characterized in various ways; however, in this dissertation, the similarity between different points is determined by their mechanical behaviour. More precisely, points that exhibit similar mechanical behaviour are placed together into one material cluster. That similarity can be expressed through a well-known quantity in the field of micromechanics called the strain concentration tensor $\mathbb{A}$, defined as

$$\boldsymbol{\varepsilon}(\mathbf{x}) = \mathbb{A}(\mathbf{x}) : \overline{\boldsymbol{\varepsilon}}. \tag{2.4}$$

In the equation above, $\boldsymbol{\varepsilon}$ is the small strain tensor inside the RVE domain, i.e. at the microlevel, while $\overline{\boldsymbol{\varepsilon}}$ stands for the value of a homogenized (macro) small strain tensor. For a linear elastic material, the strain concentration tensor $\mathbb{A}$ is independent of the loading conditions and provides a connection between the micro and macro value of a small strain tensor. To be fully determined, finite element simulations inside the linear elastic region are sufficient. Therefore, values of only two material parameters, e.g. modulus of elasticity E and the Poisson coefficient ν are required to run the DNS analysis. Other metrics, such as equivalent plastic strain or damage indicator can also be added to further improve the characterization of each individual point. However, apart from being load-dependent they also require extra computation in the offline stage and therefore are not used in this dissertation.

For a two-dimensional linear elastic analysis, the strain concentration tensor $\mathbb{A}$, in each material point defined by the position vector $\mathbf{x}_a$, has nine independent components in total

$$\begin{bmatrix} \varepsilon_x(\mathbf{x}_a) \\ \varepsilon_y(\mathbf{x}_a) \\ \gamma_{xy}(\mathbf{x}_a) \end{bmatrix} = \begin{bmatrix} A_{11}(\mathbf{x}_a) & A_{12}(\mathbf{x}_a) & A_{13}(\mathbf{x}_a) \\ A_{21}(\mathbf{x}_a) & A_{22}(\mathbf{x}_a) & A_{23}(\mathbf{x}_a) \\ A_{31}(\mathbf{x}_a) & A_{32}(\mathbf{x}_a) & A_{33}(\mathbf{x}_a) \end{bmatrix} \begin{bmatrix} \overline{\varepsilon}_x \\ \overline{\varepsilon}_y \\ \overline{\gamma}_{xy} \end{bmatrix}, \tag{2.5}$$

which can be determined by conducting finite element simulations on densely discretized RVE subjected to three orthogonal loading conditions $\overline{\boldsymbol{\varepsilon}}^1$, $\overline{\boldsymbol{\varepsilon}}^2$ and $\overline{\boldsymbol{\varepsilon}}^3$, i.e.

$$\overline{\boldsymbol{\varepsilon}}^1 = \begin{bmatrix} \overline{\varepsilon}_x \\ 0 \\ 0 \end{bmatrix}, \quad \overline{\boldsymbol{\varepsilon}}^2 = \begin{bmatrix} 0 \\ \overline{\varepsilon}_y \\ 0 \end{bmatrix}, \quad \overline{\boldsymbol{\varepsilon}}^3 = \begin{bmatrix} 0 \\ 0 \\ \overline{\gamma}_{xy} \end{bmatrix}. \tag{2.6}$$

On the other hand, in the case of a three-dimensional analysis, $\mathbb{A}$ has 36 independent

components, needing a set of six finite element simulations under six different orthogonal loading conditions. If the RVE in question is discretized by e number of finite elements, with one integration point per element, then the total number of strain concentration tensors is equal to e. Although it is not mandatory, since they provide the best homogenized results, PBC are utilized in both two- and three-dimensional analyses for all orthogonal macro-loading conditions. Finally, this part of the offline stage, which includes finite element analysis with three/six orthogonal loading conditions and the construction of the strain concentration tensor for every integration point, is implemented into commercial finite element software Abaqus [217].

After computing the strain concentration tensor $\mathbb{A}$ for each element, the k-means clustering method [79] is used to group points (elements) into appropriate material clusters. For this step of the offline stage, the commercial software Matlab [218] is used to conduct k-means clustering but also to visualize the clustered data. Furthermore, Matlab provides additional functionalities regarding the k-means clustering algorithm that control properties such as the maximum number of iterations, a procedure for choosing initial cluster centroid points and some others [219].

The k-means clustering results for a two-dimensional heterogeneous RVEs consisting of 20 %, i.e. 40 % circular inclusions are provided in **Figure 2.2** and **Figure 2.3**.

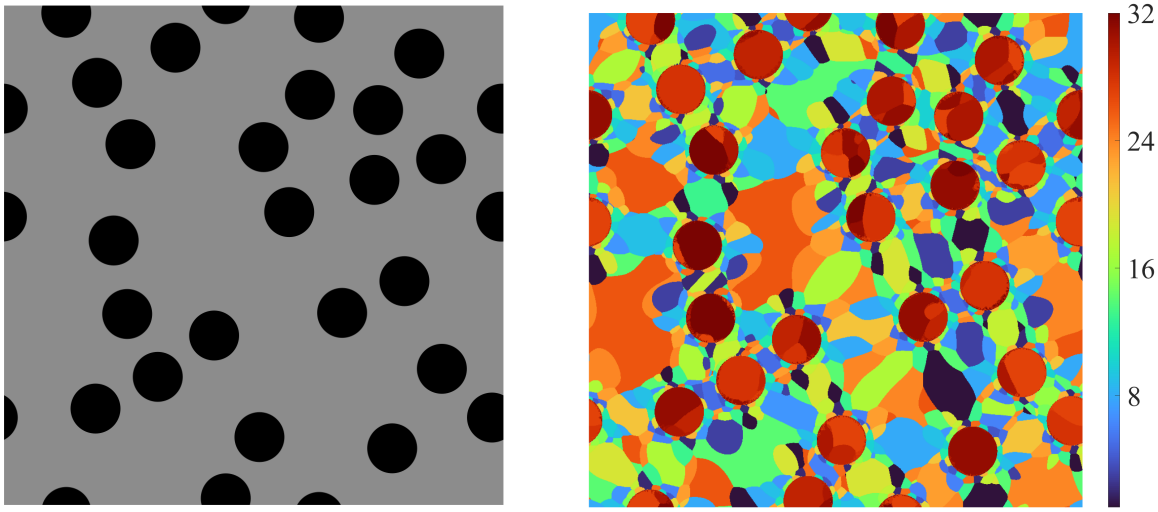

(a) Geometry of a 2D microstructure

(b) Discretization with 32 clusters

Figure 2.2: Results of the k-means clustering for a 2D microstructure with 20 % of circular inclusions

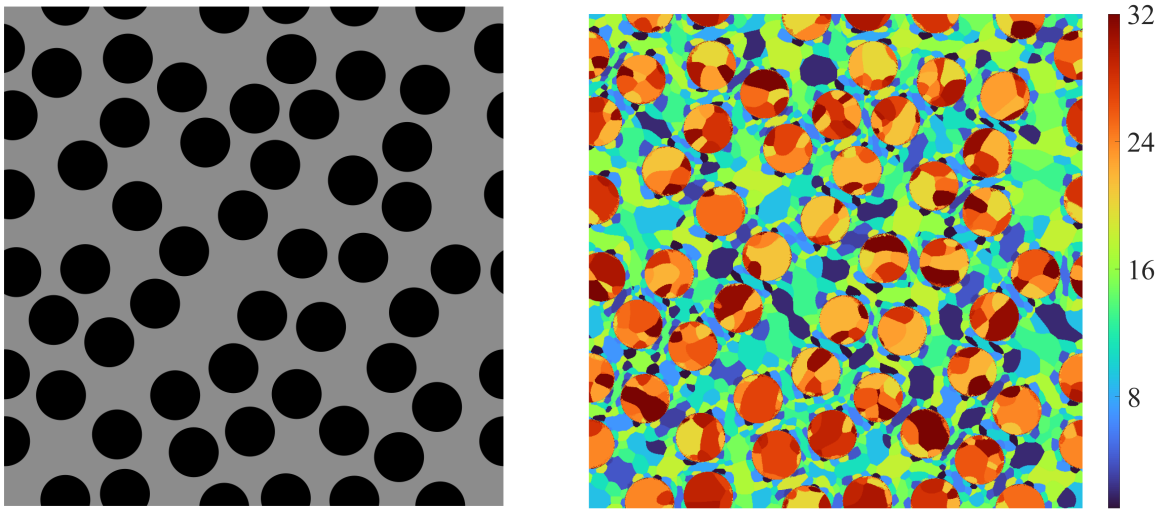

(a) Geometry of a 2D microstructure

(b) Discretization with 32 clusters

Figure 2.3: Results of the k-means clustering for a 2D microstructure with 40 % of circular inclusions

For the purposes of the DNS data collection, both microstructures were discretized by a total of 10^6 quadrilateral finite elements with one integration point, i.e. with 1000×1000 pixels. Herein, the term "pixel" is used to indicate regular finite element mesh, consisting of identical quadrilateral finite elements with one integration point in their center.

Moreover, clustering results for a three-dimensional microstructure with 10 %, i.e. 20 % of the spherical inclusions volume fraction are shown in **Figure 2.4** and **Figure 2.5**.

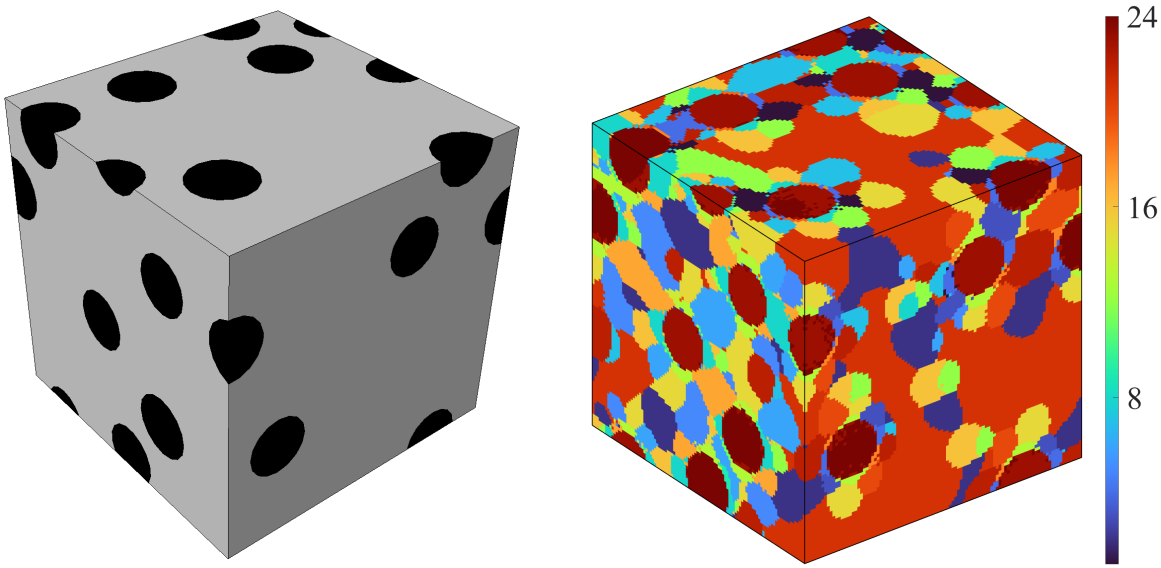

(a) Geometry of a 3D microstructure **(b)** Discretization with 24 clusters

Figure 2.4: Results of the k-means clustering for a 3D microstructure with 10 % of spherical inclusions

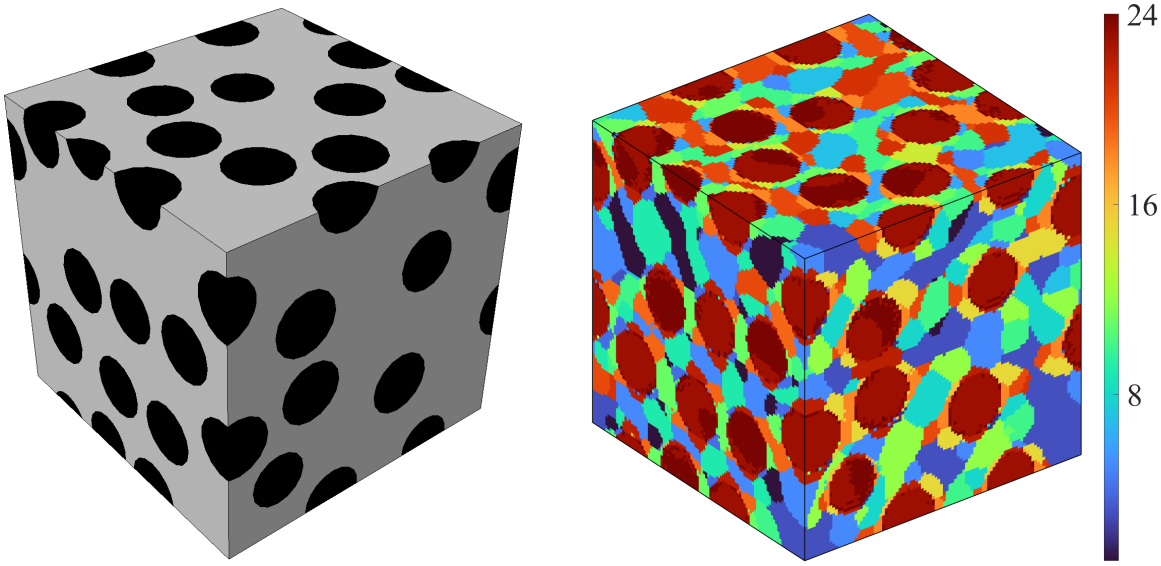

(a) Geometry of a 3D microstructure **(b)** Discretization with 24 clusters

Figure 2.5: Results of the k-means clustering for a 3D microstructure with 20 % of spherical inclusions

In the case of three-dimensional DNS analysis, the microstructures shown above were discretized with 10^6 hexahedra finite elements containing one integration point, i.e. with $100 \times 100 \times 100$ voxels (three-dimensional pixels). This extraordinary fine discretization for both two- and three-dimensional finite element simulations is beneficial for clustering analysis since it allows for an accurate description of the strain

field inside the RVE, and therefore improves the quality of the RVE decomposition into a specific number of clusters.

As mentioned before, the offline stage has to be conducted only once, but the quality of its execution will have a significant impact on the overall accuracy. The physical discretization into material clusters can now be used for any type of material configuration at the microlevel, and for any type of loading. The question that now arises is: how to model and implement the RVE boundary value problem if the domain is discretized with material clusters? Obviously, the ellipticity of the partial differential equations has to be preserved, i.e. the change in one material cluster has to have an impact on all other clusters and vice versa. The problem in question is addressed through the Lippmann-Schwinger equation, the derivation of which is presented for both small and finite strains.

2.3. Lippmann-Schwinger equation

The Lippmann-Schwinger equation is one of the most used equations for describing particle collisions, or more precisely, scattering in quantum mechanics. Although it was originally derived to tackle problems of particle physics, the Lippmann-Schwinger equation found its place in the field of continuum mechanics for analyzing heterogeneous materials systems. In [220] Kröner utilized the Lippmann-Schwinger integral equation to model and analyze the average behaviour of heterogeneous materials during static loading, in the linear elastic region. It has been also extended by Lee and Mal [221] to consider multiple scattering problems in elastodynamics, while referring to it as a volume integral equation. Moreover, the equivalent inclusion method [222], which introduces the concept of eigenstrain, is actually an alternative interpretation of the Lippmann-Schwinger integral equation.

Obtaining exact analytical solutions of the Lippmann-Schwinger integral equation is only possible in cases of linear elastic behaviour and simple RVE geometry. Micromechanical methods such as Mori-Tanaka [223] and the self-consistent method [52] are able to provide only approximate solutions whose accuracy is highly dependent on the complexity of the given problem. On the other hand, FFT-based solvers can be utilized to obtain numerical solutions to the equation considering both small [55] and finite strains [224, 225]. In the following pages, the Lippmann-Schwinger integral equation will be derived from the equilibrium conditions based on Green's function, for both small and finite strains.

2.3.1. Small strain formulation

For small strain assumption, the equilibrium equation can be written in the most general form as

$$\nabla \cdot \boldsymbol{\sigma}(\mathbf{x},t) + \mathbf{b}(\mathbf{x},t) = \rho(\mathbf{x},t)\,\ddot{\mathbf{u}}(\mathbf{x},t)\,. \tag{2.7}$$

In Eq. (2.7) ∇ and $\boldsymbol{\sigma}$ denote gradient operator and Cauchy stress tensor, respectively. $\mathbf{b}$ represents body force vector, ρ is the body's density, while $\ddot{\mathbf{u}}$ stands for vector of the acceleration. The mentioned quantities depend on time t and the position vector $\mathbf{x}$. Considering only static/ quasi-static problems and neglecting the body force vector $\mathbf{b}$, equilibrium (2.7) is reduced to

$$\nabla \cdot \boldsymbol{\sigma}(\mathbf{x}) = \mathbf{0}. \tag{2.8}$$

For a homogeneous elastic body of volume Ω^0 and a material stiffness tensor $\mathbb{C}^0$, Cauchy stress tensor $\boldsymbol{\sigma}$ can be expressed through Hoke's law as

$$\boldsymbol{\sigma}(\mathbf{x}) = \mathbb{C}^0 : \boldsymbol{\varepsilon}(\mathbf{x}) = \lambda^0 \mathrm{tr}\left[\boldsymbol{\varepsilon}(\mathbf{x})\right]\mathbf{I} + 2\mu^0 \boldsymbol{\varepsilon}(\mathbf{x})\,. \tag{2.9}$$

Here λ^0 and μ^0 are the Lamé constant and the shear modulus, $\mathbf{I}$ is a second-order identity tensor, "tr" denotes a trace of the matrix, while $\boldsymbol{\varepsilon}$ represents a small strain tensor. For the purposes of further derivation, the material with stiffness tensor $\mathbb{C}^0$ will from now on be called reference material. Let a small part of the homogeneous elastic body now be changed into a heterogeneous one with the volume Ω and unknown stiffness $\mathbb{C}$ as depicted in **Figure 2.6**

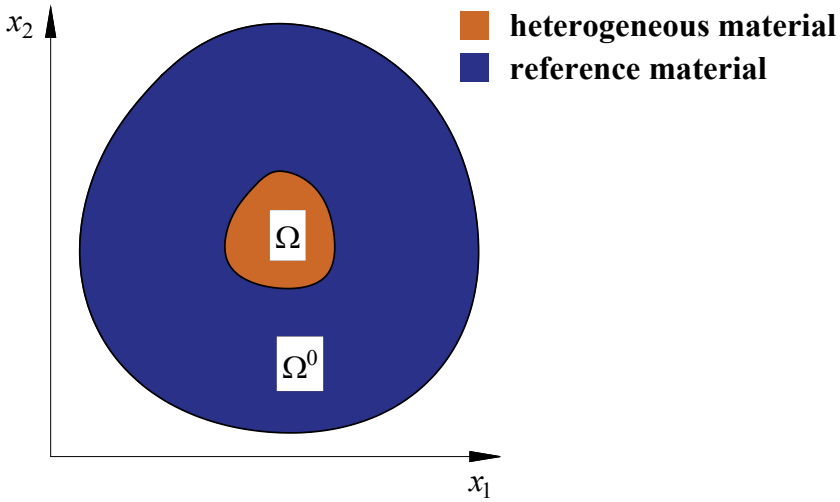

Figure 2.6: Schematic plot for the computational set-up of the SCA

The Cauchy stress tensor can now be divided into two parts, i.e.

$$\boldsymbol{\sigma}(\mathbf{x}) = \mathbb{C}^0 : \boldsymbol{\varepsilon}(\mathbf{x}) + \mathbf{q}(\mathbf{x}), \tag{2.10}$$

where $\mathbf{q}$ is the so-called *polarization stress tensor*, denoting the difference between the Cauchy stress tensor in the heterogeneous and reference material with the same strain. Moreover, according to [57, 226] the Cauchy stress tensor is defined as a piecewise function

$$\boldsymbol{\sigma}(\mathbf{x}) = \begin{cases} \mathbb{C} : \boldsymbol{\varepsilon}(\mathbf{x}) = \mathbb{C}^0 : \boldsymbol{\varepsilon}(\mathbf{x}) + \mathbf{q}(\mathbf{x}), & \mathbf{x} \in \Omega \\ \mathbb{C}^0 : \boldsymbol{\varepsilon}(\mathbf{x}), & \mathbf{x} \in \Omega^0, \end{cases} \tag{2.11}$$

from which it is not difficult to conclude that the polarization stress tensor $\mathbf{q}$ vanishes outside of the heterogeneous material. Also, by using the first expression in (2.11), the initial equilibrium defined by Eq. (2.8) can be rewritten as

$$\nabla \cdot \left(\mathbb{C}^0 : \boldsymbol{\varepsilon}(\mathbf{x})\right) = -\nabla \cdot \mathbf{q}(\mathbf{x}), \text{ in } \Omega. \tag{2.12}$$

With the help of Green's function $\mathbb{\Phi}^0(\mathbf{x}, \mathbf{x}')$, which represents the strain at $\mathbf{x}$ (inside the heterogeneous material) contributed by a stress at $\mathbf{x}'$ (inside the reference material), and by regarding the polarization stress tensor $\mathbf{q}$ as an external stress on the reference material, the following integral equation can be written [67]

$$\boldsymbol{\varepsilon}(\mathbf{x}) + \int_\Omega \mathbb{\Phi}^0(\mathbf{x}, \mathbf{x}') : \mathbf{q}(\mathbf{x}')\, \mathrm{d}\mathbf{x}' - \boldsymbol{\varepsilon}^{\mathbf{0}} = \mathbf{0}, \tag{2.13}$$

where $\boldsymbol{\varepsilon}^{\mathbf{0}}$ is the far-field small strain tensor, which is homogeneous for a homogeneous reference material and for which the following is true [93]

$$\lim_{\mathbf{x}\to\infty} \boldsymbol{\varepsilon}(\mathbf{x}) = \boldsymbol{\varepsilon}^0. \tag{2.14}$$

Substituting (2.10) into (2.13) an integral form of the Lippmann-Schwinger equation is obtained as

$$\boldsymbol{\varepsilon}(\mathbf{x}) + \int_\Omega \mathbb{\Phi}^0(\mathbf{x}, \mathbf{x}') : \left[\boldsymbol{\sigma}(\mathbf{x}') - \mathbb{C}^0 : \boldsymbol{\varepsilon}(\mathbf{x}')\right] \mathrm{d}\mathbf{x}' - \boldsymbol{\varepsilon}^0 = \mathbf{0}. \tag{2.15}$$

Eq. (2.15) can also, for convenience, be written in the incremental form as

$$\Delta\boldsymbol{\varepsilon}(\mathbf{x}) + \int_\Omega \mathbb{\Phi}^0(\mathbf{x}, \mathbf{x}') : \left[\Delta\boldsymbol{\sigma}(\mathbf{x}') - \mathbb{C}^0 : \Delta\boldsymbol{\varepsilon}(\mathbf{x}')\right] \mathrm{d}\mathbf{x}' - \Delta\boldsymbol{\varepsilon}^0 = \mathbf{0}. \tag{2.16}$$

Moreover, by using the integral property of Green's function, i.e.

$$\int_{\Omega} \mathbb{\Phi}^0 (\mathbf{x}, \mathbf{x}') \, \mathrm{d}\mathbf{x} = \mathbf{0}, \tag{2.17}$$

it can be shown that the incremental far-field small strain tensor $\Delta\boldsymbol{\varepsilon}^0$ is equal to the homogenized incremental strain of the RVE. By averaging Eq. (2.16) in the domain Ω,

$$\begin{aligned} &\frac{1}{\Omega}\int_{\Omega} \Delta\boldsymbol{\varepsilon}(\mathbf{x}) \, \mathrm{d}\mathbf{x} + \\ &\frac{1}{\Omega}\int_{\Omega} \left[\int_{\Omega} \mathbb{\Phi}^0 (\mathbf{x}, \mathbf{x}') \, \mathrm{d}\mathbf{x}\right] : \left[\Delta\boldsymbol{\sigma}(\mathbf{x}') - \mathbb{C}^0 : \Delta\boldsymbol{\varepsilon}(\mathbf{x}')\right] \mathrm{d}\mathbf{x}' - \Delta\boldsymbol{\varepsilon}^0 = \mathbf{0}, \end{aligned} \tag{2.18}$$

and with the use of Eq. (2.17), incremental far-field small strain tensor $\Delta\boldsymbol{\varepsilon}^0$ can be expressed as

$$\Delta\boldsymbol{\varepsilon}^0 = \frac{1}{\Omega}\int_{\Omega} \Delta\boldsymbol{\varepsilon}(\mathbf{x}) \, \mathrm{d}\mathbf{x}. \tag{2.19}$$

In order to solve (2.16) for $\Delta\boldsymbol{\varepsilon}(\mathbf{x})$ constraints are needed from the macroscopic boundary conditions. Two basic types of constraints are available: the macro-strain constraint

$$\frac{1}{\Omega}\int_{\Omega} \Delta\boldsymbol{\varepsilon}(\mathbf{x}) \, \mathrm{d}\mathbf{x} = \Delta\overline{\boldsymbol{\varepsilon}} \rightarrow \Delta\boldsymbol{\varepsilon}^0 = \Delta\overline{\boldsymbol{\varepsilon}}, \tag{2.20}$$

where $\Delta\overline{\boldsymbol{\varepsilon}}$ is the homogenized (average) value of the incremental small strain tensor $\Delta\boldsymbol{\varepsilon}$. Or the macro-stress constraint

$$\frac{1}{\Omega}\int_{\Omega} \Delta\boldsymbol{\sigma}(\mathbf{x}) \, \mathrm{d}\mathbf{x} = \Delta\overline{\boldsymbol{\sigma}}, \tag{2.21}$$

where $\Delta\overline{\boldsymbol{\sigma}}$ is a homogenized (average) value of the incremental Cauchy stress tensor $\Delta\boldsymbol{\sigma}$. Here the boundary conditions are applied as constraints on the volume average of strain or stress inside the RVE. This is different from the standard FEM where the boundary conditions constrain the displacement or force on the RVE boundaries.

Expression (2.16) implies that the reference material is homogeneous; however, in a more general sense, that is not the case and the stiffness of the reference material is then expressed as a function of the position vector $\mathbf{x}$

$$\mathbb{C}^0 = \mathbb{C}^0(\mathbf{x}). \tag{2.22}$$

The derivation of the incremental integral equation is the same as the one for a homogeneous reference material, except that the incremental far-field strain tensor

$\Delta\boldsymbol{\varepsilon}^0$ also becomes inhomogeneous. The new incremental Lippmann-Schwinger equation takes the following form

$$\Delta\boldsymbol{\varepsilon}(\mathbf{x}) + \int_\Omega \mathbb{\Phi}^0(\mathbf{x},\mathbf{x}') : \left[\Delta\boldsymbol{\sigma}(\mathbf{x}') - \mathbb{C}^0(\mathbf{x}) : \Delta\boldsymbol{\varepsilon}(\mathbf{x}')\right] \mathrm{d}\mathbf{x}' - \Delta\boldsymbol{\varepsilon}^0(\mathbf{x}) = \mathbf{0}, \tag{2.23}$$

where $\mathbb{\Phi}^0(\mathbf{x},\mathbf{x}')$ is now Green's function of the heterogeneous elastic reference material. By averaging Eq. (2.23) and utilizing the property of Green's function in (2.17), for incremental far-field small strain tensor $\Delta\boldsymbol{\varepsilon}^0$ it is valid to write

$$\frac{1}{\Omega}\int_\Omega \Delta\boldsymbol{\varepsilon}(\mathbf{x})\,\mathrm{d}\mathbf{x} = \frac{1}{\Omega}\int_\Omega \Delta\boldsymbol{\varepsilon}^0(\mathbf{x}) = \Delta\overline{\boldsymbol{\varepsilon}}. \tag{2.24}$$

Furthermore, a new strain concentration tensor, that conncects $\Delta\overline{\boldsymbol{\varepsilon}}$ with $\Delta\boldsymbol{\varepsilon}^0(\mathbf{x})$ is now defined as

$$\Delta\boldsymbol{\varepsilon}^0(\mathbf{x}) = \mathbb{A}(\mathbf{x}) : \Delta\overline{\boldsymbol{\varepsilon}}. \tag{2.25}$$

Substituting (2.25) into (2.23) gives

$$\Delta\boldsymbol{\varepsilon}(\mathbf{x}) = \mathbb{A}(\mathbf{x}) : \Delta\overline{\boldsymbol{\varepsilon}} - \int_\Omega \mathbb{\Phi}^0(\mathbf{x},\mathbf{x}') : \left[\Delta\boldsymbol{\sigma}(\mathbf{x}') - \mathbb{C}^0(\mathbf{x}) : \Delta\boldsymbol{\varepsilon}(\mathbf{x}')\right] \mathrm{d}\mathbf{x}'. \tag{2.26}$$

Eq. (2.26) is more complex and provides a higher level of accuracy than (2.16) since it allows for more realistic material behaviour. However, in the case of heterogeneous reference material, the determination of the strain concentration tensor $\mathbb{A}$ and Green's function $\mathbb{\Phi}^0(\mathbf{x},\mathbf{x}')$ is not a trivial task and has to be done numerically by solving the RVE problem using DNS methods [67]. The integral identity (2.16) based on the homogeneous reference material will be used in this dissertation and will serve as the basis for further analysis.

2.3.2. Finite strain formulation

Although the transition from small to finite strains often includes more complex expressions, the derivation of the Lippmann-Schwinger integral equation for finite strains follows the same procedure that was outlined in the previous subsection. Therefore, the extension is a straightforward task with the only two differences being: (1) formulation of the equilibrium condition and the integral equation in the reference (non-deformed) configuration, and (2) replacement of the strain and Cauchy stress tensor with the deformation gradient $\mathbf{F}$ and first Piola-Kirchhoff stress tensor $\mathbf{P}$, respectively [67]. The equilibrium condition, i.e. equivalent of Eq. (2.8) in the reference

configuration is equal to

$$\nabla_0 \cdot \mathbf{P}(\mathbf{X}) = \mathbf{0}, \tag{2.27}$$

with ∇_0 and $\mathbf{X}$ being the gradient operator and the position vector in the reference configuration. As well as in the case of small strains, a reference material with the stiffness tensor $\mathbb{C}^0$ is introduced, and its constitutive law is given by

$$\mathbf{P}(\mathbf{X}) = \mathbb{C}^0 : \mathbf{F}(\mathbf{X}) = \lambda^0 \mathrm{tr}\left[\mathbf{F}(\mathbf{X})\right]\mathbf{I} + 2\mu^0 \mathbf{F}(\mathbf{X}). \tag{2.28}$$

It is important to emphasize that the law written above is not physical, and it requires the deformation gradient to be defined as

$$\mathbf{F}(\mathbf{X}) = \frac{\partial \mathbf{x}(\mathbf{X})}{\partial \mathbf{X}} - \mathbf{I} = \frac{\partial \mathbf{u}(\mathbf{X})}{\partial \mathbf{X}}. \tag{2.29}$$

In Eq. (2.29) the deformation gradient is represented simply as the gradient of the displacement vector $\mathbf{u}$, without the second-order identity tensor $\mathbf{I}$. The main reason for the identities (2.28) and (2.29) is the ease of deriving the incremental integral equation along with Green's function [67]. Following Eq. (2.10) and **Figure 2.6**, the first Piola-Kirchhoff stress tensor is equal to

$$\mathbf{P}(\mathbf{X}) = \mathbb{C}^0 : \mathbf{F}(\mathbf{X}) + \mathbf{Q}(\mathbf{X}), \tag{2.30}$$

where $\mathbf{Q}$ is the polarization stress tensor in the reference configuration, denoting the difference between the first Piola-Kirchhoff stress tensor in the heterogeneous and reference material. As in the case of small strains, its value is equal to zero outside of the heterogeneous material. With the use of Green's function $\mathbb{\Phi}^0(\mathbf{X}, \mathbf{X}')$ Eq. (2.13) is expressed in terms of reference configuration and the deformation gradient tensor as

$$\mathbf{F}(\mathbf{X}) + \int_{\Omega_0} \mathbb{\Phi}^0(\mathbf{X}, \mathbf{X}') : \mathbf{Q}(\mathbf{X}')\, \mathrm{d}\mathbf{X}' - \mathbf{F}^0 = \mathbf{0}. \tag{2.31}$$

Here, Ω_0 is the reference volume of the heterogeneous material, while $\mathbf{F}^0$ represents far-field deformation gradient, which is homogeneous for a homogeneous reference material, obeying the same rule as the small strain tensor, i.e.

$$\lim_{\mathbf{X}\to\infty} \mathbf{F}(\mathbf{X}) = \mathbf{F}^0. \tag{2.32}$$

The Lippmann-Schwinger integral equation for the case of finite deformations takes the following form

$$\mathbf{F}(\mathbf{x}) + \int_{\Omega_0} \mathbb{\Phi}^0(\mathbf{X}, \mathbf{X}') : \left[\mathbf{P}(\mathbf{X}') - \mathbb{C}^0 : \mathbf{F}(\mathbf{X}')\right] \mathrm{d}\mathbf{X}' - \mathbf{F}^0 = \mathbf{0}. \tag{2.33}$$

or in terms of the increments of the deformation gradient and first Piola-Kirchhoff stress tensor

$$\Delta\mathbf{F}(\mathbf{X}) + \int_{\Omega_0} \mathbb{\Phi}^0(\mathbf{X}, \mathbf{X}') : \left[\Delta\mathbf{P}(\mathbf{X}') - \mathbb{C}^0 : \Delta\mathbf{F}(\mathbf{X}')\right] \mathrm{d}\mathbf{X}' - \Delta\mathbf{F}^0 = \mathbf{0}. \tag{2.34}$$

Through the integral property of Green's function for finite strains

$$\int_{\Omega_0} \mathbb{\Phi}^0(\mathbf{X}, \mathbf{X}') \, \mathrm{d}\mathbf{X} = \mathbf{0} \tag{2.35}$$

and by applying the averaging scheme shown in (2.18), for the incremental far-field deformation gradient $\Delta\mathbf{F}^0$ it is valid to write

$$\Delta\mathbf{F}^0 = \frac{1}{\Omega_0} \int_{\Omega_0} \Delta\mathbf{F}(\mathbf{X}) \, \mathrm{d}\mathbf{X}. \tag{2.36}$$

In the case of finite strain macroscopic constraints can be expressed through homogenized incremental deformation gradient $\Delta\overline{\mathbf{F}}$

$$\frac{1}{\Omega_0} \int_{\Omega_0} \Delta\mathbf{F}(\mathbf{X}) \, \mathrm{d}\mathbf{X} = \Delta\overline{\mathbf{F}} \rightarrow \Delta\mathbf{F}^0 = \Delta\overline{\mathbf{F}}, \tag{2.37}$$

or homogenized incremental first Piola-Kirchhoff stress tensor $\Delta\overline{\mathbf{P}}$

$$\frac{1}{\Omega_0} \int_{\Omega_0} \Delta\mathbf{P}(\mathbf{X}) \, \mathrm{d}\mathbf{X} = \Delta\overline{\mathbf{P}}. \tag{2.38}$$

As in the case of small strain formulation, reference material does not need to be homogenous, i.e.

$$\mathbb{C}^0 = \mathbb{C}^0(\mathbf{X}), \tag{2.39}$$

which entails the need for numerical determination of Green's function $\mathbb{\Phi}^0(\mathbf{X}, \mathbf{X}')$ and the deformation gradient concentration tensor $\mathbb{A}$. A problem that goes beyond the scope of this dissertation.

2.4. Green's function

Since the term "Green's function" has been mentioned multiple times in the previous section, it is important to give a more detailed insight and provide a derivation of this important mathematical concept.

Consider a one-dimensional linear second-order inhomogeneous differential equation

$$\frac{\mathrm{d}^2 y\left(x\right)}{\mathrm{d}x^2} + \frac{\mathrm{d}y\left(x\right)}{\mathrm{d}x} + y\left(x\right) = g\left(x\right), \tag{2.40}$$

where y and g are analytic scalar functions of the variables x, that are continuous on an interval $[a, b]$. Eq. (2.40) can also be written in a more compact form as

$$\mathscr{L}\left[y\left(x\right)\right] = g\left(x\right), \tag{2.41}$$

with $\mathscr{L}$ being a linear differential operator given by

$$\mathscr{L} = \frac{\mathrm{d}^2}{\mathrm{d}x^2} + \frac{\mathrm{d}}{\mathrm{dx}} + 1. \tag{2.42}$$

Now, the solution to Eq. (2.41) can be expressed in the form of the inverse of $\mathscr{L}$, i.e.

$$y\left(x\right) = \mathscr{L}^{-1}\left[\left(x\right)\right], \tag{2.43}$$

or through an integral of Green's function $\Phi\left(x, x'\right)$

$$y\left(x\right) = \int_a^b \Phi\left(x, x'\right) g\left(x'\right) \mathrm{d}x', \tag{2.44}$$

which is defined as the impulse response of an inhomogeneous linear differential equation operator defined on a domain with specified initial, i.e. boundary conditions. Identity (2.44) is also called convolution, a term that will be important in **section 2.5**. In the physical sense, Green's function always gives information about the influence on the position x, affected by the source at x'. By defining appropriate boundary conditions, and through the use of the following identity

$$\mathscr{L}\left[\Phi\left(x, x'\right)\right] = \delta(x - x'), \tag{2.45}$$

where $\delta(x - x')$ is the Dirac delta function defined as

$$\delta\left(x-x'\right)=\begin{cases}1, & \left(x-x'\right)=0\\ 0, & \left(x-x'\right)\neq 0,\end{cases} \tag{2.46}$$

Green's function can be used to solve a broad range of ordinary and partial differential equations. However, as usual in mathematics, closed-form solutions of Green's function are available only for linear problems, since (2.41) and (2.43) require the differential operator $\mathscr{L}$ to be linear.

2.4.1. Green's function for small strains

The key to Eq. (2.16) is the corresponding Green's function of the reference material, and in this subsection, it will be derived for the case of small strains and a homogeneous reference material with the stiffness tensor $\mathbb{C}^0$. The system of two equations

$$\begin{cases}\sigma\left(\mathbf{x}\right)=\mathbb{C}^0:\boldsymbol{\varepsilon}\left(\mathbf{x}\right)+\mathbf{q}\left(\mathbf{x}\right)\\ \nabla\cdot\boldsymbol{\sigma}\left(\mathbf{x}\right)=\mathbf{0},\end{cases} \tag{2.47}$$

where small strain tensor $\boldsymbol{\varepsilon}$ is expressed in terms of displacement vector $\mathbf{u}$

$$\boldsymbol{\varepsilon}\left(\mathbf{x}\right)=\frac{1}{2}\left(\nabla\mathbf{u}\left(\mathbf{x}\right)+\nabla^T\mathbf{u}\left(\mathbf{x}\right)\right), \tag{2.48}$$

fully determines the problem of the body depicted in **Figure 2.6** that is subjected to the specific boundary conditions. Since micromechanics always presupposes the periodicity of the RVE, distribution of the quantities such as displacement, small strain and the stress tensor inside the RVE can be expressed in the form of a single wave, i.e.

$$\mathbf{u}\left(\mathbf{x}\right)=\hat{\mathbf{u}}\left(\boldsymbol{\xi}\right)\exp\left(i\boldsymbol{\xi}\cdot\mathbf{x}\right), \tag{2.49}$$

$$\boldsymbol{\varepsilon}\left(\mathbf{x}\right)=\hat{\boldsymbol{\varepsilon}}\left(\boldsymbol{\xi}\right)\exp\left(i\boldsymbol{\xi}\cdot\mathbf{x}\right), \tag{2.50}$$

$$\boldsymbol{\sigma}\left(\mathbf{x}\right)=\hat{\boldsymbol{\sigma}}\left(\boldsymbol{\xi}\right)\exp\left(i\boldsymbol{\xi}\cdot\mathbf{x}\right), \tag{2.51}$$

$$\mathbf{q}\left(\mathbf{x}\right)=\hat{\mathbf{q}}\left(\boldsymbol{\xi}\right)\exp\left(i\boldsymbol{\xi}\cdot\mathbf{x}\right). \tag{2.52}$$

In the expressions above, $\boldsymbol{\xi}$ is a wave vector corresponding to the periodicity of the RVE, i is the complex number $\left(i=\sqrt{-1}\right)$, while $\hat{\mathbf{u}}$, $\hat{\boldsymbol{\varepsilon}}$, $\hat{\boldsymbol{\sigma}}$ and $\hat{\mathbf{q}}$ denote displacement, strain, Cauchy and polarization stress expressed in the Fourier space, i.e. frequency domain. Considering that the strain field is a function of a displacement, it is convenient to rewrite the first identity in the system (2.47) in terms of displacement. In index notation, which will be used for further derivation of Green's function, the new system

of equations is

$$\begin{cases} \sigma_{ij}(\mathbf{x}) = C^0_{ijkl} u_{k,l}(\mathbf{x}) + q_{ij}(\mathbf{x}) \\ \sigma_{ij,j} = 0. \end{cases} \tag{2.53}$$

Now, by using (2.49), (2.50), (2.51) and (2.52), the system of equations in (2.53) can be expressed in the frequency domain as

$$\begin{cases} \hat{\sigma}_{ij}(\boldsymbol{\xi}) = iC^0_{ijkl}\xi_l \hat{u}_k(\boldsymbol{\xi}) + \hat{q}_{ij}(\boldsymbol{\xi}) \\ i\hat{\sigma}_{ij}(\boldsymbol{\xi})\xi_j = 0. \end{cases} \tag{2.54}$$

Multiplying the first identity in (2.54) with $i\xi_j$ and subtracting it from the second one yields

$$K^0_{ik}(\boldsymbol{\xi})\,\hat{u}_k(\boldsymbol{\xi}) = i\hat{q}_{ij} \tag{2.55}$$

where K^0_{ik} is a symmetric second-order tensor given by

$$K^0_{ik}(\boldsymbol{\xi}) = C^0_{ijkl}\xi_l\xi_j = \left[\lambda^0\delta_{ij}\delta_{kl} + \mu^0\left(\delta_{ik}\delta_{jl} + \delta_{il}\delta_{jk}\right)\right]\xi_l\xi_j, \tag{2.56}$$

or in a more compact form

$$K^0_{ik}(\boldsymbol{\xi}) = \left(\lambda^0 + \mu^0\right)\xi_i\xi_k + \mu^0\delta_{ik}\xi_j\xi_j, \tag{2.57}$$

that is obtained through the property of the Kronecker delta symbol δ_{ij}. The displacement field $\hat{u}_k$ is now solved as

$$\hat{u}_k(\boldsymbol{\xi}) = iN^0_{ki}(\boldsymbol{\xi})\,\xi_j\hat{q}_{ij}(\boldsymbol{\xi}), \tag{2.58}$$

where N^0_{ki} is a second-order tensor obtained by inverting K^0_{ik}, i.e.

$$N^0_{ki}(\boldsymbol{\xi}) = {K^0_{ik}}^{-1}(\boldsymbol{\xi}). \tag{2.59}$$

Based on the symmetry of the polarization stress $\hat{q}_{ij}$, Eq. (2.55) is expressed in the following form

$$\hat{u}_k(\boldsymbol{\xi}) = \frac{i}{2}\left[N^0_{ki}(\boldsymbol{\xi})\,\xi_j + N^0_{kj}(\boldsymbol{\xi})\,\xi_i\right]\hat{q}_{ij}(\boldsymbol{\xi}). \tag{2.60}$$

and by means of Eq. (2.48) and (2.50), for the strain field $\hat{\varepsilon}_{kl}$ it is valid to write

$$\hat{\varepsilon}_{kl}\left(\boldsymbol{\xi}\right) = \frac{i}{2}\left[\xi_l \hat{u}_k\left(\boldsymbol{\xi}\right) + \xi_k \hat{u}_l\left(\boldsymbol{\xi}\right)\right]. \tag{2.61}$$

Finally, by substituting (2.60) into (2.61), the strain field $\hat{\varepsilon}_{kl}$ is expressed in terms of polarization stress $\hat{q}_{ij}$ as

$$\hat{\varepsilon}_{kl} = -\hat{\Phi}^0_{klij}\left(\boldsymbol{\xi}\right)\hat{q}_{ij}, \tag{2.62}$$

where $\hat{\Phi}^0_{klij}\left(\boldsymbol{\xi}\right)$ is the fourth-order tensor, i.e. Green's function for small strains expressed in Fourier space (frequency domain)

$$\hat{\Phi}^0_{klij} = \frac{1}{4}\left[N^0_{ki}\left(\boldsymbol{\xi}\right)\xi_j\xi_l + N^0_{kj}\left(\boldsymbol{\xi}\right)\xi_i\xi_l + N^0_{li}\left(\boldsymbol{\xi}\right)\xi_j\xi_k + N^0_{lj}\left(\boldsymbol{\xi}\right)\xi_i\xi k\right]. \tag{2.63}$$

As shown in [222], the expression of N^0_{ki} can be quite complex for orthotropic and anisotropic materials. However, its form becomes particularly simple in the case of an isotropic (homogeneous) elastic material. Based on the identities (2.56), (2.57) and (2.59), it can be derived that

$$N^0_{ij} = \frac{1}{\mu^0\xi_m\xi_m}\left(\delta_{ij} - \frac{\lambda^0+\mu^0}{\lambda^0+2\mu^0}\frac{\xi_i\xi_j}{\xi_n\xi_n}\right). \tag{2.64}$$

Substituting (2.64) into (2.63), Green's function is obtained as

$$\hat{\Phi}^0_{ijkl}\left(\boldsymbol{\xi}\right) = \frac{1}{4\mu^0}\hat{\Phi}^1_{ijkl}\left(\boldsymbol{\xi}\right) + \frac{\lambda^0+\mu^0}{\mu^0\left(\lambda^0+2\mu^0\right)}\hat{\Phi}^2_{ijkl}\left(\boldsymbol{\xi}\right), \tag{2.65}$$

with $\hat{\Phi}^1_{ijkl}\left(\boldsymbol{\xi}\right)$ and $\hat{\Phi}^2_{ijkl}\left(\boldsymbol{\xi}\right)$ being

$$\hat{\Phi}^1_{ijkl}\left(\boldsymbol{\xi}\right) = \frac{1}{\xi_m\xi_m}\left(\delta_{ik}\xi_j\xi_l + \delta_{il}\xi_j\xi_k + \delta_{jl}\xi_i\xi_k + \delta_{jk}\xi_i\xi_l\right), \tag{2.66}$$

$$\hat{\Phi}^2_{ijkl}\left(\boldsymbol{\xi}\right) = -\frac{\xi_i\xi_j\xi_k\xi_l}{\xi_m\xi_m\xi_n\xi_n}. \tag{2.67}$$

Notation in (2.65), where $\hat{\Phi}^1_{ijkl}\left(\boldsymbol{\xi}\right)$ and $\hat{\Phi}^2_{ijkl}\left(\boldsymbol{\xi}\right)$ are independent of the reference material parameters λ^0 and μ^0, is extremely usefull and will be heavily exploited in the online stage. Due to the symmetry of the small strain and Cauchy stress tensor, Green's function possesses all four symmetries, i.e

$$\hat{\Phi}^0_{ijkl}\left(\boldsymbol{\xi}\right) = \hat{\Phi}^0_{klij}\left(\boldsymbol{\xi}\right) = \hat{\Phi}^0_{jikl}\left(\boldsymbol{\xi}\right) = \hat{\Phi}^0_{ijlk}\left(\boldsymbol{\xi}\right), \tag{2.68}$$

and therefore can be simplified as a second-order tensor through Voigt notation. It is

also possible to write Green's function of the isotropic linear elastic reference material in the real space, i.e. Cartesian coordinates with the use of inverse Fourier transform. This procedure is presented in detail in **Appendix A**.

2.4.2. Green's function for finite strains

Following the procedure outlined in the previous subsection, Green's function for the case of finite strains will be also derived in the Fourier space. The initial system of equations in the reference configuration is defined as

$$\begin{cases} \mathbf{P}(\mathbf{X}) = \mathbb{C}^0 : \mathbf{F}(\mathbf{X}) + \mathbf{Q}(\mathbf{X}) \\ \nabla_0 \cdot \mathbf{P}(\mathbf{X}) = \mathbf{0}, \end{cases} \tag{2.69}$$

where the deformation gradient $\mathbf{F}$ is determined as a gradient of displacement, i.e.

$$\mathbf{F}(\mathbf{X}) = \frac{\partial \mathbf{u}(\mathbf{X})}{\partial \mathbf{X}}. \tag{2.70}$$

Using index notation and Eq. (2.70), system of equations (2.69) is expressed in the spatial domain as

$$\begin{cases} P_{ij}(\mathbf{X}) = C^0_{ijkl} u_{k,l}(\mathbf{X}) + Q_{ij}(\mathbf{X}) \\ P_{ij,j} = 0, \end{cases} \tag{2.71}$$

or, by means of identities (2.49), (2.50), (2.51) and (2.52), in the frequency domain

$$\begin{cases} \hat{P}_{ij}(\boldsymbol{\Xi}) = iC^0_{ijkl}\Xi_l \hat{u}_k(\boldsymbol{\Xi}) + \hat{Q}_{ij}(\boldsymbol{\Xi}) \\ i\hat{P}_{ij}(\boldsymbol{\Xi})\Xi_j = 0. \end{cases} \tag{2.72}$$

Here, it is important to note that unlike the spatial (Cartesian) coordinates, where one can define clear difference between coordinate vector $\mathbf{x}$ and $\mathbf{X}$, in Fourier space, i.e. frequency domain there exists no distinction between reference and current configuration. Still, for the sake of clarity and consistency the capital of $\boldsymbol{\xi}$ is used to emphasize the reference configuration. Multiplying the first expression in (2.72) with $i\Xi_j$ and subtracting it from the second one yields

$$K^0_{ik}(\boldsymbol{\Xi})\,\hat{u}_k(\boldsymbol{\Xi}) = i\hat{Q}_{ij}, \tag{2.73}$$

where K^0_{ik} is a symmetric second-order tensor expressed in the same way as in the case of small strains, i.e.

$$K_{ik}^{0}\left(\boldsymbol{\Xi}\right)=\left(\lambda^{0}+\mu^{0}\right)\Xi_{i}\Xi_{k}+\mu^{0}\delta_{ik}\Xi_{j}\Xi_{l}. \tag{2.74}$$

Since K_{ik}^{0} is the same for both small and finite strains, its inverse N_{ki}^{0} is simply

$$N_{ki}^{0}\left(\boldsymbol{\Xi}\right)=\frac{1}{\mu^{0}\Xi_{m}\Xi_{m}}\left(\delta_{ki}-\frac{\lambda^{0}+\mu^{0}}{\lambda^{0}+2\mu^{0}}\frac{\Xi_{k}\Xi_{i}}{\Xi_{n}\Xi_{n}}\right). \tag{2.75}$$

In contrast to small strains, the polarization stress tensor $\hat{Q}_{ij}$ in the case of finite strains is, generally, non-symmetric, and therefore the rule for an arbitrary symmetric tensor Z_{ij}

$$Z_{ij}=\frac{1}{2}\left(Z_{ij}+Z_{ji}\right), \tag{2.76}$$

cannot be applied. Because of that, for the displacement field $\hat{u}_{k}$ it is valid to write

$$\hat{u}_{k}\left(\boldsymbol{\Xi}\right)=iN_{ki}^{0}\left(\boldsymbol{\Xi}\right)\Xi_{j}\hat{Q}_{ij}\left(\boldsymbol{\Xi}\right), \tag{2.77}$$

and by expressing Eq. (2.70) in the frequency domain

$$\hat{F}_{kl}\left(\boldsymbol{\Xi}\right)=i\Xi_{l}\hat{u}_{k}\left(\boldsymbol{\Xi}\right), \tag{2.78}$$

the deformation gradient $\hat{F}_{kl}$ is expressed in terms of the polarization stress $\hat{Q}_{ij}$ as

$$\hat{F}_{kl}\left(\boldsymbol{\Xi}\right)=-\hat{\Phi}_{klij}^{0}\left(\boldsymbol{\Xi}\right)\hat{Q}_{ij}\left(\boldsymbol{\Xi}\right). \tag{2.79}$$

where $\hat{\Phi}_{klij}\left(\boldsymbol{\Xi}\right)$ is Green's function for the case of finite strains, i.e.

$$\hat{\Phi}_{ijkl}^{0}\left(\boldsymbol{\Xi}\right)=\frac{1}{\mu^{0}\Xi_{m}\Xi_{m}}\left(\delta_{ik}\Xi_{j}\Xi_{l}-\frac{\lambda^{0}+\mu^{0}}{\lambda^{0}+2\mu^{0}}\frac{\Xi_{i}\Xi_{j}\Xi_{k}\Xi_{l}}{\Xi_{n}\Xi_{n}}\right). \tag{2.80}$$

Again, identity above can be written in a more compact form

$$\hat{\Phi}_{ijkl}^{0}\left(\boldsymbol{\Xi}\right)=\frac{1}{\mu^{0}}\hat{\Phi}_{ijkl}^{1}\left(\boldsymbol{\Xi}\right)+\frac{\lambda^{0}+\mu^{0}}{\lambda^{0}+2\mu^{0}}\hat{\Phi}_{ijkl}^{2}\left(\boldsymbol{\Xi}\right), \tag{2.81}$$

with $\hat{\Phi}_{ijkl}^{1}\left(\boldsymbol{\Xi}\right)$ and $\hat{\Phi}_{ijkl}^{2}\left(\boldsymbol{\Xi}\right)$ being

$$\hat{\Phi}_{ijkl}^{1}\left(\boldsymbol{\Xi}\right)=\delta_{ik}\Xi_{j}\Xi_{l}, \tag{2.82}$$

$$\hat{\Phi}_{ijkl}^{2}\left(\boldsymbol{\Xi}\right)=-\frac{\Xi_{i}\Xi_{j}\Xi_{k}\Xi l}{\Xi_{m}\Xi_{m}\Xi_{n}\Xi_{n}}. \tag{2.83}$$

Since the deformation gradient $\mathbf{F}$ and first Piola-Kirchhoff stress tensor $\mathbf{P}$ are, generally, non-symmetric second-order tensors, Green's function $\mathbb{\Phi}^0(\boldsymbol{\Xi})$ only has major symmetry

$$\hat{\Phi}^0_{ijkl}(\boldsymbol{\Xi}) = \hat{\Phi}^0_{klij}(\boldsymbol{\Xi}), \tag{2.84}$$

and therefore cannot be written in Voigt notation. Compact notation of (2.81) is again beneficial as it allows for the calculation of $\hat{\Phi}^1_{ijkl}(\boldsymbol{\Xi})$ and $\hat{\Phi}^2_{ijkl}(\boldsymbol{\Xi})$ independently from the reference material parameters λ^0 and μ^0. As in the case of small strains, using inverse Fourier transform it is possible to express Green's function in terms of spatial coordinates. For more details see **Appendix B**

2.5. Online stage

In the field of reduced-order microscopic approaches, the term "online stage" refers to the process in which, for a given macroscopic constraint, the solution of a reduced set of equations is solved and the homogenized, i.e. average values of stress, material stiffness tensor, strain energy, etc. are obtained and upscaled to the macrolevel. The computational efficiency of the online stage will determine the overall efficiency of the multiscale concurrent procedure that is being simulated. As stated in **section 2.1**, the reduction of the complexity of the RVE boundary value problem will impair accuracy to some extent. However, the increase in efficiency is often tremendous, which makes sacrificing a few percent of the accuracy worthwhile.

In order to conduct the online stage, i.e. self-consistent clustering analysis, the incremental Lippmann-Schwinger equation, derived for both small and finite strains needs to be defined for each material cluster. Here, the emphasis will be on the small strain formulation; however, as shown in **section 2.3** and **2.4** the extension to the finite strains is a straightforward task. With the successive homogenization of Eq. (2.16), the incremental Lippmann-Schwinger equation is averaged for each material cluster [67, 78]

$$\begin{aligned} &\frac{1}{c^I\Omega}\int_\Omega \chi^I(\mathbf{x})\,\Delta\boldsymbol{\varepsilon}(\mathbf{x})\,\mathrm{d}\mathbf{x} + \\ &\frac{1}{c^I\Omega}\int_\Omega\int_\Omega \chi^I(\mathbf{x})\,\mathbb{\Phi}^O(\mathbf{x},\mathbf{x}') : \left[\Delta\boldsymbol{\sigma}(\mathbf{x}') - \mathbf{C}^0 : \Delta\boldsymbol{\varepsilon}(\mathbf{x}')\right]\mathrm{d}\mathbf{x}'\mathrm{d}\mathbf{x} - \Delta\boldsymbol{\varepsilon}^0 = \mathbf{0}. \end{aligned} \tag{2.85}$$

where c^I is the volume fraction of the I-th material cluster inside the RVE with volume Ω. The equation above follows directly from the averaging of the original Eq. (2.16) within the I-th material cluster. Averaging is performed since the local variable β in

each material cluster is uniform, i.e. homogeneous. Using identity (2.1) for incremental small strain and Cauchy stress tensor, inside the RVE that is discretized with k number of clusters, it is valid to write

$$\Delta\boldsymbol{\varepsilon}\left(\mathbf{x}\right)=\sum_{I=1}^{k}\chi^{I}\left(\mathbf{x}\right)\Delta\boldsymbol{\varepsilon}^{I}, \tag{2.86}$$

$$\Delta\boldsymbol{\sigma}\left(\mathbf{x}\right)=\sum_{I=1}^{k}\chi^{I}\left(\mathbf{x}\right)\Delta\boldsymbol{\sigma}^{I}. \tag{2.87}$$

Using averaging identity defined in (2.3), Eq. (2.85) can be written for each material cluster I as

$$\begin{gathered}\Delta\boldsymbol{\varepsilon}^{I}+\sum_{J=1}^{k}\left[\frac{1}{c^{I}\Omega}\int_{\Omega}\int_{\Omega}\chi^{I}\left(\mathbf{x}\right)\chi^{J}\left(\mathbf{x}'\right)\mathbb{\Phi}^{0}\left(\mathbf{x},\mathbf{x}'\right)\mathrm{d}\mathbf{x}\mathrm{d}\mathbf{x}'\right]:\left[\Delta\boldsymbol{\sigma}^{J}-\mathbf{C}^{0}:\Delta\boldsymbol{\varepsilon}^{J}\right]-\\ \Delta\boldsymbol{\varepsilon}^{\mathbf{0}}=\mathbf{0}.\end{gathered} \tag{2.88}$$

In Eq. (2.88) term inside the square brackets represents a well-known quantity in micromechanics called the interaction tensor [67]

$$\mathbb{D}^{IJ}=\frac{1}{c^{I}\Omega}\int_{\Omega}\int_{\Omega}\chi^{I}\left(\mathbf{x}\right)\chi^{J}\left(\mathbf{x}'\right)\mathbb{\Phi}^{0}\left(\mathbf{x},\mathbf{x}'\right)\mathrm{d}\mathbf{x}'\mathrm{d}\mathbf{x}, \tag{2.89}$$

which represents the influence of the stress in the J-th cluster on the strain in the I-th cluster [67]. In the case of periodic RVE, the interaction tensor $\mathbb{D}^{IJ}$ is a fourth-order tensor that is determined through a double integral of Green's function $\mathbb{\Phi}^{0}\left(\mathbf{x},\mathbf{x}'\right)$. Now, using (2.89), Eq. (2.88) can be written in a more compact form as

$$\Delta\boldsymbol{\varepsilon}^{I}+\sum_{J=1}^{k}\mathbb{D}^{IJ}:\left[\Delta\boldsymbol{\sigma}^{J}-\mathbf{C}^{0}:\Delta\boldsymbol{\varepsilon}^{J}\right]-\Delta\boldsymbol{\varepsilon}^{0}=\mathbf{0}, \tag{2.90}$$

that is qualitatively quite similar to Eq. (2.13), i.e.

$$\boldsymbol{\varepsilon}\left(\mathbf{x}\right)+\int_{\Omega}\mathbb{\Phi}^{0}\left(\mathbf{x},\mathbf{x}'\right):\mathbf{q}\left(\mathbf{x}'\right)-\boldsymbol{\varepsilon}^{0}=\mathbf{0}. \tag{2.91}$$

Expression (2.90) can be regarded as the equilibrium that needs to be satisfied for each material cluster I. Unlike FEM, where homogenized value $\overline{\square}$ is calculated through e number of finite elements

$$\overline{\square}=\frac{1}{\Omega}\sum_{I=1}^{e}\square^{I}\Omega^{I}, \tag{2.92}$$

in the SCA, $\overline{\square}$ is determined through k number of clusters

$$\overline{\square} = \frac{1}{\Omega}\sum_{I=1}^{k} \square^I \Omega^I, \tag{2.93}$$

which is significantly smaller than the total number of finite elements.

After the discretization, the incremental far-field small strain tensor $\Delta\boldsymbol{\varepsilon}^0$ is still equal to the average strain in the RVE

$$\Delta\boldsymbol{\varepsilon}^0 = \sum_{I=1}^{k} c^I \Delta\boldsymbol{\varepsilon}^I. \tag{2.94}$$

Meanwhile, the macroscopic boundary conditions defined by (2.20) and (2.21) are also required to be discretized. Discretized macro-strain constraint can be written as

$$\Delta\overline{\boldsymbol{\varepsilon}} = \sum_{I=1}^{k} c^I \Delta\boldsymbol{\varepsilon}^I \rightarrow \Delta\boldsymbol{\varepsilon}^0 = \Delta\overline{\boldsymbol{\varepsilon}} \tag{2.95}$$

while for the macro-stress constraint it is valid to write

$$\Delta\overline{\boldsymbol{\sigma}} = \sum_{I=1}^{k} c^I \Delta\boldsymbol{\sigma}^I \tag{2.96}$$

For the problems that involve finite strains, Eq. (2.90), (2.94), (2.95) and (2.96) take the following form

$$\begin{cases} \Delta\mathbf{F}^I + \sum_{J=1}^{k} \mathbb{D}^{IJ} : \left[\Delta\mathbf{P}^J - \mathbf{C}^0 : \Delta\mathbf{F}^J\right] - \Delta\mathbf{F}^0 = \mathbf{0} \\ \Delta\mathbf{F}^0 = \sum_{I=1}^{k} c^I \Delta\mathbf{F}^I \\ \Delta\overline{\mathbf{F}} = \sum_{I=1}^{k} c^I \Delta\mathbf{F}^I \rightarrow \Delta\mathbf{F}^0 = \Delta\overline{\mathbf{F}} \\ \Delta\overline{\mathbf{P}} = \sum_{I=1}^{k} c^I \Delta\mathbf{P}^I, \end{cases} \tag{2.97}$$

where $\mathbb{D}^{IJ}$ is now the interaction tensor obtained through a double integral of Green's function $\mathbb{\Phi}^0(\mathbf{X}, \mathbf{X}')$

$$\mathbb{D}^{IJ} = \frac{1}{c^I \Omega_0} \int_{\Omega_0}\int_{\Omega_0} \chi^I(\mathbf{X})\, \chi^J(\mathbf{X}')\, \mathbb{\Phi}^0(\mathbf{X}, \mathbf{X}')\, \mathrm{d}\mathbf{X}'\mathrm{d}\mathbf{X}. \tag{2.98}$$

To obtain the interaction tensor $\mathbb{D}^{IJ}$, double integral in Eq. (2.89), i.e. (2.98)

needs to be solved. For an RVE that is discretized with uniform finite element mesh of $p \times p$ pixels (in 2D), or $p \times p \times p$ voxels (in 3D) and later decomposed with k number of material clusters, the interaction tensor $\mathbb{D}^{IJ}$ can be computed as

$$\mathbb{D}^{IJ} = \frac{1}{\Omega^I} \sum_{i \in \Omega^I} \sum_{j \in \Omega^J} \int_{\Omega^i} \int_{\Omega^j} \mathbb{\Phi}^0 (\mathbf{x}, \mathbf{x}') \, \mathrm{d}\mathbf{x}' \mathrm{d}\mathbf{x}, \quad I, J = 1, 2, 3, ..., k. \tag{2.99}$$

Here, indices i and j refer to the i-th, i.e. j-th pixel/voxel, which implies that the double integration is performed for all the interaction terms between a pixel/voxel in Ω^I and a pixel/voxel in Ω^J. As reported in [93], this procedure can be computationally quite expensive, especially in the case of three-dimensional RVEs. To increase the computational efficiency, Tang et al. [227] proposed a reduced method to approximate (2.99). However, from the author's own experience, the procedure outlined in [227] provided a good approximation of the interaction tensor $\mathbb{D}^{IJ}$ only for certain types of RVE material configuration. On the other hand, Cheng et al. [228] developed a fully numeric procedure for evaluating double integral (2.99) that does not include evaluation or the construction of Green's function in any way.

In contrast to [93, 227, 228], in [78, 85] $\mathbb{D}^{IJ}$ was computed through the convolution theorem, which is directly related to the inverse Fourier transform. Using Eq. (2.44), the relation between convolution integral and inverse Fourier transform is expressed in the following form

$$y(x) = \int_a^b \Phi(x, x') \, g(x') \, \mathrm{d}x' = \mathscr{F}^{-1} \left[\hat{\Phi}(\xi) \, \hat{g}(\xi) \right]. \tag{2.100}$$

where $\mathscr{F}^{-1}$ stands for inverse Fourier transform, ξ is the one-dimensional coordinate in Fourier space, while $\hat{\Phi}$ and $\hat{g}$ denote one-dimensional scalar functions expressed through the frequency domain. Applying (2.100) on (2.89), interaction tensor $\mathbb{D}^{IJ}$ is calculated as

$$\mathbb{D}^{IJ} = \frac{1}{c^I \Omega} \int_{\Omega} \chi^I (\mathbf{x}) \, \mathscr{F}^{-1} \left[\hat{\mathbb{\Phi}}^0 (\boldsymbol{\xi}) \, \mathscr{F} \left[\chi^J (\mathbf{x}') \right] \right], \tag{2.101}$$

where $\mathscr{F}$ is the Fourier transform of a function in the spatial domain. In the case of finite strains, Eq. (2.101) becomes

$$\mathbb{D}^{IJ} = \frac{1}{c^I \Omega_0} \int_{\Omega_0} \chi^I (\mathbf{X}) \, \mathscr{F}^{-1} \left[\hat{\mathbb{\Phi}}^0 (\boldsymbol{\Xi}) \, \mathscr{F} \left[\chi^J (\mathbf{X}') \right] \right]. \tag{2.102}$$

Before applying (2.101), i.e. (2.102) it is important to notice that expressions for both $\hat{\mathbb{\Phi}}^0 (\boldsymbol{\xi})$ (Eq. (2.63)) and $\hat{\mathbb{\Phi}}^0 (\boldsymbol{\Xi})$ (Eq. (2.78)) are not determined for $\boldsymbol{\xi} = \boldsymbol{\Xi} = \mathbf{0}$.

However, a uniformly distributed polarization stress (which follows from the frequency value of zero) will not induce any strain field inside the RVE, indicating

$$\hat{\mathbb{\Phi}}^0(\boldsymbol{\xi} = \mathbf{0}) = \hat{\mathbb{\Phi}}^0(\boldsymbol{\Xi} = \mathbf{0}) = \mathbf{0}. \tag{2.103}$$

An important feature of the continuous Lippmann-Schwinger equation, for both small (2.16) and finite strains (2.34) is that its solution $\Delta\boldsymbol{\varepsilon}(\mathbf{x})$, i.e. $\Delta\mathbf{F}(\mathbf{X})$ is independent of the choice of material parameters λ^0 and μ^0 that determine the stiffness of the reference material. This can be explained by the fact that the physical problem is fully described by the equilibrium condition and the prescribed macroscopic boundary conditions [67]. However, once the continuous integral equation is discretized based on the piecewise uniform assumption, the equilibrium is not strictly satisfied at every point in the RVE, and the solution of the reduced system of equations therefore depends on the choice of λ^0 and μ^0. This discrepancy can be reduced by increasing the number of material clusters; however, this will have a negative effect on overall computational efficiency due to the increase in DOF. Self-consistent clustering analysis aims to mitigate this issue differently, by applying a self-consistent scheme during the online stage, i.e. after each converged increment.

2.5.1. Self-consistent scheme - update of $\mathbb{C}^0$

Originally proposed by Hill [52], the self-consistent scheme is utilized to improve the level of accuracy without the increase in the number of material clusters. This is achieved by setting the material stiffness tensor of the reference material approximately the same as the homogenized material stiffness tensor of the whole RVE, i.e.

$$\mathbb{C}^0 \rightarrow \overline{\mathbb{C}}, \tag{2.104}$$

where the material stiffness tensor $\mathbb{C}^0$ can be expressed in terms of bulk modulus κ^0 and shear modulus μ^0 as

$$\mathbb{C}^0 = \kappa^0 \mathbf{I} \otimes \mathbf{I} + \mu^0 \left(2\mathbb{I}_S - \frac{2}{n}\mathbf{I} \otimes \mathbf{I} \right), \tag{2.105}$$

with $\mathbb{I}_S$ being the symmetric part of the fourth-order identity tensor

$$\mathbb{I}_S = \frac{1}{2}\left(\delta_{ik}\delta_{jl} + \delta_{il}\delta_{jk}\right), \tag{2.106}$$

and n denoting the number of dimensions. In (2.105), instead of Lamé parameter λ^0, which is present in the expressions for Green's function, bulk modulus κ^0 is used. Its

relationship with μ^0 and λ^0 is determined by the following identity

$$\kappa^0 = \lambda^0 + \frac{2}{n}\mu^0, \tag{2.107}$$

where n, as stated before, defines the number of dimensions. On the other hand, homogenized material stiffness tensor $\overline{\mathbb{C}}$ needs to be computed and its value follows directly from the homogenized incremental small strain and Cauchy stress tensor

$$\overline{\mathbb{C}} = \frac{\partial \Delta\overline{\boldsymbol{\sigma}}}{\partial \Delta\overline{\boldsymbol{\varepsilon}}} = \frac{\partial}{\partial \Delta\overline{\boldsymbol{\varepsilon}}}\left(\sum_{I=1}^{k} c^I \Delta\boldsymbol{\sigma}^I\right) = \sum_{I=1}^{k} c^I \frac{\partial \Delta\boldsymbol{\sigma}^I}{\partial \Delta\boldsymbol{\varepsilon}^I} : \frac{\partial \Delta\boldsymbol{\varepsilon}^I}{\partial \Delta\overline{\boldsymbol{\varepsilon}}} = \sum_{I=1}^{k} c^I \mathbb{C}^I : \mathbb{A}^I, \tag{2.108}$$

i.e. from the homogenized incremental deformation gradient and first Piola-Kirchhoff stress tensor

$$\overline{\mathbb{C}} = \frac{\partial \Delta\overline{\mathbf{P}}}{\partial \Delta\overline{\mathbf{F}}} = \frac{\partial}{\partial \Delta\overline{\mathbf{F}}}\left(\sum_{I=1}^{k} c^I \Delta\mathbf{P}^I\right) = \sum_{I=1}^{k} c^I \frac{\partial \Delta\mathbf{P}^I}{\partial \Delta\mathbf{F}^I} : \frac{\partial \Delta\mathbf{F}^I}{\partial \Delta\overline{\mathbf{F}}} = \sum_{I=1}^{k} c^I \mathbb{C}^I : \mathbb{A}^I. \tag{2.109}$$

$\mathbb{C}^I$ in Eq. (2.108) and (2.109) represents stiffness tensor in the I-th material cluster depending on the constitutive law at the microlevel, while $\mathbb{A}^I$ denotes small strain/deformation gradient concentration tensor that provides a quantitative connection between strain/deformation gradient in the I-th material cluster and at the macrolevel. Since both $\mathbb{A}^I$ and $\overline{\mathbb{C}}$ are required for the self-consistent scheme, their calculation is performed once after the convergence of the Newton's iterative method in order to save computational time.

In the case of material or geometrical nonlinearities, it is not possible to determine $\mathbb{C}^0$ which provides an exact match with $\overline{\mathbb{C}}$. Still, the calculation of the new material parameters that form $\mathbb{C}^0$ is extremely beneficial, since the values of $\overline{\mathbb{C}}$ can change significantly during the analysis. In [67], two types of self-consistent schemes were proposed: (1) regression-based scheme, and (2) projection-based scheme.

In the regression based scheme, the self-consistent scheme is formulated as an optimization problem with the goal of finding λ^0 and μ^0 that minimize the cost function w

$$w\left(\lambda', \mu'\right) = \left|\left|\Delta\overline{\boldsymbol{\sigma}} - \mathbb{C}^0\left(\lambda', \mu'\right) : \Delta\overline{\boldsymbol{\varepsilon}}\right|\right|^2, \tag{2.110}$$

where $||\mathbf{Z}||^2 = \mathbf{Z} : \mathbf{Z}$ for an arbitrary second-order tensor $\mathbf{Z}$. In the case of finite strain analysis, expression (2.110) takes the following form

$$w\left(\lambda', \mu'\right) = \left|\left|\Delta\overline{\mathbf{P}} - \mathbb{C}^0\left(\lambda', \mu'\right) : \Delta\overline{\mathbf{F}}\right|\right|^2. \tag{2.111}$$

Now, the optimal point is obtained via the respective partial derivative of the cost function w, i.e.

$$\left.\frac{\partial w\left(\lambda', \mu'\right)}{\partial \lambda'}\right|_{\lambda^0, \mu^0} = 0, \tag{2.112}$$

$$\left.\frac{\partial w\left(\lambda', \mu'\right)}{\partial \mu'}\right|_{\lambda^0, \mu^0} = 0. \tag{2.113}$$

which forms a system of two linear equations in terms of λ' and μ'. The system always has a unique solution except for pure shear or hydrostatic conditions. In the former, Lamé parameter λ^0 cannot be determined and therefore is not updated, while in the latter shear modulus μ^0 is not updated. Additionally, $w\left(\lambda^0, \mu^0\right)$ vanishes when the effective macroscopic homogeneous material is also isotropic and linear elastic.

However, apart from being under-determined for pure shear and hydrostatic type loading, the optimization problem defined by (2.112) and (2.113) can also produce non-physical values for λ^0 and μ^0. More precisely, the material parameters of the reference material may become negative in the case of complex loading conditions, which is deleterious to the convergence in the online stage.

In contrast to the regression based scheme, the projection based scheme aims to find the optimal values of the reference material parameters by defining a set of two, one-dimensional cost functions: w_1

$$w_1\left(\kappa'\right) = \left|\left|\left[\overline{\mathbb{C}} - \mathbb{C}^0\left(\kappa'\right)\right] : \Delta\overline{\boldsymbol{\varepsilon}}_{\mathrm{h}}\right|\right|^2, \tag{2.114}$$

and w_2

$$w_2\left(\mu'\right) = \left|\left|\left[\overline{\mathbb{C}} - \mathbb{C}^0\left(\mu'\right)\right] : \Delta\overline{\boldsymbol{\varepsilon}}_{\mathrm{dev}}\right|\right|^2, \tag{2.115}$$

where $\Delta\overline{\boldsymbol{\varepsilon}}_{\mathrm{h}}$ and $\Delta\overline{\boldsymbol{\varepsilon}}_{\mathrm{dev}}$ represent hydrostatic, i.e. deviatoric part of the homogenized incremental small strain tensor, which can be calculated through

$$\Delta\overline{\boldsymbol{\varepsilon}}_{\mathrm{h}} = \frac{1}{n}\mathrm{tr}\left[\Delta\overline{\boldsymbol{\varepsilon}}\right]\mathbf{I}, \tag{2.116}$$

$$\Delta\overline{\boldsymbol{\varepsilon}}_{\mathrm{dev}} = \Delta\overline{\boldsymbol{\varepsilon}} - \frac{1}{n}\mathrm{tr}\left[\Delta\overline{\boldsymbol{\varepsilon}}\right]. \tag{2.117}$$

After taking derivative of the cost functions w_1 and w_2, the following system of equations is obtained

$$\left.\frac{\mathrm{d}w_1\left(\kappa'\right)}{\mathrm{d}\kappa'}\right|_{\kappa^0,\mu^0} = 0, \tag{2.118}$$

$$\left.\frac{\mathrm{d}w_2\left(\mu'\right)}{\mathrm{d}\mu'}\right|_{\kappa^0,\mu^0} = 0, \tag{2.119}$$

which, in contrast to the regression based scheme, is independent, since Eq. (2.118) is solved independently from Eq. (2.119). Using index notation, κ^0 and μ^0 for the case of small strains are expressed as

$$\kappa^0 = \frac{\overline{C}_{iijj}}{n}, \tag{2.120}$$

$$\mu^0 = \frac{\overline{C}_{ijkl}\Delta\overline{\varepsilon}^{\mathrm{dev}}_{ij}\Delta\overline{\varepsilon}^{\mathrm{dev}}_{kl}}{2\Delta\overline{\varepsilon}^{\mathrm{dev}}_{ij}\Delta\overline{\varepsilon}^{\mathrm{dev}}_{ij}}, \tag{2.121}$$

while their values in finite strain configuration can be obtained as

$$\kappa^0 = \frac{\overline{C}_{iijj}}{n}, \tag{2.122}$$

$$\mu^0 = \frac{\overline{C}_{ijkl}\Delta\overline{F}^{\mathrm{dev}}_{kl}\left(\Delta\overline{F}^{\mathrm{dev}}_{ij} + \Delta\overline{F}^{\mathrm{dev}}_{ji}\right)}{\left(\Delta\overline{F}^{\mathrm{dev}}_{ij} + \Delta\overline{F}^{\mathrm{dev}}_{ji}\right)\left(\Delta\overline{F}^{\mathrm{dev}}_{ij} + \Delta\overline{F}^{\mathrm{dev}}_{ji}\right)}. \tag{2.123}$$

From (2.120) and (2.122) it is clear that the value of the bulk modulus κ^0 depends solely on the value of the homogenized material stiffness tensor $\overline{\mathbb{C}}$ and therefore can be computed regardless of the loading conditions. On the other hand, shear modulus μ^0 is, as in the case of the regression based scheme, undetermined for the hydrostatic type of loading, since there exists no deviatoric part of the homogenized incremental small strain, i.e. deformation gradient tensor. An effective way of updating $\mathbb{C}^0$ is to consider both schemes that can be utilized depending on the loading conditions. The regression based scheme provides a higher level of accuracy since it relies on the optimization that does not include macroscopic material stiffness tensor $\overline{\mathbb{C}}$ and should be used whenever possible. On the other hand, the projection based scheme yields poorer accuracy but ensures physical values of κ^0 and μ^0 when complex loading conditions are in question.

The material stiffness tensor of the reference material $\mathbb{C}^0$ is not the only value that will be updated after every converged increment. Interaction tensor $\mathbb{D}^{IJ}$, defined by (2.89), i.e. (2.98) will also be subject to change during the SCA since its value derives directly from Green's function. However, this does not imply that it is necessary

to resolve double integral after every converged increment of the analysis. Recall that Green's function in the Fourier space, for both small and finite strains, is expressed in a compact form where the reference material parameters λ^0 and μ^0 are independent of the Fourier coordinates, i.e.

$$\hat{\Phi}^0_{ijkl}(\boldsymbol{\xi}) = \frac{1}{4\mu^0}\hat{\Phi}^1_{ijkl}(\boldsymbol{\xi}) + \frac{\lambda^0+\mu^0}{\mu^0(\lambda^0+2\mu^0)}\hat{\Phi}^2_{ijkl}(\boldsymbol{\xi}), \tag{2.124}$$

$$\hat{\Phi}^0_{ijkl}(\boldsymbol{\Xi}) = \frac{1}{\mu^0}\hat{\Phi}^1_{ijkl}(\boldsymbol{\Xi}) + \frac{\lambda^0+\mu^0}{\lambda^0+2\mu^0}\hat{\Phi}^2_{ijkl}(\boldsymbol{\Xi}). \tag{2.125}$$

Therefore, $\hat{\Phi}^1_{ijkl}$ and $\hat{\Phi}^2_{ijkl}$ can be computed once in the offline stage, and their values can be used during the whole online stage. If the reference material is changed in the self-consistent scheme during the online stage, only the coefficients relating to its Lamé constants need to be updated.

2.5.2. Numerical implementation

In general case, where RVE exhibits nonlinear behaviour such as plasticity, damage, or large deformations, it is not possible to obtain the exact solution of the equilibrium (2.90), i.e. (2.97). This implies that the solution has to be obtained numerically through a series of iterations at every loading increment. Herein, an implicit scheme is adopted and the numerical implementation, following [78], for both small and finite strains is presented. As in previous sections, the emphasis will be on the small strain configuration.

To begin, the residual of the discretized Lippmann-Schwinger equation in the I-th cluster is defined as

$$\mathbf{r}^I = \Delta\boldsymbol{\varepsilon}^I + \sum_{J=1}^{k} \mathbb{D}^{IJ} : \left[\Delta\boldsymbol{\sigma}^J - \mathbf{C}^0 : \Delta\boldsymbol{\varepsilon}^J\right] - \Delta\boldsymbol{\varepsilon}^0, \quad I = 1, 2, ..., k, \tag{2.126}$$

while the residual of the macro-strain/macro-stress constraint is

$$\mathbf{r}^{k+1} = \sum_{I=1}^{k} c^I \Delta\boldsymbol{\varepsilon}^I - \Delta\overline{\boldsymbol{\varepsilon}}, \quad \Delta\boldsymbol{\varepsilon}^0 = \Delta\overline{\boldsymbol{\varepsilon}} \tag{2.127}$$

$$\mathbf{r}^{k+1} = \sum_{I=1}^{k} c^I \Delta\boldsymbol{\sigma}^I - \Delta\overline{\boldsymbol{\sigma}}. \tag{2.128}$$

In the implicit scheme, the residual $\mathbf{r} = \{\mathbf{r}^1; \mathbf{r}^2; ...; \mathbf{r}^{k+1}\}$, is linearized with respect to the incremental small strain tensor $\Delta\boldsymbol{\varepsilon} = \{\Delta\boldsymbol{\varepsilon}^1; \Delta\boldsymbol{\varepsilon}^2; ...; \Delta\boldsymbol{\varepsilon}^0\}$. After dropping terms

of higher order, the following system is obtained

$$\mathbf{r} + \mathbb{M}\delta\boldsymbol{\varepsilon} = \mathbf{0}, \tag{2.129}$$

where $\mathbb{M}$ is a system Jacobian matrix obtained through

$$\mathbb{M} = \frac{\partial \mathbf{r}}{\partial \Delta\boldsymbol{\varepsilon}}. \tag{2.130}$$

For $I, J = 1, 2, ..., k$, the components of $\mathbb{M}$ are

$$\mathbb{M}^{IJ} = \delta_{IJ}\mathbb{I} + \mathbb{D}^{IJ} : \left(\mathbb{C}^J - \mathbb{C}^0\right), \tag{2.131}$$

where δ_{IJ} is the Kronecker delta symbol in terms of I and J, $\mathbb{I}$ denotes fourth-order identity tensor

$$\mathbb{I} = \delta_{ik}\delta_{jl}, \tag{2.132}$$

while $\mathbb{C}^J$ is the material stiffness matrix in the J-th material cluster defined as

$$\mathbb{C}^J = \frac{\partial \Delta\boldsymbol{\sigma}^J}{\partial \Delta\boldsymbol{\varepsilon}^J}. \tag{2.133}$$

Under the macro-strain constraint, the remaining components of the system Jacobian matrix $\mathbb{M}$ are

$$\mathbb{M}^{(k+1)I} = c^I\mathbb{I}, \tag{2.134}$$

and

$$\mathbb{M}^{(k+1)(k+1)} = \mathbf{0}. \tag{2.135}$$

On the other hand, for the macro-stress constraint, it is valid to write

$$\mathbb{M}^{(k+1)I} = c^I\mathbb{C}^I, \tag{2.136}$$

$$\mathbb{M}^{(k+1)(k+1)} = \mathbf{0}. \tag{2.137}$$

The remaining part of the system Jacobian matrix $\mathbb{M}$ is the same regardless of the constraints, i.e.

$$\mathbb{M}^{I(k+1)} = -\mathbb{I}. \tag{2.138}$$

Finally, the correction of the incremental strain can be expressed as

$$\delta\boldsymbol{\varepsilon} = -\mathbb{M}^{-1}\mathbf{r}. \tag{2.139}$$

Based on the updated incremental small strain tensor and a specific material constitutive law, it is possible to obtain the new value of the incremental stress tensor in each material cluster. In the case of finite strains, all that is needed is to replace the small strain tensor with a deformation gradient and Cauchy stress tensor with first Piola-Kirchhoff stress tensor. Of course, one also has to replace the constitutive law that was used for small strain configuration with the constitutive law for finite strains. To finish, a general numerical algorithm of the self-consistent clustering analysis is given in Box I.

Box I: General algorithm for the self-consistent clustering analysis

1. Initial condition and initialization: set (κ^0, μ^0); $n = 0$; $\Delta\boldsymbol{\varepsilon}_n = \Delta\boldsymbol{\sigma}_n = \mathbf{0}$.
2. Start new increment n: $n = n + 1$.
3. For a load increment n use (2.127), i.e. (2.128) and define $\mathbf{r}^{k+1}$, update the interaction tensor $\mathbb{D}^{IJ}$ and the material stiffness tensor of the reference material $\mathbb{C}^0$ based on κ^0 and μ^0.
4. Newton iterations for load increment n: set iteration $i = 0$.
   (a) Start new iteration i: $i = i + 1$.
   (b) Compute incremental Cauchy stress tensor $\Delta\boldsymbol{\sigma}$ in each cluster based on the specific material constitutive law.
   (c) Use (2.126) and (2.127), or (2.126) and 2.128 to compute residual $\mathbf{r}$.
   (d) Use (2.131), (2.134), (2.135) and (2.138) or (2.131), (2.136), (2.137) and (2.138) to compute system Jacobian $\mathbb{M}$.
   (e) Use (2.139) to compute the correction of the incremental strain $\delta\boldsymbol{\varepsilon}$.
   (f) Update the incremental small strain tensor $\Delta\boldsymbol{\varepsilon} = \Delta\boldsymbol{\varepsilon} + \delta\boldsymbol{\varepsilon}$.
   (g) Check the stopping criterion. If not met: go to 4 (a).
5. Compute the macroscopic material stiffness tensor $\overline{\mathbb{C}}$ and calculate optimal values for κ^0 and μ^0 using either regression or projection based self-consistent scheme.
6. Update the values for the small strain and Cauchy stress tensor: $\boldsymbol{\sigma}_n = \boldsymbol{\sigma}_{n-1} + \Delta\boldsymbol{\sigma}_n$, $\boldsymbol{\varepsilon}_n = \boldsymbol{\varepsilon}_{n-1} + \Delta\boldsymbol{\varepsilon}_n$.
7. If simulation not complete: go to 2.

2.6. Numerical validation

In this section, a thorough numerical validation is conducted in order to test the capability of the self-consistent clustering analysis to compute the homogenized response of the complex microstructure subjected to various macro-loading conditions and with different number of clusters. The goal is to evaluate the accuracy and computational

time of the SCA by comparing it to the DNS which is carried out using FEM. The expectation is that the SCA will offer significant savings in the computational time and resources, while at the same time ensuring a minimum deviation from the homogenized results obtained by the DNS.

Analyses are performed for both two- and three-dimensional microstructures all consisting of two material phases - matrix (material phase 1) and inclusions (material phase 2). In all examples, the matrix material phase is treated as an elastoplastic material with the following material properties

$$\begin{aligned} E = 70000 \text{ MPa}, \;\; \nu = 0.33, \\ \sigma_y^0 = 150 \text{ MPa}, \;\; k = 150\text{MPa}, \;\; r = 0.15. \end{aligned} \tag{2.140}$$

Here, E is the modulus of elasticity, ν stands for Poisson ratio, σ_y^0 denotes the initial yield strength, while k and r are material parameters of Swift's non-linear isotropic hardening law that is given by

$$\sigma_y\left(\varepsilon_{\text{eq}}^{\text{p}}\right) = \sigma_y^0\left(1 + k\varepsilon_{\text{eq}}^{\text{p}}\right)^r, \tag{2.141}$$

with σ_y being the hardening function depending on the value of equivalent plastic strain $\varepsilon_{\text{eq}}^{\text{p}}$ whose evolution is modelled through von Mises (J_2) yield criterion, i.e.

$$f = \sqrt{\frac{3}{2}\mathbf{S} : \mathbf{S}} - \sigma_y\left(\varepsilon_{\text{eq}}^{\text{p}}\right). \tag{2.142}$$

In Eq. (2.142) f is a yield surface, while $\mathbf{S}$ denotes deviatoric part of the Cauchy stress tensor that is calculated through

$$\mathbf{S} = \boldsymbol{\sigma} - \frac{1}{n}\text{tr}\left[\boldsymbol{\sigma}\right]\mathbf{I}, \tag{2.143}$$

where n defines the number of dimensions, "tr" represents the trace operator, while $\mathbf{I}$ stands for second-order identity tensor.

On the other hand, the second material phase, which is represented by inclusions that are embedded into the matrix, is (in all examples) treated as a linear elastic material. However, two material configurations are considered

$$\begin{aligned} \text{hard inclusions} \rightarrow \{E = 200000 \text{ MPa}, \;\; \nu = 0.29\}, \\ \text{soft inclusions} \rightarrow \{E = 5000 \text{ MPa}, \;\; \nu = 0.29\}. \end{aligned} \tag{2.144}$$

Therefore, each microstructure has two different material configurations: (1) matrix

with embedded hard inclusions, and (2) matrix with embedded soft inclusions.

In terms of macroscopic boundary conditions, only macro-strain constraints are utilized. Recall that in the Lippmann-Schwinger equation boundary conditions are applied as constraints on the volume average of the small strain or stress tensor, i.e. deformation gradient or first Piola-Kirchhoff stress tensor. The number of different macro-strain constraints is obviously infinite; however, focusing on several characteristic ones will be sufficient to demonstrate the effectiveness of the SCA. Here, four different macro-strain constraints are defined. For small strain configuration, they are expressed in Voigt notation for both two-

$$\begin{cases} \overline{\boldsymbol{\varepsilon}}^1 = \eta \left[\overline{\varepsilon}_x = 1, \quad \overline{\varepsilon}_y = 0, \quad \overline{\varepsilon}_z = 0, \quad \overline{\gamma}_{xy} = 0\right]^T \\ \overline{\boldsymbol{\varepsilon}}^2 = \eta \left[\overline{\varepsilon}_x = 0, \quad \overline{\varepsilon}_y = 0, \quad \overline{\varepsilon}_z = 0, \quad \overline{\gamma}_{xy} = 1\right]^T \\ \overline{\boldsymbol{\varepsilon}}^3 = \eta \left[\overline{\varepsilon}_x = 1, \quad \overline{\varepsilon}_y = 1, \quad \overline{\varepsilon}_z = 0, \quad \overline{\gamma}_{xy} = 0\right]^T \\ \overline{\boldsymbol{\varepsilon}}^4 = \eta \left[\overline{\varepsilon}_x = 1, \quad \overline{\varepsilon}_y = 1, \quad \overline{\varepsilon}_z = 0, \quad \overline{\gamma}_{xy} = 1\right]^T \end{cases} \tag{2.145}$$

and three-dimensional analysis

$$\begin{cases} \overline{\boldsymbol{\varepsilon}}^1 = \eta \left[\overline{\varepsilon}_x = 1, \quad \overline{\varepsilon}_y = 0, \quad \overline{\varepsilon}_z = 0, \quad \overline{\gamma}_{xy} = 0, \quad \overline{\gamma}_{xz} = 0, \quad \overline{\gamma}_{yz} = 0\right]^T \\ \overline{\boldsymbol{\varepsilon}}^2 = \eta \left[\overline{\varepsilon}_x = 0, \quad \overline{\varepsilon}_y = 0, \quad \overline{\varepsilon}_z = 0, \quad \overline{\gamma}_{xy} = 1, \quad \overline{\gamma}_{xz} = 0, \quad \overline{\gamma}_{yz} = 0\right]^T \\ \overline{\boldsymbol{\varepsilon}}^3 = \eta \left[\overline{\varepsilon}_x = 1, \quad \overline{\varepsilon}_y = 1, \quad \overline{\varepsilon}_z = 1, \quad \overline{\gamma}_{xy} = 0, \quad \overline{\gamma}_{xz} = 0, \quad \overline{\gamma}_{yz} = 0\right]^T \\ \overline{\boldsymbol{\varepsilon}}^4 = \eta \left[\overline{\varepsilon}_x = 1, \quad \overline{\varepsilon}_y = 1, \quad \overline{\varepsilon}_z = 1, \quad \overline{\gamma}_{xy} = 1, \quad \overline{\gamma}_{xz} = 1, \quad \overline{\gamma}_{yz} = 1\right]^T \end{cases} \tag{2.146}$$

Here, η is a scalar value that multiplies each member in a small strain vector. Its value is set to 0.05, i.e. to 5 % of macroscopic deformation. Notice that in (2.145) homogenized normal strain in z direction is present, and its value is constantly equal to zero. This is because all 2D analyses are carried out under plane strain assumption, which implies that the value of strain in the z direction is always equal to zero. For each macro-strain constraint listed in (2.145), i.e. (2.146), the following homogenized strain-stress relations are depicted using 2D diagrams

$$\overline{x} - \overline{y} = \begin{cases} \overline{\varepsilon}_x - \overline{\sigma}_x, & \overline{\boldsymbol{\varepsilon}} = \overline{\boldsymbol{\varepsilon}}^1 \\ \overline{\gamma}_{xy} - \overline{\tau}_{xy}, & \overline{\boldsymbol{\varepsilon}} = \overline{\boldsymbol{\varepsilon}}^2 \\ \overline{\varepsilon}_{\mathrm{h}} - \overline{\sigma}_{\mathrm{h}}, & \overline{\boldsymbol{\varepsilon}} = \overline{\boldsymbol{\varepsilon}}^3 \\ \overline{\varepsilon}_x - \overline{\sigma}_{\mathrm{eq}}, & \overline{\boldsymbol{\varepsilon}} = \overline{\boldsymbol{\varepsilon}}^4. \end{cases} \tag{2.147}$$

In (2.147) $\overline{x} - \overline{y}$ denotes a specific homogenized strain-homogenized stress relation that depends on the type of macro-strain constraint. Notice that for $\overline{\boldsymbol{\varepsilon}}^3$, which is actually pure hydrostatic loading, homogenized hydrostatic strain $\overline{\varepsilon}_{\mathrm{h}}$ and homogenized hydrostatic stress $\overline{\sigma}_{\mathrm{h}}$ are computed and visualized. On the other hand, for $\overline{\boldsymbol{\varepsilon}}^4$, which includes all components of the small strain vector, homogenized equivalent (von Mises) stress $\overline{\sigma}_{\mathrm{eq}}$ is displayed on the ordinate axis.

Last but not least, SCA, as a numerical procedure, is implemented in the commercial software Matlab, while DNS (conducted through FEM) is performed using commercial finite element software Abaqus. By applying fixed incrementation, both SCA and DNS are carried out in a total of 100 increments, which ensures the maximum level of objectivity. The workstation standing behind every Matlab and every two-dimensional Abaqus simulation is driven by the Intel Xeon E5-1620 (version 2) processor alongside 24 GB of DDR3 RAM. In the case of all three-dimensional DNS analyses, a more powerful workstation containing an AMD Ryzen 3900x processor and 128 GB of DDR4 RAM is utilized. All Matlab and all two-dimensional Abaqus simulations were conducted on a single CPU, while all three-dimensional Abaqus simulations were performed using four CPUs in parallel.

2.6.1. Two-dimensional elastoplastic material

Microstructures depicted in **Figure 2.7** represent two different RVEs that were generated for the purposes of the numerical validation of the SCA in 2D space. Microstructures are identical in terms of

- size - both with a length of 0.2 mm,
- material composition - both consisting of matrix and circular inclusions with fixed radius of 0.01 mm,
- material configuration - both possessing one elastoplastic material phase (matrix) and one linear elastic material phase (circular inclusions).

Two characteristics that set them apart are

- volume fraction - one with 20 % and the other with 40 % of circular inclusions share,
- minimum neighbour distance [229] - one with 8 μm and the other with 4 μm of the minimum neighbour distance.

As mentioned in **section 2.6**, each microstructure will have two different material configurations in total. One with elastoplastic matrix and hard circular inclusions, and one with elastoplastic matrix and soft circular inclusions. Therefore in this subsection results for four different microstructures are presented. Also, as can be seen from **Figure 2.7**, both RVEs possess periodicity in their geometry, which is a necessary condition in the field of micromechanics and Fourier analysis.

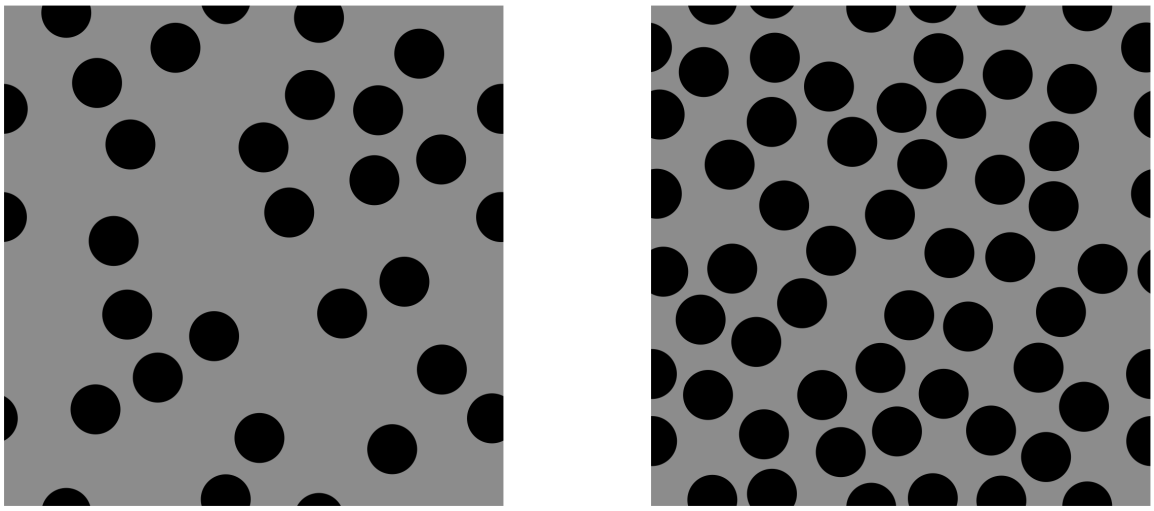

(a) 2D RVE with 20 % of circular inclusions

(b) 2D RVE with 40 % of circular inclusions

Figure 2.7: Geometry of the 2D RVEs

Before the actual comparison between the SCA and DNS, several analyses need to be carried out first. In order to conduct the SCA, all four microstructures need to be decomposed into k number of clusters. As stated in **section 2.2**, the minimum number of clusters must be equal to the number of material phases, while the maximum number of clusters is limited by the total number of points for which the strain concentration tensor $\mathbb{A}$ is being calculated. With the goal of performing a detailed assessment of the SCA, all RVEs are decomposed into 8, 32 and 128 material clusters. This diversity of cluster numbers will provide a better understanding of the computational efficiency of the SCA since it allows for the study of convergence and computational time. In order to ensure a high quality of the clustering results, finite element simulations under three orthogonal loading conditions were carried out on the extraordinary fine mesh of 10^6 quadrilateral finite elements with one integration point in their center, i.e. 1000×1000 pixels. The results of the k-means clustering for all four RVEs are depicted in **Figures 2.8**, **2.9**, **2.10** and **2.11**.

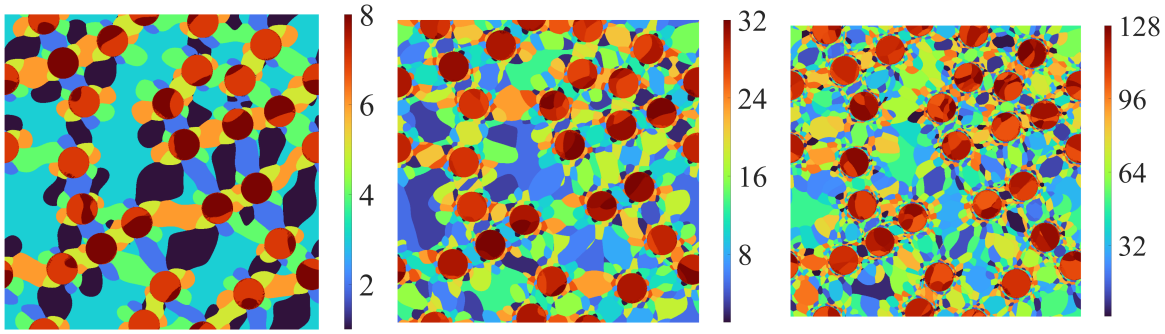

(a) $k = 8$ **(b)** $k = 32$ **(c)** $k = 128$

Figure 2.8: Results of the k-means clustering for a 2D RVE with 20 % of hard inclusions

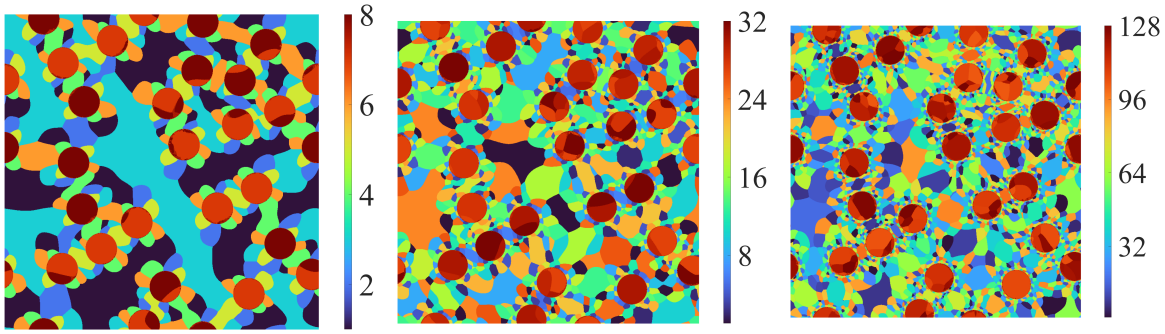

(a) $k = 8$ **(b)** $k = 32$ **(c)** $k = 128$

Figure 2.9: Results of the k-means clustering for a 2D RVE with 20 % of soft inclusions

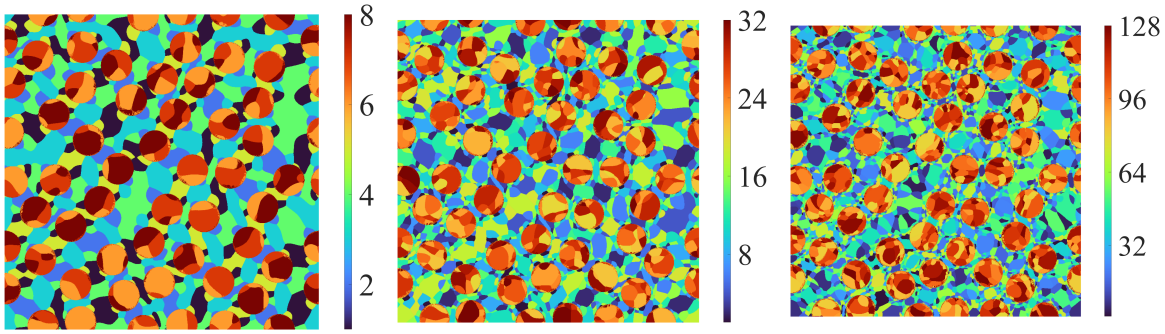

(a) $k = 8$ **(b)** $k = 32$ **(c)** $k = 128$

Figure 2.10: Results of the k-means clustering for a 2D RVE with 40 % of hard inclusions

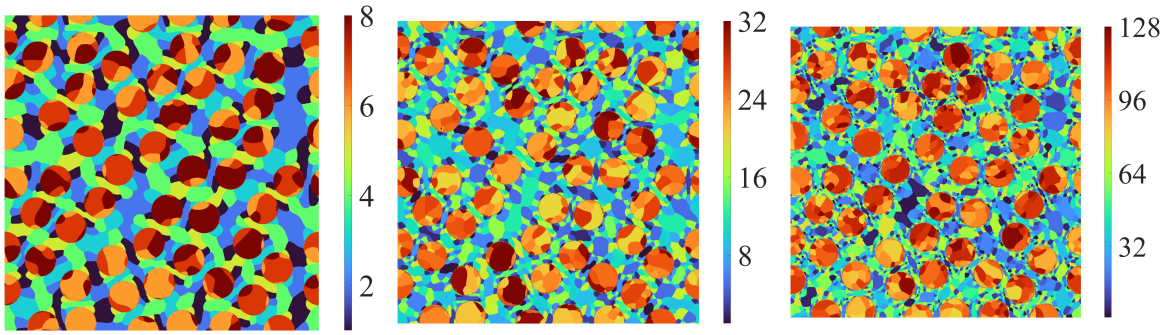

(a) $k = 8$ **(b)** $k = 32$ **(c)** $k = 128$

Figure 2.11: Results of the k-means clustering for a 2D RVE with 40 % of soft inclusions

From **Figure 2.8** and **Figure 2.9**, it is clear that although both microstructures have identical geometrical configuration, due to their different material configuration k-means clustering produces a completely different decomposition for the same number of clusters. Also, notice that one material cluster can be located in several different positions. This is because different locations in the RVE can have similar mechanical response, i.e. similar values of the strain concentration tensor $\mathbb{A}$. After the domain decomposition into the appropriate number of clusters, the next step includes the calculation of the interaction tensor $\mathbb{D}^{IJ}$ using (2.101), i.e. (2.102). As well as the k-means clustering, this part of the offline stage is carried out using Matlab.

Alongside the SCA, finite element simulations also need to be carried out for four different macro-strain constraints defined by (2.145). However, the use of a finite element mesh that contains 10^6 quadrilateral finite elements is not necessary since accurate homogenized results can be obtained with a significantly sparser mesh. To get a rough estimate of the finite element mesh that is sufficient, finite element simulations with two different discretizations were carried out on the pure shear loading condition, i.e. using macro-strain constraint $\overline{\boldsymbol{\varepsilon}}^2$. The homogenized stress-strain relations for 100×100 and 200×200 pixels discretization are depicted in **Figure 2.12**.

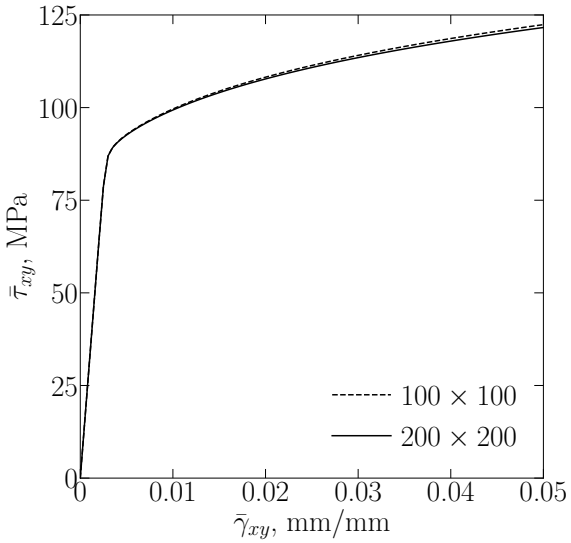

(a) 2D RVE with 20 % of hard inclusions

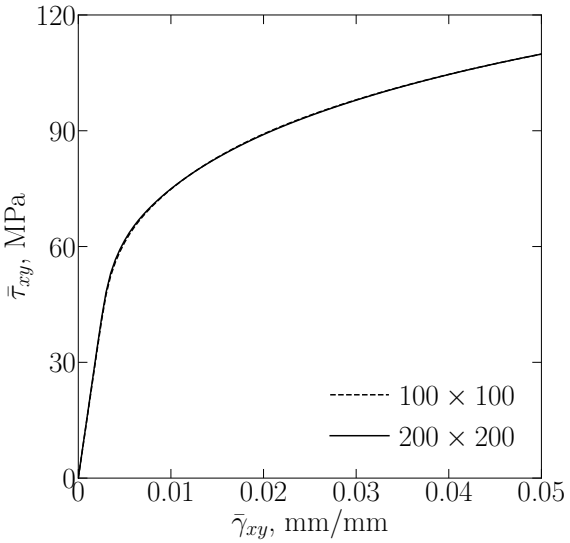

(b) 2D RVE with 20 % of soft inclusions

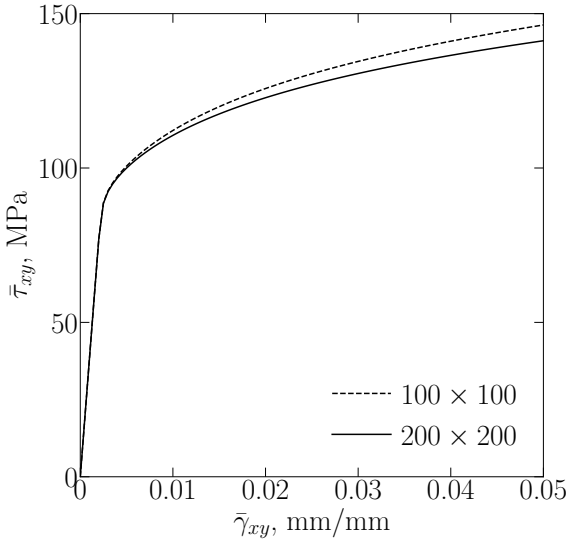

(c) 2D RVE with 40 % of hard inclusions

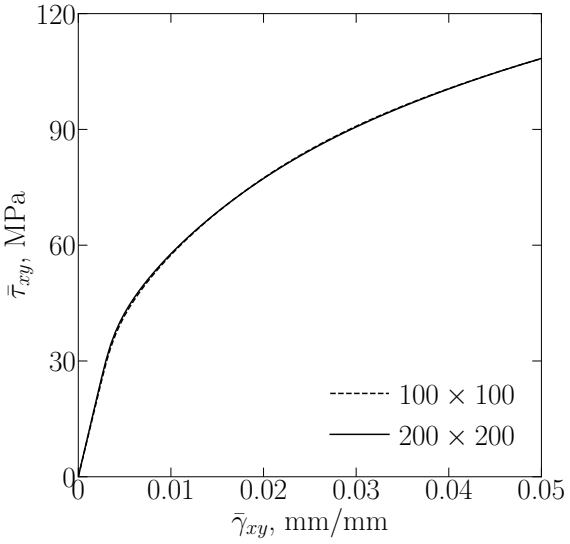

(d) 2D RVE with 40 % of soft inclusions

Figure 2.12: Influence of the finite element discretization on the homogenized values for the case of $\overline{\boldsymbol{\varepsilon}} = \overline{\boldsymbol{\varepsilon}}^2$

For all RVEs, except for the RVE with 40 % of hard inclusions, the maximum relative difference between two discretizations is less than 1 %. This deviation is higher in the case of the RVE with 40 % of hard inclusions; however, at only 3.6 % it is still negligible.

In the next four figures and four tables comparisons of the macroscopic stress-strain relations and computational times for both SCA and DNS are presented.

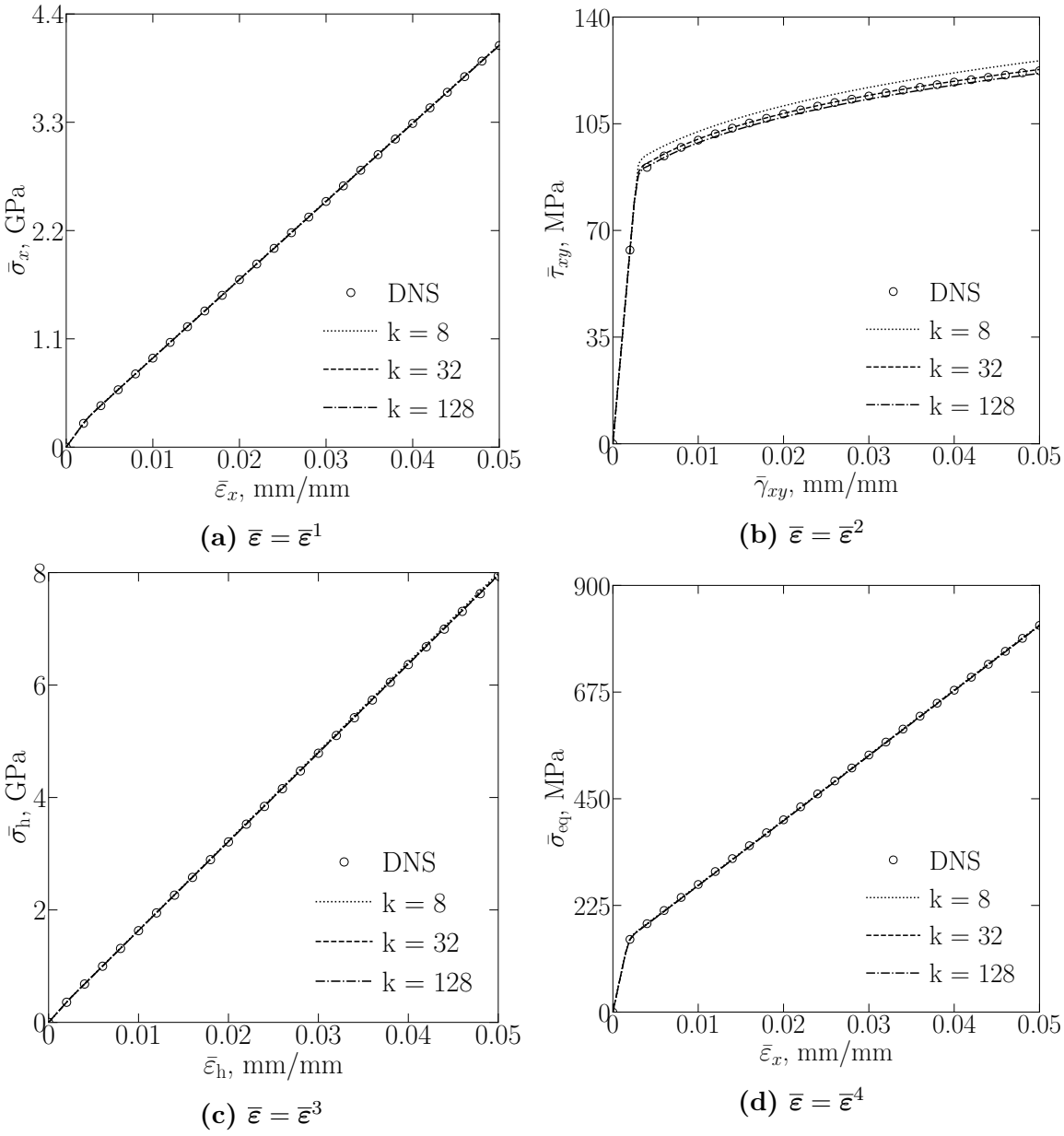

Figure 2.13: Comparisons of the homogenized stress-strain curves for a 2D RVE with 20 % of hard inclusions subjected to different macro-strain constraints

By taking only a glance at **Figure 2.13** it is not difficult to notice an impressive level of accuracy that the SCA is able to achieve with only 8 material clusters. With that discretization, for macro-strain constraints $\overline{\boldsymbol{\varepsilon}}^1$, $\overline{\boldsymbol{\varepsilon}}^3$ and $\overline{\boldsymbol{\varepsilon}}^4$, the difference between homogenized values obtained by the SCA and DNS is almost nonexistent. For macro-strain constraint $\overline{\boldsymbol{\varepsilon}}^2$, which is actually a pure shear type of loading, the maximum relative difference is only 2.7 %. However, it too quickly evaporates when the number of material clusters is increased to 32. Also, it is clear that the increase from 32 to

128 clusters does not lead to any major improvement in accuracy for any type of macro-strain constraint. It is important to emphasize that these results were obtained for an RVE with matrix (material phase 1) and hard inclusions (material phase 2) with a total volume fraction of 20 %. In general, this level of accuracy is not guaranteed, as will be seen from the following diagrams.

Table 2.1: Comparisons of the computational time for a 2D RVE with 20 % of hard inclusions subjected to different macro-strain constraints

$\overline{\boldsymbol{\varepsilon}} = \overline{\boldsymbol{\varepsilon}}^1$				
Method	SCA			DNS
Discretization	$k = 8$	$k = 32$	$k = 128$	100×100
CPU time, s	0.1536	0.4342	10.4709	107
$\overline{\boldsymbol{\varepsilon}} = \overline{\boldsymbol{\varepsilon}}^2$				
Method	SCA			DNS
Discretization	$k = 8$	$k = 32$	$k = 128$	100×100
CPU time, s	0.1713	0.5147	12.7332	131
$\overline{\boldsymbol{\varepsilon}} = \overline{\boldsymbol{\varepsilon}}^3$				
Method	SCA			DNS
Discretization	$k = 8$	$k = 32$	$k = 128$	100×100
CPU time, s	0.1052	0.3657	4.0603	108
$\overline{\boldsymbol{\varepsilon}} = \overline{\boldsymbol{\varepsilon}}^4$				
Method	SCA			DNS
Discretization	$k = 8$	$k = 32$	$k = 128$	100×100
CPU time, s	0.1433	0.4087	7.6238	111

From **Table 2.1** it is clear that for the discretization with 8, i.e. 32 material clusters, the SCA provides tremendous savings in the computational time for all four macro-strain constraints. Notice that an increase from 8 to 32 material clusters (four times) results in about three times longer computational time. This is because the numerical implementation of the SCA was conducted by fully vectorizing Matlab code, which can then achieve a maximum level of efficiency. However, the increase from 32 to 128 material clusters results in a significantly longer computational time, which is especially pronounced for macro-strain constraint $\overline{\boldsymbol{\varepsilon}}^2$. The main reason for this behaviour is the large number of iterations that need to be performed in order to satisfy the equilibrium. Therefore, as stated in **section 2.1**, it is important to find the optimal balance between the computational efficiency and overall accuracy.

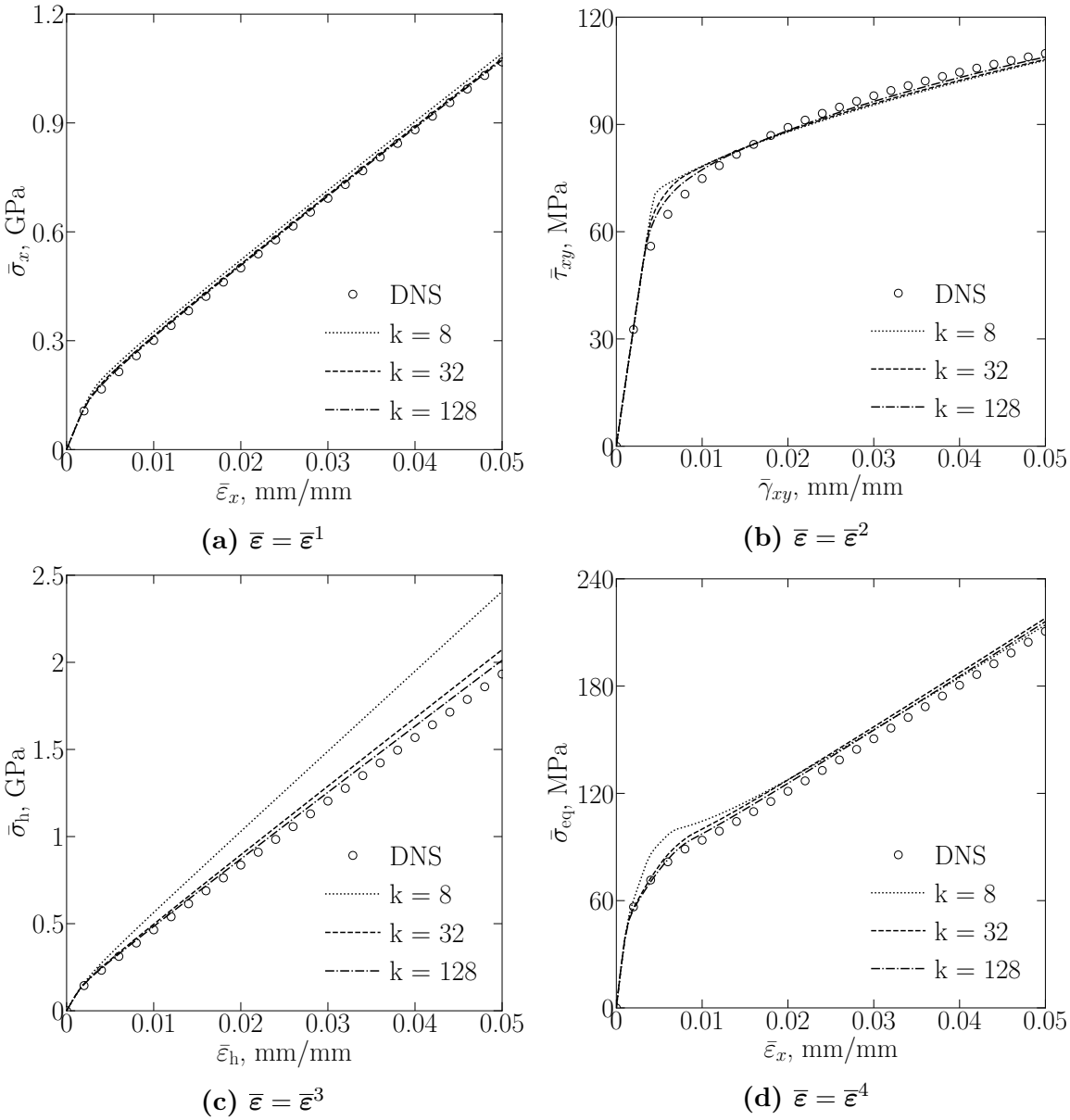

(a) $\overline{\boldsymbol{\varepsilon}} = \overline{\boldsymbol{\varepsilon}}^1$ **(b)** $\overline{\boldsymbol{\varepsilon}} = \overline{\boldsymbol{\varepsilon}}^2$

(c) $\overline{\boldsymbol{\varepsilon}} = \overline{\boldsymbol{\varepsilon}}^3$ **(d)** $\overline{\boldsymbol{\varepsilon}} = \overline{\boldsymbol{\varepsilon}}^4$

Figure 2.14: Comparisons of the homogenized stress-strain curves for a 2D RVE with 20 % of soft inclusions subjected to different macro-strain constraints

In contrast to RVE with 20 % of hard inclusions, the RVE with the same volume fraction of soft inclusions represents a more challenging microstructure for the SCA. Notice that mechanical behaviour for macro-strain constraints $\overline{\boldsymbol{\varepsilon}}^3$ and $\overline{\boldsymbol{\varepsilon}}^4$ cannot be well captured with only 8 material clusters and therefore requires a finer discretization. Also, from **Figure 2.14 (b)** it is clear that the algorithm's ability to capture the homogenized response of the RVE is weaker in the transitional area, i.e. in the moments where material transitions from elastic to elastoplastic type behaviour. Still, with the increase in the number of material clusters the relative error can be reduced; however,

the convergence is non-linear. More precisely, with every four-fold increase in the number of material clusters, the relative error decreases by approximately a factor of 2.

Table 2.2: Comparisons of the computational time for a 2D RVE with 20 % of soft inclusions subjected to different macro-strain constraints

$\overline{\boldsymbol{\varepsilon}} = \overline{\boldsymbol{\varepsilon}}^1$				
Method	SCA			DNS
Discretization	$k = 8$	$k = 32$	$k = 128$	100×100
CPU time, s	0.3478	0.8035	11.5453	120
$\overline{\boldsymbol{\varepsilon}} = \overline{\boldsymbol{\varepsilon}}^2$				
Method	SCA			DNS
Discretization	$k = 8$	$k = 32$	$k = 128$	100×100
CPU time, s	0.1382	0.4628	6.4346	127
$\overline{\boldsymbol{\varepsilon}} = \overline{\boldsymbol{\varepsilon}}^3$				
Method	SCA			DNS
Discretization	$k = 8$	$k = 32$	$k = 128$	100×100
CPU time, s	0.1923	0.4618	5.7213	118
$\overline{\boldsymbol{\varepsilon}} = \overline{\boldsymbol{\varepsilon}}^4$				
Method	SCA			DNS
Discretization	$k = 8$	$k = 32$	$k = 128$	100×100
CPU time, s	0.7784	1.3375	13.6587	116

Table 2.2 shows again that the use of the SCA can lead to significant savings in the computational time in comparison to the DNS. However, in the case of soft inclusions, the time needed to complete the analysis with 100 fixed increments is, for a given number of clusters and macro-strain constraint, significantly higher than in the case of hard inclusions. The primary and only reason for that is the number of iterations the SCA needs to perform in each increment before the equilibrium is achieved. This amount of iterations is higher when soft inclusions are embedded in the elastoplastic matrix since they allow for more flexible behaviour near the boundaries of the matrix and inclusions. This ultimately creates higher levels of strain concentrations and a greater degree of material nonlinearity and overall inhomogenity.

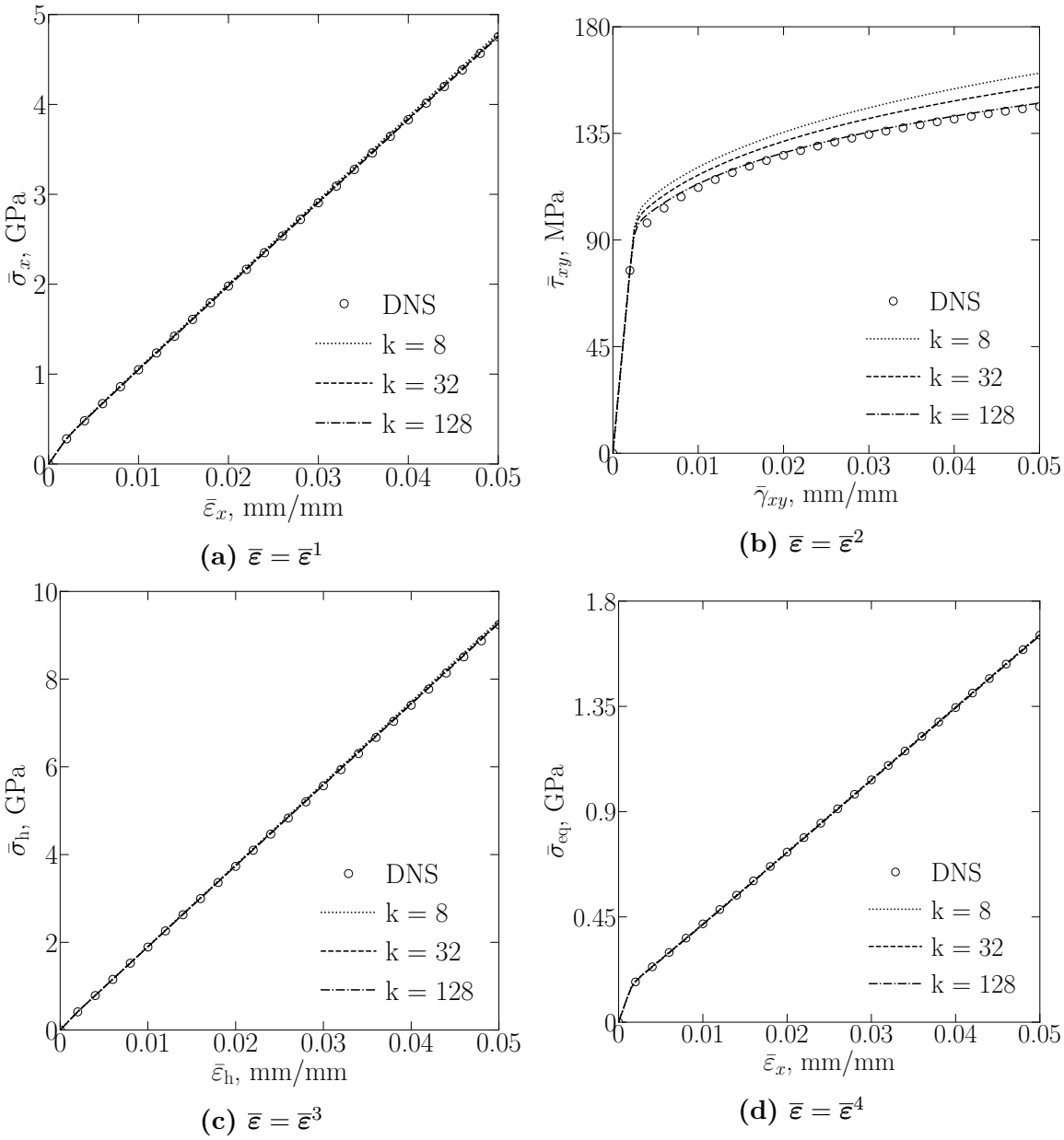

Figure 2.15: Comparisons of the homogenized stress-strain curves for a 2D RVE with 40 % of hard inclusions subjected to different macro-strain constraints

Increasing the volume fraction of the hard inclusions from 20 % to 40 % does not (significantly) affect the ability of the SCA to calculate the macroscopic value of stress for a given macro-strain constraint. Results displayed in **Figure 2.15** show a negligible difference between the two approaches as far as macro-strain constraints $\overline{\boldsymbol{\varepsilon}}^1$, $\overline{\boldsymbol{\varepsilon}}^2$ and $\overline{\boldsymbol{\varepsilon}}^4$ are concerned. For $\overline{\boldsymbol{\varepsilon}}^2$, the maximum relative error at only 8 material clusters is a single-digit number, i.e. 9.58 %, which can be further decreased by applying finer discretization.

Table 2.3: Comparisons of the computational time for a 2D RVE with 40 % of hard inclusions subjected to different macro-strain constraints

$\overline{\boldsymbol{\varepsilon}} = \overline{\boldsymbol{\varepsilon}}^1$				
Method	SCA			DNS
Discretization	$k = 8$	$k = 32$	$k = 128$	100×100
CPU time, s	0.1607	0.4771	8.9301	114
$\overline{\boldsymbol{\varepsilon}} = \overline{\boldsymbol{\varepsilon}}^2$				
Method	SCA			DNS
Discretization	$k = 8$	$k = 32$	$k = 128$	100×100
CPU time, s	0.2264	1.3534	22.5117	133
$\overline{\boldsymbol{\varepsilon}} = \overline{\boldsymbol{\varepsilon}}^3$				
Method	SCA			DNS
Discretization	$k = 8$	$k = 32$	$k = 128$	100×100
CPU time, s	0.1289	0.3586	4.0413	110
$\overline{\boldsymbol{\varepsilon}} = \overline{\boldsymbol{\varepsilon}}^4$				
Method	SCA			DNS
Discretization	$k = 8$	$k = 32$	$k = 128$	100×100
CPU time, s	0.1539	0.3677	7.6749	111

From the data in **Table 2.3** and **Table 2.1**, it is clear that the increase in hard inclusions volume fraction from 20 % to 40 % did not have a major impact on the computational efficiency of the SCA. This is true for all macro-strain constraints with the exception of $\overline{\boldsymbol{\varepsilon}}^2$, i.e. pure shear loading, for which the computational time more than doubled. However, **Figure 2.15 (b)** already hinted at possible issues with that type of macro-strain constraint. Also, notice that the longest computational time for the RVE with 20 % of hard inclusions was also under pure shear loading. The reason lies in the fact that hard inclusions have higher stiffness than the elastoplastic matrix and they therefore significantly affect the overall stiffness of the heterogeneous material. This is particularly pronounced where there exists a hydrostatic component of the stress tensor, which does not contribute to the plastic evolution of the matrix material phase. However, when pure shear, i.e. pure deviatoric loading is applied, the elastoplastic behaviour of the matrix is more significant. This ultimately leads to stronger material nonlinearity for which a higher number of iterations is needed in order to satisfy the equilibrium.

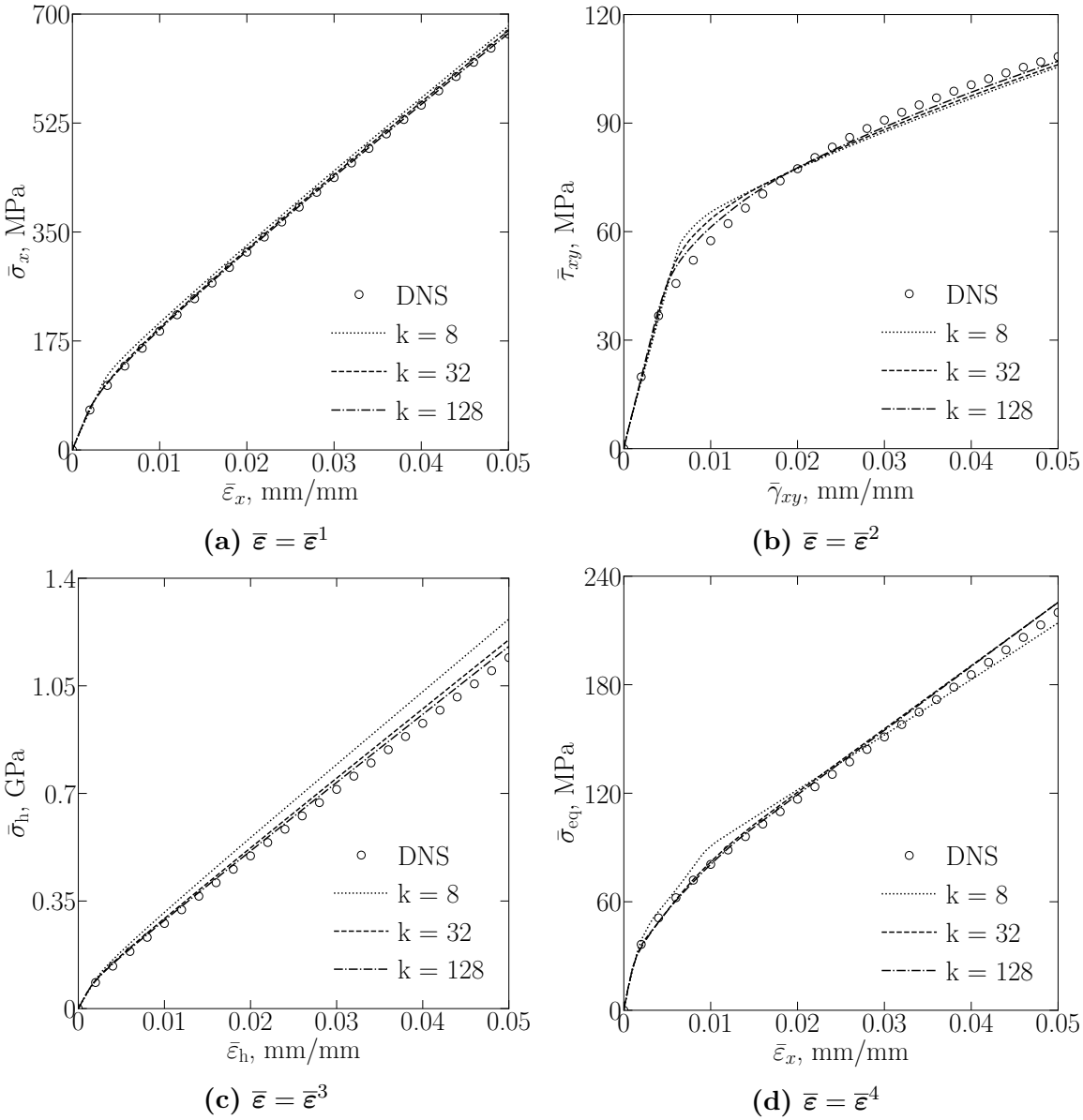

Figure 2.16: Comparisons of the homogenized stress-strain curves for a 2D RVE with 40 % of soft inclusions subjected to different macro-strain constraints

By comparing **Figure 2.14** and **Figure 2.16** it is clear that the ability of the SCA to compute the macroscopic response of heterogeneous material does not significantly change with the increase in soft inclusions volume fraction either. Qualitatively speaking, the algorithm again is not able to accurately predict macroscopic values of stress in the case of macro-strain constraints $\overline{\boldsymbol{\varepsilon}}^3$ and $\overline{\boldsymbol{\varepsilon}}^4$ with only 8 material clusters. Also, deviation from the results obtained by the DNS is again more pronounced in the transitional area, as can be seen from **Figure 2.16 (b)**.

Table 2.4: Comparisons of the computational time for a 2D RVE with 40 % of soft inclusions subjected to different macro-strain constraints

$\overline{\boldsymbol{\varepsilon}} = \overline{\boldsymbol{\varepsilon}}^1$				
Method	SCA			DNS
Discretization	$k = 8$	$k = 32$	$k = 128$	100×100
CPU time, s	0.2566	0.6866	11.2523	138
$\overline{\boldsymbol{\varepsilon}} = \overline{\boldsymbol{\varepsilon}}^2$				
Method	SCA			DNS
Discretization	$k = 8$	$k = 32$	$k = 128$	100×100
CPU time, s	0.1913	0.7474	8.3361	145
$\overline{\boldsymbol{\varepsilon}} = \overline{\boldsymbol{\varepsilon}}^3$				
Method	SCA			DNS
Discretization	$k = 8$	$k = 32$	$k = 128$	100×100
CPU time, s	0.1847	0.5655	6.2783	121
$\overline{\boldsymbol{\varepsilon}} = \overline{\boldsymbol{\varepsilon}}^4$				
Method	SCA			DNS
Discretization	$k = 8$	$k = 32$	$k = 128$	100×100
CPU time, s	0.4431	0.8355	12.6719	125

As was the case when the volume fraction of hard inclusions was raised from 20 % to 40 %, the increase in the volume fraction of soft inclusion does not have a major impact on the overall computational efficiency of the SCA. As evidenced by **Table 2.4**, if the number of material clusters is kept below 32, one can expect a reduction of the computational time by a minimum of 140 times! This degree of acceleration is valid for almost all analyses that were conducted in 2D space with no more than 32 material clusters. Discretization with 32 material clusters also proved to be efficient enough in obtaining a satisfactory level of accuracy, ensuring a single-digit (percentage-wise) relative error throughout the whole analysis.

Before moving on to finite strains, one last comparison in small strain configuration is shown in **Figure 2.17** and **Table 2.5**. More precisely, displayed results represent the influence of the regression based (Update 1), i.e. projection based (Update 2) scheme on the overall accuracy and the computational efficiency of the SCA. The comparison is related to all four RVEs that are discretized with 128 clusters and exclusively for the macro-strain constraint $\overline{\boldsymbol{\varepsilon}}^1$.

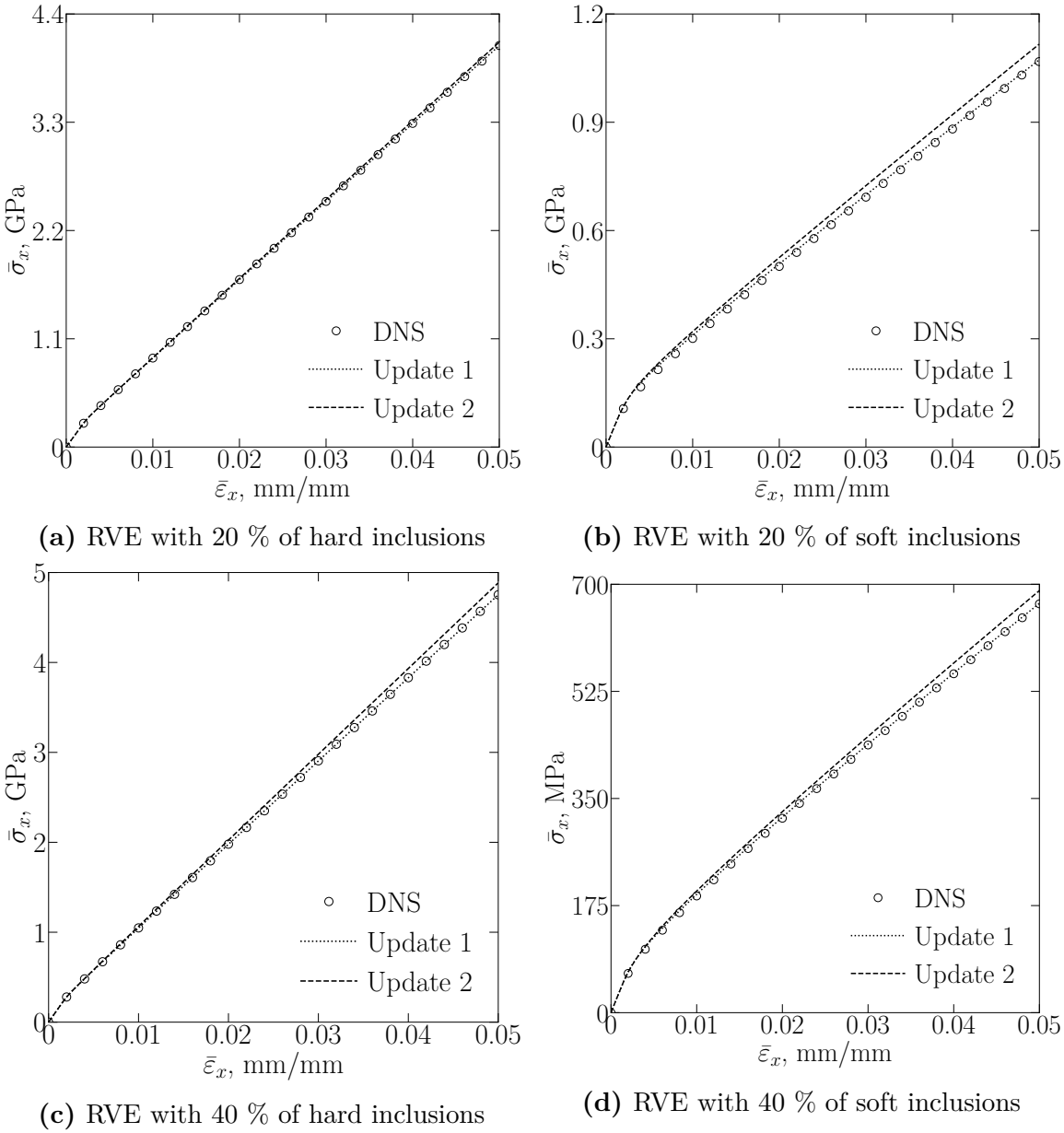

(a) RVE with 20 % of hard inclusions

(b) RVE with 20 % of soft inclusions

(c) RVE with 40 % of hard inclusions

(d) RVE with 40 % of soft inclusions

Figure 2.17: Comparisons of the homogenized stress-strain curves for a regression and projection based types of update for the case of $\overline{\boldsymbol{\varepsilon}} = \overline{\boldsymbol{\varepsilon}}^1$ and with 128 clusters

Table 2.5: Comparisons of the computational time for a regression and projection based types of update for the case of $\overline{\boldsymbol{\varepsilon}} = \overline{\boldsymbol{\varepsilon}}^1$ and with 128 clusters

RVE inclusions share	20 % (hard)	20 % (soft)	40 % (hard)	40 % (soft)
Update 1 (CPU time, s)	10.4709	11.5453	8.9301	11.2523
Update 2 (CPU time, s)	5.3571	7.0121	4.8817	7.9121

From **Figure 2.17** it can be seen that the homogenized results obtained by both regression based (Update 1) and projection based (Update 2) scheme are in good agreement with the results obtained through DNS. However, it is also clear that for all macro-strain constraints, the regression based scheme provides more accurate results, which is especially noticeable when soft inclusions are embedded in the elastoplastic matrix. Although less accurate, the projection based scheme is characterized by a noticeably higher degree of computational efficiency for a discretization with 128 clusters. This is particularly important when large-scale concurrent analyses are in question, as the new Lamé parameters have to be calculated for each macroscopic point in each increment of the analysis.

Figures and tables in previous pages clearly demonstrate the ability of the SCA to efficiently and accurately predict the macroscopic behaviour of various heterogeneous materials for different loading types under small strain assumption. Now, the same detailed analysis should be done for finite strains. After all, in the previous sections, the extension from small to finite strains was presented as a straightforward task. The macro-deformation gradient constraints for the two-dimensional analysis, i.e. the equivalent to the macro-strain constraints in (2.145) are given by

$$\begin{cases} \overline{\mathbf{F}}^1 = \eta \left[\overline{F}_{11} = 1, \quad \overline{F}_{21} = 0, \quad \overline{F}_{12} = 0, \quad \overline{F}_{22} = 0, \quad \overline{F}_{33} = 0 \right]^T \\ \overline{\mathbf{F}}^2 = \eta \left[\overline{F}_{11} = 0, \quad \overline{F}_{21} = 0.5, \quad \overline{F}_{12} = 0.5, \quad \overline{F}_{22} = 0, \quad \overline{F}_{33} = 0 \right]^T \\ \overline{\mathbf{F}}^3 = \eta \left[\overline{F}_{11} = 1, \quad \overline{F}_{21} = 0, \quad \overline{F}_{12} = 0, \quad \overline{F}_{22} = 1, \quad \overline{F}_{33} = 0 \right]^T \\ \overline{\mathbf{F}}^4 = \eta \left[\overline{F}_{11} = 1, \quad \overline{F}_{21} = 0.5, \quad \overline{F}_{12} = 0.5, \quad \overline{F}_{22} = 1, \quad \overline{F}_{33} = 0 \right]^T \end{cases} \tag{2.148}$$

Here, η is again a scalar value that multiplies all elements in a defined vector, and its value is set to 0.15. Recall that the deformation gradient in the SCA is defined simply as a gradient of a displacement, i.e. second-order identity tensor is removed. Since the deformation gradient is, generally, non-symmetric, Voigt notation cannot be utilized. Also, in order to ensure pure shear loading, both $\overline{F}_{12}$ and $\overline{F}_{21}$ are set at exactly half of the desired total value of the macroscopic deformation. Since the two-dimensional analysis is performed under plane strain assumption, the value of $\overline{F}_{33}$ is in all constraints set to zero.

However, although the extension is a straightforward task, the developed algorithm behaves unexpectedly. Mainly, if the macro-deformation gradient constraint $\overline{\mathbf{F}}^1$ is enforced, analyses with all four RVEs behave in the same manner - they break before the total load is applied, which can be seen in **Figure 2.18**.

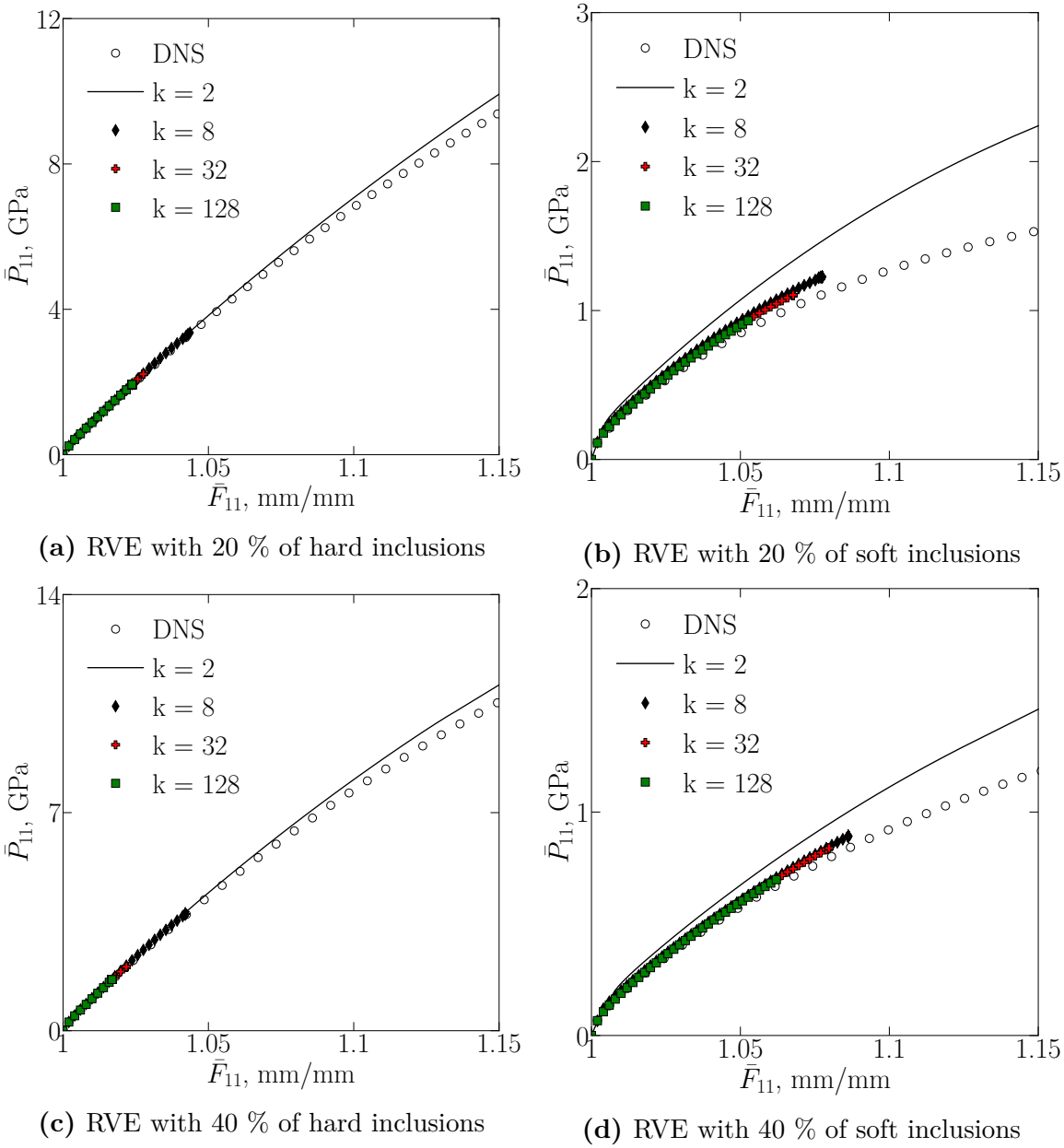

(a) RVE with 20 % of hard inclusions

(b) RVE with 20 % of soft inclusions

(c) RVE with 40 % of hard inclusions

(d) RVE with 40 % of soft inclusions

Figure 2.18: Comparisons of the homogenized curves under finite strain configuration and for the case of $\overline{\mathbf{F}} = \overline{\mathbf{F}}^1$

If the regression based scheme is utilized, the phenomenon mentioned above occurs for any type of macro-deformation gradient constraint and for any type of the RVE. One of the ways the author has been able to mitigate this issue was to use one material cluster for each material phase. However, the discretization with only two material clusters is sufficient only for simple microstructures that are subjected to specific loading types. Generally, it will produce inaccurate results, like the ones depicted in **Figure 2.18 (b)** and **(d)**.

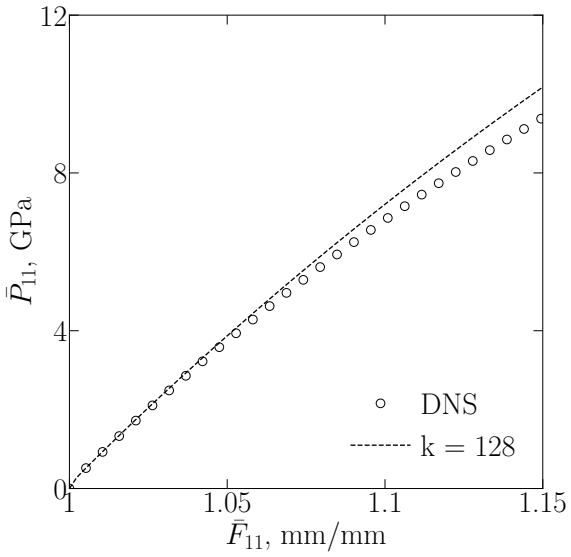

(a) RVE with 20 % of hard inclusions

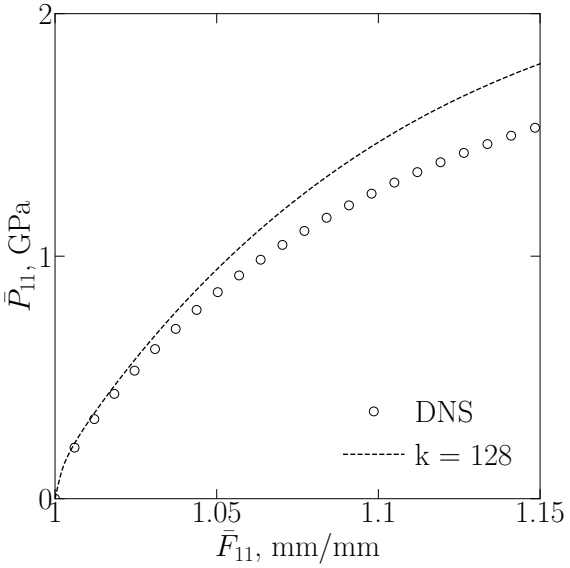

(b) RVE with 20 % of soft inclusions

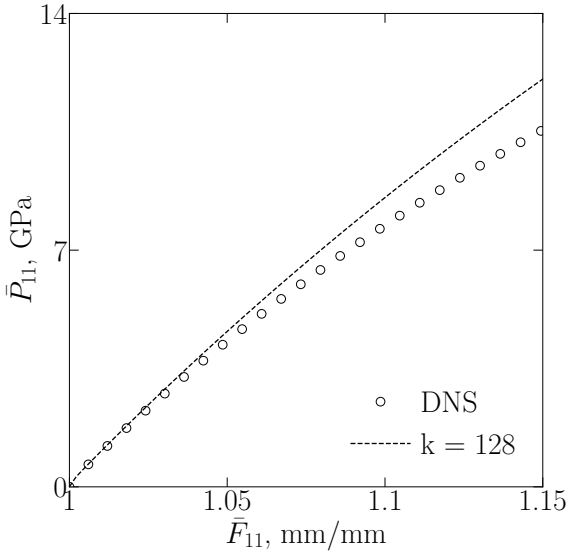

(c) RVE with 40 % of hard inclusions

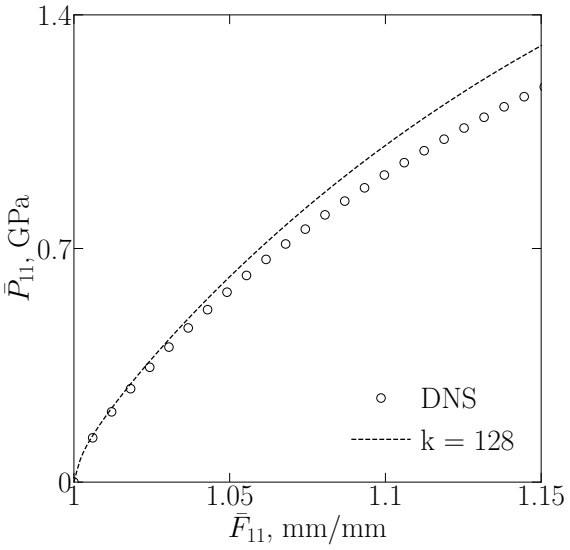

(d) RVE with 40 % of soft inclusions

Figure 2.19: Comparisons of the homogenized curves for a projection based type of update for the case of $\overline{\mathbf{F}} = \overline{\mathbf{F}}^1$ and with 128 clusters

The second way in which the author was able to conduct the full analysis was to utilize projection based scheme. Although more stable than the regression based scheme, the projection based scheme does not give satisfactory results even with 128 material clusters - **Figure 2.19**. This is because, unlike regression based scheme, the new Lamé parameters in the projection based scheme are obtained through homogenized material stiffness tensor $\overline{\mathbb{C}}$, which in the case of finite strains cannot be well captured using cluster decomposition.

The author of this thesis is unable to provide a physical or mathematical interpretation of the phenomenon that occurs when a regression based scheme is utilized. Why exactly the numerical algorithm is able to perform the whole analysis only if two material clusters are used is an open question. It is worth noting that in [85], i.e. [67] the maximum value of macroscopic logarithmic strain was set to 2.5 %, i.e. 5 %. This also points to potential problems with the SCA algorithm in finite strains configuration, since both 2.5 % and 5 % cannot be considered large deformations. This part of the SCA clearly requires further numerical and mathematical investigation and therefore won't be the subject of further discussion.

2.6.2. Three-dimensional elastoplastic material

With the two-dimensional numerical validation being successfully carried out, it is time to validate the SCA in 3D space. For that purpose, as was the case in the previous subsection, two RVEs with different spherical inclusions volume fraction were generated. Along with the microstructure itself, **Figure 2.20** shows both matrix and spherical inclusions, since the 3D isometric view of the microstructure does not provide an overview of its interior. Both microstructures are identical in terms of:

- size - both with a length of 0.2 mm,
- material composition - both consisting of matrix and spherical inclusions with fixed radius of 0.02 mm
- material configuration - both possessing one elastoplastic material phase (matrix) and one linear elastic material phase (spherical inclusions).

Two characteristics that set them apart are

- volume fraction - one with 10 % and the other with 20 % of spherical inclusions share,
- minimum neighbour distance - one with 16 μm and the other with 8 μm of the minimum neighbour distance.

Again, each RVE has two different material configurations: (1) elastoplastic matrix and hard spherical inclusions, and (2) elastoplastic matrix and soft spherical inclusions, which makes a total of four different microstructures. As was the case for two-dimensional RVEs, both RVEs possess periodicity in their geometry; however, in 3D isogeometric view that is not as obvious as in the case of two dimensions.

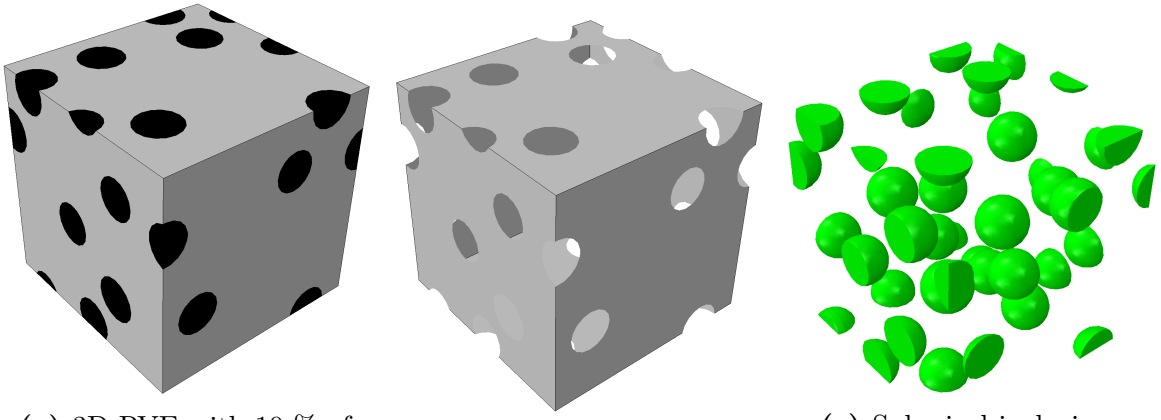

(a) 3D RVE with 10 % of spherical inclusions

(b) Matrix

(c) Spherical inclusions

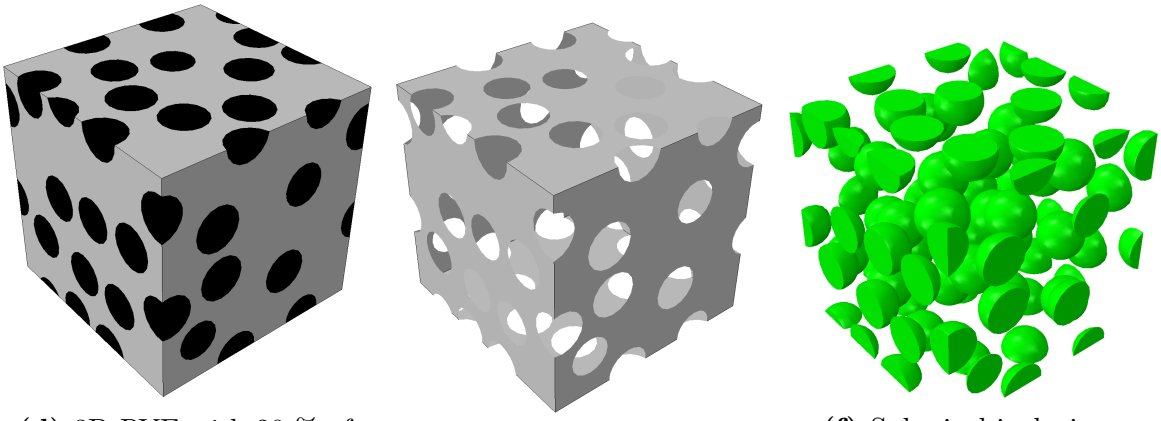

(d) 3D RVE with 20 % of spherical inclusions

(e) Matrix

(f) Spherical inclusions

Figure 2.20: Geometry of the 3D RVEs

In order to conduct the SCA, all four RVEs need to be decomposed into k number of material clusters. In contrast to two-dimensional analysis, where discretization with 8, 32, i.e. 128 clusters was carried out, in three-dimensional analysis RVEs are decomposed in 6, 24 and 96 material clusters. This reduction in the number of material clusters is done solely for the purpose of computational efficiency. Since the k-means clustering and the calculation of the interaction tensor in three dimensions represent a significantly more demanding task than in two. Still, the chosen discretizations will be sufficient for getting a clear picture of the SCA's capabilities in a three-dimensional configuration.

In the previous subsection, finite element mesh that was present in the calculation of strain concentration tensor consisted of 1000 $\times$ 1000 pixels, i.e. 1000 finite elements per edge. Unfortunately, in the case of three-dimensional RVEs, the number of voxels per edge cannot be nearly that high. Discretization with 1000 $\times$ 1000 $\times$

1000 voxels would produce a finite element mesh of one billion hexahedral elements. Running DNS with that discretization would require hundreds of gigabytes of RAM alongside dozens of CPUs. Due to that limitation, the finite element mesh needed for the calculation of the strain concentration tensor was kept at 10^6 hexahedral elements with one integration point in their center. 100 voxels per edge cannot be considered a fine discretization, as can be seen from **Figure 2.21**. However, running a single finite element simulation with 10^6 hexahedral elements already requires almost 100 gigabytes of RAM. In the future, other procedures that include running an iterative solver (instead of direct) on the sparse linear system and utilization of an FFT-based solver can be adopted to further improve the discretization of 3D RVEs. In contrast to direct solvers such as LU decomposition or Cholesky factorization, iterative solvers do not perform decomposition of the sparse linear system but execute a series of iterations to find the approximate solution. In that way RAM required to run the analysis is significantly lower. Fast Fourier transform on the other hand can also be utilized, as it requires memory for storing only data in each pixel/voxel. For example, a 3D RVE discretized with 100 × 100 × 100 voxels would require only 8 megabytes of RAM.

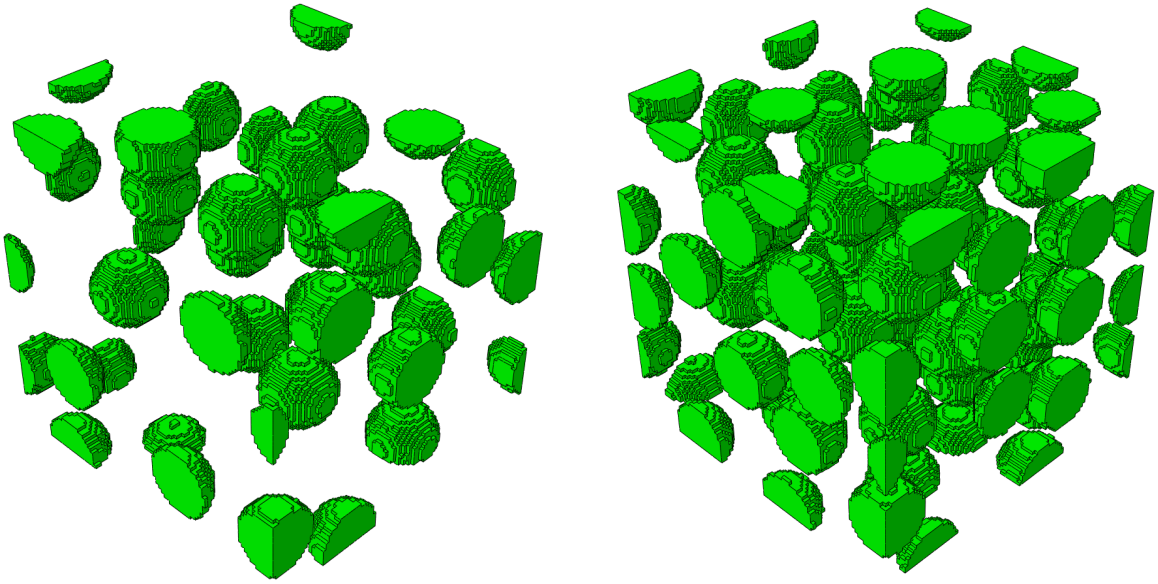

(a) 10 % inclusions **(b)** 20 % inclusions

Figure 2.21: Discretization of spherical inclusions for the case of 100 voxels per RVE edge

The results of the k-means clustering for all four RVEs are depicted in **Figures 2.22**, **2.23**, **2.24** and **2.25**.

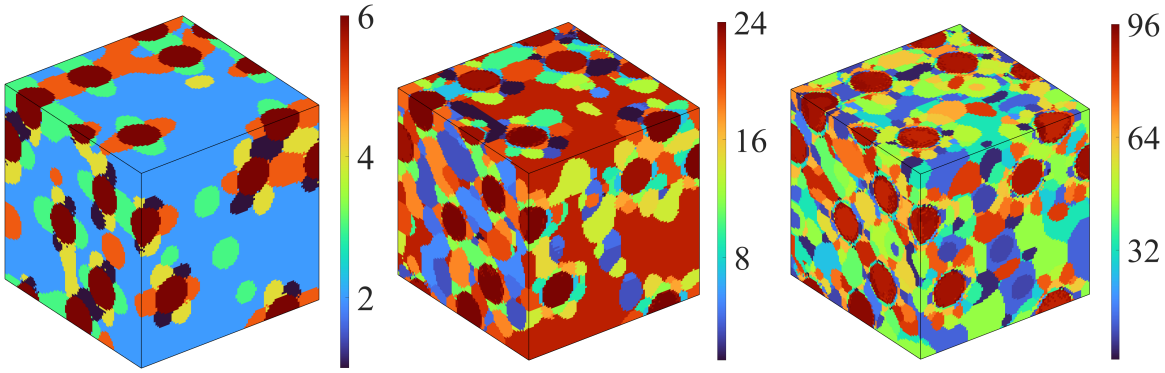

(a) k = 6 **(b)** k = 24 **(c)** k = 96

Figure 2.22: Results of the k-means clustering for a 3D RVE with 10 % of hard inclusions

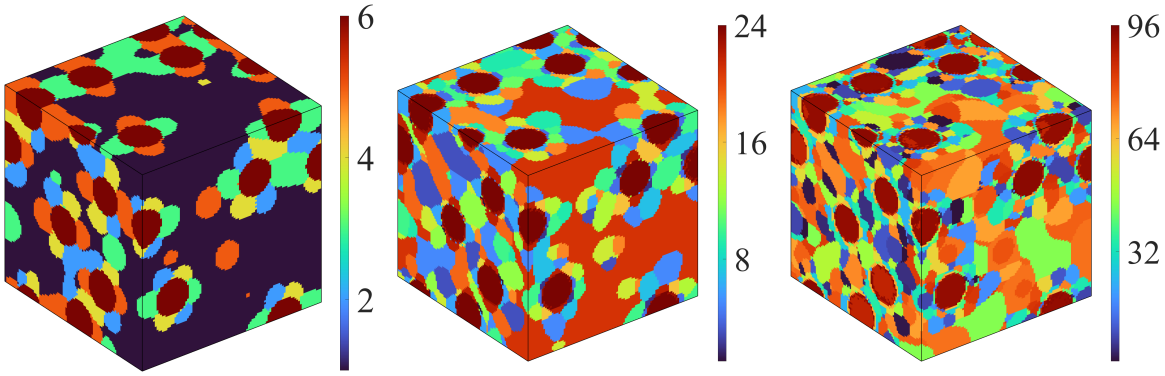

(a) $k = 6$ **(b)** $k = 24$ **(c)** $k = 96$

Figure 2.23: Results of the k-means clustering for a 3D RVE with 10 % of soft inclusions

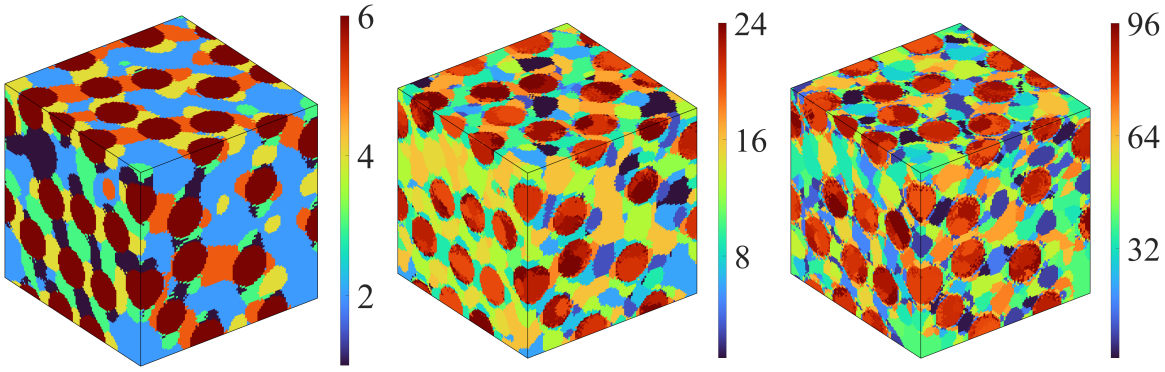

(a) $k = 6$ **(b)** $k = 24$ **(c)** $k = 96$

Figure 2.24: Results of the k-means clustering for a 3D RVE with 20 % of hard inclusions

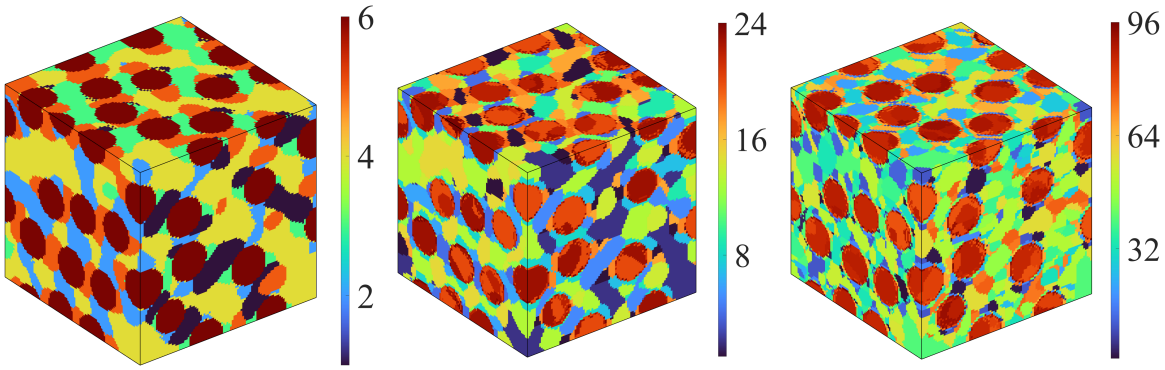

(a) $k = 6$ **(b)** $k = 24$ **(c)** $k = 96$

Figure 2.25: Results of the k-means clustering for a 3D RVE with 20 % of soft inclusions

Behaviour that was characteristic of 2D RVEs is again present in 3D RVEs. From **Figure 2.22** and **Figure 2.23**, i.e. **Figure 2.24** and **Figure 2.25** it is clear that identical geometrical but different material configuration produces completely distinctive cluster decomposition. Also, as was the case in two-dimensional analysis, one material cluster can occupy different positions inside the RVE. This is again because different material points inside the RVE can have similar mechanical behaviour. After the domain decomposition into the appropriate number of clusters, the calculation of the interaction tensor is performed using (2.101). Of course, this part is also performed using Matlab.

FEM analyses that need to be performed for four distinctive macro-strain constraints definitely do not require 10^6 hexahedral finite elements and can be carried out by using significantly sparser mesh. The procedure of defining appropriate mesh for running FEM analyses again boils down to conducting simulations of pure shear loading, i.e. using macro-strain constraint $\overline{\boldsymbol{\varepsilon}}^2$ with two different discretizations. The homogenized stress-strain relations for discretizations with $50 \times 50 \times 50$, i.e. $60 \times 60 \times 60$ voxels are depicted in **Figure 2.26**.

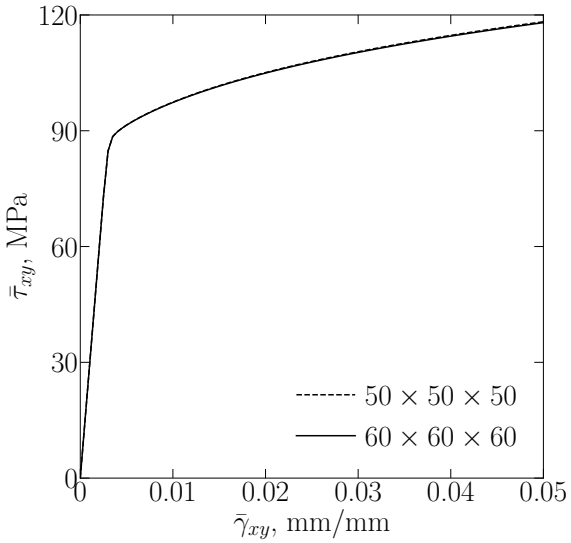

(a) 3D RVE with 10 % of hard inclusions

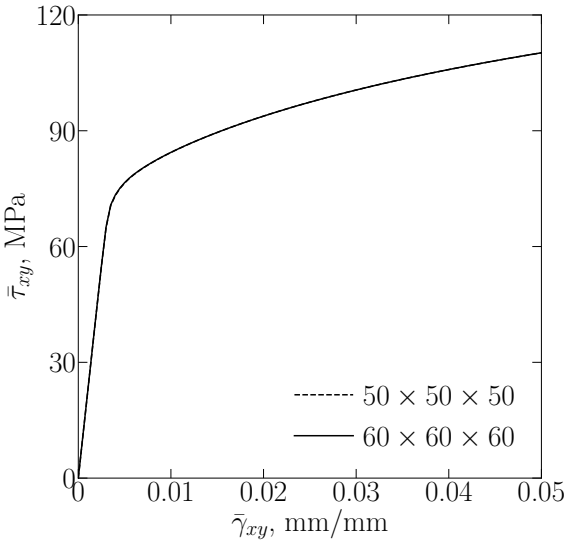

(b) 3D RVE with 10 % of soft inclusions

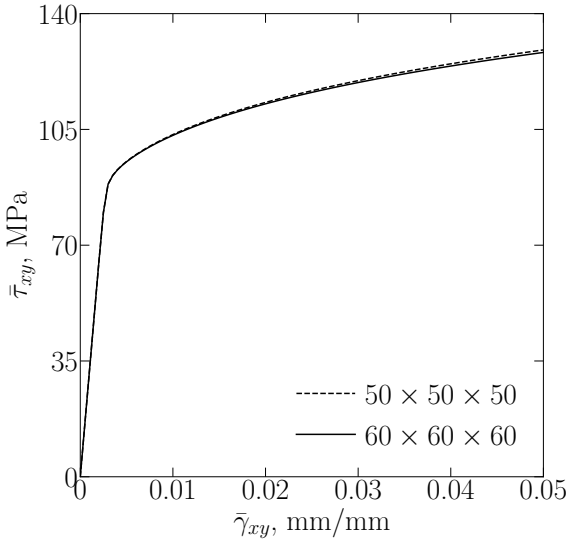

(c) 3D RVE with 20 % of hard inclusions

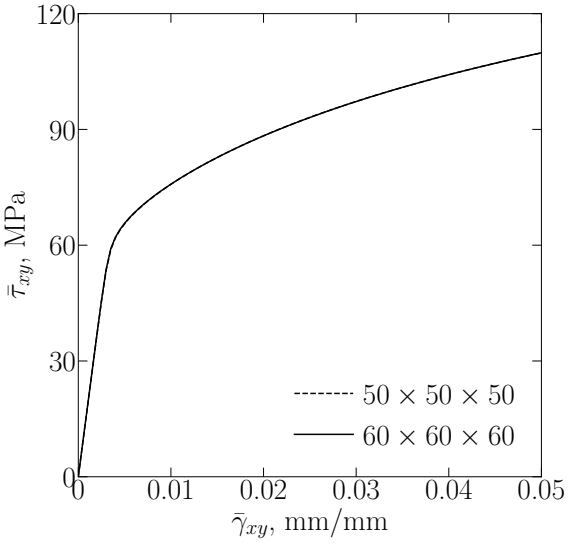

(d) 3D RVE with 20 % of soft inclusions

Figure 2.26: Influence of the finite element mesh discretization on the homogenized values for the case $\overline{\boldsymbol{\varepsilon}} = \overline{\boldsymbol{\varepsilon}}^2$

From **Figure 2.26** it is clear that the difference between coarser and finer discretization for all RVEs is almost non-existent. Therefore, for running all DNS simulations for all macro-strain constraints and for all RVEs, the discretization with 125,000 hexahedral elements is utilized.

In the next four figures and four tables comparisons of the macroscopic stress-strain relations and computational efficiency for both SCA and DNS are presented.

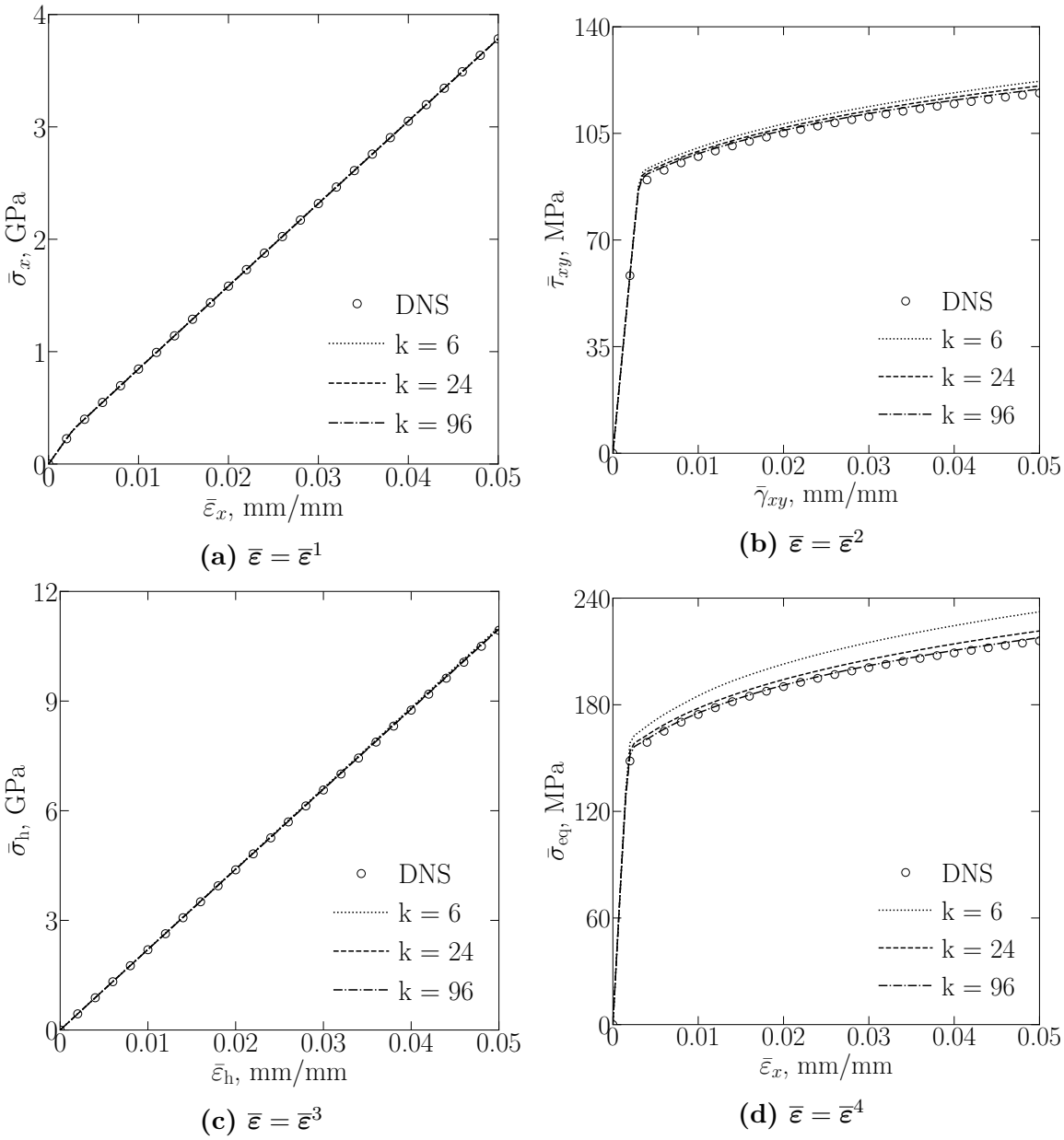

Figure 2.27: Comparisons of the homogenized stress-strain curves for a 3D RVE with 10 % of hard inclusions subjected to different macro-strain constraints

Figure 2.27 shows good agreement of homogenized results obtained by the SCA and ones obtained by DNS through FEM. For the case of macro-strain constraints $\overline{\boldsymbol{\varepsilon}}^1$ and $\overline{\boldsymbol{\varepsilon}}^3$ the difference barely exists, while for other constraints similar accuracy can be achieved with 96 material clusters. However, even with only 6 material clusters, the maximum relative error, which appears for macro-strain constraint $\overline{\boldsymbol{\varepsilon}}^4$, amounts to "only" 7.4 %.

Table 2.6: Comparisons of the computational time for a 3D RVE with 10 % of hard inclusions subjected to different macro-strain constraints

$\overline{\boldsymbol{\varepsilon}} = \overline{\boldsymbol{\varepsilon}}^1$				
Method	SCA			DNS
Discretization	$k = 6$	$k = 24$	$k = 96$	$50 \times 50 \times 50$
CPU time, s	0.1753	0.6798	10.7506	56808
$\overline{\boldsymbol{\varepsilon}} = \overline{\boldsymbol{\varepsilon}}^2$				
Method	SCA			DNS
Discretization	$k = 6$	$k = 24$	$k = 96$	$50 \times 50 \times 50$
CPU time, s	0.1982	0.5655	11.8646	68022
$\overline{\boldsymbol{\varepsilon}} = \overline{\boldsymbol{\varepsilon}}^3$				
Method	SCA			DNS
Discretization	$k = 6$	$k = 24$	$k = 96$	$50 \times 50 \times 50$
CPU time, s	0.1173	0.4139	5.4219	54960
$\overline{\boldsymbol{\varepsilon}} = \overline{\boldsymbol{\varepsilon}}^4$				
Method	SCA			DNS
Discretization	$k = 6$	$k = 24$	$k = 96$	$50 \times 50 \times 50$
CPU time, s	0.1452	0.8366	12.6445	55182

In contrast to two-dimensional analysis, where the increase in computational efficiency was measured in hundreds, **Table 2.6** shows that SCA can offer significantly higher savings in computational time if three-dimensional simulations are considered. Even with 96 material clusters the time needed to complete the analysis is on average 5800 times shorter in the case of SCA than it is for DNS. Recall that all three-dimensional Abaqus analyses were carried out using 4 threads of the AMD Ryzen 3900x processor, while the SCA was conducted on a single thread of the Intel Xeon E5-1620 v2 processor. If the SCAs were to be carried out with multiple threads the difference in computational times would be even greater. Also, notice that the increase from 24 to 96 material clusters leads to significantly longer computational time, which is true for all four macro-strain constraints. This was also present in two-dimensional analysis and the main reason is, again, a significantly higher number of iterations that the algorithm needs to perform in order to satisfy the equilibrium.

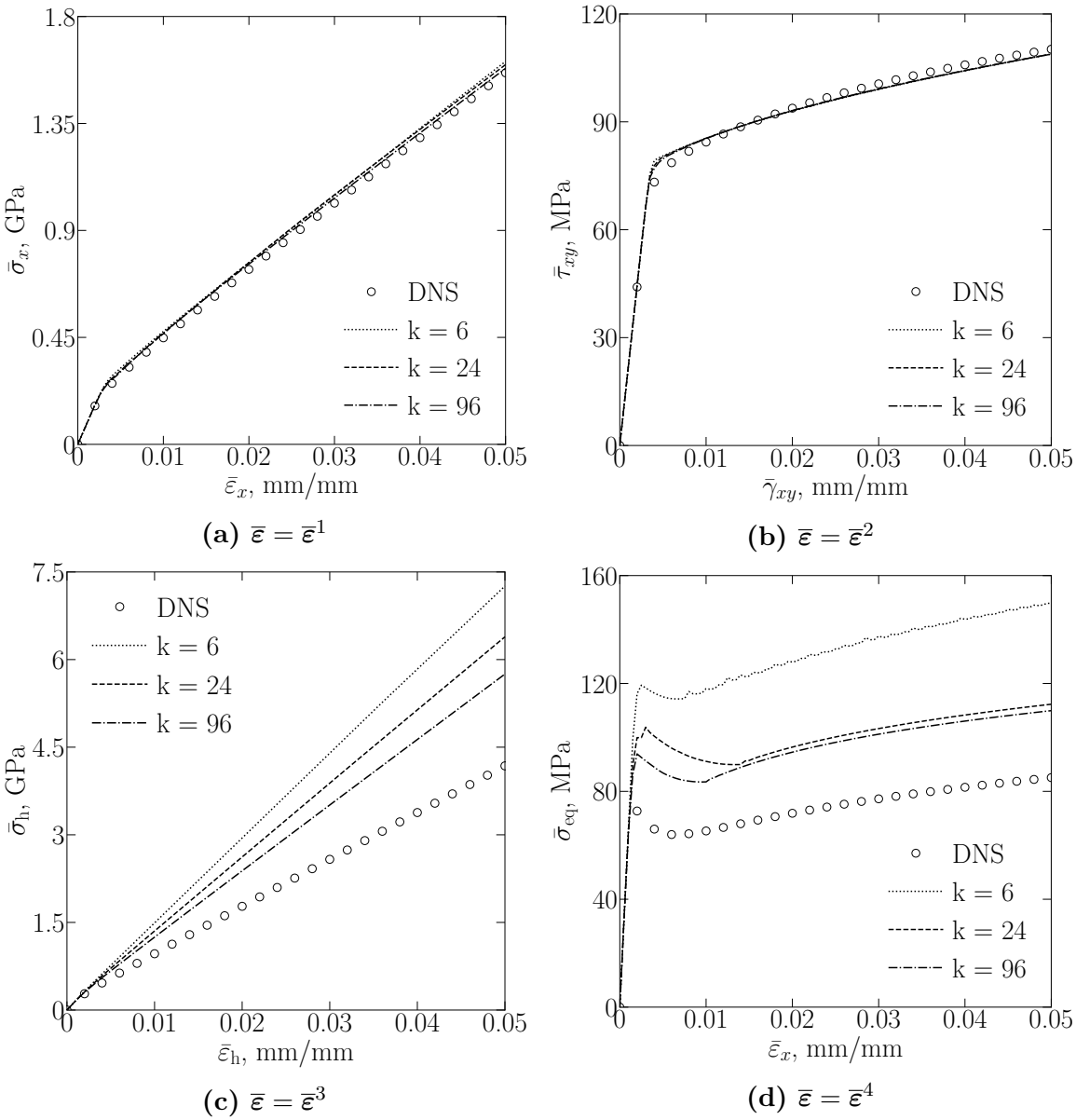

Figure 2.28: Comparisons of the homogenized stress-strain curves for a 3D RVE with 10 % of soft inclusions subjected to different macro-strain constraints

Changing the material configuration, i.e. switching from hard to soft inclusions has as a consequence lower level of agreement between the SCA and DNS. In **Figure 2.28** it is clear that for macro-strain constraints $\overline{\boldsymbol{\varepsilon}}^3$ and $\overline{\boldsymbol{\varepsilon}}^4$, the SCA is not able to properly capture the macroscopic response of the RVE with 10 % of soft inclusions. The difference is more than significant, even with 96 material clusters. Recall that the macro-strain constraint $\overline{\boldsymbol{\varepsilon}}^3$ is actually a pure hydrostatic loading, for which the optimal value shear modulus μ^0 is undetermined for both regression and projection based scheme. Although constrain $\overline{\boldsymbol{\varepsilon}}^4$ is not pure hydrostatic loading, it does possess

the hydrostatic component which has a negative impact on the self-consistent scheme. In contrast to $\overline{\boldsymbol{\varepsilon}}^3$ and $\overline{\boldsymbol{\varepsilon}}^4$, macro-strain constraints $\overline{\boldsymbol{\varepsilon}}^1$ and $\overline{\boldsymbol{\varepsilon}}^2$ can be captured well with the use of the SCA, and the increase in clusters does not lead to major changes in homogenized results. The overall accuracy could certainly be improved by applying finer discretization during DNS data collection. That "simple" change would have a positive impact for two reasons: (1) higher quality in the description of the inhomogeneous strain field inside the RVE, and (2) higher level of accuracy during the process of interaction tensor calculation.

Table 2.7: Comparisons of the computational time for a 3D RVE with 10 % of soft inclusions subjected to different macro-strain constraints

$\overline{\boldsymbol{\varepsilon}} = \overline{\boldsymbol{\varepsilon}}^1$				
Method	SCA			DNS
Discretization	$k = 6$	$k = 24$	$k = 96$	$50 \times 50 \times 50$
CPU time, s	0.3233	1.5342	23.7773	61558
$\overline{\boldsymbol{\varepsilon}} = \overline{\boldsymbol{\varepsilon}}^2$				
Method	SCA			DNS
Discretization	$k = 6$	$k = 24$	$k = 96$	$50 \times 50 \times 50$
CPU time, s	0.1309	0.4564	7.0555	77875
$\overline{\boldsymbol{\varepsilon}} = \overline{\boldsymbol{\varepsilon}}^3$				
Method	SCA			DNS
Discretization	$k = 6$	$k = 24$	$k = 96$	$50 \times 50 \times 50$
CPU time, s	0.1755	0.5677	8.6768	63094
$\overline{\boldsymbol{\varepsilon}} = \overline{\boldsymbol{\varepsilon}}^4$				
Method	SCA			DNS
Discretization	$k = 6$	$k = 24$	$k = 96$	$50 \times 50 \times 50$
CPU time, s	0.5729	2.2853	33.5189	56797

The change in the material configuration at the microscale definitely had an impact on the computational efficiency of the SCA. From **Table 2.7** and **Table 2.6** it is clear that for macro-strain constraints $\overline{\boldsymbol{\varepsilon}}^1$ and $\overline{\boldsymbol{\varepsilon}}^4$ the time needed to complete the analysis more than doubled. The increase in computational time is also present in the other two constraints; however, at noticeably lower levels. Despite this, SCA is still providing an immense reduction in the overall CPU time which is especially pronounced in the case of pure shear conditions, i.e. macro-strain constraint $\overline{\boldsymbol{\varepsilon}}^2$.

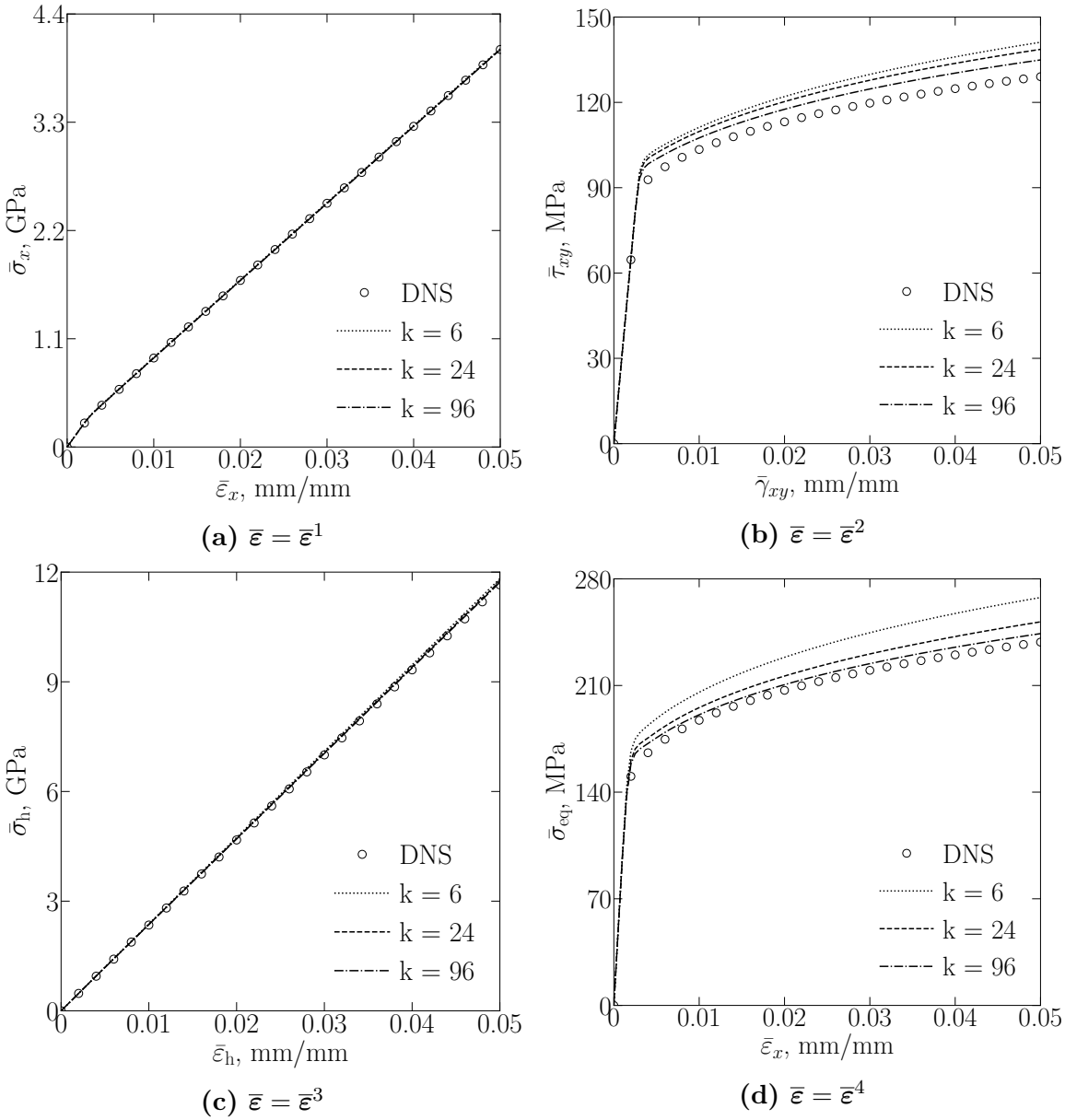

Figure 2.29: Comparisons of the homogenized stress-strain curves for a 3D RVE with 20 % of hard inclusions subjected to different macro-strain constraints

As far as macro-strain constraints $\overline{\boldsymbol{\varepsilon}}^1$ and $\overline{\boldsymbol{\varepsilon}}^3$ are concerned, an increase in the volume fraction of hard inclusions has almost no influence on the accuracy of the SCA. **Figure 2.29** also shows that for the other two constraints, the deviation from DNS results are slightly larger than in the case of 3D RVE with 10 % of spherical inclusions share - **Figure 2.27**. Although not as precise as it was for the mentioned RVE, the SCA with 96 material clusters is still able to provide good results for which the maximum relative error is less than 5 %.

Table 2.8: Comparisons of the computational time for a 3D RVE with 20 % of hard inclusions subjected to different macro-strain constraints

$\overline{\boldsymbol{\varepsilon}} = \overline{\boldsymbol{\varepsilon}}^1$				
Method	SCA			DNS
Discretization	$k = 6$	$k = 24$	$k = 96$	$50 \times 50 \times 50$
CPU time, s	0.1685	0.5265	7.9663	57289
$\overline{\boldsymbol{\varepsilon}} = \overline{\boldsymbol{\varepsilon}}^2$				
Method	SCA			DNS
Discretization	$k = 6$	$k = 24$	$k = 96$	$50 \times 50 \times 50$
CPU time, s	0.1755	0.7018	12.1756	69063
$\overline{\boldsymbol{\varepsilon}} = \overline{\boldsymbol{\varepsilon}}^3$				
Method	SCA			DNS
Discretization	$k = 6$	$k = 24$	$k = 96$	$50 \times 50 \times 50$
CPU time, s	0.1284	0.3759	5.3041	56772
$\overline{\boldsymbol{\varepsilon}} = \overline{\boldsymbol{\varepsilon}}^4$				
Method	SCA			DNS
Discretization	$k = 6$	$k = 24$	$k = 96$	$50 \times 50 \times 50$
CPU time, s	0.1883	0.5761	11.6052	56747

From both **Table 2.8** and **Table 2.6** it is clear that computational times of the SCA for all discretizations and macro-strain constraints did not experience any major changes. The difference in CPU times for both SCA and DNS is still tremendous even with the maximum number of clusters. As was the case for all two-dimensional analyses, a four-fold increase in the total number of material clusters (from 24 to 96) will extend the computational time by more than 10 times. Proving once again that it is necessary to perform multiple analyses in order to find an appropriate balance between computational efficiency and overall accuracy.

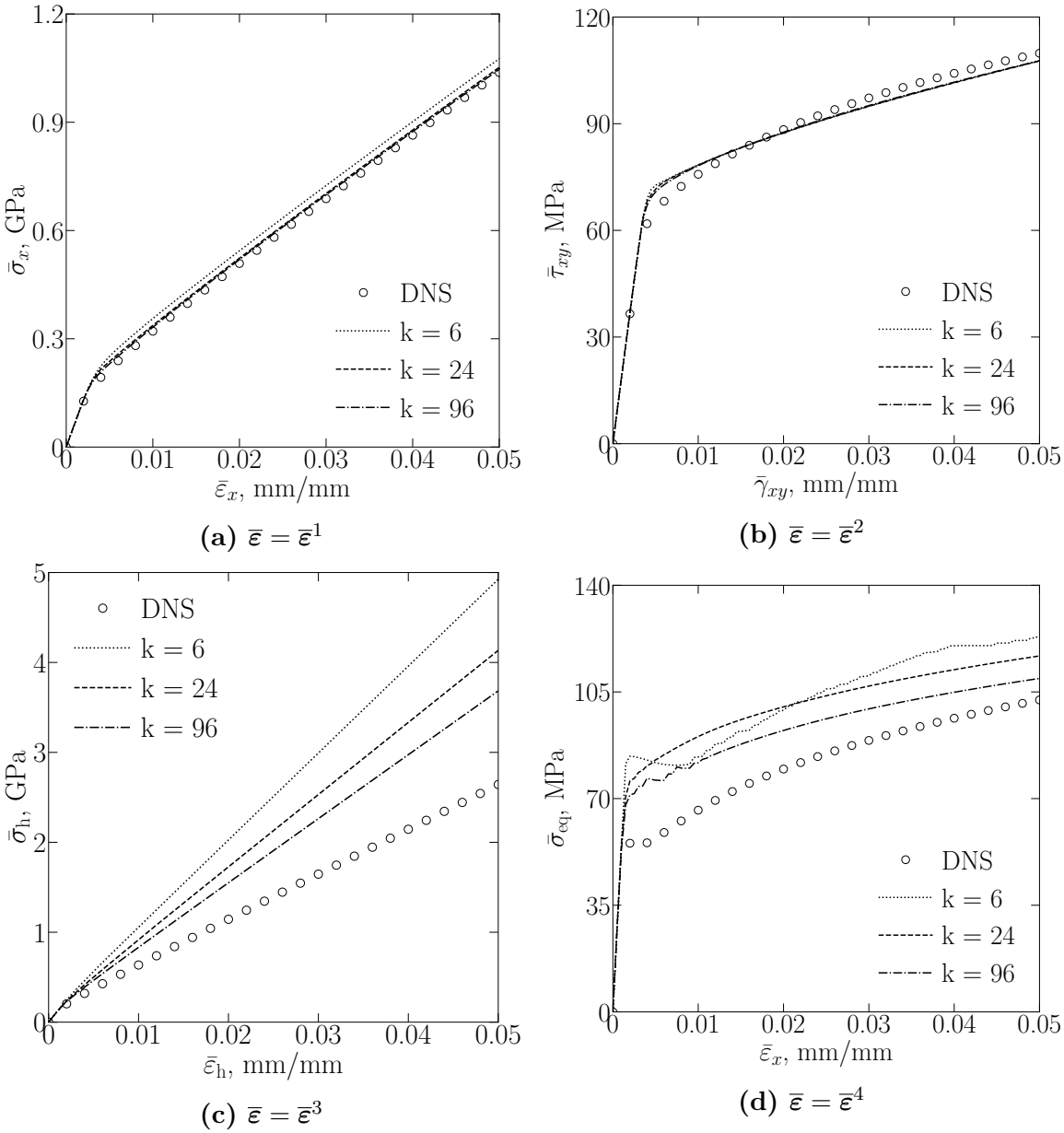

Figure 2.30: Comparisons of the homogenized stress-strain curves for a 3D RVE with 20 % of soft inclusions subjected to different macro-strain constraints

The last comparison in this chapter is related to the 3D RVE in which the total volume fraction of soft inclusions is 20 %. As can be seen from **Figure 2.30**, good agreements between the SCA and DNS results cannot be obtained for all constraints. Pure hydrostatic loading and the macro-strain constraint $\overline{\boldsymbol{\varepsilon}}^4$ are again poorly approximated by the SCA. This behaviour was also present in the RVE with 10 % of soft inclusions. Notice also that discretization with 6 material clusters produces a non-physical stress-strain relation for macro-strain constraint $\overline{\boldsymbol{\varepsilon}}$. Although at a

much lower intensity, **Figure 2.28 (d)** shows a similar phenomenon when identical discretization and constraints are utilized. The "vibrating" stress-strain relation occurs when the optimal value of one of two Lamé parameters of the reference material becomes negative. In that case, the calculated negative value is replaced by the value obtained in the previous increment.

Table 2.9: Comparisons of the computational time for a 3D RVE with 20 % of soft inclusions subjected to different macro-strain constraints

$\overline{\boldsymbol{\varepsilon}} = \overline{\boldsymbol{\varepsilon}}^1$				
Method	SCA			DNS
Discretization	$k = 6$	$k = 24$	$k = 96$	$50 \times 50 \times 50$
CPU time, s	0.3416	1.1517	16.1357	54160
$\overline{\boldsymbol{\varepsilon}} = \overline{\boldsymbol{\varepsilon}}^2$				
Method	SCA			DNS
Discretization	$k = 6$	$k = 24$	$k = 96$	$50 \times 50 \times 50$
CPU time, s	0.1382	0.4579	7.3445	79857
$\overline{\boldsymbol{\varepsilon}} = \overline{\boldsymbol{\varepsilon}}^3$				
Method	SCA			DNS
Discretization	$k = 6$	$k = 24$	$k = 96$	$50 \times 50 \times 50$
CPU time, s	0.1741	0.5505	8.1476	51418
$\overline{\boldsymbol{\varepsilon}} = \overline{\boldsymbol{\varepsilon}}^4$				
Method	SCA			DNS
Discretization	$k = 6$	$k = 24$	$k = 96$	$50 \times 50 \times 50$
CPU time, s	0.5261	2.1736	32.4882	52105

The last table in this chapter does not show any unexpected results. The increase in computational efficiency, which happens when the SCA is utilized, is again tremendous. This is especially pronounced for pure shear conditions. Related to that macro-strain constraint, from **Table 2.9** it is not difficult to conclude that by far the longest CPU time for the case of DNS appears exactly when pure shear macro-strain constraint is applied. However, this is not typical only for 3D RVE with 20 % of soft inclusions, but for each and every RVE that was the subject of numerical validation.

3. Phase-field fracture formulation

3.1. Background

Although there exists a significant number of non-local continuum damage models, as presented in **subsection 1.3.2**, the phase-field modelling approach is certainly one of the most popular ones. Interestingly, the phase-field fracture framework has been independently developed by the physics and mechanics community with considerably different approaches and starting points. The physics community developed dynamic fracture models [230, 231] using the Ginzburg-Landau theory [232], which was originally derived for electromagnetic second-order phase transition phenomena. On the other hand, the phase-field fracture models which this dissertation is focused on, originates from the variational approach to brittle fracture proposed by Francfort and Marigo [131]. Even though phase-field fracture formulation was developed through a variational approach to fracture, i.e. using energy minimization, it shares some similarities and differences with other non-local continuum models, most notably the gradient damage model [130] and gradient-enhanced continuum damage model [129].

From the perspective of partial differential equations, both phase-field and gradient-enhanced damage model are quite similar, as they are defined through the second-order, Helmholtz-type partial differential equation in which the Laplacian operator ∇^2 is applied to the non-local scalar variable. Not only that, but in both models the material length parameter, that helps to diffuse the discrete crack over the finite region, is multiplied by the Laplacian term. Moreover, boundary conditions for both approaches are defined as a dot product between the outer normal vector and the gradient of the non-local scalar variable. However, the non-local scalar variable, i.e. damage driving force in the gradient-enhanced damage model is the non-local equivalent strain, while in the phase-field fracture model, it is the value of the crack phase-field itself. Also, the major difference is that in the phase-field model, the crack driving force vanishes for a fully damaged material, which is not the case in the gradient-enhanced damage model. In addition, boundary conditions in the case

of phase-field fracture formulation follow naturally from its derivation (which will be shown in the following pages), while for gradient-enhanced continuum damage approach they are introduced separately.

Although they originated from rather distinct points of view, the phase-field method resembles the gradient damage model quite significantly, provided the incorporated length parameter is treated as a purely material property rather than a numerical one. The gradient damage model, originally proposed by Frémond and Nedjar [130], was derived by extending the virtual power principle in order to incorporate the damage gradient accounting for microscopic non-local interactions. The resulting macroscopic balance equation and the damage evolution law possess the same format as one in the phase-field model. However, in gradient damage models the fracture energy does not enter the formulation from the beginning, but rather, it is later identified heuristically from the 1-D analytical solution. Moreover, the notion of approximating the sharp crack topology by the crack phase-field does not appear at all, even in the newer gradient damage models [233, 234].

From this discussion, it can be stated that phase-field combines some of the features of both gradient damage and gradient-enhanced continuum damage models. However, since it is derived through minimization of the total energy functional, governing equations of the phase-field model follow naturally from the derivation itself. This is not present in either of the two non-local approaches that are mentioned above. Also, phase-field relies on two parameters, i.e. length parameter and a critical value of strain energy release rate, to regularise the original ill-posed boundary value problem. The length parameter helps to diffuse (smear) the sharp crack topology over a finite domain region, while the critical value of strain energy release rate limits the energy dissipation per unit area in the crack. How exactly this works is presented in the following pages.

3.2. Governing equations

For a body of volume Ω and surface $\partial\Omega$, the total energy functional (also known as the free energy functional) Π is a function of a displacement field $\mathbf{u}$, and in the quasi-static regime of loading it is defined as

$$\Pi = \Pi^{\text{int}} + \Pi^{\text{ext}}. \tag{3.1}$$

In Eq. (3.1) Π^{int} is the internal part of the potential energy calculated through the

integral of strain energy density function ψ

$$\Pi^{\text{int}} = \int_{\Omega} \psi\left(\boldsymbol{\varepsilon}\left(\mathbf{u}\right)\right) \mathrm{d}\Omega, \tag{3.2}$$

while Π^{ext} denotes potential energy produced by the external loading

$$\Pi^{\text{ext}} = -\int_{\Omega} \mathbf{u} \cdot \mathbf{b}\, \mathrm{d}\Omega - \int_{\partial\Omega} \mathbf{u} \cdot \mathbf{h}\, \mathrm{d}\partial\Omega \tag{3.3}$$

where $\mathbf{b}$ and $\mathbf{h}$ are prescribed volume, i.e. surface force vector and "$\cdot$" indicates the dot product between two vectors. Identity (3.2) is valid for any deformable body without any flaws, i.e. cracks. However, if at any point, under the influence of static external load, a crack appears, the internal part of the total energy functional is additively decomposed into two parts, i.e.

$$\Pi^{\text{int}} = \Pi^{\text{b}} + \Pi^{\text{s}} = \int_{\Omega\backslash\Gamma} \psi\left(\boldsymbol{\varepsilon}\left(\mathbf{u}\right), \Gamma\right)\, \mathrm{d}\Omega + \int_{\Gamma} G_{\text{c}}\, \mathrm{d}\Gamma. \tag{3.4}$$

The first integral in Eq. (3.4) defines body's bulk energy, while the second integral represents *fracture-induced dissipating surface energy*. In the first integral of Eq. (3.4), the symbol $\Omega\backslash\Gamma$ indicates that the integration is performed over the finite volume Ω with the exclusion of the crack surface Γ. Scalar value G_{c}, which appears in the second integral of Eq. (3.4) is called critical Griffith force (it is also known as the critical value of energy release rate), and in the case of brittle and quasi-brittle type materials can be considered as a material's fracture toughness. The variational approach to fracture, proposed by Francfort and Marigo [131], implies that the cracked body deformes and the crack(s) propagates in a way that ensures minimum values of total potential energy. More precisely, fracture is regarded as an energy minimization problem, in which the pair $(\mathbf{u}, \Gamma)$ are the global minimizers of the total energy functional Π, i.e.

$$(\mathbf{u}, \Gamma) = \text{Arg}\{\min\left[\Pi\left(\mathbf{u}, \Gamma\right)\right]\}. \tag{3.5}$$

This implies that the internal part of total energy functional Π^{int} can be minimized with respect to both strain field and the crack itself

$$\delta\Pi^{\text{int}} = \frac{\partial\Pi^{\text{int}}}{\partial\boldsymbol{\varepsilon}} : \delta\boldsymbol{\varepsilon} + \frac{\partial\Pi^{\text{int}}}{\partial\Gamma}\, \delta\Gamma, \tag{3.6}$$

while the external part of free energy functional is, as usual, minimized with respect to displacement field $\mathbf{u}$

$$\delta\Pi^{\text{ext}} = \frac{\partial \Pi^{\text{extp}}}{\partial \mathbf{u}} \cdot \delta\mathbf{u}. \tag{3.7}$$

For a body with crack surface Γ, the equilibrium state is reached if the variation of the total energy functional is equal to zero, i.e.

$$\delta\Pi = \delta\Pi^{\text{int}} + \delta\Pi^{\text{ext}} = 0. \tag{3.8}$$

Substituting Eq. (3.6) and (3.7) into identity (3.8) yields

$$\delta\Pi = \frac{\partial \Pi^{\text{int}}}{\partial \boldsymbol{\varepsilon}} : \delta\boldsymbol{\varepsilon} + \frac{\partial \Pi^{\text{int}}}{\partial \Gamma}\delta\Gamma + \frac{\partial \Pi^{\text{extp}}}{\partial \mathbf{u}} : \delta\mathbf{u} = 0. \tag{3.9}$$

Although a variational approach to fracture [131] was initially proposed for brittle and quasi-brittle materials, as will be seen in the following pages, the principle defined by (3.4) and (3.6) can be applied to ductile materials as well. Not only that, but in **subsection 1.3.3** several contributions were listed in which the phase-field (which is based on the variational approach to fracture) was successfully utilized in multiphysics problems such as thermomechanics and electromechanics.

Eq. (3.9) represents a free discontinuity problem, in which displacement field $\mathbf{u}$ and the crack surface Γ are both *a priori* unknown. In order to numerically implement the resulting free discontinuity problem, Bourdin et al. [145] proposed using the so-called *regularized variational fracture model*, based on Ambrosio and Tortorelli [147] regularisation in image segmentation. That is, a discontinuous crack of zero width is approximated (replaced) by a diffusive crack of a finite width - **Figure 3.1**.

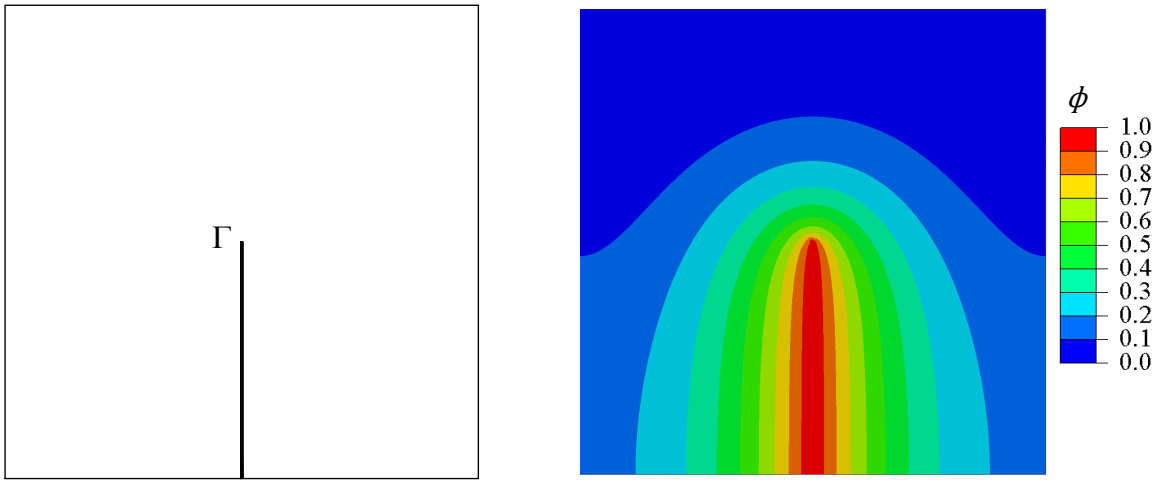

(a) Discrete crack surface Γ **(b)** Regularized discrete crack surface Γ

Figure 3.1: Phase-field regularisation of the discrete crack surface Γ

Without the loss of generality, in the phase-field formulation the sharp crack surface Γ is regularised by the functional Γ_l

$$\Gamma \approx \Gamma_l(\phi) = \int_\Omega \gamma(\phi; \nabla\phi)\, \mathrm{d}\Omega, \tag{3.10}$$

such that the fracture-induced surface energy Π^s is approximated as

$$\Pi^s = \int_\Gamma G_c\, \mathrm{d}\Gamma \approx \int_\Omega G_c \gamma(\phi; \nabla\phi)\, \mathrm{d}\Omega, \tag{3.11}$$

where γ represents the *crack surface density function* [150], which is expressed in terms of the crack phase-field parameter ϕ and its gradient $\nabla\phi$. Here, the crack phase-field parameter ϕ represents a scalar value that ranges between 0 and 1 - $\phi \in [0, 1]$. A value of 0 indicates virgin material, while a value of 1 means the material is fully broken. Notice from (3.11) that the integral is no longer performed on the surface Γ but on the finite volume Ω. This is because a discontinuous crack is now smeared over a finite volume using scalar value of ϕ. Now, the internal part of the free energy functional, i.e. expression (3.4) can be rewritten in the following form

$$\Pi^{\text{int}} = \Pi^b + \Pi^s = \int_\Omega g(\phi)\, \psi(\boldsymbol{\varepsilon}(\mathbf{u}))\, \mathrm{d}\Omega + \int_\Omega G_c \gamma(\phi; \nabla\phi)\, \mathrm{d}\Omega, \tag{3.12}$$

where g is called the degradation function, which controls the value of damage the material has sustained. Notice that the first integral in (3.4), which was initially performed over the volume Ω with the exclusion of the fracture surface Γ, is now performed on the finite volume Ω. This is again the result of crack smearing over a finite region through the use of ϕ.

The total energy functional Π can now be written as

$$\begin{aligned} \Pi = \Pi^{\text{int}} + \Pi^{\text{ext}} = \int_\Omega g(\phi)\, \psi(\boldsymbol{\varepsilon}(\mathbf{u}))\, \mathrm{d}\Omega + \int_\Omega G_c \gamma(\phi; \nabla\phi)\, \mathrm{d}\Omega - \\ \int_\Omega \mathbf{u} \cdot \mathbf{b}\, \mathrm{d}\Omega - \int_{\partial\Omega} \mathbf{u} \cdot \mathbf{h}\, \mathrm{d}\partial\Omega, \end{aligned} \tag{3.13}$$

and its variation is now expressed through

$$\delta\Pi = \frac{\partial \Pi^{\text{int}}}{\partial \boldsymbol{\varepsilon}} : \delta\boldsymbol{\varepsilon} + \frac{\partial \Pi^{\text{int}}}{\partial \phi}\, \delta\phi + \frac{\partial \Pi^{\text{extp}}}{\partial \mathbf{u}} \cdot \delta\mathbf{u} = 0. \tag{3.14}$$

From Eq. (3.14) it is clear that the internal part of the free energy functional is minimized with respect to both small strain tensor $\boldsymbol{\varepsilon}$ and the crack phase-field parameter ϕ, while the external part is minimized solely with respect to displacement field $\mathbf{u}$.

The minimization of Π^{int} yields

$$\begin{aligned}\delta\Pi^{\text{int}} = \int_\Omega g(\phi)\,\boldsymbol{\sigma} : \delta\boldsymbol{\varepsilon}\,\mathrm{d}\Omega + \int_\Omega \psi(\boldsymbol{\varepsilon}(\mathbf{u}))\,\frac{\mathrm{d}g(\phi)}{\mathrm{d}\phi}\,\delta\phi\,\mathrm{d}\Omega + \\ \int_\Omega G_\mathrm{c}\left(\frac{\partial\gamma(\phi;\nabla\phi)}{\partial\phi}\delta\phi + \frac{\partial\gamma(\phi;\nabla\phi)}{\partial\nabla\phi}\cdot\delta\nabla\phi\right)\mathrm{d}\Omega,\end{aligned} \tag{3.15}$$

while for the external part of the free energy functional, the following is true

$$\delta\Pi^{\text{ext}} = -\int_\Omega \mathbf{b}\cdot\delta\mathbf{u}\,\mathrm{d}\Omega - \int_{\partial\Omega}\mathbf{h}\cdot\delta\mathbf{u}\,\mathrm{d}\partial\Omega. \tag{3.16}$$

With the help of the divergence theorem, the first integral in Eq. (3.15) is expressed in terms of displacement field differential $\delta\mathbf{u}$ and a unit normal $\mathbf{n}$, i.e.

$$\int_\Omega g(\phi)\,\boldsymbol{\sigma} : \delta\boldsymbol{\varepsilon}\,\mathrm{d}\Omega = \int_{\partial\Omega} g(\phi)\,\boldsymbol{\sigma}\cdot\mathbf{n}\cdot\delta\mathbf{u}\,\mathrm{d}\partial\Omega - \int_\Omega g(\phi)\,\nabla\cdot\boldsymbol{\sigma}\cdot\delta\mathbf{u}\,\mathrm{d}\Omega, \tag{3.17}$$

The divergence theorem is also applied to the second term of the third integral of Eq. (3.15) in order to exclude the differential of the phase-field gradient

$$\begin{aligned}\int_\Omega \frac{\partial\gamma(\phi;\nabla\phi)}{\partial\nabla\phi}\cdot\delta\nabla\phi\,\mathrm{d}\Omega = \int_{\partial\Omega}\frac{\partial\gamma(\phi;\nabla\phi)}{\partial\nabla\phi}\cdot\mathbf{n}\delta\phi\,\mathrm{d}\partial\Omega - \\ \int_\Omega \nabla\cdot\frac{\partial\gamma(\phi;\nabla\phi)}{\partial\nabla\phi}\delta\phi\,\mathrm{d}\Omega.\end{aligned} \tag{3.18}$$

Substituting (3.17) and (3.18) into (3.15) yields the following expression

$$\begin{aligned}\delta\Pi^{\text{int}} = \int_{\partial\Omega} g(\phi)\,\boldsymbol{\sigma}\cdot\mathbf{n}\cdot\delta\mathbf{u}\,\mathrm{d}\partial\Omega - \int_\Omega g(\phi)\,\nabla\cdot\boldsymbol{\sigma}\cdot\delta\mathbf{u}\,\mathrm{d}\Omega + \\ \int_\Omega \psi(\boldsymbol{\varepsilon}(\mathbf{u}))\,\frac{\mathrm{d}g(\phi)}{\mathrm{d}\phi}\delta\phi\,\mathrm{d}\Omega + \int_{\partial\Omega} G_\mathrm{c}\frac{\partial\gamma(\phi;\nabla\phi)}{\partial\nabla\phi}\cdot\mathbf{n}\delta\phi\,\mathrm{d}\partial\Omega - \\ \int_\Omega G_\mathrm{c}\nabla\cdot\frac{\partial\gamma(\phi;\nabla\phi)}{\partial\nabla\phi}\delta\phi\,\mathrm{d}\Omega + \int_\Omega G_\mathrm{c}\frac{\partial\gamma(\phi;\nabla\phi)}{\partial\phi}\delta\phi\,\mathrm{d}\Omega.\end{aligned} \tag{3.19}$$

Now the variation of total energy functional Π is expressed through variation of the displacement field $\mathbf{u}$ and the crack phase-field parameter ϕ

$$\begin{aligned}\delta\Pi = \int_{\partial\Omega} g(\phi)\,\boldsymbol{\sigma}\cdot\mathbf{n}\cdot\delta\mathbf{u}\,\mathrm{d}\partial\Omega - \int_\Omega g(\phi)\,\nabla\cdot\boldsymbol{\sigma}\cdot\delta\mathbf{u}\,\mathrm{d}\Omega + \\ \int_\Omega \psi(\boldsymbol{\varepsilon}(\mathbf{u}))\,\frac{\mathrm{d}g(\phi)}{\mathrm{d}\phi}\delta\phi\,\mathrm{d}\Omega + \int_{\partial\Omega} G_\mathrm{c}\frac{\partial\gamma(\phi;\nabla\phi)}{\partial\nabla\phi}\cdot\mathbf{n}\delta\phi\,\mathrm{d}\partial\Omega - \\ \int_\Omega G_\mathrm{c}\nabla\cdot\frac{\partial\gamma(\phi;\nabla\phi)}{\partial\nabla\phi}\delta\phi\,\mathrm{d}\Omega + \int_\Omega G_\mathrm{c}\frac{\partial\gamma(\phi;\nabla\phi)}{\partial\phi}\delta\phi\,\mathrm{d}\Omega - \\ \int_\Omega \mathbf{b}\cdot\delta\mathbf{u}\,\mathrm{d}\Omega - \int_{\partial\Omega}\mathbf{h}\cdot\delta\mathbf{u}\,\mathrm{d}\partial\Omega,\end{aligned} \tag{3.20}$$

which yields the following system of equations

$$g\left(\phi\right)\nabla\cdot\boldsymbol{\sigma}+\mathbf{b}=\mathbf{0},\ \text{in }\Omega, \tag{3.21}$$

$$g\left(\phi\right)\boldsymbol{\sigma}\cdot\mathbf{n}-\mathbf{h}=\mathbf{0},\ \text{on }\partial\Omega_{\mathrm{h}}, \tag{3.22}$$

$$\psi\left(\boldsymbol{\varepsilon}\left(\mathbf{u}\right)\right)\frac{\mathrm{d}g\left(\phi\right)}{\mathrm{d}\phi}+G_{\mathrm{c}}\left(\frac{\partial\gamma\left(\phi;\nabla\phi\right)}{\partial\phi}-\nabla\cdot\frac{\partial\gamma\left(\phi;\nabla\phi\right)}{\partial\nabla\phi}\right)=0,\ \text{in }\Omega, \tag{3.23}$$

$$G_{\mathrm{c}}\frac{\partial\gamma\left(\phi;\nabla\phi\right)}{\partial\nabla\phi}\cdot\mathbf{n}=\mathbf{0},\ \text{on }\partial\Omega. \tag{3.24}$$

For a given set of boundary conditions, the above set of equations has a unique solution in terms of displacement field $\mathbf{u}$ and the crack phase-field parameter ϕ. However, the model obtained from (3.20) has one critical flaw - it does not distinguish between compressive and tensile loading. More precisely, the crack forms and propagates regardless of loading type, which does not reflect reality. To correct this error, Eq. (3.20) needs to be reformulated so that only positive values of stress and strain energy density are connected to the phase-field variable ϕ, i.e.

$$\begin{aligned}\delta\Pi=&\int_{\partial\Omega}\left[g\left(\phi\right)\boldsymbol{\sigma}^{+}+\boldsymbol{\sigma}^{-}\right]\cdot\mathbf{n}\cdot\delta\mathbf{u}\,\mathrm{d}\partial\Omega-\int_{\Omega}\left[g\left(\phi\right)\nabla\cdot\boldsymbol{\sigma}^{+}+\nabla\cdot\boldsymbol{\sigma}^{-}\right]\cdot\delta\mathbf{u}\,\mathrm{d}\Omega+\\&\int_{\Omega}\psi^{+}\left(\boldsymbol{\varepsilon}\left(\mathbf{u}\right)\right)\frac{\mathrm{d}g\left(\phi\right)}{\mathrm{d}\phi}\delta\phi\,\mathrm{d}\Omega+\int_{\partial\Omega}G_{\mathrm{c}}\frac{\partial\gamma\left(\phi;\nabla\phi\right)}{\partial\nabla\phi}\cdot\mathbf{n}\delta\phi\,\mathrm{d}\partial\Omega-\\&\int_{\Omega}G_{\mathrm{c}}\nabla\cdot\frac{\partial\gamma\left(\phi;\nabla\phi\right)}{\partial\nabla\phi}\delta\phi\,\mathrm{d}\Omega+\int_{\Omega}G_{\mathrm{c}}\frac{\partial\gamma\left(\phi;\nabla\phi\right)}{\partial\phi}\delta\phi\,\mathrm{d}\Omega-\\&\int_{\Omega}\mathbf{b}\cdot\delta\mathbf{u}\,\mathrm{d}\Omega-\int_{\partial\Omega}\mathbf{h}\cdot\delta\mathbf{u}\,\mathrm{d}\partial\Omega,\end{aligned} \tag{3.25}$$

which then leads to a modified set of equations

$$\left[g\left(\phi\right)\nabla\cdot\boldsymbol{\sigma}^{+}+\nabla\cdot\boldsymbol{\sigma}^{-}\right]+\mathbf{b}=\mathbf{0},\ \text{in }\Omega, \tag{3.26}$$

$$\left[g\left(\phi\right)\boldsymbol{\sigma}^{+}+\boldsymbol{\sigma}^{-}\right]\cdot\mathbf{n}-\mathbf{h}=\mathbf{0},\ \text{on }\partial\Omega_{\mathrm{h}}, \tag{3.27}$$

$$\psi^{+}\left(\boldsymbol{\varepsilon}\left(\mathbf{u}\right)\right)\frac{\mathrm{d}g\left(\phi\right)}{\mathrm{d}\phi}+G_{\mathrm{c}}\left(\frac{\partial\gamma\left(\phi;\nabla\phi\right)}{\partial\phi}-\nabla\cdot\frac{\partial\gamma\left(\phi;\nabla\phi\right)}{\partial\nabla\phi}\right)=0,\ \text{in }\Omega, \tag{3.28}$$

$$G_{\mathrm{c}}\frac{\partial\gamma\left(\phi;\nabla\phi\right)}{\partial\nabla\phi}\cdot\mathbf{n}=\mathbf{0},\ \text{on }\partial\Omega. \tag{3.29}$$

In the identities above, $\boldsymbol{\sigma}^{+}$ and $\boldsymbol{\sigma}^{-}$ are positive, i.e negative part of the Cauchy stress tensor, while ψ^{+} and ψ^{-} denote positive, i.e. negative part of strain energy density.

The formulation described in strong from through expressions (3.21)-(3.24) does not include the split of strain energy density function or Cauchy stress tensor, and is also known as the isotropic model [146]. On the other hand, equations (3.26)-(3.29) describe what is known as anisotropic phase-field formulation, which prevents crack formation and evolution during compressive loading. Some techniques for splitting, i.e. finding the positive and negative parts of the strain energy density, Cauchy stress tensor and the material stiffness tensor $\mathbb{C}$ are presented in **subsection 3.3.1**.

3.2.1. Phase-field representation of the fractured surface

The key ingredient of phase-field fracture models is the approximation of the sharp crack topologies (geometries) by a diffusive crack smeared within a localization band of finite width, that is controlled by length-scale parameters l. In the 1-D configuration, this can be visualized by the following exponential function

$$\phi(x) = \exp\left(-\frac{|x|}{l}\right), \tag{3.30}$$

which satisfies the following properties

$$\phi(x=0) = 1 \text{ and } \lim_{x\to\pm\infty} \phi(x) = 0, \tag{3.31}$$

for a specific value of a length-scale parameter l, which is illustrated in **Figure 3.2**.

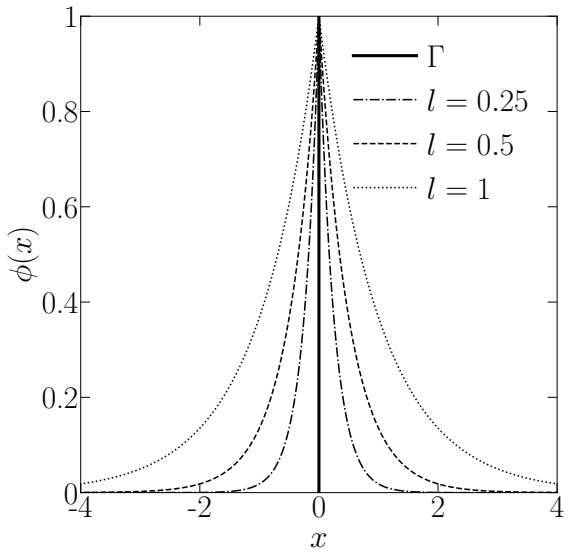

Figure 3.2: Diffusive representation of a 1D discrete crack Γ for various length-scale parameters l

It can be easily verified that the scalar function given by (3.30) is a solution of the following ordinary differential equation

$$\frac{\phi(x)}{l} - l\phi''(x) = 0, \tag{3.32}$$

supplemented with the boundary conditions in (3.31). Following (3.10), the goal is to find functional Γ_l that approximates the sharp discontinuity and whose minimization yields back the ordinary differential equation given by (3.32). For the problem defined in **Figure 3.2**, the following can be written

$$\Gamma \approx \Gamma_l(\phi) = \int_{-\infty}^{+\infty} \frac{1}{2}\left[\frac{1}{l}\phi^2 + l\left(\phi'\right)^2\right] \mathrm{d}x = \int_{-\infty}^{+\infty} \gamma\left(\phi, \phi'\right) \mathrm{d}x, \tag{3.33}$$

where $\gamma\left(\phi, \phi'\right)$ is, as previously mentioned, crack surface density function - a term first introduced in Miehe et al. [150]. For the one-dimensional case, it is defined as

$$\gamma\left(\phi, \phi'\right) = \frac{1}{2}\left(\frac{1}{l}\phi^2 + l\left(\phi'\right)^2\right), \tag{3.34}$$

while its form in multidimensional problems is equal to

$$\gamma\left(\phi, \nabla\phi\right) = \frac{1}{2}\left(\frac{1}{l}\phi^2 + l\nabla\phi \cdot \nabla\phi\right). \tag{3.35}$$

From **Figure 3.2** it is clear that the length-scale parameter l has a direct control of the discrete crack approximation by the phase-field variable ϕ. When $l \to 0$, a discrete crack surface Γ is recovered. The influence of the value of length-scale parameter l on the phase-field crack approximation is more vividly shown in **Figure 3.3**. Therein, four different values of length-scale parameter l (each next one twice as small as the previous one) provide different approximations of the sharp crack topology on the square domain of unit length. However, length-scale parameter l is not only related to the geometry of the crack surface, but it also influences material behaviour during fracture. More precisely, different values of length-scale parameter will lead to different values of peak stress/force in the underlying model. This is because, with every decrease in l, there will be a decrease in the surface on which fracture energy can be dissipated. In order to ensure the same energy dissipation, i.e. same energy release rate for different values of l the value of peak stress ultimately needs to increase. For a length-scale parameter of value 0, the peak stress would go to infinity.

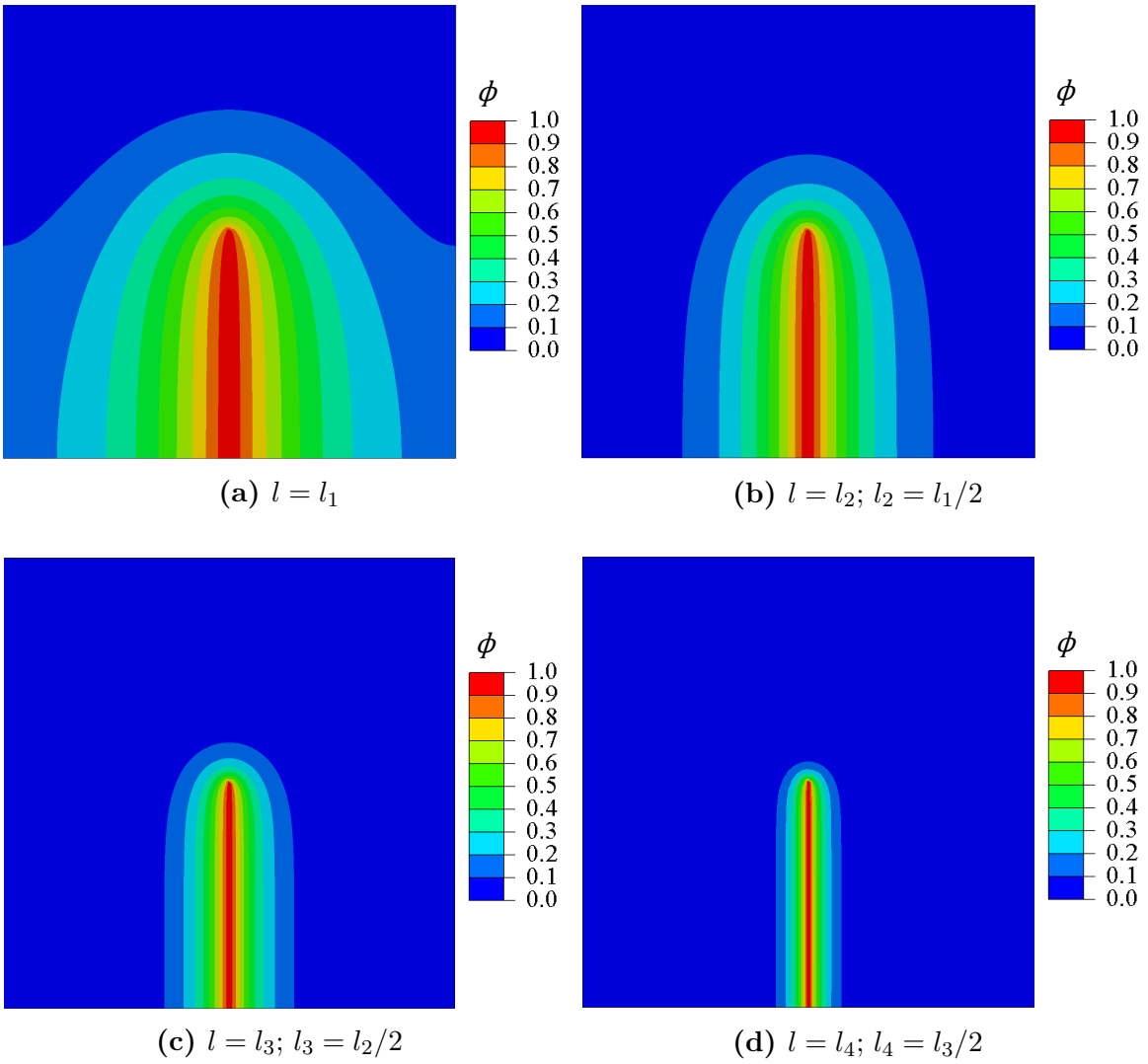

(a) $l = l_1$ **(b)** $l = l_2;\ l_2 = l_1/2$

(c) $l = l_3;\ l_3 = l_2/2$ **(d)** $l = l_4;\ l_4 = l_3/2$

Figure 3.3: Influence of the length-scale parameter l on the diffusive representation of the discrete crack surface

It is important to note that the crack surface density function γ, given by Eq. (3.35), is not the unique one that can be used to regularise the sharp crack topology. Its form can vary, but in general, can be expressed as [235]

$$\gamma\left(\phi;\nabla\phi\right) = \frac{1}{c_0}\left(\frac{1}{l}\alpha\left(\phi\right) + l\nabla\phi\cdot\nabla\phi\right), \tag{3.36}$$

where α is the so-called *geometric crack function*, which can be expressed through

$$\alpha\left(\phi\right) = \xi\phi + \left(1-\xi\right)\phi^2, \tag{3.37}$$

for a non-negative parameters $\xi \in [0,2]$; otherwise, $\alpha\left(\phi\right) \in [0,1]$ cannot be guaranteed. Different values of ξ will produce various crack surface density functions and therefore

different crack topologies. However, for the purposes of this dissertation, crack density function of the form given by (3.35) will be used.

3.2.2. Bulk energy degradation

The stored energy functional, i.e. the body's bulk energy Π^{b}

$$\Pi^{\mathrm{b}} = \int_{\Omega} g(\phi)\, \psi(\boldsymbol{\varepsilon}(\mathbf{u}))\, \mathrm{d}\Omega, \tag{3.38}$$

describes the smooth transition from the intact bulk material to the fully cracked state - through the use of strain energy density ψ and the energetic/stress degradation function g. In the phase-field fracture formulation, the energetic degradation function g plays an important role since it links the crack phase-field and the mechanical properties. More precisely, it determines how the stored energy functional responds to changes in the crack phase-field. However, there are four conditions that every stress degradation function needs to satisfy:

(1) $g(0) = 1$,

(2) $g(1) = 0$,

(3) $g'(1) = 0$,

(4) $g'(\phi) < 0$.

The first and second condition describes intact and fully broken material, respectively. The third condition ensures that the degradation function is monotonically increasing, thus ensuring an increase in the material's degradation as the phase-field ϕ is increasing. The last condition guarantees that the localization band does not grow orthogonally as usually observed in the gradient-enhanced damage model [129].

There exists a broad range of functions that satisfy all four conditions and thus can be used in (3.38). A common choice for the degradation function g, which will also be the case in this dissertation, is a simple quadratic function first utilized in Bourdin et al. [145]

$$g(\phi) = (1-\phi)^2. \tag{3.39}$$

On the other hand, a cubic degradation function of the general form

$$g(\phi) = (3-s)(1-\phi)^2 - (2-s)(1-\phi)^3, \tag{3.40}$$

was introduced in Borden et al [163]. In (3.40) s is the scalar value that controls the overall slope of the function. Kuhn et al. [236] introduced a fourth-degree polynomial degradation function

$$g(\phi) = 4(1-\phi)^3 - 3(1-\phi)^4. \tag{3.41}$$

Moreover, Sargado et al. [237] proposed a family of exponential-type degradation function with three additional parameters and a corrector term and made a detailed comparison with the already mentioned degradation functions.

The degradation function is ultimately the key factor that controls the degree of material damage, and its value is not the reflection of the value held by the crack phase-field parameter ϕ, since the relationship between g and ϕ is non-linear. More precisely, the value of ϕ by itself does not determine the value of damage the material has endured. For example, the value of $\phi = 0.5$ (at a specific material point) does not imply that the material has degraded by 50 %. This is another important difference that arises when comparing phase-field to gradient-enhanced continuum damage models, as in the latter the relationship between the damage variable and the function that degrades the stiffness of the material is linear - see **Figure 3.4**. Because of that, the choice of degradation function will greatly influence the overall solution of the underlying problem.

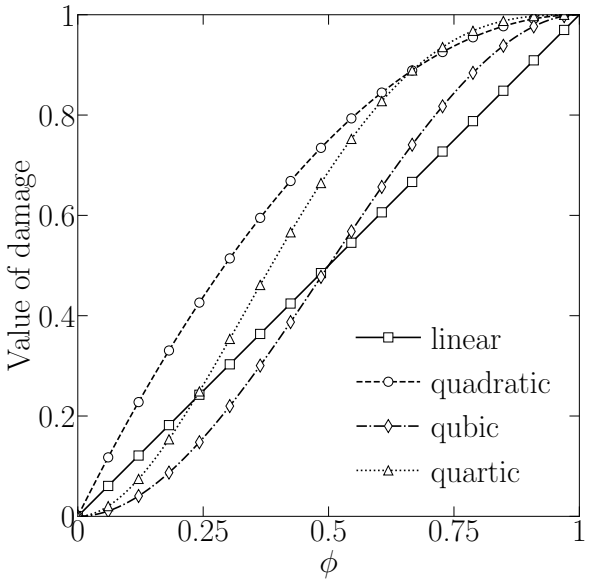

Figure 3.4: Relationships between the crack phase-field parameter ϕ and the value of overall damage, for different degradation functions

3.3. Phase-field for brittle fracture

In cases of brittle (and sometimes quasi-brittle) materials, the behaviour of the material is assumed to be linear elastic, i.e. total small strain tensor $\boldsymbol{\varepsilon}$ consists exclusively of elastic deformations. Therefore, strain energy density function ψ is only influenced by the elastic strain tensor $\boldsymbol{\varepsilon}^{\mathrm{e}}$ through the following relation

$$\psi\left(\boldsymbol{\varepsilon}\right) = \psi_{\mathrm{e}}\left(\boldsymbol{\varepsilon}^{\mathrm{e}}\right) = \frac{1}{2}\lambda \mathrm{tr}^2\left[\boldsymbol{\varepsilon}\right] + \mu \mathrm{tr}\left[\boldsymbol{\varepsilon} : \boldsymbol{\varepsilon}\right]. \tag{3.42}$$

Here λ and μ denote the Lamé constant and the shear modulus, respectively. The relation (3.42) can also be written using bulk modulus κ as

$$\psi\left(\boldsymbol{\varepsilon}\right) = \frac{1}{2}\kappa \mathrm{tr}^2\left[\boldsymbol{\varepsilon}\right] + \mu \boldsymbol{\varepsilon}_{\mathrm{dev}} : \boldsymbol{\varepsilon}_{\mathrm{dev}}, \tag{3.43}$$

with $\boldsymbol{\varepsilon}_{\mathrm{dev}}$ being the deviatoric part of the small strain tensor $\boldsymbol{\varepsilon}$ that is equal to

$$\boldsymbol{\varepsilon}_{\mathrm{dev}} = \boldsymbol{\varepsilon} - \frac{1}{n}\mathrm{tr}\left[\boldsymbol{\varepsilon}\right]\mathbf{I}, \tag{3.44}$$

where $\mathbf{I}$ is the second-order identity tensor. Lamé parameters λ, μ and κ are related to each other through the following expression

$$\kappa = \lambda + \frac{2}{n}\mu, \tag{3.45}$$

where n defines the number of dimensions. The Cauchy stress tensor $\boldsymbol{\sigma}$ is calculated directly from elastic strain energy density, i.e.

$$\boldsymbol{\sigma} = \frac{\partial \psi\left(\boldsymbol{\varepsilon}\right)}{\partial \boldsymbol{\varepsilon}}, \tag{3.46}$$

which, using (3.42), i.e. (3.43) is equal to

$$\boldsymbol{\sigma} = \lambda \mathrm{tr}\left[\boldsymbol{\varepsilon}\right]\mathbf{I} + 2\mu\boldsymbol{\varepsilon} = \kappa \mathrm{tr}\left[\boldsymbol{\varepsilon}\right]\mathbf{I} + 2\mu\boldsymbol{\varepsilon}_{\mathrm{dev}}. \tag{3.47}$$

Since degradation function g is applied to positive parts of both Cauchy stress tensor $\boldsymbol{\sigma}$ and elastic strain energy density ψ, their values are in the end equal to

$$\psi\left(\boldsymbol{\varepsilon}\right) = g\left(\phi\right)\psi^{+}\left(\boldsymbol{\varepsilon}\right) + \psi^{-}\left(\boldsymbol{\varepsilon}\right) \tag{3.48}$$

$$\boldsymbol{\sigma} = g\left(\phi\right)\boldsymbol{\sigma}^{+} + \boldsymbol{\sigma}^{-} = g\left(\phi\right)\frac{\partial \psi^{+}\left(\boldsymbol{\varepsilon}\right)}{\partial \boldsymbol{\varepsilon}} + \frac{\partial \psi^{-}\left(\boldsymbol{\varepsilon}\right)}{\partial \boldsymbol{\varepsilon}}. \tag{3.49}$$

3.3.1. Strain energy density decomposition

In order to ensure physical behaviour, i.e. prevent the formation and propagation of cracks under compression, both elastic strain energy density and Cauchy stress tensor need to be additively decomposed on their negative, i.e. positive parts. The split on positive and negative values also needs to be performed on the underlying elastic stiffness tensor $\mathbb{C}$, which is expressed as

$$\mathbb{C} = \kappa \mathbf{I} \otimes \mathbf{I} + \mu \left(2\mathbb{I}_{\mathrm{s}} - \frac{2}{n} \mathbf{I} \otimes \mathbf{I} \right), \tag{3.50}$$

or

$$\mathbb{C} = \lambda \mathbf{I} \otimes \mathbf{I} + 2\mu \mathbb{I}_{\mathrm{s}}, \tag{3.51}$$

where $\mathbb{I}_{\mathrm{s}}$ is the symmetric part of the fourth-order identity tensor expressed in terms of Kronecker delta symbol δ_{ij} as

$$\mathbb{I}_{\mathrm{s}} = \frac{1}{2} \left(\delta_{ik}\delta_{jl} + \delta_{il}\delta_{jk} \right). \tag{3.52}$$

The two most common energy decompositions in the phase-field fracture models are considered here and will be used in the later examples, when necessary.

The first split to be described refers to the decomposition proposed by Amor et al. [135] in which the strain energy density ψ is additively decomposed into volumetric and deviatoric part, i.e.

$$\psi_{\mathrm{e}}^{\pm} = \frac{1}{2} \kappa \left\langle \mathrm{tr}\left[\boldsymbol{\varepsilon}\right] \right\rangle_{\pm}^{2} + \mu \boldsymbol{\varepsilon}_{\mathrm{dev}} : \boldsymbol{\varepsilon}_{\mathrm{dev}}, \tag{3.53}$$

Here $< x >_{\pm} = \frac{1}{2}\left(x \pm |x|\right)$ is the Macaulay bracket, while $\psi^{\pm}$ refers to positive/negative part of strain energy density. From Eq. (3.53) it is clear that in a volumetric-deviatoric split, the deviatoric part of ψ is always considered to have a positive impact on the crack formation and propagation, while the volumetric (hydrostatic) part can act in both ways - depending on the sign of the hydrostatic strain. Following (3.49) the Cauchy stress tensor is now obtained through

$$\boldsymbol{\sigma} = g\left(\phi\right) \left[\kappa \left\langle \mathrm{tr}\left[\boldsymbol{\varepsilon}\right] \right\rangle_{+} \mathbf{I} + 2\mu \boldsymbol{\varepsilon}_{\mathrm{dev}} \right] + \kappa \left\langle \mathrm{tr}\left[\boldsymbol{\varepsilon}\right] \right\rangle_{-} \mathbf{I} \tag{3.54}$$

while the material stiffness tensor $\mathbb{C}$ is equal to

$$\mathbb{C} = g\left(\phi\right) \left(\kappa \mathbf{I} \otimes \mathbf{I}\mathcal{H}\left[\mathrm{tr}\left[\boldsymbol{\varepsilon}\right]\right] + 2\mu \mathbb{I}_{\mathrm{s}} \right) + \kappa \mathbf{I} \otimes \mathbf{I}\mathcal{H}\left[-\mathrm{tr}\left[\boldsymbol{\varepsilon}\right]\right]. \tag{3.55}$$

In (3.55) $\mathcal{H}$ is the Heavyside function defined as

$$\mathcal{H}\left[\mathrm{tr}\left[\boldsymbol{\varepsilon}\right]\right] = \begin{cases} 1, \ \mathrm{tr}\left[\boldsymbol{\varepsilon}\right] \geq 0 \\ 0, \ \mathrm{tr}\left[\boldsymbol{\varepsilon}\right] < 0. \end{cases} \tag{3.56}$$

The second energy split, proposed by Miehe et al. [150], is based on the spectral decomposition of the small strain tensor $\boldsymbol{\varepsilon}$, i.e.

$$\psi_{\mathrm{e}}^{\pm} = \frac{1}{2}\lambda \left\langle \mathrm{tr}\left[\boldsymbol{\varepsilon}\right]\right\rangle_{\pm}^{2} + \mu \boldsymbol{\varepsilon}^{\pm} : \boldsymbol{\varepsilon}^{\pm}, \tag{3.57}$$

where $\boldsymbol{\varepsilon}^{\pm}$ denotes the positive and negative part of the strain tensor, which, for the purposes of spectral decomposition is expressed using the following identity

$$\boldsymbol{\varepsilon}^{\pm} = \sum_{a=1}^{n} \left\langle \lambda_a \right\rangle_{\pm} \mathbf{n}_a \otimes \mathbf{n}_a = \sum_{a=1}^{n} \left\langle \lambda_a \right\rangle_{\pm} \mathbf{M}_a. \tag{3.58}$$

In Eq. (3.58) λ_a is the a-th eigenvalue, while $\mathbf{M}_a$ is the projection matrix, defined for a given eigenvalue and obtained as a tensor product of eigenvector $\mathbf{n}_a$. Following again (3.49) the Cauchy stress tensor is calculated as

$$\boldsymbol{\sigma} = g\left(\phi\right)\left[\lambda \left\langle \mathrm{tr}\left[\boldsymbol{\varepsilon}\right]\right\rangle_{+} \mathbf{I} + 2\mu\boldsymbol{\varepsilon}_{+}\right] + \lambda \left\langle \mathrm{tr}\left[\boldsymbol{\varepsilon}\right]\right\rangle_{-} \mathbf{I} + 2\mu\boldsymbol{\varepsilon}_{-}, \tag{3.59}$$

while the material stiffness tensor $\mathbb{C}$ is given by

$$\mathbb{C} = g\left(\phi\right)\left[\lambda\mathcal{H}\left[\mathrm{tr}\left[\boldsymbol{\varepsilon}\right]\right] + 2\mu\frac{\partial\boldsymbol{\varepsilon}^{+}}{\partial\boldsymbol{\varepsilon}}\right] + \lambda\mathcal{H}\left[-\mathrm{tr}\left[\boldsymbol{\varepsilon}\right]\right] + 2\mu\frac{\partial\boldsymbol{\varepsilon}^{-}}{\partial\boldsymbol{\varepsilon}}. \tag{3.60}$$

The second-order tensor $\frac{\partial\boldsymbol{\varepsilon}^{\pm}}{\partial\boldsymbol{\varepsilon}}$, which appears in the identity above, can be calculated by following the procedure presented in [238]

$$\frac{\partial\boldsymbol{\varepsilon}^{\pm}}{\partial\boldsymbol{\varepsilon}} = \sum_{a=1}^{n}\left[\mathcal{H}\left[\pm\lambda_a\right]\mathbf{M}_a \otimes \mathbf{M}_a + \left\langle\lambda_a\right\rangle_{\pm}\sum_{b\neq a}^{n}\frac{1}{2\left(\lambda_a - \lambda_b\right)}\left(\mathbb{G}_{ab} + \mathbb{G}_{ba}\right)\right], \tag{3.61}$$

where $\mathbb{G}_{ab}^{ijkl}$ and $\mathbb{G}_{ba}^{ijkl}$ are the fourth-order tensors that are obtained from projection matrices $\mathbf{M}_a$ and $\mathbf{M}_b$

$$\mathbb{G}_{ab}^{ijkl} = \mathbf{M}_a^{ik}\mathbf{M}_b^{jl} + \mathbf{M}_a^{il}\mathbf{M}_b^{jk}, \tag{3.62}$$

$$\mathbb{G}_{ba}^{ijkl} = \mathbf{M}_b^{ik}\mathbf{M}_a^{jl} + \mathbf{M}_b^{il}\mathbf{M}_a^{jk}. \tag{3.63}$$

While effective in preventing the formation and propagation of cracks during

compression, the decompositions discussed above encounter specific challenges with the so-called *crack boundary conditions* [239]. More advanced energy split has been proposed by Freddi and Royer-Carfagni [240] to model *no-tension masonry-like materials*. This approach selectively degrades only the energy associated with the positive-definite symmetric part of the small strain tensor. Wu et al. [241] proposed a similar split based on the effective stress tensor projection in energy norm thus alleviating some spurious behaviour of [240]. The directional split is presented in Steinke et al. [239], in which the Cauchy stress tensor is decomposed with respect to the crack orientation. Both spectral and volumetric-deviatoric energy decompositions will eventually lead to different crack paths and force-displacement diagrams when complex microstructural geometries are considered, as illustrated by Seleš et al. [242].

3.4. Phase-field for ductile fracture

The phase-field theory for brittle and quasi-brittle fracture has also been extended to describe fracture processes in ductile materials [157–163, 243]. Contributions [157–159, 243] have considered small strains, while in [160–163] ductile fracture under finite strain configuration was modelled. The common point of all contributions listed above is the additive decomposition of the body's bulk energy into an elastic and plastic part. Following this statement and expression (3.4), the internal part of the total energy functional is

$$\Pi^{\mathrm{int}} = \Pi^{\mathrm{b}} + \Pi^{\mathrm{s}} = \int_{\Omega\setminus\Gamma} \left[\psi_{\mathrm{e}}\left(\boldsymbol{\varepsilon}^{\mathrm{e}}\left(\mathbf{u}\right),\Gamma\right) + \psi_{\mathrm{p}}\left(\boldsymbol{\varepsilon}^{\mathrm{p}}\left(\mathbf{u}\right),\Gamma\right)\right] \mathrm{d}\Omega + \int_{\Gamma} G_{\mathrm{c}}\,\mathrm{d}\Gamma, \tag{3.64}$$

where ψ^{p} and $\boldsymbol{\varepsilon}^{\mathrm{p}}$ denote the plastic part of strain energy density and small strain tensor, respectively. Together with their elastic counterparts, they form total strain energy density and total small strain tensor, i.e.

$$\psi = \psi_{\mathrm{e}} + \psi_{\mathrm{p}}, \tag{3.65}$$

$$\boldsymbol{\varepsilon} = \boldsymbol{\varepsilon}^{\mathrm{e}} + \boldsymbol{\varepsilon}^{\mathrm{p}}. \tag{3.66}$$

When considering ductile fracture, material parameter G_{c} in Eq. (3.64) cannot be treated as a value of fracture toughness, as ductile fracture in contrast to brittle and quasi-brittle represents a more complex phenomenon.

When applying phase-field regularization to the internal part of the free energy functional (3.64), two different procedures are available. In the first approach, the

plastic part of the body's bulk energy is not affected by the phase-field crack growth and vice versa. This approach was adopted in [157, 161] and the internal part of the free energy functional was defined as

$$\Pi^{\text{int}} = \int_{\Omega} \left[g\left(\phi\right) \psi_{\text{e}}^{+}\left(\boldsymbol{\varepsilon}^{\text{e}}\right) + \psi_{\text{e}}^{-}\left(\boldsymbol{\varepsilon}^{\text{e}}\right) + \psi_{\text{p}}\left(\boldsymbol{\varepsilon}^{\text{p}}\right) \right] \, \mathrm{d}\Omega + \int_{\Omega} G_{\text{c}} \gamma\left(\phi; \nabla\phi\right) \, \mathrm{d}\Omega. \tag{3.67}$$

This first approach implies that only the positive part of the elastic strain energy density drives the phase-field crack evolution and the plastic part of the small strain tensor $\boldsymbol{\varepsilon}^{\text{p}}$ is not affected by the phase-field variable ϕ in any way. On the other hand, the second, and more often used, approach in the phase-field ductile fracture modelling, which is adopted in this dissertation, was proposed by Miehe et al. [244]. The second approach, in contrast to the first, relies on the plastic degradation function g^p to connect the crack phase-field and plastic part of stored energy functional, i.e.

$$\begin{aligned} \Pi^{\text{int}} = \int_{\Omega} \left[g\left(\phi\right) \psi_{\text{e}}^{+}\left(\boldsymbol{\varepsilon}^{\text{e}}\right) + \psi_{\text{e}}^{-}\left(\boldsymbol{\varepsilon}^{\text{e}}\right) \right] \, \mathrm{d}\Omega + \int_{\Omega} g^{\text{p}}\left(\phi\right) \psi_{\text{p}}\left(\boldsymbol{\varepsilon}^{\text{p}}\right) \, \mathrm{d}\Omega + \\ \int_{\Omega} G_{\text{c}} \gamma\left(\phi; \nabla\phi\right) \, \mathrm{d}\Omega. \end{aligned} \tag{3.68}$$

Generally, for both degradations functions, g and g^p, the same type of functions are adopted. In the resulting phase-field model for ductile fracture, the evolution of the crack phase-field is now affected by both parts of the strain energy density. For more details on the differences and advantages of these two different approaches see Alessi et al. [245].

In order to model the evolution of the plastic strain field and the plastic part of the strain energy density, in this dissertation, the plasticity model employing the von Mises yield criterion and non-linear isotropic hardening is utilized

$$f = \sqrt{\frac{3}{2} \mathbf{S}^{*} : \mathbf{S}^{*}} - \sigma_y\left(\varepsilon_{\text{eq}}^{\text{p}}\right) \leq 0. \tag{3.69}$$

In Eq. (3.69) f is the von Mises yield surface, $\mathbf{S}^{*}$ denotes the effective (non-degraded) deviatoric part of the Cauchy stress tensor, while σ_y stands for non-linear isotropic hardening law that is given by

$$\sigma_y\left(\varepsilon_{\text{eq}}^{\text{p}}\right) = \sigma_y^0 \left(1 + k\varepsilon_{\text{eq}}^{\text{p}}\right)^r, \tag{3.70}$$

where σ_y^0 is the initial yield strength, while k and r are material parameters. The equation given by (3.70) is also known as Swift's non-linear isotropic hardening law. The value of equivalent plastic strain $\varepsilon_{\text{eq}}^{\text{p}}$ is obtained directly from the plastic strain

tensor $\boldsymbol{\varepsilon}^{\mathrm{p}}$ as

$$\varepsilon_{\mathrm{eq}}^{\mathrm{p}} = \sqrt{\frac{2}{3}\boldsymbol{\varepsilon}^{\mathrm{p}} : \boldsymbol{\varepsilon}^{\mathrm{p}}}. \tag{3.71}$$

Last but not least, the plastic energy dissipation potential, i.e. plastic part of the strain energy density is obtained through

$$\psi_{\mathrm{p}}\left(\boldsymbol{\varepsilon}^{\mathrm{p}}\right) = \int_0^t \mathbf{S}^* : \boldsymbol{\varepsilon}^{\mathrm{p}} \, \mathrm{d}t. \tag{3.72}$$

When considering multiscale modelling of damage in heterogeneous materials, variables such as elastic/plastic strain energy density, equivalent plastic strain, Cauchy stress tensor and the material stiffness tensor need to be obtained directly from the microstructure of the heterogeneous material. In that way, each material point will receive homogenized (averaged) values of the aforementioned variables, which are required in the phase-field fracture algorithm. The procedure behind this is explained in detail in **Chapter 4**.

3.5. Numerical implementation

In general, numerical implementation of non-local continuum damage models is a relatively simple task, especially when considering mesh-based numerical methods such as FEM. This is because in the continuum, i.e. diffusive damage modelling approaches the non-local variable that controls the value of damage and therefore determines the crack topology, is obtained as part of the solution. In the case of FEM, in addition to displacement, the non-local variable is simply another degree of freedom for which the internal force vector and stiffness matrix need to be defined.

In the phase-field fracture model, this additional degree of freedom is the crack phase-field parameter ϕ - **Figure 3.5**. When considering orthotropic or anisotropic damage, scalar parameter ϕ will be replaced by the vector, i.e. second-order tensor. However, as stated in **subsection 1.3.2**, this dissertation will be focused on isotropic damage models in which the damage parameter is the scalar variable. Due to that fact, the number of DOF in each node of the finite element is increased by one. This also means that it is computationally less expensive to solve phase-field boundary value problem than it is displacement, as the partial differential equation that governs phase-field evolution is a scalar - not a vector equation.

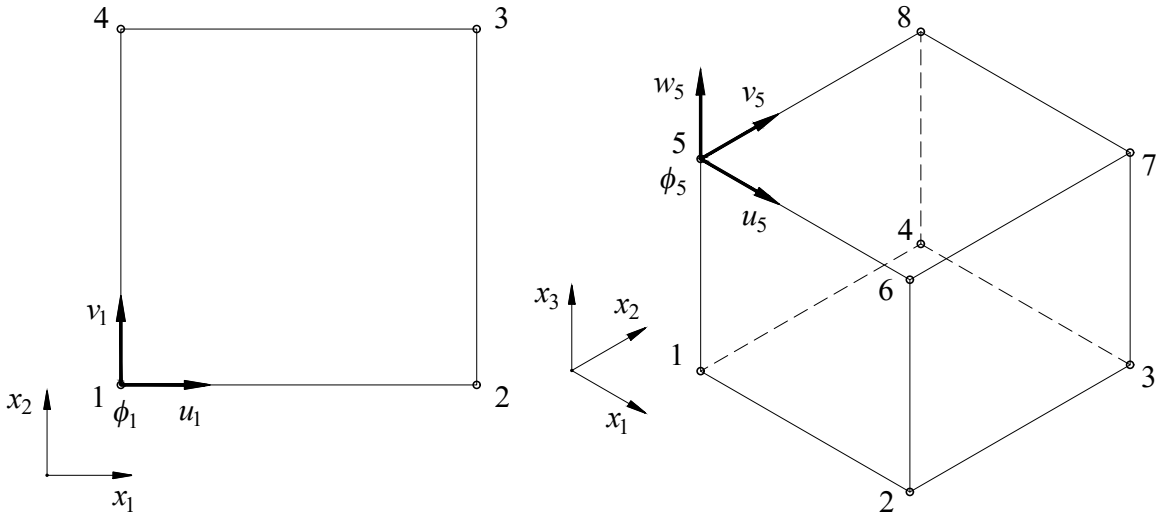

(a) Four node quadrilateral element **(b)** Eight node hexahedral element

Figure 3.5: Implementation of the phase-field variable ϕ into FEM

3.5.1. Fracture irreversibility

Before the actual implementation and finite element discretization, the principle of fracture irreversibility needs to be addressed. Namely, Eq. (3.4) and (3.64) by themselves do not ensure irreversibility condition, which represents the second law of thermodynamics demanding that the rate of dissipative fracture energy $\dot{\Pi}^s$ has to be non-negative value - $\dot{\Pi}^s \geq 0$. This ultimately implies that the crack surface Γ cannot decrease in size over time t, but can either grow or stay the same. This condition is not included in any equation and needs to be enforced subsequently.

In the phase-field fracture framework, the irreversibility condition is achieved by preventing the decrease of the crack phase-field parameter ϕ, i.e. $\dot{\phi} \geq 0$. However, there exist several different methods that can produce the desired outcome, each one with some side effect.

A direct way of introducing the irreversibility condition is by enforcing the monotonicity of the phase-field parameter through the variational inequality condition [135, 246], which unfortunately comes with additional computational cost. In [145, 185], a computationally more efficient method was utilized where the irreversibility condition was enforced through the use of a variational equality, which ensures the irreversibility condition only on the fully developed crack(s), while at the same time allowing the transition zone to heal. Penalized methods introduce irreversibility through penalty functions [187, 194]. In contrast, Miehe et al. [151] proposed an implicit way of incorporating the irreversibility condition that is based on the introduction of the

strain energy density history field $\mathscr{H}$, i.e.

$$\mathscr{H}(t) = \max_{\tau \in [0,t]} \left[\psi_{\mathrm{e}}^{+}(\boldsymbol{\varepsilon}^{\mathrm{e}}, t) + \psi_{\mathrm{p}}(\boldsymbol{\varepsilon}^{\mathrm{p}}, t) \right]. \tag{3.73}$$

By preventing a decrease in the positive part of strain energy density, the above expression ensures fracture irreversibility, as the history field variable $\mathscr{H}$ will never decline during the analysis. When considering ductile fracture, both plastic and the positive part of the strain energy density enter the condition (3.73). On the other hand, if brittle, i.e. quasi-brittle fracture is in question, the plastic part of the strain energy density is always equal to zero. Using this information, Eq. (3.28) is now rewritten in terms of $\mathscr{H}$

$$\mathscr{H}(t) \frac{\mathrm{d}g(\phi)}{\mathrm{d}\phi} + G_{\mathrm{c}} \left(\frac{\partial \gamma(\phi; \nabla\phi)}{\partial \phi} - \nabla \cdot \frac{\partial \gamma(\phi; \nabla\phi)}{\partial \nabla\phi} \right) = \mathbf{0}, \text{ in } \Omega. \tag{3.74}$$

Although it violates the full variational nature of the phase-field approach, the implicit method of enforcing the irreversibility condition is particularly attractive due to its simplicity and computational efficiency. It has been used in the majority of works on the topic of phase-field fracture modelling as well as in this dissertation.

3.5.2. Finite element discretization

Implementation of the phase-field fracture method into the finite element framework relies on domain discretization with finite elements, in whose nodes both displacement vector $\mathbf{v}$

$$\mathbf{v}^{\mathrm{T}} = \begin{bmatrix} u_1 & v_1 & w_1 & u_2 & v_2 & w_2 & \dots & u_p & v_p & w_p, \end{bmatrix} \tag{3.75}$$

and the phase-field vector $\boldsymbol{\phi}$

$$\boldsymbol{\phi}^{\mathrm{T}} = \begin{bmatrix} \phi_1 & \phi_2 & \dots & \phi_p \end{bmatrix} \tag{3.76}$$

are located. In Eq. (3.75) u, v and w are displacements in x, y and z direction of a local coordinate system, respectively, while index p, which occurs in the identities above, defines the total number of nodes that are present in the finite element.

In the 3D finite element framework, both displacement vector $\mathbf{u}$ and the scalar phase-field variable ϕ are expressed using matrices of shape functions

$$\mathbf{u} = \mathbf{N}_{\mathbf{v}}\, \mathbf{v}, \tag{3.77}$$

$$\phi = \mathbf{N}_{\boldsymbol{\phi}}\, \boldsymbol{\phi}, \tag{3.78}$$

where for both $\mathbf{N}_{\mathbf{v}}$ and $\mathbf{N}_{\boldsymbol{\phi}}$ same shape functions N_i are used

$$\mathbf{N}_{\mathbf{v}} = \begin{bmatrix} N_1 & 0 & 0 & N_2 & 0 & 0 & ... & N_p & 0 & 0 \\ 0 & N_1 & 0 & 0 & N_2 & 0 & ... & 0 & N_p & 0 \\ 0 & 0 & N_1 & 0 & 0 & N_2 & ... & 0 & 0 & N_p \end{bmatrix}, \tag{3.79}$$

$$\mathbf{N}_{\boldsymbol{\phi}} = \begin{bmatrix} N_1 & N_2 & ... & N_p \end{bmatrix}. \tag{3.80}$$

Notice that the dimension of $\mathbf{N}_{\mathbf{v}}$ is completely different from $\mathbf{N}_{\boldsymbol{\phi}}$ as the former is used to describe the vector of displacement $\mathbf{u}$, while the latter ensures the description of the scalar variable ϕ. Besides the displacement vector $\mathbf{u}$ and the crack phase-field parameter ϕ, Eq. (3.25) also demands interpolation of the small strain tensor $\boldsymbol{\varepsilon}$ and the gradient of crack phase-field $\nabla\phi$. This is performed using matrices of shape functions derivatives $\mathbf{B}_{\mathbf{v}}$ and $\mathbf{B}_{\boldsymbol{\phi}}$

$$\mathbf{B}_{\mathbf{v}} = \begin{bmatrix} N_{1,1} & 0 & 0 & N_{2,1} & 0 & 0 & ... & N_{p,1} & 0 & 0 \\ 0 & N_{1,2} & 0 & 0 & N_{2,2} & 0 & ... & 0 & N_{p,2} & 0 \\ 0 & 0 & N_{1,3} & 0 & 0 & N_{2,3} & ... & 0 & 0 & N_{p,3} \\ N_{1,2} & N_{1,1} & 0 & N_{2,2} & N_{2,1} & 0 & ... & N_{p,2} & N_{p,1} & 0 \\ N_{1,3} & 0 & N_{1,1} & N_{2,3} & 0 & N_{2,1} & ... & N_{p,3} & 0 & N_{p,1} \\ 0 & N_{1,3} & N_{1,2} & 0 & N_{2,3} & N_{2,2} & ... & 0 & N_{p,3} & N_{p,2} \end{bmatrix}, \tag{3.81}$$

$$\mathbf{B}_{\boldsymbol{\phi}} = \begin{bmatrix} N_{1,1} & N_{2,1} & ... & N_{p,1} \\ N_{1,2} & N_{2,2} & ... & N_{p,2} \\ N_{1,3} & N_{2,3} & ... & N_{p,3} \end{bmatrix} \tag{3.82}$$

Small strain tensor $\boldsymbol{\varepsilon}$ is now expressed as

$$\boldsymbol{\varepsilon} = \mathbf{B}_{\mathbf{v}}\, \mathbf{v}, \tag{3.83}$$

while the gradient of phase-field $\nabla\phi$ is equal to

$$\nabla\phi = \mathbf{B}_{\boldsymbol{\phi}}\, \boldsymbol{\phi}. \tag{3.84}$$

Notice that $\boldsymbol{\varepsilon}$ in (3.83) needs to be written as a vector, i.e.

$$\boldsymbol{\varepsilon}^{\mathrm{T}} = \begin{bmatrix} \varepsilon_x & \varepsilon_y & \varepsilon_z & \gamma_{xy} & \gamma_{xz} & \gamma_{yz} \end{bmatrix}. \tag{3.85}$$

This notation is also required for the degraded Cauchy stress tensor $\boldsymbol{\sigma}$

$$\boldsymbol{\sigma}^{\mathrm{T}} = \begin{bmatrix} \sigma_x & \sigma_y & \sigma_z & \tau_{xy} & \tau_{xz} & \tau_{yz}. \end{bmatrix} \tag{3.86}$$

Now, substituting (3.77), (3.78), (3.83) and (3.84) into (3.15) and (3.16), and with the use of identity (3.73), the variation of the total energy functional is equal to

$$\begin{gathered} \delta\Pi = \int_{\Omega} \boldsymbol{\sigma}^{\mathrm{T}}\, \delta\left(\mathbf{B}_{\mathbf{v}}\, \mathbf{v}\right)\, \mathrm{d}\Omega + \int_{\Omega} \mathscr{H}\left(t\right) \frac{\mathrm{d}g\left(\phi\right)}{\mathrm{d}\phi} \delta\left(\mathbf{N}_{\boldsymbol{\phi}}\, \boldsymbol{\phi}\right)\, \mathrm{d}\Omega + \\ \int_{\Omega} G_{\mathrm{c}} \left[\frac{\mathbf{N}_{\boldsymbol{\phi}}\, \boldsymbol{\phi}}{l} \delta\left(\mathbf{N}_{\boldsymbol{\phi}}\, \boldsymbol{\phi}\right) + l\left(\mathbf{B}_{\boldsymbol{\phi}}\, \boldsymbol{\phi}\right)^{\mathrm{T}}\, \mathbf{B}_{\boldsymbol{\phi}}\, \delta\boldsymbol{\phi} \right] \mathrm{d}\Omega - \int_{\Omega} \delta\left(\mathbf{N}_{\mathbf{v}}\, \mathbf{v}\right)^{\mathrm{T}}\, \mathbf{b}\, \mathrm{d}\Omega - \\ \int_{\partial\Omega} \delta\left(\mathbf{N}_{\mathbf{v}}\, \mathbf{v}\right)^{\mathrm{T}}\, \mathbf{h}\, \mathrm{d}\partial\Omega, \end{gathered} \tag{3.87}$$

which in simple terms represents balance of internal and external forcers

$$\delta\mathbf{v}^{\mathrm{T}} \left(\mathbf{f}_{\mathbf{v}}^{\mathrm{int}} - \mathbf{f}_{\mathbf{v}}^{\mathrm{ext}}\right) + \delta\boldsymbol{\phi}^{\mathrm{T}} \left(\mathbf{f}_{\boldsymbol{\phi}}^{\mathrm{int}} - \mathbf{f}_{\boldsymbol{\phi}}^{\mathrm{ext}}\right) = 0. \tag{3.88}$$

In Eq. (3.88) $\mathbf{f}_{\mathbf{v}}^{\mathrm{int}}$ and $\mathbf{f}_{\boldsymbol{\phi}}^{\mathrm{int}}$ correspond to the local internal force vectors associated with the discretized displacement and phase-field, respectively, as follows

$$\mathbf{f}_{\mathbf{v}}^{\mathrm{int}} = \int_{\Omega} \mathbf{B}_{\mathbf{v}}^{\mathrm{T}}\, \boldsymbol{\sigma}\, \mathrm{d}\Omega, \tag{3.89}$$

$$\mathbf{f}_{\boldsymbol{\phi}}^{\mathrm{int}} = \int_{\Omega} \left[\mathscr{H}\left(t\right) \frac{\mathrm{d}g\left(\phi\right)}{\mathrm{d}\phi} \mathbf{N}_{\boldsymbol{\phi}}^{\mathrm{T}} + G_{\mathrm{c}} \left(\frac{\phi}{l} \mathbf{N}_{\boldsymbol{\phi}}^{\mathrm{T}} + l\, \mathbf{B}_{\boldsymbol{\phi}}^{\mathrm{T}}\, \mathbf{B}_{\boldsymbol{\phi}}\, \boldsymbol{\phi} \right) \right] \mathrm{d}\Omega, \tag{3.90}$$

while $\mathbf{f}_{\mathbf{v}}^{\mathrm{ext}}$ and $\mathbf{f}_{\boldsymbol{\phi}}^{\mathrm{ext}}$ denote local external force vectors for the displacement and the crack phase-field, respectively

$$\mathbf{f}_{\mathbf{v}}^{\mathrm{ext}} = \int_{\Omega} \mathbf{N}_{\mathbf{v}}^{\mathrm{T}}\, \mathbf{b}\, \mathrm{d}\Omega + \int_{\partial\Omega} \mathbf{N}_{\mathbf{v}}^{\mathrm{T}}\, \mathbf{h}\, \mathrm{d}\partial\Omega, \tag{3.91}$$

$$\mathbf{f}_{\boldsymbol{\phi}}^{\mathrm{ext}} = \mathbf{0}. \tag{3.92}$$

Local residual vectors $\mathbf{r}_{\mathbf{v}}$ and $\mathbf{r}_{\boldsymbol{\phi}}$ are now obtained through

$$\mathbf{r}_{\mathbf{v}} = \mathbf{f}_{\mathbf{v}}^{\mathrm{int}} - \mathbf{f}_{\mathbf{v}}^{\mathrm{ext}} = \int_{\Omega} \mathbf{B}_{\mathbf{v}}^{\mathrm{T}}\, \boldsymbol{\sigma}\, \mathrm{d}\Omega - \int_{\Omega} \mathbf{N}_{\mathbf{v}}^{\mathrm{T}}\, \mathbf{b}\, \mathrm{d}\Omega - \int_{\partial\Omega} \mathbf{N}_{\mathbf{v}}^{\mathrm{T}}\, \mathbf{h}\, \mathrm{d}\partial\Omega, \tag{3.93}$$

$$\mathbf{r}_{\boldsymbol{\phi}} = \mathbf{f}_{\boldsymbol{\phi}}^{\mathrm{int}} - \mathbf{f}_{\boldsymbol{\phi}}^{\mathrm{ext}} = \int_{\Omega} \left[\mathbf{N}_{\boldsymbol{\phi}}^{\mathrm{T}} \left(\mathscr{H}\left(t\right) \frac{\mathrm{d}g\left(\phi\right)}{\mathrm{d}\phi} + \frac{G_{\mathrm{c}}}{l} \phi \right) + G_{\mathrm{c}}\, l\, \mathbf{B}_{\boldsymbol{\phi}}^{\mathrm{T}}\, \mathbf{B}_{\boldsymbol{\phi}}\, \boldsymbol{\phi} \right] \mathrm{d}\Omega. \tag{3.94}$$

Finally, using local residual vectors $\mathbf{r}_{\mathbf{v}}$ and $\mathbf{r}_{\boldsymbol{\phi}}$, local stiffness matrices $\mathbf{k}_{\mathbf{v}\,\mathbf{v}}$, $\mathbf{k}_{\mathbf{v}\,\boldsymbol{\phi}}$, $\mathbf{k}_{\boldsymbol{\phi}\,\mathbf{v}}$

and $\mathbf{k}_{\boldsymbol{\phi}\,\boldsymbol{\phi}}$ are given by

$$\mathbf{k}_{\mathbf{v}\,\mathbf{v}} = \frac{\partial \mathbf{r}_{\mathbf{v}}}{\partial \mathbf{v}} = \int_{\Omega} \mathbf{B}_{\mathbf{v}}^{\mathrm{T}}\, \mathbf{C}\, \mathbf{B}_{\mathrm{v}}\, \mathrm{d}\Omega, \tag{3.95}$$

$$\mathbf{k}_{\mathbf{v}\,\boldsymbol{\phi}} = \frac{\partial \mathbf{r}_{\mathbf{v}}}{\partial \boldsymbol{\phi}} = \int_{\Omega} \frac{\mathrm{d}g\left(\phi\right)}{\mathrm{d}\phi}\, \mathbf{B}_{\mathbf{v}}^{\mathrm{T}}\, \boldsymbol{\sigma}\, \mathbf{N}_{\boldsymbol{\phi}}\, \mathrm{d}\Omega, \tag{3.96}$$

$$\mathbf{k}_{\boldsymbol{\phi}\,\mathbf{v}} = \frac{\partial \mathbf{r}_{\boldsymbol{\phi}}}{\partial \mathbf{v}} = \int_{\Omega} \frac{\mathrm{d}g\left(\phi\right)}{\mathrm{d}\phi}\, \mathbf{N}_{\boldsymbol{\phi}}^{\mathrm{T}}\, \boldsymbol{\sigma}^{\mathrm{T}}\, \mathbf{B}_{\mathbf{v}}\, \mathrm{d}\Omega, \tag{3.97}$$

$$\mathbf{k}_{\boldsymbol{\phi}\,\boldsymbol{\phi}} = \frac{\partial \mathbf{r}_{\boldsymbol{\phi}}}{\partial \boldsymbol{\phi}} = \int_{\Omega} \left[G_{\mathrm{c}}\, l\, \mathbf{B}_{\boldsymbol{\phi}}^{\mathrm{T}}\, \mathbf{B}_{\boldsymbol{\phi}} + \mathbf{N}_{\boldsymbol{\phi}}^{\mathrm{T}}\, \mathbf{N}_{\boldsymbol{\phi}} \left(\frac{G_{\mathrm{c}}}{l} + \mathscr{H}\left(t\right) \frac{\mathrm{d}^2 g\left(\phi\right)}{\mathrm{d}\phi^2} \right) \right] \mathrm{d}\Omega. \tag{3.98}$$

Identities (3.93)-(3.98) participate in the formation of a linear system of equations. In Eq. (3.95), $\mathbf{C}$ is the degraded material stiffness matrix written in Voigt notation. Despite the introduction of one additional degree of freedom, all matrices defined by integrals (3.95)-(3.98) are symmetric, which will ultimately result in a symmetric system of equations. As stated in **subsection 1.3.3**, there are two essential algorithms through which the solution of the displacement and the crack phase-field can be obtained - monolithic and staggered.

3.5.3. Monolithic solvers

In a monolithic phase-field algorithm, the system of equations is fully coupled, i.e. values of both displacement and the crack phase-field are obtained simultaneously as part of one solution. The value of the global displacement vector $\mathbf{V}$ and global phase-field vector $\boldsymbol{\Phi}$, at the increment n and for iteration $i+1$, is obtained as

$$\begin{bmatrix} \mathbf{V} \\ \boldsymbol{\Phi} \end{bmatrix}_{n}^{i+1} = \begin{bmatrix} \mathbf{V} \\ \boldsymbol{\Phi} \end{bmatrix}_{n}^{i} - \begin{bmatrix} \mathbf{K}_{\mathbf{V}\,\mathbf{V}} & \mathbf{K}_{\mathbf{V}\,\boldsymbol{\Phi}} \\ \mathbf{K}_{\boldsymbol{\Phi}\,\mathbf{V}} & \mathbf{K}_{\boldsymbol{\Phi}\,\boldsymbol{\Phi}} \end{bmatrix}_{n}^{i-1} \begin{bmatrix} \mathbf{R}_{\mathbf{V}} \\ \mathbf{R}_{\boldsymbol{\Phi}} \end{bmatrix}_{n}^{i}, \tag{3.99}$$

where $\mathbf{K}_{\mathbf{V}\,\mathbf{V}}$, $\mathbf{K}_{\mathbf{V}\,\boldsymbol{\Phi}}$, $\mathbf{K}_{\boldsymbol{\Phi}\,\mathbf{V}}$ and $\mathbf{K}_{\boldsymbol{\Phi}\,\boldsymbol{\Phi}}$ denote global stiffness matrices, while $\mathbf{R}_{\mathbf{V}}$ and $\mathbf{R}_{\boldsymbol{\Phi}}$ represent global residual vectors.

However, as stated in **subsection 1.3.3**, due to the non-convexity of the free energy functional Π, monolithic solvers can exhibit significant convergence issues, especially during the process of crack propagation. There are some procedures that are able to mitigate this problem [185–188]; however, they are dependent on the type of loading and do not guarantee successful convergence of the analysis. Moreover, the fact that in this dissertation the values of the strain energy density, Cauchy stress tensor, equivalent plastic strain and the material stiffness tensor are computed from

heterogeneous microstructure, puts additional pressure on the algorithm's stability. Due to these reasons, monolithic solver won't be used in this dissertation.

3.5.4. Staggered solvers

Unlike monolithic solvers, staggered algorithms rely on the observation that, while the free energy functional Π is generally non-convex, it is convex with respect to either displacement or the phase-field variable, if the other one is held constant [145]. Through this property, the coupled system (3.99) is written in the following form

$$\begin{bmatrix} \mathbf{V} \\ \mathbf{\Phi} \end{bmatrix}_n^{i+1} = \begin{bmatrix} \mathbf{V} \\ \mathbf{\Phi} \end{bmatrix}_n^{i} - \begin{bmatrix} \mathbf{K}_{\mathbf{V}\,\mathbf{V}} & \mathbf{0} \\ \mathbf{0} & \mathbf{K}_{\mathbf{\Phi}\,\mathbf{\Phi}} \end{bmatrix}_n^{i^{-1}} \begin{bmatrix} \mathbf{R}_{\mathbf{V}} \\ \mathbf{R}_{\mathbf{\Phi}} \end{bmatrix}_n^{i} . \tag{3.100}$$

The decoupled system (3.100) implies that the displacement and crack phase-field are solved independently one from another. This ensures stable convergence as both equations are ultimately derived from the convex functional. By comparing (3.100) and (3.99) it can be concluded that the staggered algorithms are computationally more efficient, as there is no reason for the calculation of global stiffness matrices $\mathbf{K}_{\mathbf{V}\,\mathbf{\Phi}}$ and $\mathbf{K}_{\mathbf{\Phi}\,\mathbf{V}}$.

The general idea in staggered solvers is to solve the decoupled system (3.100) at time t and iteration i by first computing one field using the other field's solution computed in iteration i. Then, the obtained solution is used to solve the other field at the iteration $i+1$. This procedure repeats until the defined stopping criterion is met. This is schematically depicted in **Box II**.

Box II: General phase-field staggered solution scheme

1. Start new increment n: $n = n + 1$.
2. Newton iterations for load increment n: set iteration $i = 0$.
   (a) Start new iteration i: $i = i + 1$.
   (b) Loop over first layer of elements: **Displacement equation**.
   (c) Use (3.100) and obtain new value of global displacement vector as: $\mathbf{V}_n^{i+1} = \mathbf{V}_n^i - \mathbf{K}_{\mathbf{V}\mathbf{V}}(\mathbf{\Phi}_n^i, \mathbf{V}_n^i)\,\mathbf{R}_{\mathbf{V}}(\mathbf{\Phi}_n^i, \mathbf{V}_n^i)$.
   (d) Loop over second layer of elements: **Phase-field equation**.
   (e) Use (3.100) and obtain new value of global phase-field vector as: $\mathbf{\Phi}_n^{i+1} = \mathbf{\Phi}_n^i - \mathbf{K}_{\phi\phi}(\mathbf{\Phi}_n^i, \mathbf{V}_n^{i+1})\,\mathbf{R}_{\mathbf{\Phi}}(\mathbf{\Phi}_n^i, \mathbf{V}_n^{i+1})$.
   (f) Check the stopping criterion. If not met: go to 2 (a).
3. If analysis not complete: go to 1.

The efficiency and convergence rate of staggered algorithms depends on the stopping criterion, which differs between the implementations as discussed in **subsection 1.3.3**. In this dissertation, the staggered phase-field algorithm presented by Lesičar et al. [183] is used. In that contribution, the stopping criterion is defined as the relative change between values of the global phase-field vector between two iterations - i and $i + 1$

$$\frac{||\mathbf{\Phi}_n^{i+1}|| - ||\mathbf{\Phi}_n^i||}{||\mathbf{\Phi}_n^i||} \leq \varepsilon, \tag{3.101}$$

where ε is a scalar value defined at the beginning of the analysis. The algorithm was thoroughly tested and verified on several different benchmark examples. Its computational efficiency was shown to be higher than the algorithm presented in Seleš et al. [190]. Due to that fact, this chapter won't include any numerical examples.

4. Multiscale modelling of damage

4.1. Background

Numerical modelling of material fracture requires the incorporation of the multiscale approach since fracture in any material is highly sensitive to the microstructure that forms it. A material's microstructure can consist of voids or inclusions that can exhibit different shape, spatial distribution and volume fraction. Ultimately, the microstructure's spatial and material configuration will lead to a non-uniform stress and strain state, which will create areas suitable for the occurrence and development of damage. Multiscale modelling has the ability to couple the microstructural stress state with the macroscopic calculation to capture the effect of behaviour of the microstructure in a macroscopic calculation - see **Figure 1.2**

Unlike the stress tensor and some other values that are connected to it, such as strain energy density or material stiffness tensor, for which there exists a clear procedure for calculating their average (macroscopic) values, the clear and unique procedure for acquiring the macroscopic value of damage is still not defined. The classical first-order computational homogenization is not suitable, as it will produce results that highly underestimate the true value of the overall damage. Also, during the period of damage accumulation, the representativeness of the RVE may come into question and the PBC start to lose their meaning. Moreover, the utilization of any damage algorithm on the complex geometry of the RVE will be numerically quite intense and will lead to stability issues.

Besides physical aspects, the computational cost of the multiscale damage models is another obstacle that needs to be overcome. As stated in **subsection 1.2.1**, a concurrent multiscale procedure that tackles the RVE boundary value problem either through FEM or FFT-based numerical solver will experience tremendous computational costs. This will be even more elevated if damage comes into the equation.

An additional condition that needs to be satisfied is the finite element mesh independence at the macrolevel. Concurrent multiscale approaches can be performed

using either discontinuous (discrete) or continuous (diffusive) damage approach at the macrolevel. If the former is applied, a specific remeshing algorithm or XFEM will have to be utilized in order to avoid dependence of final results on the mesh size and element orientation. On top of that, as stated in **subsection 1.3.1**, an additional criterion will be needed in order to address questions about the crack's topology. On the other hand, if the latter is used, some form of non-locality has to be introduced at the macrolevel, otherwise, a pathological mesh dependence will prevail.

Most of the issues mentioned above were addressed in [67, 82] through the utilization of SCA at the microlevel, a new three-step homogenization scheme and a non-local formulation at the macrolevel. Significantly reducing the computational complexity, while at the same time retaining a noticeable level of accuracy, the use of the SCA (which is valid for any type of constitutive law) managed to resolve problems of concurrent multiscale computational complexity. A second, quite important part of the contributions [67, 82], is the so-called *three-step homogenization scheme*, where the evolution of damage and plastic deformations at the microlevel is decoupled. This innovation managed to provide an additional level of stability and ensured physical values of the macroscopic damage parameter. Last but not least, a non-local formulation at the macrolevel, which introduced a length parameter and a non-local equivalent plastic strain, cured the pathological mesh dependence.

However, the procedure presented in [67, 82] has two major flaws: (1) it requires running DNS simulations in order to perform energy regularization, and (2) it is applicable only to problems where energy dissipated by plasticity is relatively low. The first issue occurs due to the discretization of the RVE with a relatively small number of material clusters. More precisely, when SCA is coupled with damage calculation at the microlevel, its accuracy, i.e. deviation of final results from the results obtained by the DNS is quite significant. The only way to mitigate this issue is by performing several DNS simulations whose results are then used to adjust fracture parameters for the SCA analysis so that energy regularization can be adequately performed. The second issue is related to the derivation of the energy regularization, in which, for the ease of derivation itself, the material's fracture toughness was approximated using its fracture energy. An assumption only valid when the energy dissipated by fracture is mainly dominated by its elastic - not plastic part.

In order to bring the concurrent multiscale damage modelling one step closer to commercial use, in the following pages a new procedure, that addresses the major issues listed above is presented. This chapter ultimately represents the synergy of the self-consistent clustering analysis and the phase-field fracture formulation into one algorithm that combines the best features of both methods.

4.2. Proposed multiscale damage model

Resolving all issues that plague multiscale modelling of strain softening of heterogeneous materials is no easy task, as fixing one issue can open or create another one. Both SCA and phase-field method have specific roles in the proposed multiscale damage model. The function of the SCA at the microlevel is to:

- Ensure computational efficiency by performing fast and accurate calculation of the RVE boundary value problem.
- Link two scales by performing first-order computational homogenization on the Cauchy stress tensor, stiffness tensor, strain energy density and plastic part of the small strain tensor.
- Provide a straightforward extension to any type of constitutive law for a given material phase.
- Enable concurrent multiscale approach with complex microstructures consisting of multiple material phases.

The function of the phase-field method at the macrolevel is to:

- Cure pathological mesh dependence of the final results.
- Enable efficient and robust calculation of the fracture processes.
- Provide additional stability by being present at the macrolevel instead of the microlevel.
- Ensure physical and objective results by being present at the macrolevel instead of the microlevel.

The computational setup is complete and the algorithm of the proposed concurrent approach is summarized in **Box III**.

It should be noted that the proposed procedure requires both G_c and l to be known *a priori*, since the damage calculation is done at the macrolevel and therefore they cannot be calculated at the microlevel. Herein, both G_c and l are treated as the macroscopic properties of the heterogeneous microstructure whose values are already defined.

Box III: Concurrent multiscale damage algorithm for the increment n

1. Start increment n: with new iteration i: $i = i + 1$.
2. For increment n and iteration i go to first layer of elements: **Displacement equation.**
   (a) Increase current element number e: $e = e + 1$.
   (b) For element e obtain local displacement vector $\mathbf{v}$.
      i. Increase current integration point number j: $j = j + 1$.
      ii. For integration point j calculate macroscopic strain $\overline{\boldsymbol{\varepsilon}}$: $\overline{\boldsymbol{\varepsilon}} = \mathbf{B}_{\mathbf{v}}\,\mathbf{v}$.
      iii. Send $\overline{\boldsymbol{\varepsilon}}$ to microscale.
      iv. call the SCA - use **Box I** to solve the RVE boundary value problem.
      v. obtain macroscopic values of the Cauchy stress tensor $\overline{\boldsymbol{\sigma}}$, stiffness tensor $\overline{\mathbf{C}}$, strain energy density $\overline{\psi}$, elastic part of the strain energy density $\overline{\psi}_{\mathrm{e}}$ and plastic part of the strain energy density $\overline{\psi}_{\mathrm{p}}$.
      vi. Perform spectral or volumetric-deviatoric split if needed.
      vii. Store macroscopic values that will be needed in phase-field analysis.
      viii. If j equal to the total number of integration points: go to 3 (a).
   (c) If e equal to the total number of elements: go to 4.
3. Calculate new value of global displacement vector $\mathbf{V}_n^{i+1}$:
   $\mathbf{V}_n^{i+1} = \mathbf{V}_n^i - \mathbf{K}_{\mathbf{V}\,\mathbf{V}}\,(\boldsymbol{\Phi}_n^i,\, \mathbf{V}_n^i)\,\mathbf{R}_{\mathbf{V}}\,(\boldsymbol{\Phi}_n^i,\, \mathbf{V}_n^i)$.
4. For increment n and iteration i go to second layer of elements: **Phase-field equation.**
5. Calculate new value of global phase-field vector $\boldsymbol{\Phi}_n^{i+1}$:
   $\boldsymbol{\Phi}_n^{i+1} = \boldsymbol{\Phi}_n^i - \mathbf{K}_{\boldsymbol{\phi}\,\boldsymbol{\phi}}\,(\boldsymbol{\Phi}_n^i,\, \mathbf{V}_n^{i+1})\,\mathbf{R}_{\boldsymbol{\Phi}}\,(\boldsymbol{\Phi}_n^i,\, \mathbf{V}_n^{i+1})$.
6. Check the stopping criterion: $\frac{||\boldsymbol{\Phi}_n^{i+1}|| - ||\boldsymbol{\Phi}_n^i||}{||\boldsymbol{\Phi}_n^i||} \leq \varepsilon$. If not met: go to 1.

4.2.1. Test specimens

In order to assess the accuracy, robustness and overall computational efficiency, the proposed concurrent procedure will undergo detailed and thorough testing. For that purpose, a significant number of test specimens with different geometries and loading

conditions are generated, and are depicted in **Figure 4.1-4.7**, with all dimensions being given in millimeters.

Many of the depicted specimens are frequently used for qualitative testing of phase-field fracture algorithms and a reference is given for each one of them. All test specimens will be present in 2D plane strain examples; however, some specimens include only brittle, i.e. ductile fracture, while specimens depicted in **Figure 4.5** and **4.6** are present in both brittle and ductile fracture under 2D plane strain conditions. Moreover, some test specimens are extruded in the third dimension for the purposes of a 3D concurrent analysis, more precisely specimens in **Figure 4.1(a)**, **4.3**, **4.4**, **4.6** and **4.7**. Information on which specimens are used in which analysis, what are the values of the specimen's thicknesses in the third dimension and what are the values of prescribed displacements is presented in **Table 4.1**.

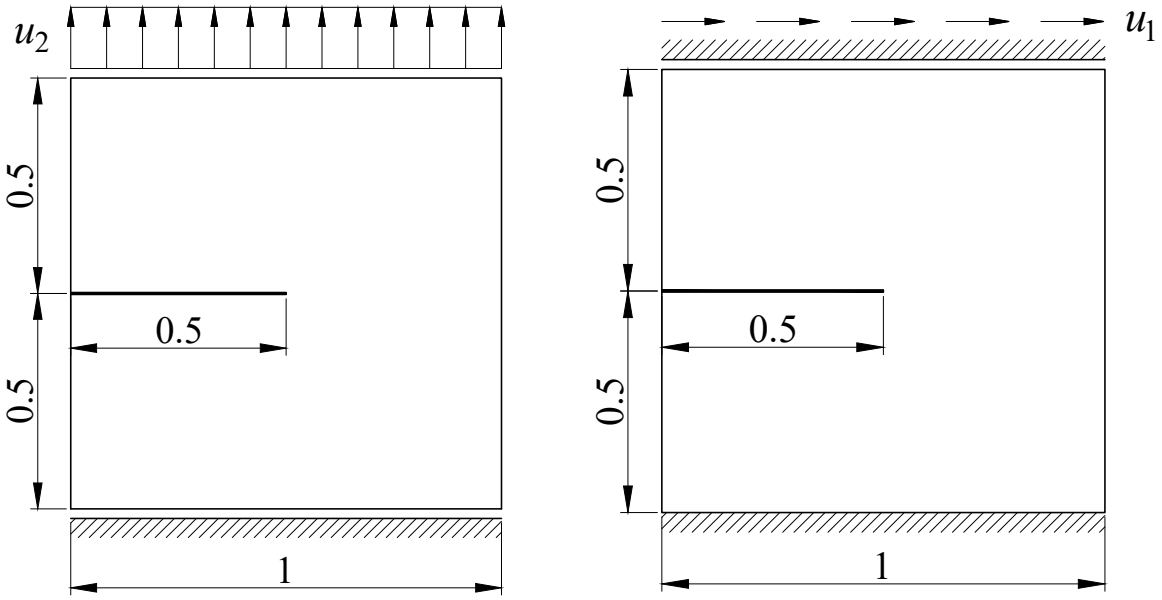

(a) Tension test [243] **(b)** Shear test [243]

Figure 4.1: Single-edge notched plate

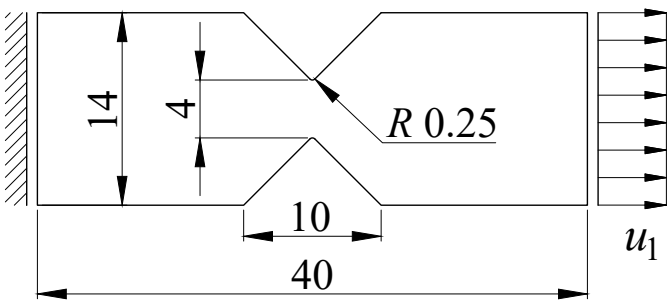

Figure 4.2: V-notch bar [243]

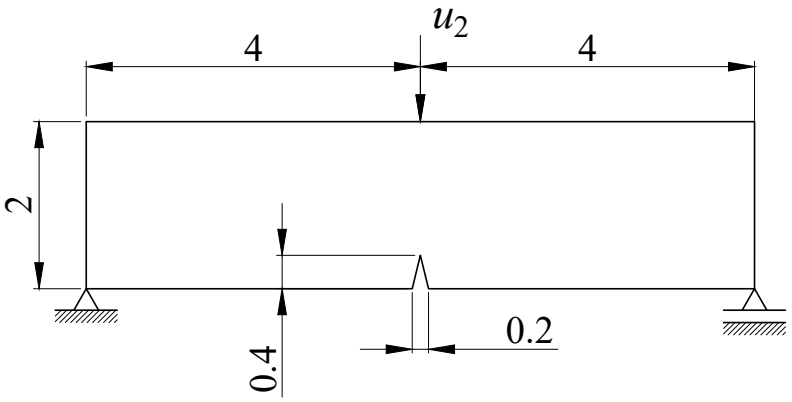

Figure 4.3: Three-point bending specimen [153]

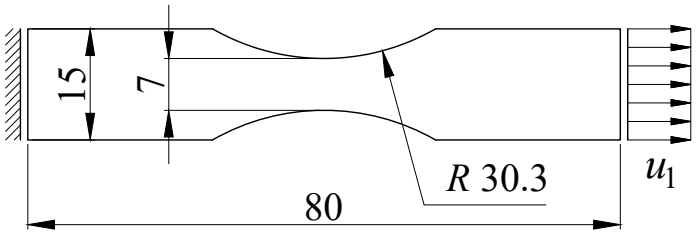

Figure 4.4: Unnotched specimen [247]

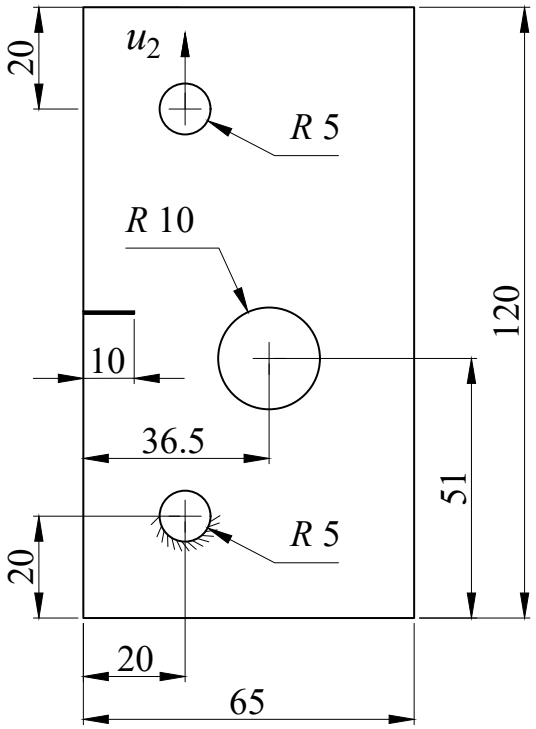

Figure 4.5: Notched plate with a hole [153]

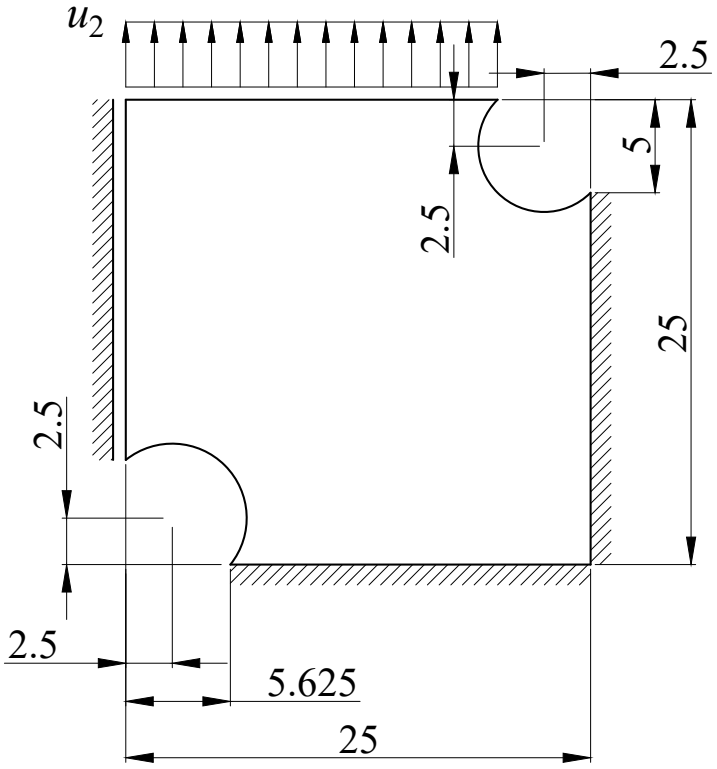

Figure 4.6: Double-notched specimen [82]

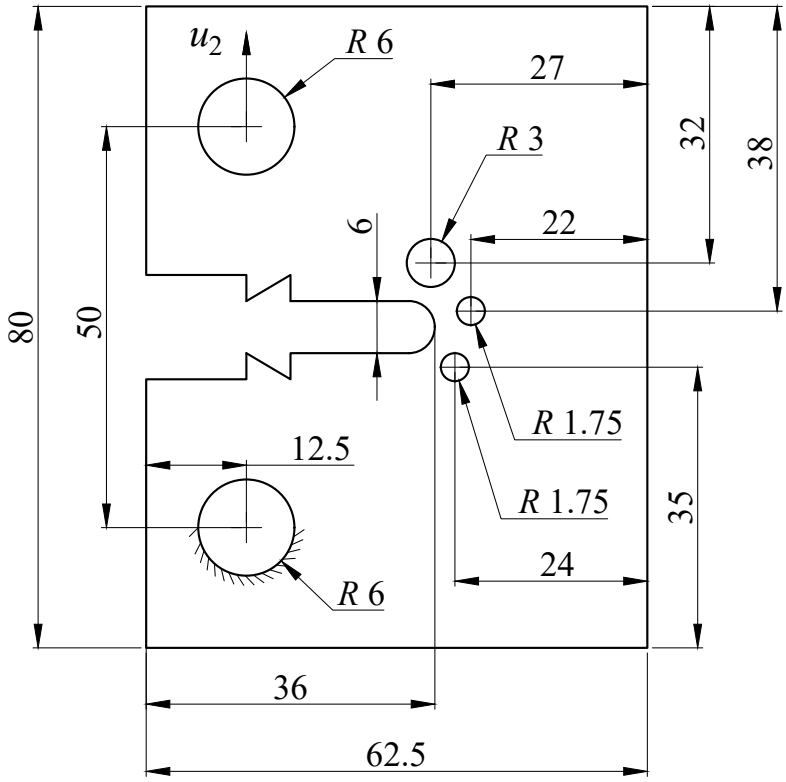

Figure 4.7: Sandia fracture challenge specimen [161]

Table 4.1: Informations about the test specimens

Single-edge notched plate - tension test				
Fracture analyses	2D brittle	2D ductile	3D brittle	3D ductile
Displacement, mm	$u_2 = 0.006$	Not performed	$u_2 = 0.0066$	Not performed
Thickness, mm	0.1			
Single-edge notched plate - shear test				
Fracture analyses	2D brittle	2D ductile	3D brittle	3D ductile
Displacement, mm	$u_1 = 0.014$	Not performed	Not performed	Not performed
Thickness, mm	Not used in 3D			
V-notch bar				
Fracture analyses	2D brittle	2D ductile	3D brittle	3D ductile
Displacement, mm	Not performed	$u_1 = 1.5$	Not performed	Not performed
Thickness, mm	Not used in 3D			
Three-point bending specimen				
Fracture analyses	2D brittle	2D ductile	3D brittle	3D ductile
Displacement, mm	$u_2 = 0.1$	Not performed	$u_2 = 0.07$	Not performed
Thickness, mm	1			
Unnotched specimen				
Fracture analyses	2D brittle	2D ductile	3D brittle	3D ductile
Displacement, mm	Not performed	$u_1 = 1.5$	Not performed	$u_1 = 2$
Thickness, mm	2.5			
Notched plate with a hole				
Fracture analyses	2D brittle	2D ductile	3D brittle	3D ductile
Displacement, mm	$u_2 = 0.45$	$u_2 = 0.75$	Not performed	Not performed
Thickness, mm	Not used in 3D			
Double-notched specimen				
Fracture analyses	2D brittle	2D ductile	3D brittle	3D ductile
Displacement, mm	$u_2 = 0.038$	$u_2 = 1.5$	$u_2 = 0.038$	$u_2 = 2$
Thickness, mm	10			
Sandia fracture challenge specimen				
Fracture analyses	2D brittle	2D ductile	3D brittle	3D ductile
Displacement, mm	Not performed	$u_2 = 7.5$	Not performed	$u_2 = 6$
Thickness, mm	2			

As can be seen from **Table 4.1**, all test specimens are loaded by enforcing displacement on specific points, i.e. by utilizing displacement-controlled boundary conditions. Because of that, the classical Newton-Raphson algorithm will be sufficient for all specimens and under any type of analysis. Also, it is important to note that in the case of three-dimensional analyses, the thickness of the specimen is taken to be half of the value that is given in **Table 4.1**. The reason for that is the utilization of a symmetry condition in the thickness direction.

4.2.2. Test microstructures

With defined test specimens, now it is time to define microstructures, i.e. RVEs that are required for the RVE boundary value problem. Two types of RVEs are generated: (1) simple unit cell, i.e. unit sphere - **Figure 4.8**, and (2) complex RVE (both 2D and 3D cases) - **Figure 4.9**. All four microstructures consist of two material phases - matrix and inclusions, whose mechanical properties will be defined later. The inclusion in the unit cell and unit sphere microstructure is represented by a circle and sphere, respectively. On the other hand, for complex RVEs in **Figure 4.9**, the inclusion is the ellipse (in the case of 2D RVE), i.e. ellipsoid (in the case of 3D RVE). Also, notice from **Figure 4.9** that the RVE in question possesses periodicity in terms of geometry. This is a necessary condition when PBC or Fourier analysis is utilized for any type of calculation.

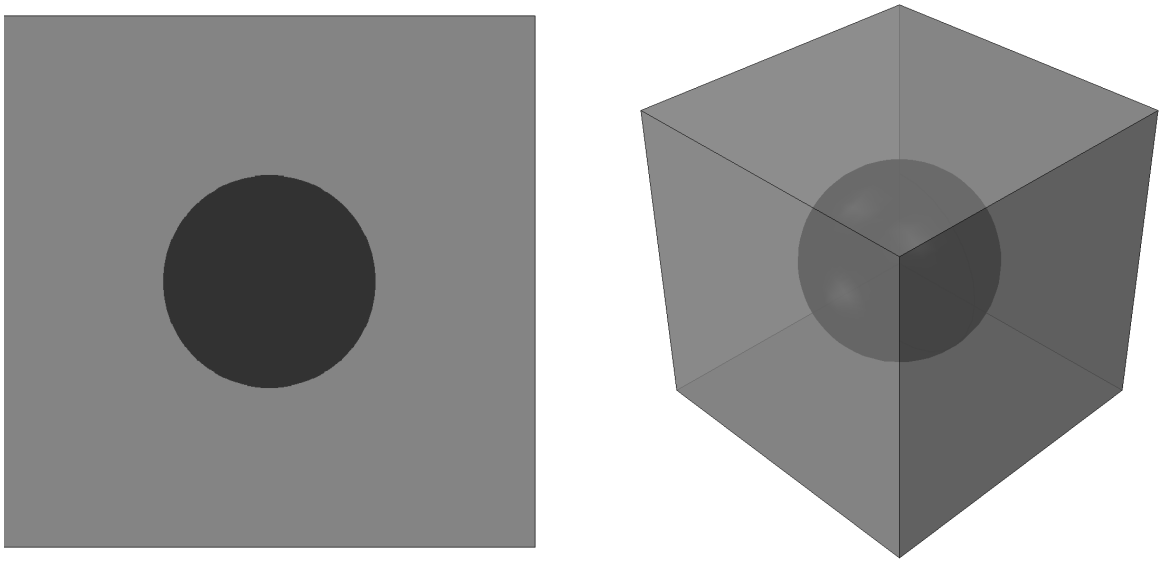

(a) Unit cell microstructure

(b) Unit sphere microstructure

Figure 4.8: 2D and 3D microstructures for the initial phase of testing

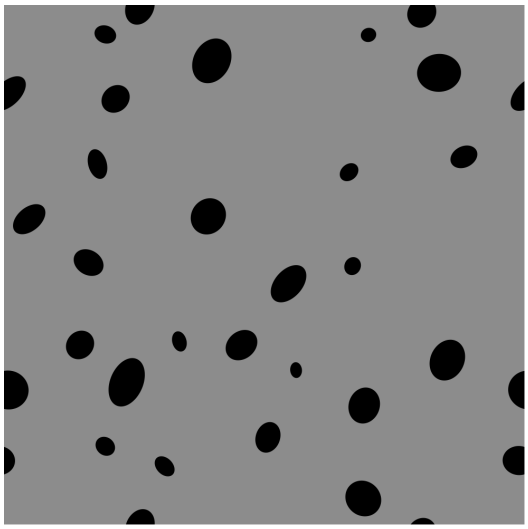

(a) 2D RVE with side length of 0.5 mm

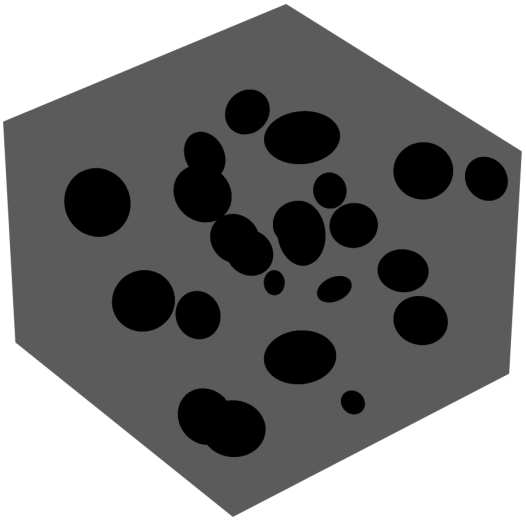

(b) 3D RVE with side length of 0.25 mm

Figure 4.9: Complex RVEs

Unit cell and unit sphere are classical examples of RVEs that are used for initial testing of the accuracy and the validity of the developed multiscale implementations. This is also true in this dissertation. Both microstructures depicted in **Figure 4.8** have side lengths of one millimeter. The unit cell contains one inclusion with a radius of 0.2 mm, making the total volume fraction equal to 12.57 %. On the other hand, inclusion in the unit sphere microstructure has a radius of 0.3 mm and therefore produces a volume fraction of 11.31 %.

Complex RVEs depicted in **Figure 4.9** will serve to evaluate the robustness of the proposed concurrent multiscale damage approach, as the random geometrical configuration of inclusions will produce a highly nonuniform distribution of stress and strain field. The basis for the generation of both RVEs was the experimental metallography of nodular cast iron produced by Tundish method of casting [248].

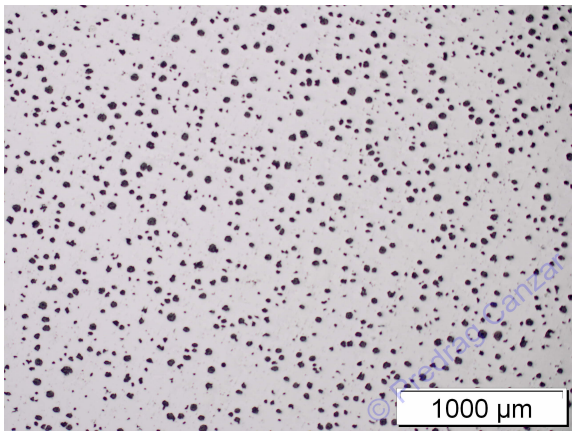

Figure 4.10: Nodular cast iron metallography - Tundish method of casting [248]

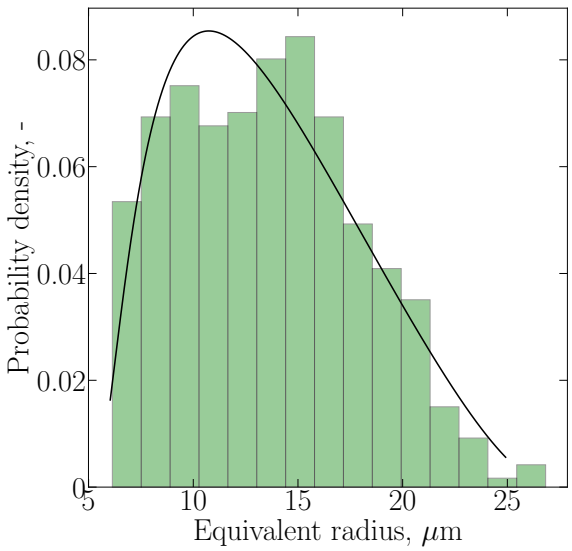

(a) Distribution of graphite nodule's radius

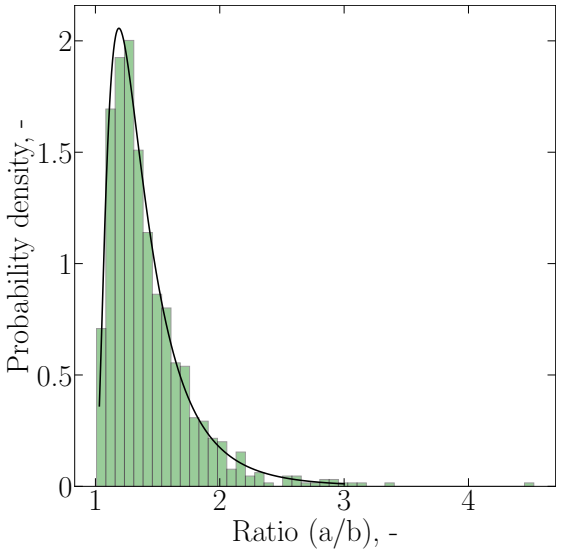

(b) Distribution of graphite nodule's shape

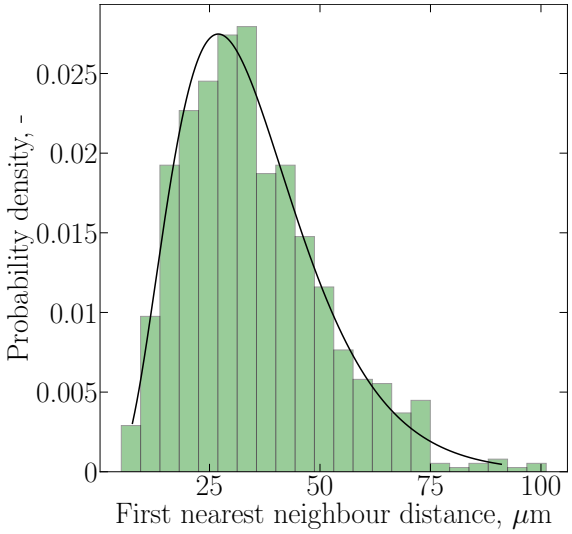

(c) Distribution of graphite nodule's first nearest neighbor distance

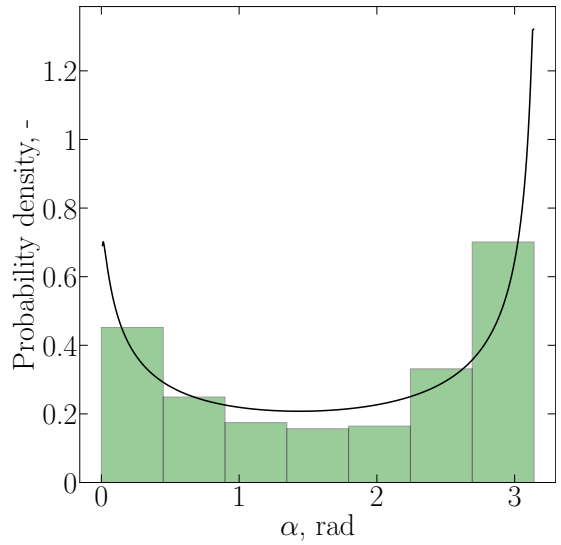

(d) Distribution of graphite nodule's orientation

Figure 4.11: Probability density distributions of the microstructural descriptors

The microstructure of this material consists of three material phases - graphite nodules and crystals of ferrite and pearlite. In the experimental investigation performed by Čanžar [248], it has been determined that the volume fraction of graphite nodules and pearlite is approximately 3.6 % and 7.64 %, respectively. Making the volume fraction of the third material phase (ferrite) almost 90 %. For the ease of microstructure generation and the multiscale implementation, the influence of the pearlite matrix was neglected, leaving only ferrite and graphite nodules as two material phases to be considered. The metallographic image in **Figure 4.10** was first transformed into

a binary-type image and then analyzed using the ImageJ software package [249] in order to obtain information about the distribution of the nodule's equivalent radius, shape (ratio between major a and minor b ellipse axis), nearest neighbor distance and orientation of the major axis. During the image analysis, the irregularly shaped graphite nodules were replaced by ellipses. All four distributions are depicted in **Figure 4.11**.

4.3. Initial phase of testing

The first, i.e. initial phase of testing will focus on the proposed algorithm's accuracy and computational efficiency. This section includes analysis done only on the unit cell and unit sphere microstructures for both brittle and ductile fracture with two different material configurations. The first material configuration essentially forms homogeneous material, as both matrix and inclusion possess identical material properties. The goal is to show that both SCA and DNS (performed with homogeneous material properties) will give almost identical results since no material heterogeneity exists. The second material configuration will downgrade, by 5 %, some mechanical properties of the inclusion. The goal now is to show there will be a difference in force-displacement diagrams, as now there exists some level of material heterogeneity. The mechanical properties chosen for the first, i.e. second configuration are given in **Table 4.2**.

Table 4.2: Mechanical properties for the initial phase of testing

Material configuration	First		Second	
Material phases	Matrix	Inclusion	Matrix	Inclusion
E, GPa	200	200	200	190
ν	0.3	0.3	0.3	0.3
σ_y^0, MPa	200	200	200	190
k, MPa	200	200	200	200
r	0.2	0.2	0.2	0.2

As can be seen from **Table 4.2**, in the second material configuration both modulus of elasticity E and initial yield strength σ_y^0 of the inclusion are degraded by 5 %. This small degree of material heterogeneity is chosen so that the clustering done with the first material configuration can be used directly for the second material configuration. In Liu et al. [78] it was shown that clustering decomposition for one material and geometrical configuration can be reused if there is no change in geometrical configuration and if the changes in material configuration are not significant. In this case, both conditions are met. The results of $k-$means clustering for both unit cell

and unit sphere are presented in **Figure 4.12** and **4.13**.

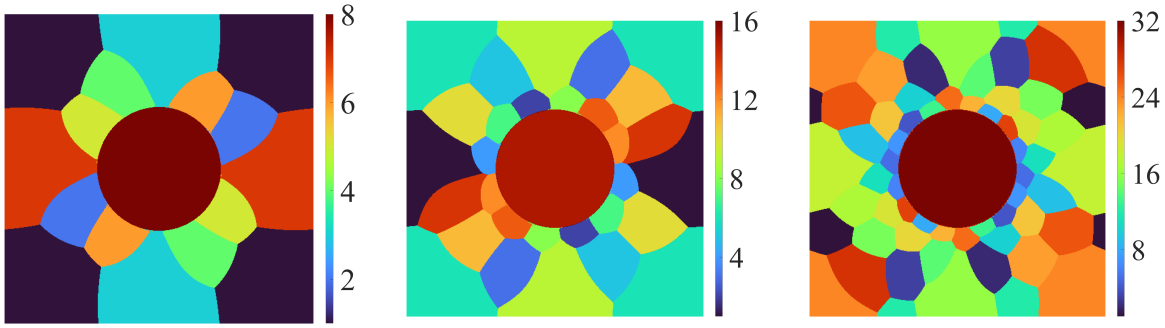

(a) $k = 8$ **(b)** $k = 16$ **(c)** $k = 32$

Figure 4.12: Results of the k-means clustering of the unit cell

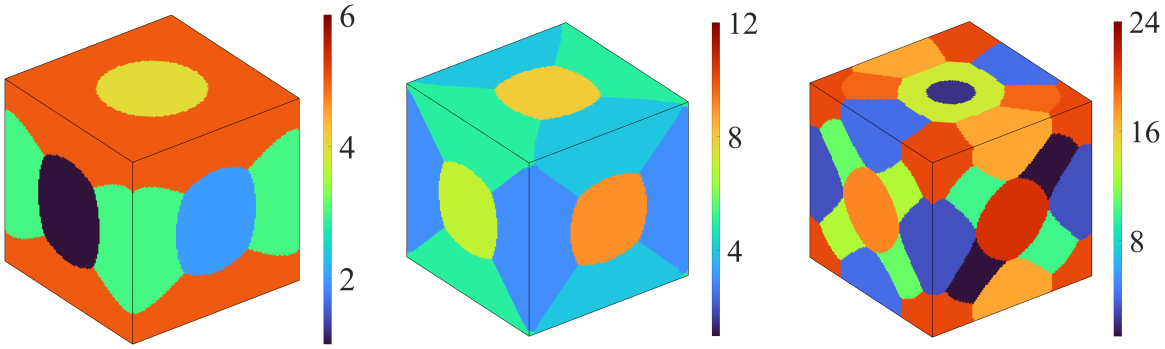

(a) $k = 6$ **(b)** $k = 12$ **(c)** $k = 24$

Figure 4.13: Results of the k-means clustering of the unit sphere

When considering brittle fracture, only the modulus of elasticity and Poisson ratio will be required as the material parameters at the microlevel, while in the case of ductile fracture, all material parameters listed in **Table 4.2** will enter the analysis. In addition to the mechanical properties needed for the RVE boundary value problem, the developed concurrent multiscale approach also requires phase-field fracture parameters at the macrolevel. Herein, for the case of all brittle fracture simulations, the critical value of the energy release rate G_c is set to 2.7 N/mm. The value of G_c for all ductile fracture analyses is chosen to be 11 times higher than the previous one, i.e. 29.7 N/mm. On the other hand, the value of the length-scale parameter l won't be constant, and will change depending on the analysis.

Before the testing begins, a "quick check" is performed in order to compare SCA and DNS (which is performed using FEM) for both unit cell and unit sphere microstructures. Tests are performed under four different macro-strain constraints (defined in **section 2.6**), using material parameters from the second material configuration, and with the clustering decomposition shown in **Figure 4.12** and **4.13**. The

homogenized stress-strain curves are depicted in **Figure 4.14** and **4.15**.

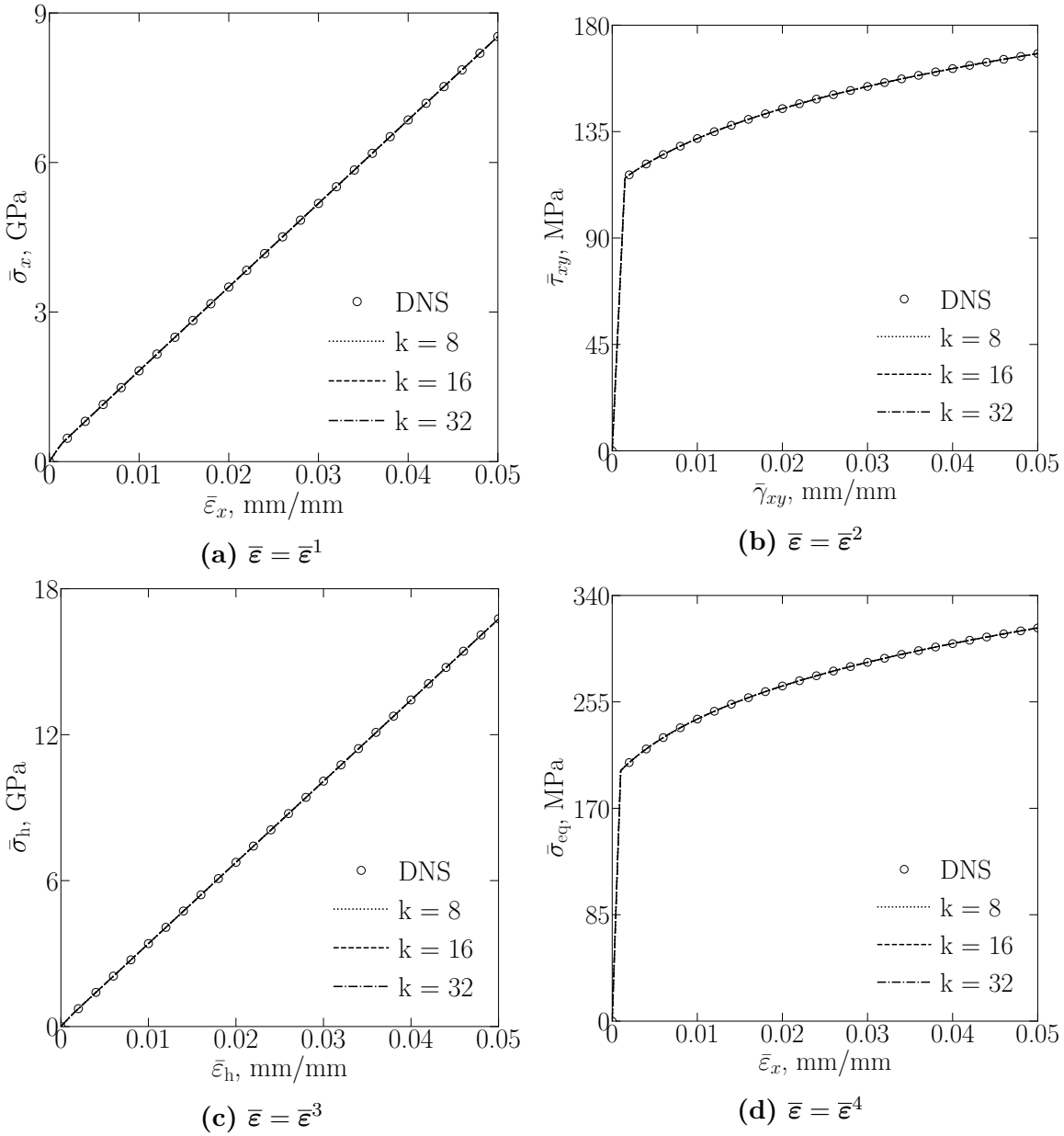

Figure 4.14: Comparisons of the homogenized stress-strain curves for a unit cell under different macro-strain constraints

Figure 4.14 shows what was expected - a perfect match between homogenized results obtained by the DNS and SCA. The maximum level of simplicity in terms of geometrical configuration and a difference of only 5 % between the modulus of elasticity and the initial yield strength are the main, and only, reasons for the almost non-existent error. Since it is possible to obtain accurate results with only eight material clusters, concurrent analyses with both material configurations are conducted

with that discretization.

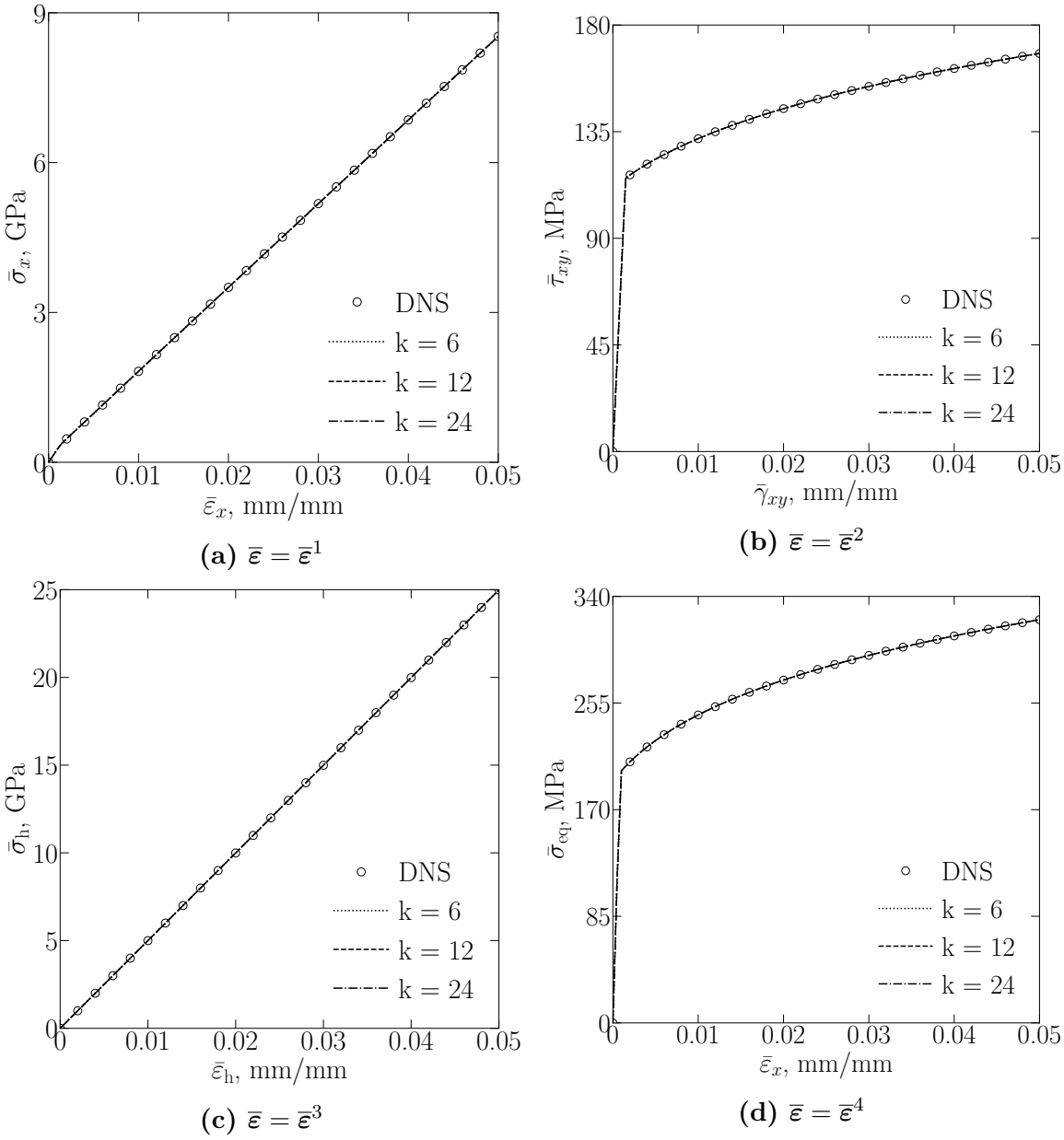

(a) $\overline{\boldsymbol{\varepsilon}} = \overline{\boldsymbol{\varepsilon}}^1$ **(b)** $\overline{\boldsymbol{\varepsilon}} = \overline{\boldsymbol{\varepsilon}}^2$

(c) $\overline{\boldsymbol{\varepsilon}} = \overline{\boldsymbol{\varepsilon}}^3$ **(d)** $\overline{\boldsymbol{\varepsilon}} = \overline{\boldsymbol{\varepsilon}}^4$

Figure 4.15: Comparisons of the homogenized stress-strain curves for a unit sphere under different macro-strain constraints

As was the case for unit cell microstructure, the SCA is able to predict homogenized values of stress and strain with pinpoint accuracy if the unit sphere is in question. Regardless if the total number of material clusters is equal to 6, 12, or 24, the difference between DNS and SCA is non-existent. Again, the discretization with the minimum number of material clusters, which in the case of three-dimensional analysis is equal to 6, is chosen for the purposes of all concurrent analyses.

In the next several pages, results obtained by the DNS, SCA with the first material configuration ("SCA homogeneous") and SCA with the second material configuration ("SCA heterogeneous") are presented. Each analysis includes the force-displacement diagram, alongside its detailed view, and images depicting the crack-phase field for both DNS and "SCA homogeneous" simulations. A detailed view of the specific part of the force-displacement diagram proves the premise that results obtained for homogeneous material under both DNS and SCA should be in a very small deviation. On the other hand, results obtained when mechanical properties of inclusion are degraded will deviate by a certain factor.

In addition to figures, each result is accompanied by a table of CPU times for all three analyses - DNS, "SCA homogeneous" and "SCA heterogeneous". Recall that the goal of this testing is to determine the computational efficiency of the proposed concurrent approach. Every analysis that is present from now on was executed using a single thread of an Intel Xeon E5-1620 (version 2) processor, which ensures an objective comparison of times needed to complete the analyses. All simulations are performed with fixed increment size and using a projection based scheme algorithm for the update of the reference material stiffness tensor. As was stated in **subsection 2.5.1**, the projection based scheme represents a more stable approach for finding the optimal values of Lamé parameters that form the stiffness of the reference homogeneous material. Not only that, but the computational efficiency of the projection based scheme sits on a higher level than the regression based scheme.

4.3.1. Brittle fracture model

The first in the line is the phenomena of brittle fracture where four material parameters are specified in total. More precisely, a modulus of elasticity, Poisson ratio, critical energy release rate and length-scale parameter. The first three parameters are given in **section 4.3**, while the length-scale parameter is provided for each analysis separately. When choosing a length-scale parameter, which is not only a geometrical parameter but also a material one, it is important to define its value to be small enough when compared to the specimen. Otherwise, incorrect crack topologies may occur during analysis. Also, due to a need for an element size that is at least two times smaller than the chosen value of the length-scale parameter, its value cannot be extremely small either. To ensure an adequate description of the diffusive layer, the element size in the region where the crack forms and propagates will always be three times lower than the chosen length-scale parameter.

The first specimen to be tested is the 2D single-edge notched plate; loaded to tension. The model is discretized by 12122 fully integrated quadrilateral plane strain elements. The chosen length-scale parameter is equal to 0.01 mm. The analysis is performed in 100 increments using no energy split.

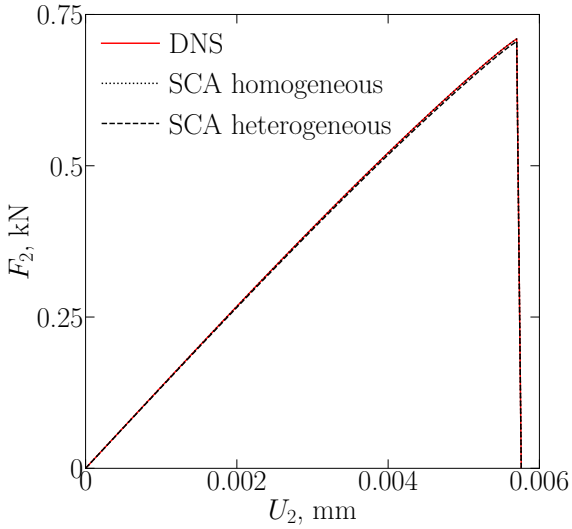

(a) Force-displacement curves

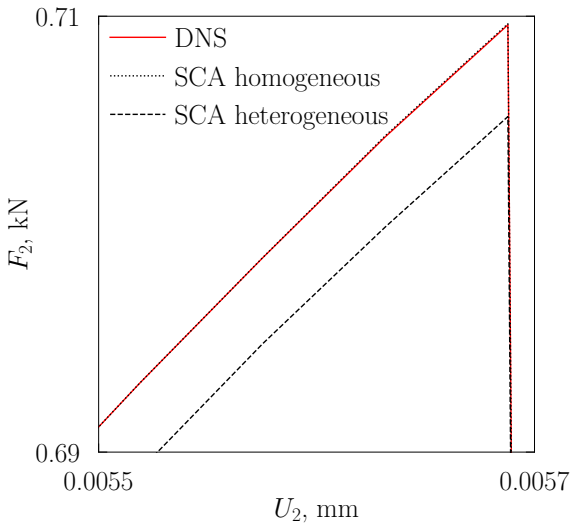

(b) Zoomed-in view

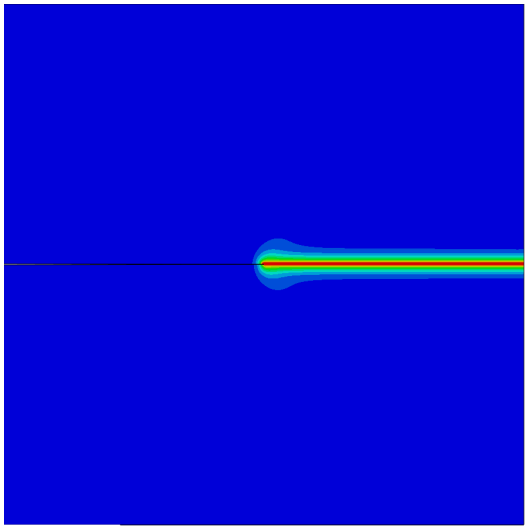

(c) Crack topology - DNS

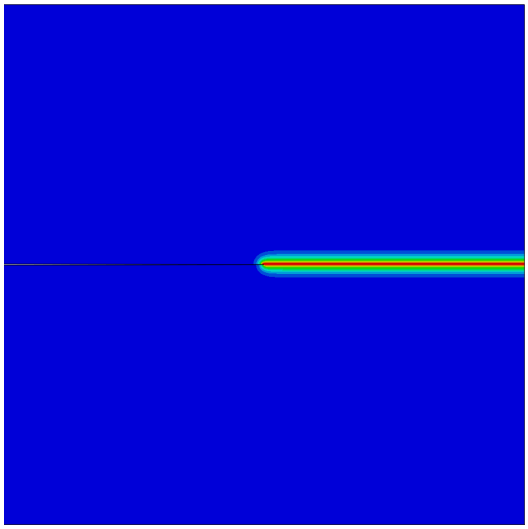

(d) Crack topology - SCA homogeneous

Figure 4.16: A 2D single-edge notched plate - tension test

Table 4.3: Comparisons of the computational time for a 2D single-edge notched plate - tension test

Analysis	DNS	SCA homogeneous	SCA heterogeneous
CPU time, min	56.75	281.02	301.13

The next specimen is the 2D single-edge notched plate; loaded to shear. The model is discretized by 28447 fully integrated quadrilateral plane strain elements. The chosen length-scale parameter is equal to 0.01 mm. The analysis is performed in 200 increments using a volumetric-deviatoric energy split.

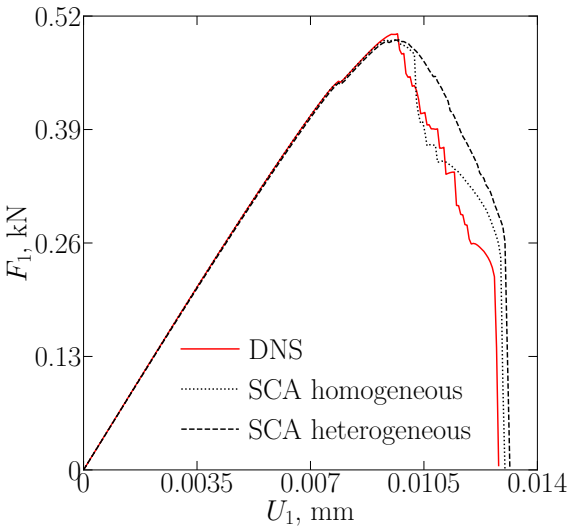

(a) Force-displacement curves

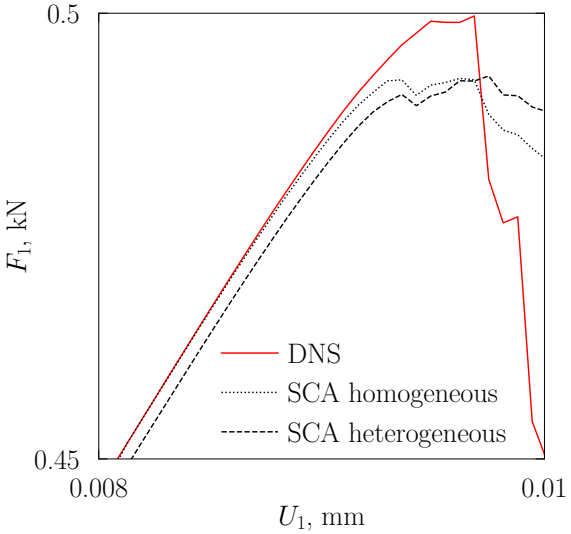

(b) Zoomed-in view

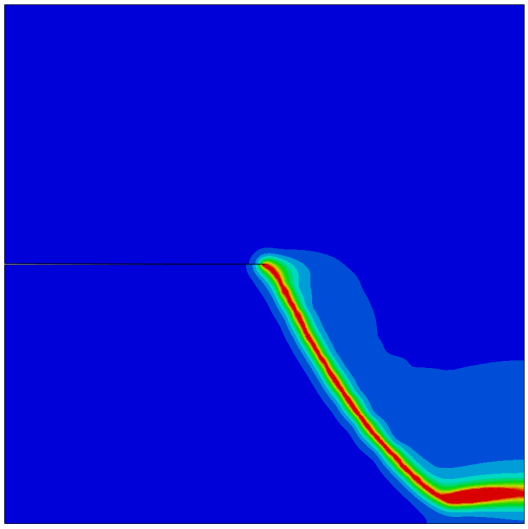

(c) Crack topology - DNS

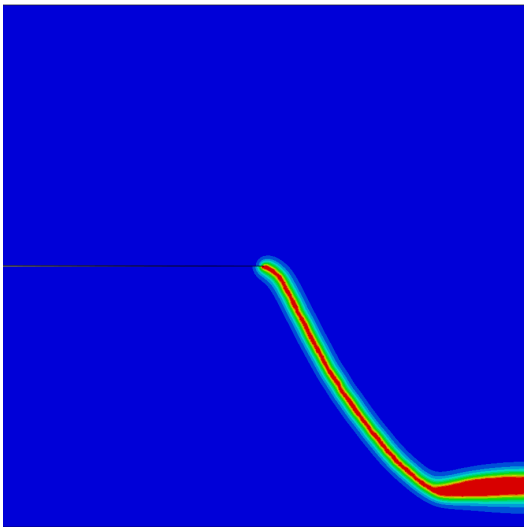

(d) Crack topology - SCA homogeneous

Figure 4.17: A 2D single-edge notched plate - shear test; volumetric-deviatoric split

Table 4.4: Comparisons of the computational time for a 2D single-edge notched plate - shear test; volumetric-deviatoric split

Analysis	DNS	SCA homogeneous	SCA heterogeneous
CPU time, min	866.08	2212.90	1156.38

Results shown below are also from the 2D single-edge notched plate; loaded to shear. The model is discretized by 28447 fully integrated quadrilateral plane strain elements. The chosen length-scale parameter is equal to 0.01 mm. The analysis is performed in 200 increments using a spectral energy split.

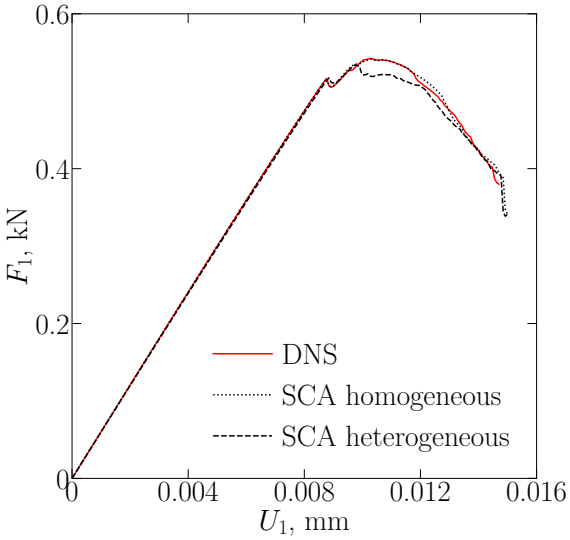

(a) Force-displacement curves

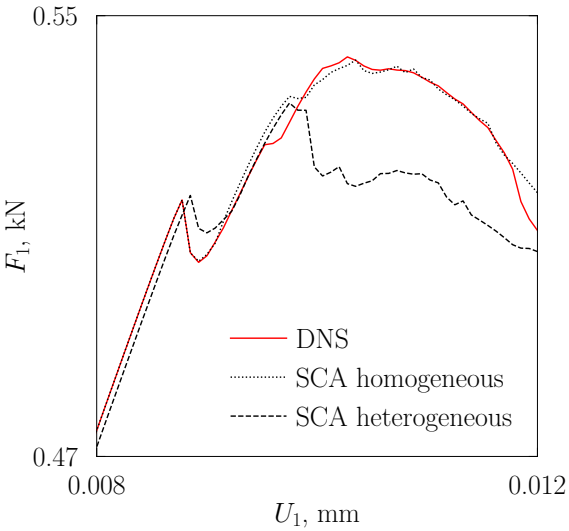

(b) Zoomed-in view

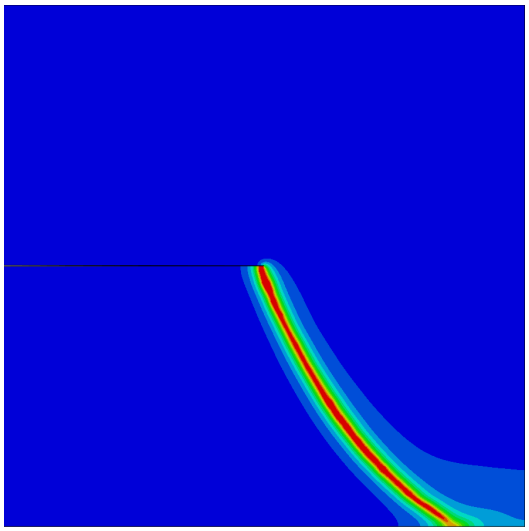

(c) Crack topology - DNS

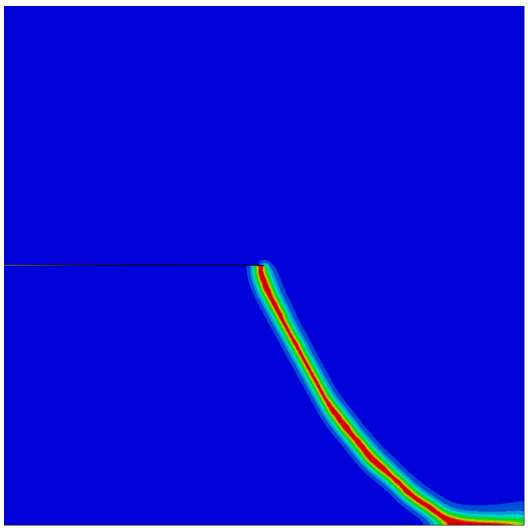

(d) Crack topology - SCA homogeneous

Figure 4.18: A 2D single-edge notched plate - shear test; spectral split

Table 4.5: Comparisons of the computational time for a 2D single-edge notched plate - shear test; spectral split

Analysis	DNS	SCA homogeneous	SCA heterogeneous
CPU time, min	394.80	1137.13	1206.13

A 2D three-point bending specimen is the next in line. The model is discretized by 12194 fully integrated quadrilateral plane strain elements. The chosen length-scale parameter is equal to 0.04 mm. The analysis is performed in 200 increments using a spectral energy split.

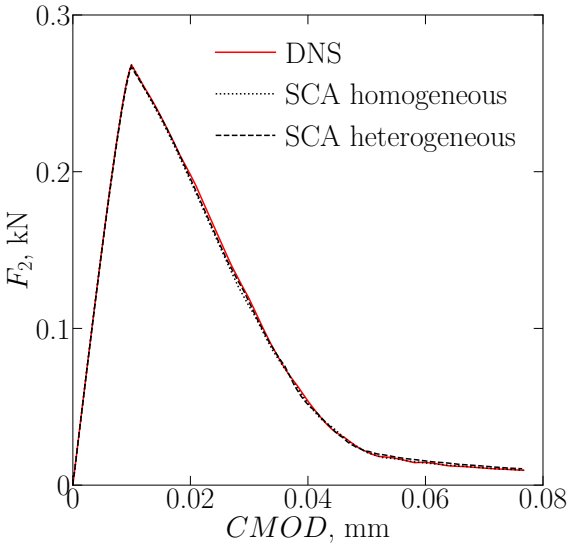

(a) Force-displacement curves

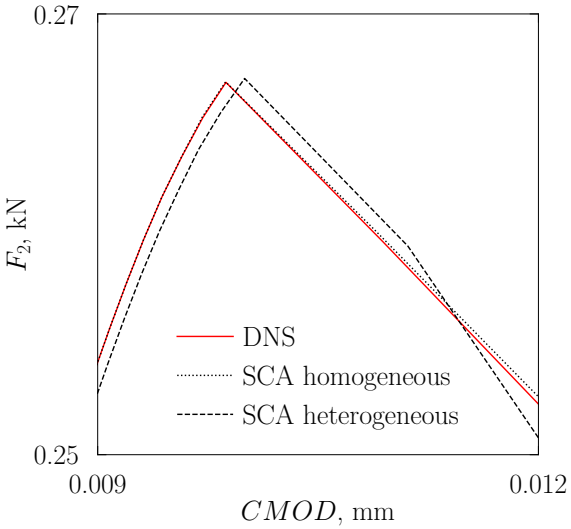

(b) Zoomed-in view

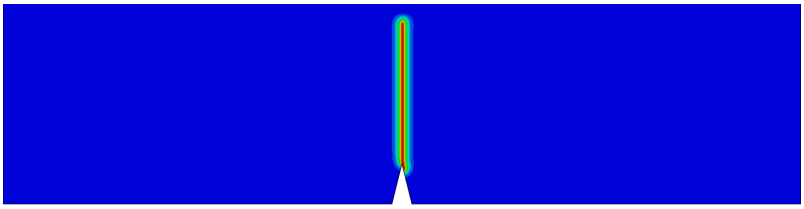

(c) Crack topology - DNS

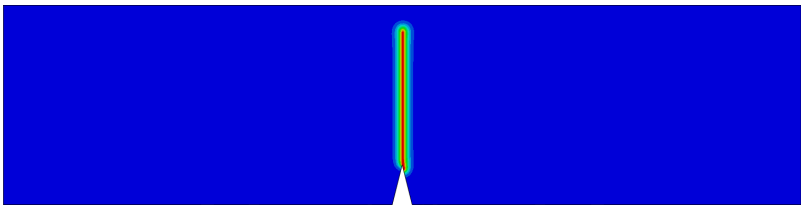

(d) Crack topology - SCA homogeneous

Figure 4.19: A 2D three-point bending specimen; spectral split

Table 4.6: Comparisons of the computational time for a 2D three-point bending specimen; spectral split

Analysis	DNS	SCA homogeneous	SCA heterogeneous
CPU time, min	69.05	198.06	198.07

Results for the 2D notched plate with a hole are depicted below. The model is discretized by 33703 fully integrated quadrilateral plane strain elements. The chosen length-scale parameter is equal to 0.1 mm. The analysis is performed in 400 increments using spectral energy split.

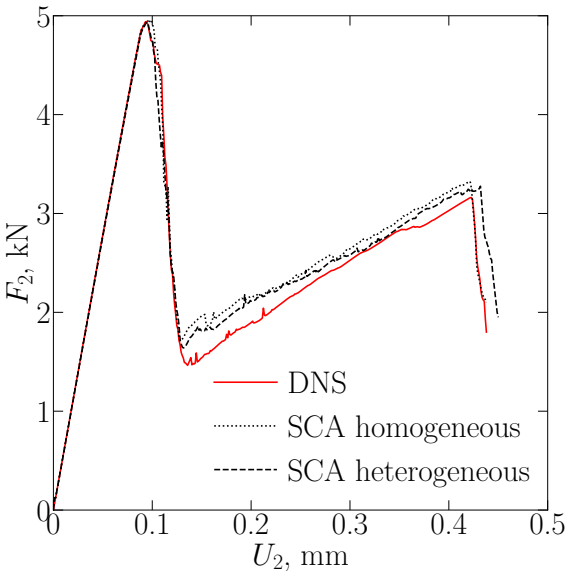

(a) Force-displacement curves

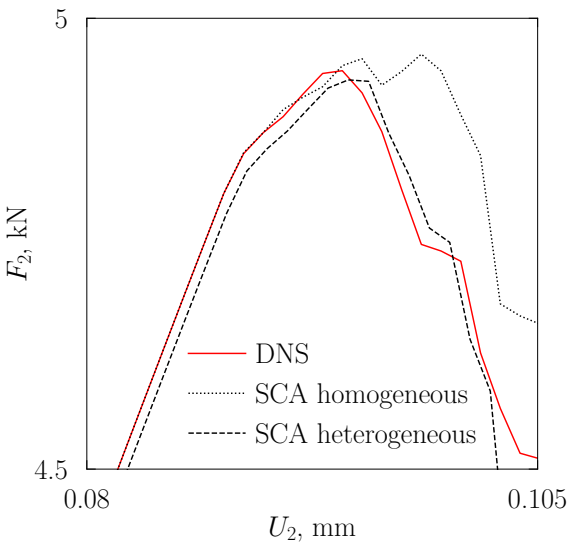

(b) Zoomed-in view

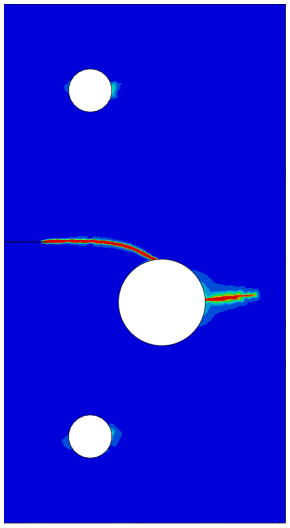

(c) Crack topology - DNS

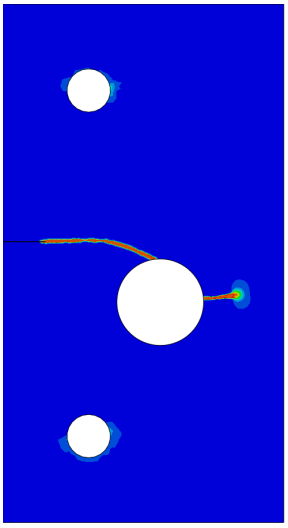

(d) Crack topology - SCA homogeneous

Figure 4.20: A 2D notched plate with a hole; spectral split

Table 4.7: Comparisons of the computational time for a 2D notched plate with a hole; spectral split

Analysis	DNS	SCA homogeneous	SCA heterogeneous
CPU time, min	568.95	2233.87	2743.43

A 2D double-notched specimen is the last example in 2D plane strain brittle fracture tests. The model is discretized by 22127 fully integrated quadrilateral plane strain elements. The chosen length-scale parameter is equal to 0.3 mm. The analysis is performed in 100 increments using no energy split.

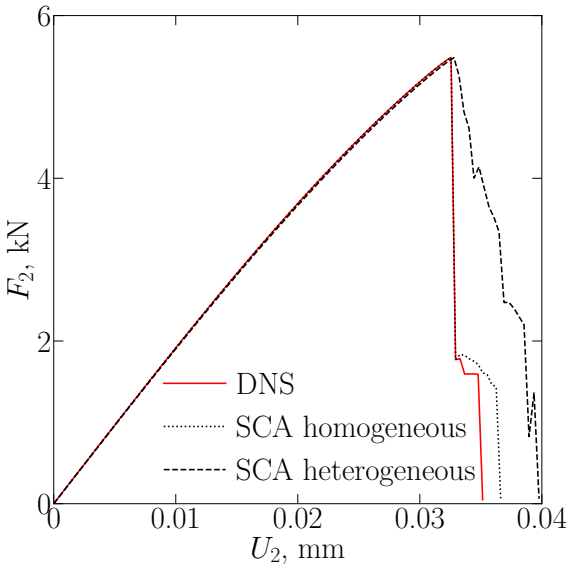

(a) Force-displacement curves

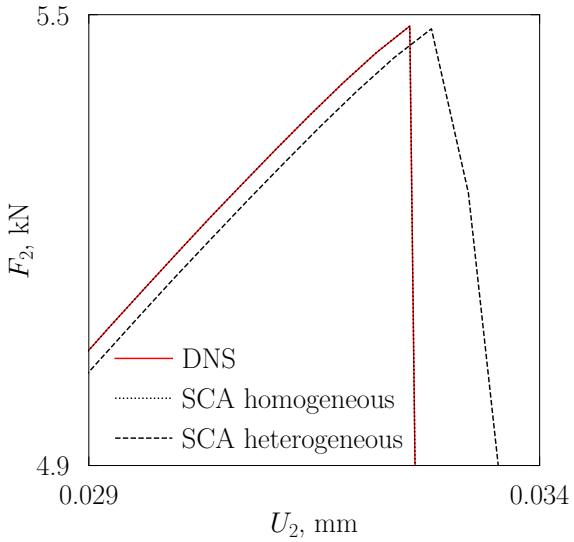

(b) Zoomed-in view

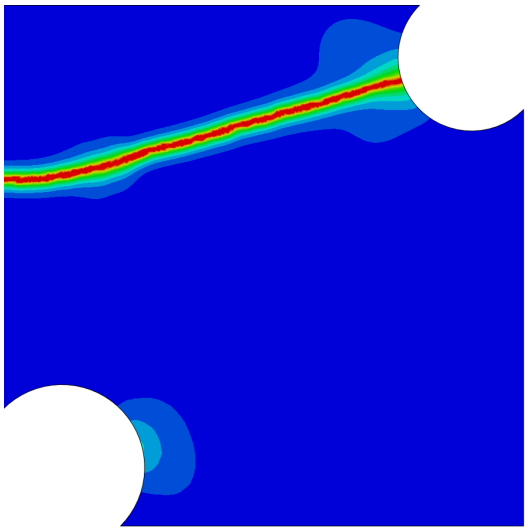

(c) Crack topology - DNS

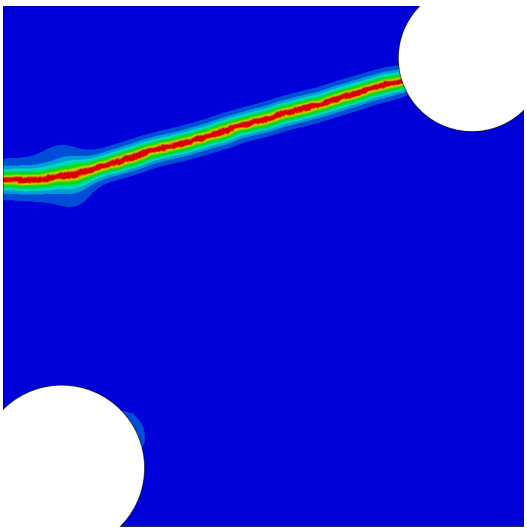

(d) Crack topology - SCA homogeneous

Figure 4.21: A 2D double-notched specimen

Table 4.8: Comparisons of the computational time for a 2D double-notched specimen

Analysis	DNS	SCA homogeneous	SCA heterogeneous
CPU time, min	161.67	436.48	305.45

A 3D single-edge notched plate loaded to tension is the first example in the 3D brittle fracture tests. The model is discretized by 13680 fully integrated hexahedral elements. The chosen length-scale parameter is equal to 0.01 mm. The analysis is performed in 100 increments using no energy split.

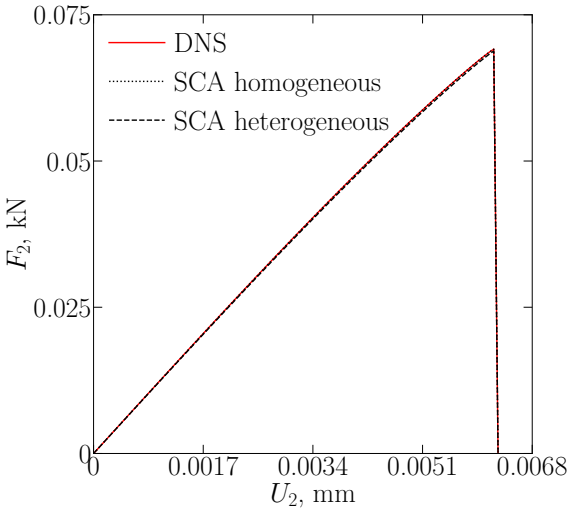

(a) Force-displacement curves

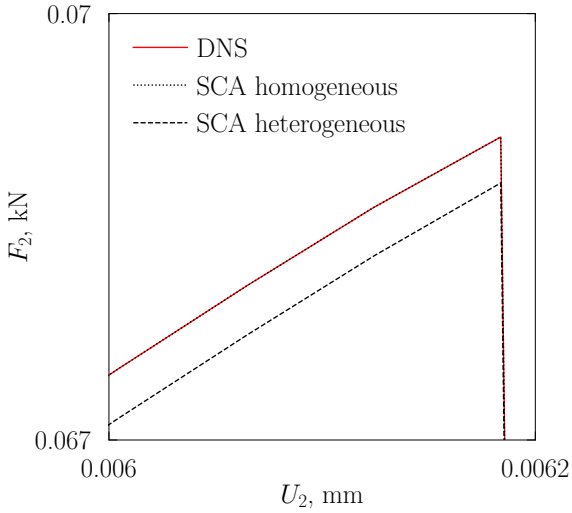

(b) Zoomed-in view

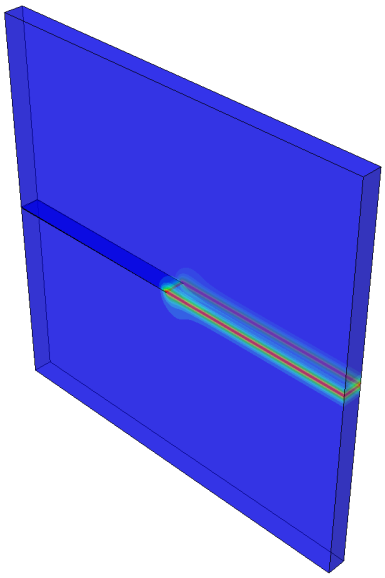

(c) Crack topology - DNS

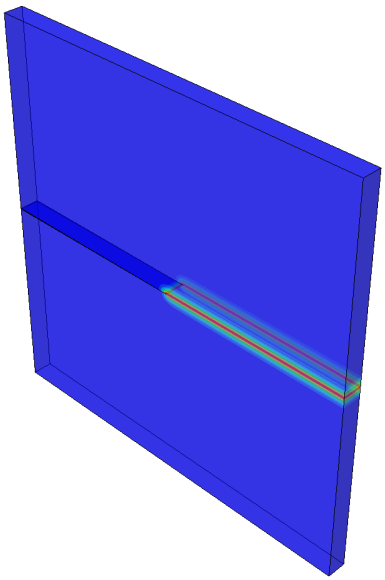

(d) Crack topology - SCA homogeneous

Figure 4.22: A 3D single-edge notched plate - tension test

Table 4.9: Comparisons of the computational time for a 3D single-edge notched plate - tension test

Analysis	DNS	SCA homogeneous	SCA heterogeneous
CPU time, min	238.52	987.45	1057.95

A volumetric-deviatoric energy split is applied for the 3D three-point bending specimen. The model is discretized by 15477 fully integrated hexahedral elements. The chosen length-scale parameter is equal to 0.04 mm. The analysis is performed in 200 increments.

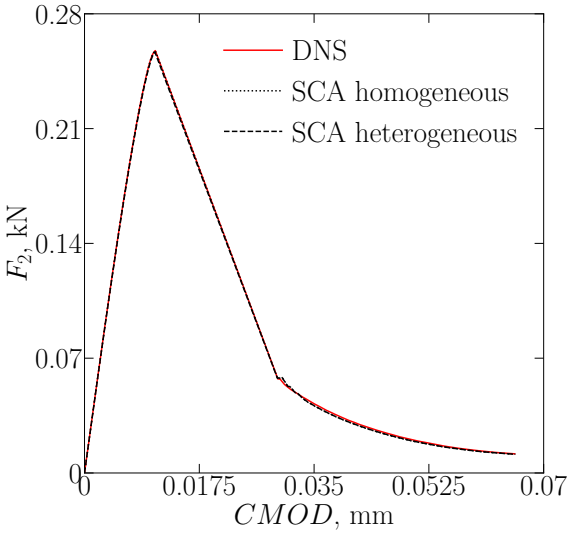

(a) Force-displacement curves

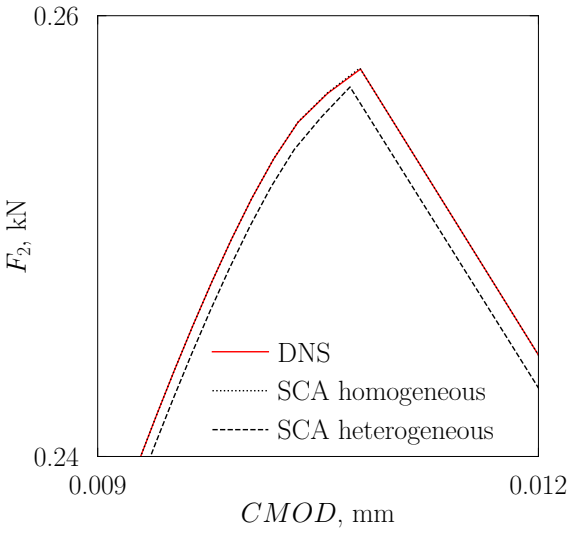

(b) Zoomed-in view

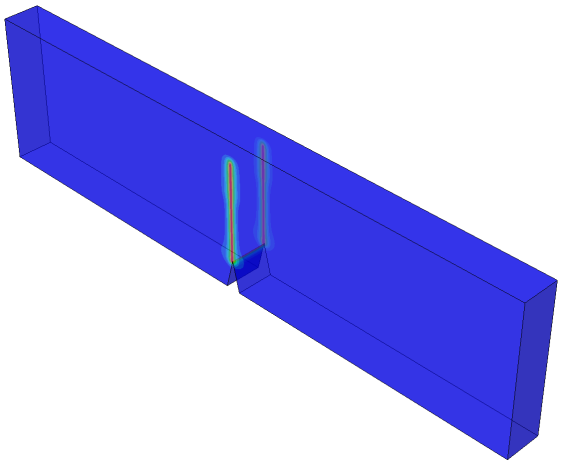

(c) Crack topology - DNS

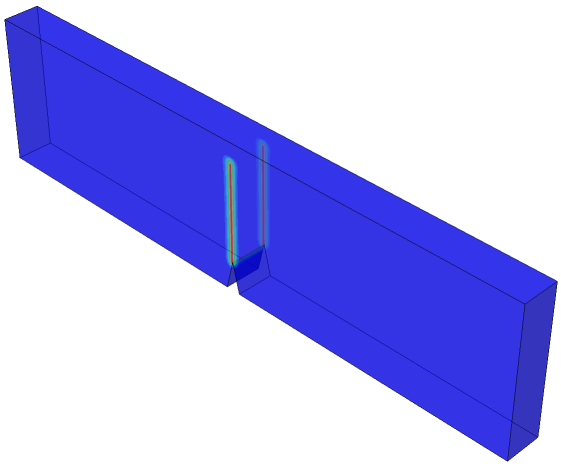

(d) Crack topology - SCA homogeneous

Figure 4.23: A 3D three-point bending specimen; volumetric-deviatoric split

Table 4.10: Comparisons of the computational time for a 3D three-point bending specimen; volumetric-deviatoric split

Analysis	DNS	SCA homogeneous	SCA heterogeneous
CPU time, min	453.47	1767.97	1779.10

A 3D three-point bending specimen was also analyzed using spectral energy split. The model is discretized by 15477 fully integrated hexahedral elements. The chosen length-scale parameter is equal to 0.04 mm. The analysis is performed in 200 increments.

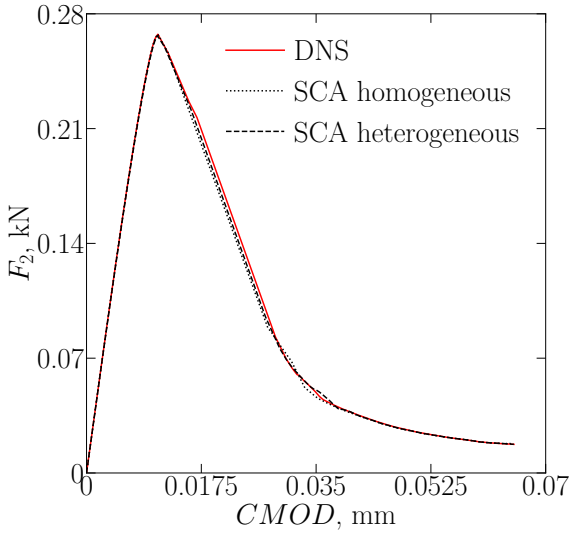

(a) Force-displacement curves

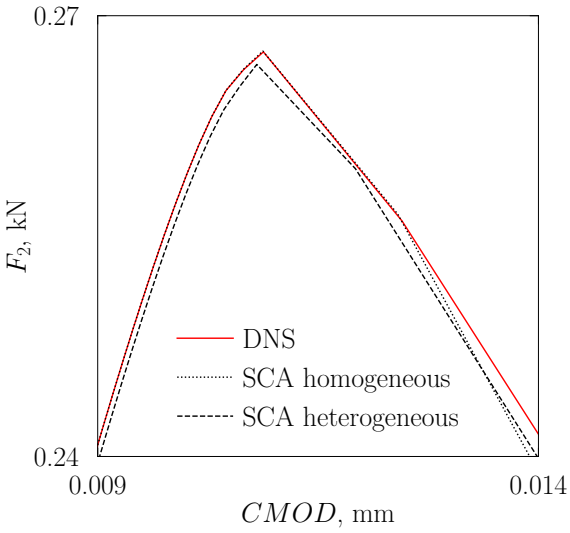

(b) Zoomed-in view

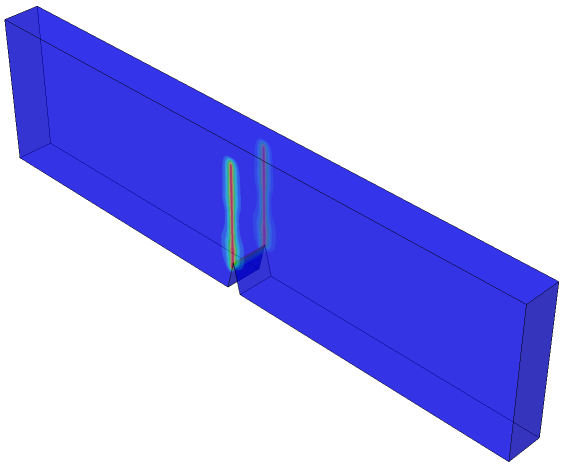

(c) Crack topology - DNS

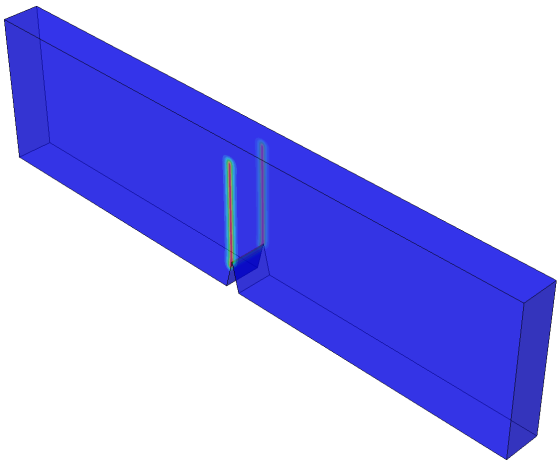

(d) Crack topology - SCA homogeneous

Figure 4.24: A 3D three-point bending specimen; spectral split

Table 4.11: Comparisons of the computational time for a 3D three-point bending specimen; spectral split

Analysis	DNS	SCA homogeneous	SCA heterogeneous
CPU time, min	616.12	1787.60	1626.13

A 3D double-notched specimen is the last example in this subsection. The model is discretized by 31389 fully integrated hexahedral elements. The chosen length-scale parameter is equal to 0.3 mm. The analysis is performed in 100 increments using no energy split.

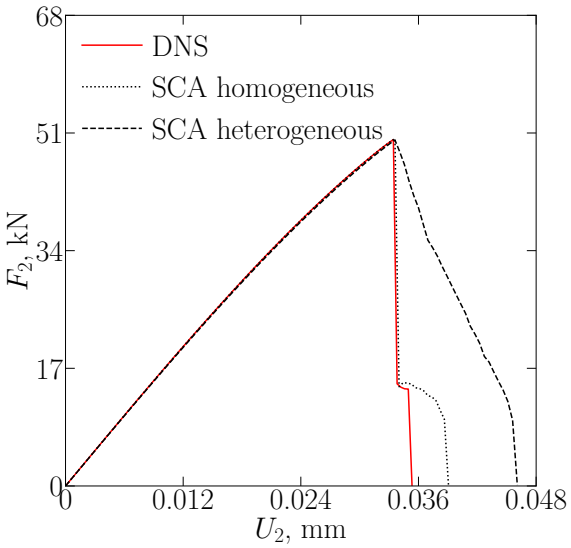

(a) Force-displacement curves

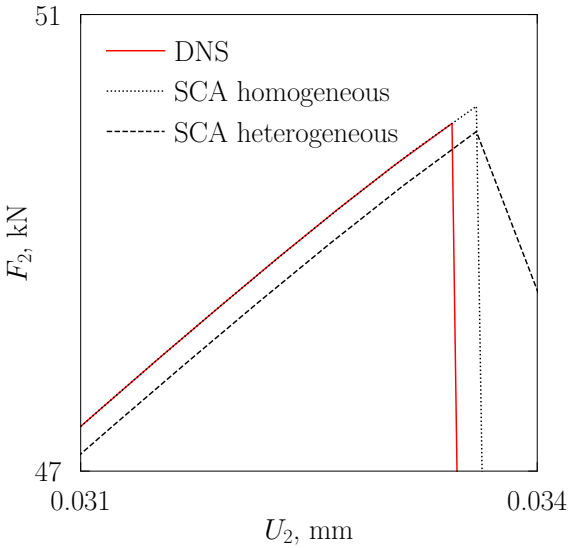

(b) Zoomed-in view

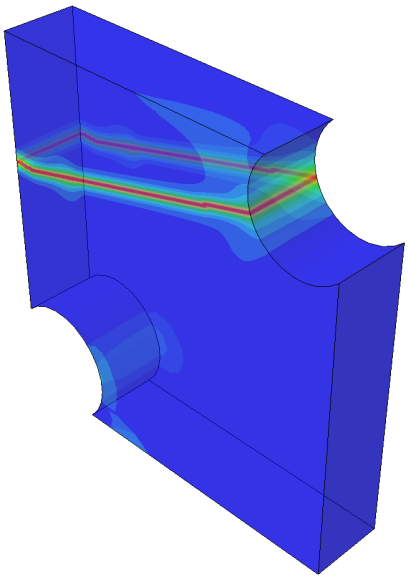

(c) Crack topology - DNS

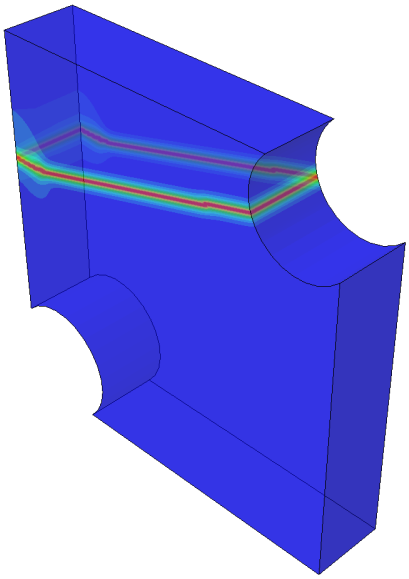

(d) Crack topology - SCA homogeneous

Figure 4.25: A 3D double-notched specimen

Table 4.12: Comparisons of the computational time for a 3D double-notched specimen

Analysis	DNS	SCA homogeneous	SCA heterogeneous
CPU time, min	1198.13	2354.17	1357.92

From the figures and tables provided in the previous pages, it can be concluded that the proposed algorithm is able to describe brittle fracture in an accurate and computationally efficient way. Force-displacement diagrams and their zoomed-in views show there exists almost no difference between DNS analysis (performed using homogeneous material properties) and the developed concurrent approach performed on the unit cell/unit sphere type microstructure with material properties from the first material configuration. In some examples such as a 2D single-edge notched plate loaded by shear (both energy decompositions), a 2D notched plate with a hole and a 2D/3D double-notched specimen, a more significant difference in force-displacement behaviour can be observed. However, this occurs only after the peak force is reached, i.e. after the crack has formed.

On the other hand, when the modulus of elasticity is degraded by 5 %, the proposed concurrent approach gives different results - which was expected. The zoomed-in views of force-displacement diagrams give a better insight into this difference since for some examples, such as 2D/3D single-edge notched plate loaded by tension, the distinction between three curves is not immediate. All zoomed-in views show that the value of peak force is always the lowest for the heterogeneous microstructure. This is extremely important, as it validates the accuracy and provides proof that the proposed concurrent approach gives physically correct results. The opposite scenario is physically not justified, as a material with the lower value of material stiffness tensor and the same value of phase-field fracture parameters cannot experience a fracture at higher levels of peak force.

Figures that depict the crack topology for both DNS and "SCA homogeneous" are also in excellent agreement. The topologies of cracks are almost identical, which is again an important result as it provides additional confirmation of the validity of the developed concurrent approach. Interestingly enough, figures of the crack topologies show that the concurrent approach gives more localized plots of the crack phase-field parameter ϕ in contrast to DNS.

In addition to being accurate and physically correct, the tables shown above confirm that the proposed concurrent approach is also computationally efficient. When compared to the DNS, the average time needed to complete concurrent multiscale analysis is increased by a factor of 3.26, for the 2D plane strain configuration, i.e. 3.17, for the 3D configuration. This is less than the total number of material clusters, which, recall, was 8 (in 2D plane strain configuration) and 6 (in 3D configuration). Unless the number of material clusters is equal to 1 (which is possible when only one material phase is present at the lower level), the computational time of the concurrent approach will certainly be longer when compared to DNS. This is because every integration

point now represents a separate analysis that includes the calculation of the small strain and Cauchy stress tensor in each material cluster. With the increase in the number of material clusters, the level of computational efficiency will undoubtedly fall, as the majority of time will be spent on solving the linear system of equations.

Although they represent the same type of analysis, "SCA homogeneous" and "SCA heterogeneous" can result in different computational time for the same specimen - in both two- and three-dimensional configuration. The reason for this lies in the different number of iterations that are performed in each increment at the macrolevel. For example, in the case of a 2D single-edge notched plate (loaded by tension), "SCA homogeneous" required 1304, while "SCA heterogeneous" performed 1333 iterations in the critical increment. On the other hand, the maximum number of iterations (in one increment) for the case of a 2D single-edge notched plate (loaded by shear; with volumetric-deviatoric energy split) was 1414 and 283 for "SCA homogeneous" and "SCA heterogeneous", respectively. The exact reason for these discrepancies in the maximum iteration number is, at this moment, unknown to the author of this thesis.

4.3.2. Ductile fracture model

The initial phase of testing is also performed for ductile fracture, as the very title of this dissertation carries this term. When considering fracture in ductile materials, seven material parameters in total are required. In addition to four material parameters, which were present in brittle fracture modelling, three new material parameters that now are coming into the equation are initial yield strength, and two parameters of Swift's non-linear hardening law - see **Table 42**. In contrast to brittle fracture, the length-scale parameter in ductile fracture will take on higher values, as crack(s) in ductile fracture do not behave the same way as in the case of brittle fracture. More precisely, when ductile material experiences damage, i.e. fracture, the formed crack(s) can dull and widen. Generally, values of the length-scale parameter for problems of ductile fracture are several times higher than in problems that involve brittle and quasi-brittle fracture. To ensure the adequate capturing of the crack phase-field, element size in the zones of damage will again be three times smaller than the chosen value of the length-scale parameter. Results that are depicted in the following pages also include some specimens that were not used in the previous subsection. These are the V-notch bar, unnotched specimen and Sandia challenge fracture specimen. Once again, it is noted that all analyses in this subsection are performed with the assumption of small elastoplastic strains. This is because the SCA algorithm for finite strain configuration was not able to produce satisfactory results - see **subsection 2.6.1**.

A 2D V-notch bar is the first example in this subsection. The model is discretized by 15441 fully integrated quadrilateral plane strain elements. The chosen length-scale parameter is equal to 0.2 mm. The analysis is performed in 200 increments using no energy split.

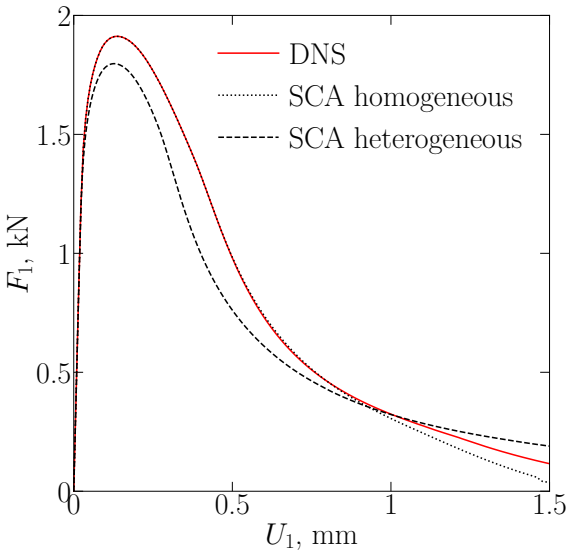

(a) Force-displacement curves

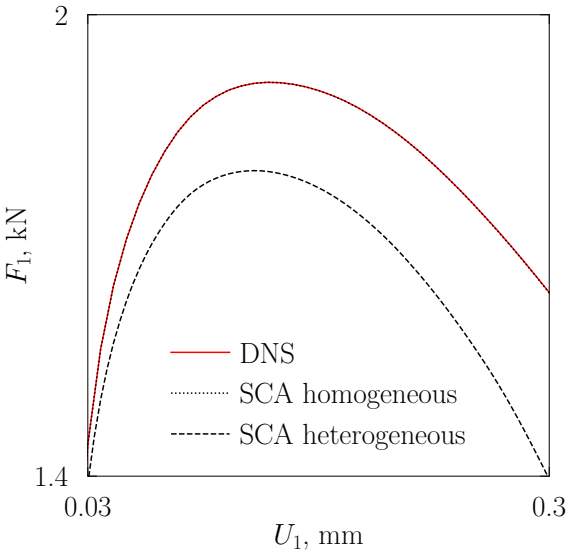

(b) Zoomed-in view

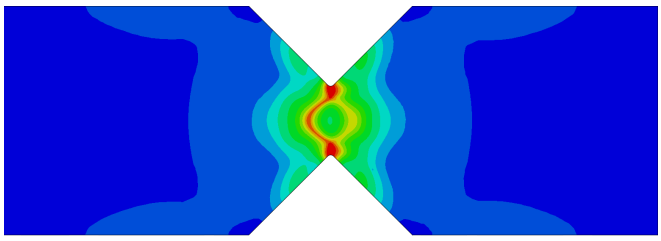

(c) Crack topology - DNS

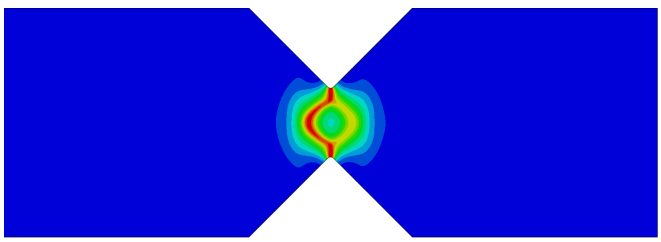

(d) Crack topology - SCA homogeneous

Figure 4.26: A 2D V-notch bar

Table 4.13: Comparisons of the computational time for a 2D V-notch bar

Analysis	DNS	SCA homogeneous	SCA heterogeneous
CPU time, min	81.42	332.1	597.68

A 2D unnotched specimen is next in line. The model is discretized by 14282 fully integrated quadrilateral plane strain elements. The chosen length-scale parameter is equal to 0.4 mm. The analysis is performed in 200 increments using no energy split.

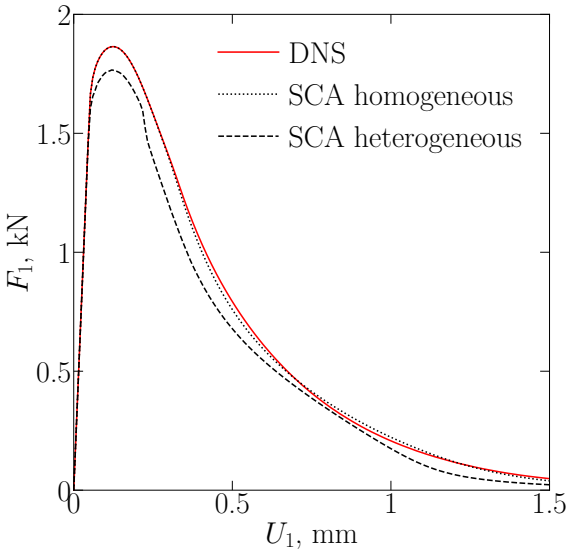

(a) Force-displacement curves

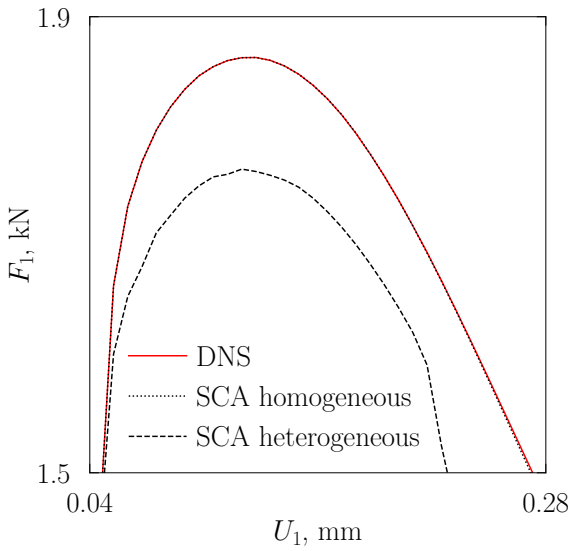

(b) Zoomed-in view

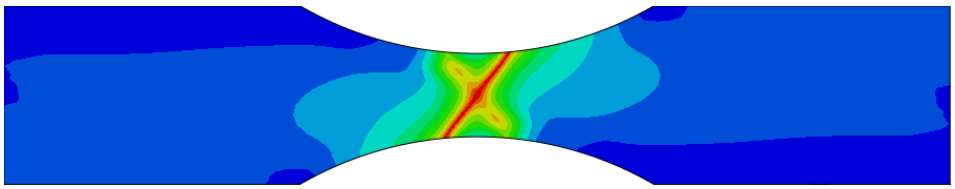

(c) Crack topology - DNS

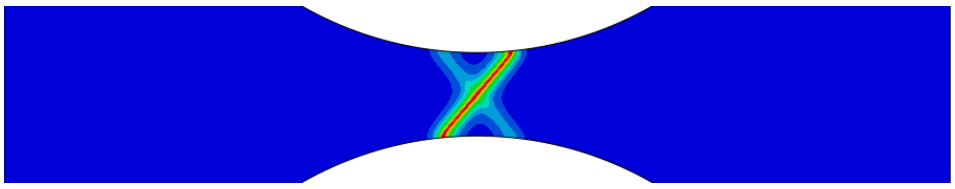

(d) Crack topology - SCA homogeneous

Figure 4.27: A 2D unnotched specimen

Table 4.14: Comparisons of the computational time for a 2D unnotched specimen

Analysis	DNS	SCA homogeneous	SCA heterogeneous
CPU time, min	52.58	242.20	437.53

Results for the 2D notched plate with a hole are depicted below. The model is discretized by 24084 fully integrated quadrilateral plane strain elements. The chosen length-scale parameter is equal to 0.4 mm. The analysis is performed in 200 increments using volumetric-deviatoric energy split.

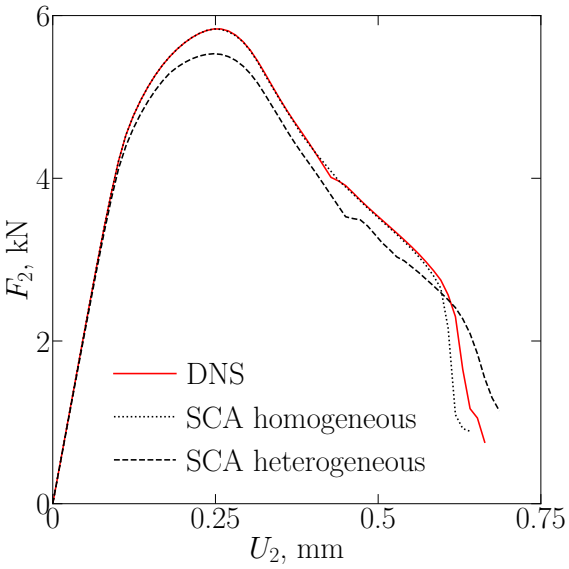

(a) Force-displacement curves

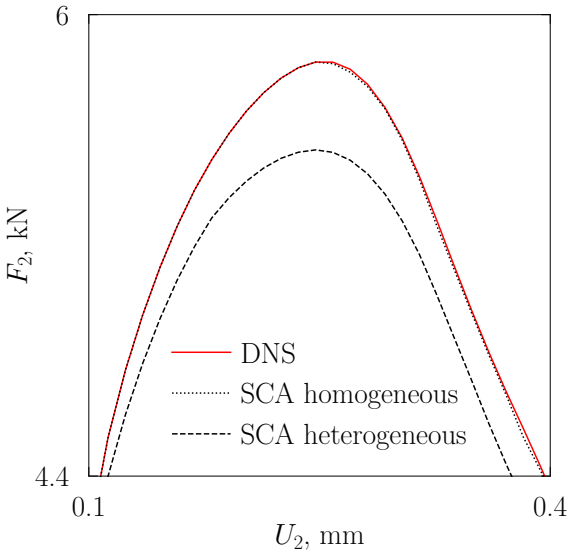

(b) Zoomed-in view

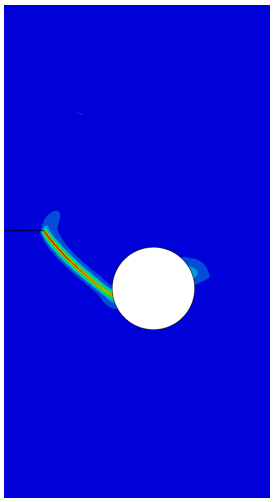

(c) Crack topology - DNS

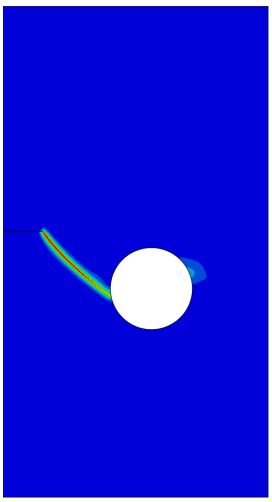

(d) Crack topology - SCA homogeneous

Figure 4.28: A 2D notched plate with a hole (ductile fracture); volumetric-deviatoric split

Table 4.15: Comparisons of the computational time for a 2D notched plate with a hole (ductile fracture); volumetric-deviatoric split

Analysis	DNS	SCA homogeneous	SCA heterogeneous
CPU time, min	126.87	768.63	1137.58

A 2D double-notched specimen is also present in ductile fracture analysis. The model is discretized by 16988 fully integrated quadrilateral plane strain elements. The chosen length-scale parameter is equal to 0.6 mm. The analysis is performed in 200 increments using no energy split.

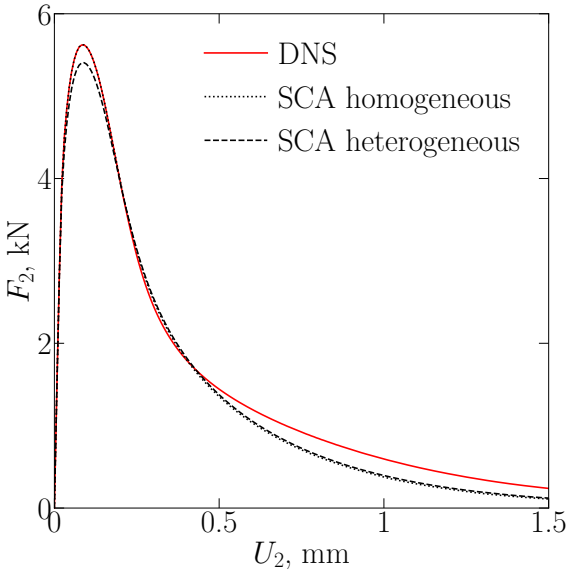

(a) Force-displacement curves

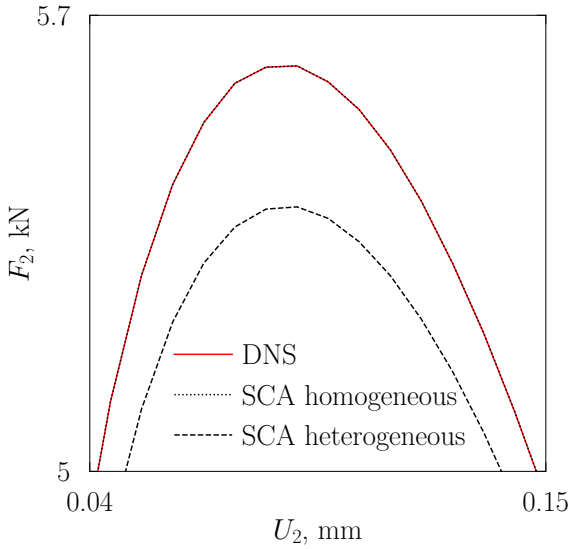

(b) Zoomed-in view

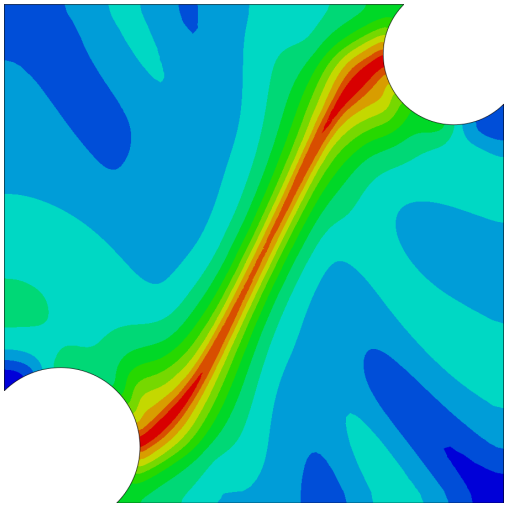

(c) Crack topology - DNS

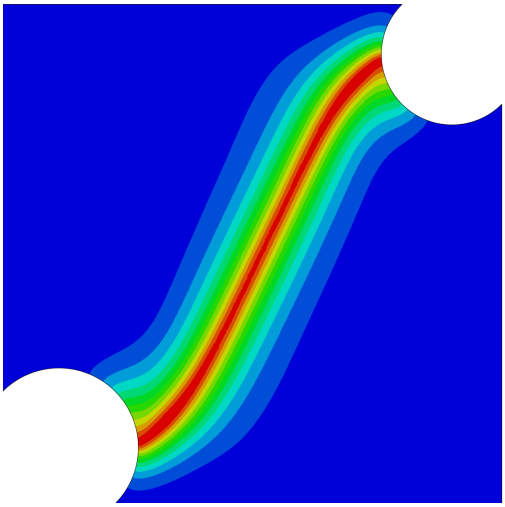

(d) Crack topology - SCA homogeneous

Figure 4.29: A 2D double-notched specimen (ductile fracture)

Table 4.16: Comparisons of the computational time for a 2D double-notched specimen (ductile fracture)

Analysis	DNS	SCA homogeneous	SCA heterogeneous
CPU time, min	77.17	301.93	385.45

A 2D Sandia fracture challenge specimen is the last example in 2D plane strain ductile fracture tests. The model is discretized by 18589 fully integrated quadrilateral plane strain elements. The chosen length-scale parameter is equal to 0.4 mm. The analysis is performed in 200 increments using volumetric-deviatoric energy split.

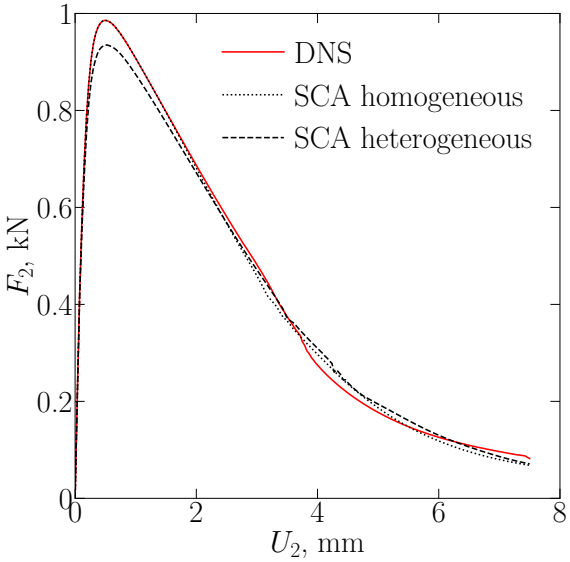

(a) Force-displacement curves

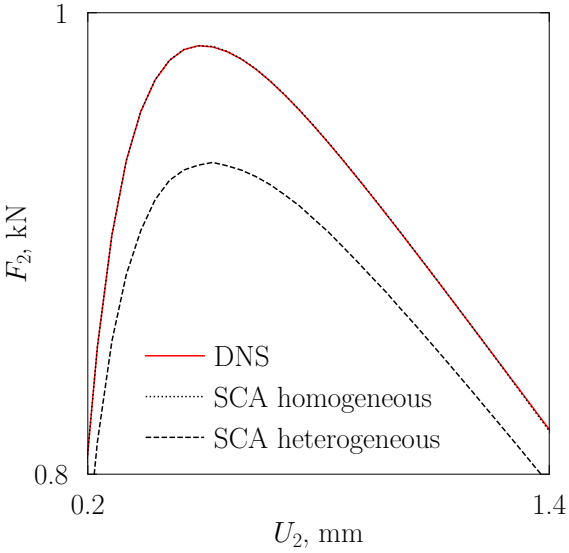

(b) Zoomed-in view

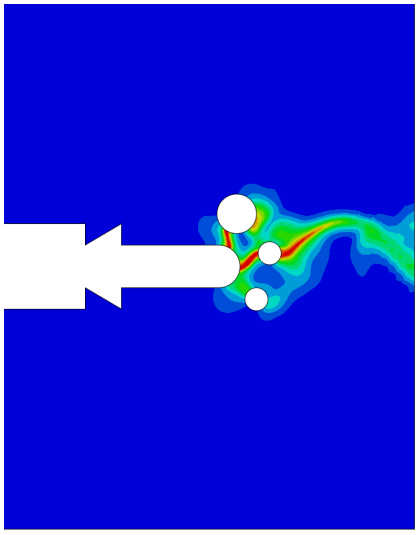

(c) Crack topology - DNS

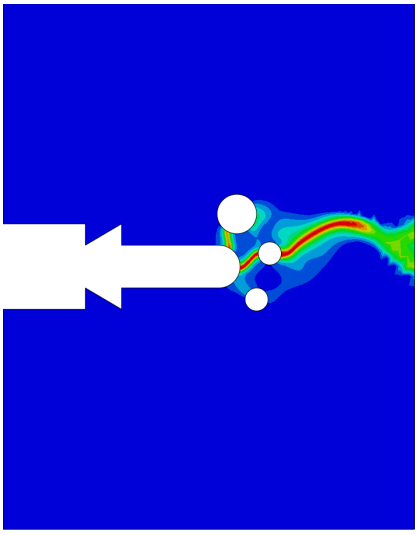

(d) Crack topology - SCA homogeneous

Figure 4.30: A 2D Sandia fracture challenge specimen; volumetric deviatoric-split

Table 4.17: Comparisons of the computational time for a 2D Sandia fracture challenge specimen; volumetric-deviatoric split

Analysis	DNS	SCA homogeneous	SCA heterogeneous
CPU time, min	90.75	522.47	1418.80

A 3D unnotched specimen is the first in line for 3D ductile fracture analysis. The model is discretized by 17673 fully integrated hexahedral elements. The chosen length-scale parameter is equal to 0.4 mm. The analysis is performed in 200 increments using no energy split.

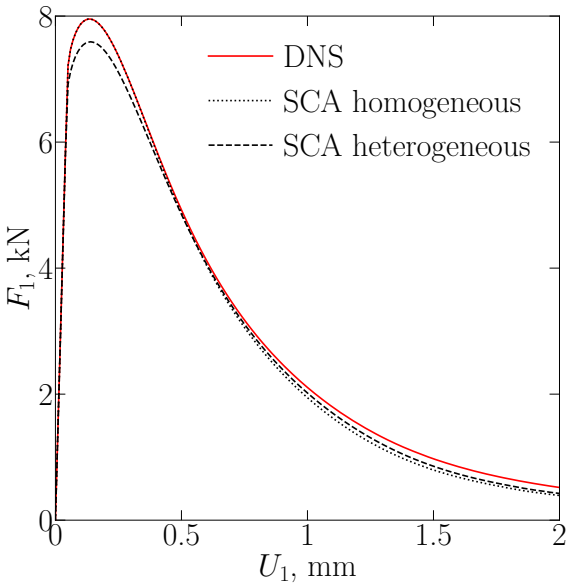

(a) Force-displacement curves

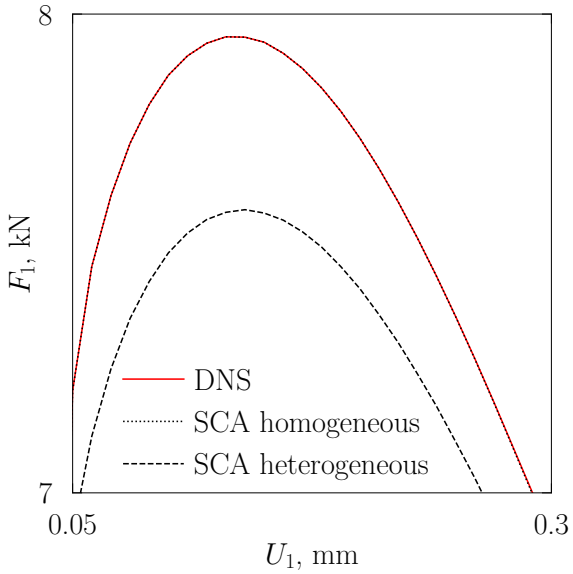

(b) Zoomed-in view

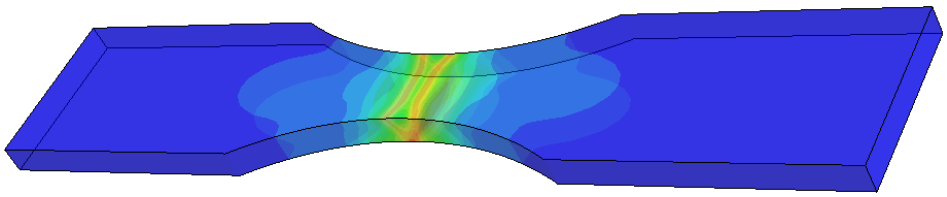

(c) Crack topology - DNS

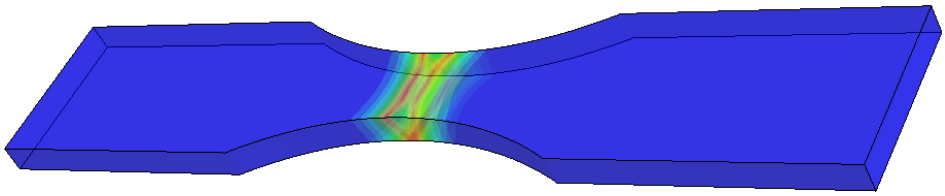

(d) Crack topology - SCA homogeneous

Figure 4.31: 3D unnotched specimen

Table 4.18: Comparisons of the computational time for a 3D unnotched specimen

Analysis	DNS	SCA homogeneous	SCA heterogeneous
CPU time, min	160.17	805.48	1123.37

A 3D double-notched specimen is also present in ductile fracture analysis. The model is discretized by 20757 fully integrated hexahedral elements. The chosen length-scale parameter is equal to 0.6 mm. The analysis is performed in 200 increments using no energy split.

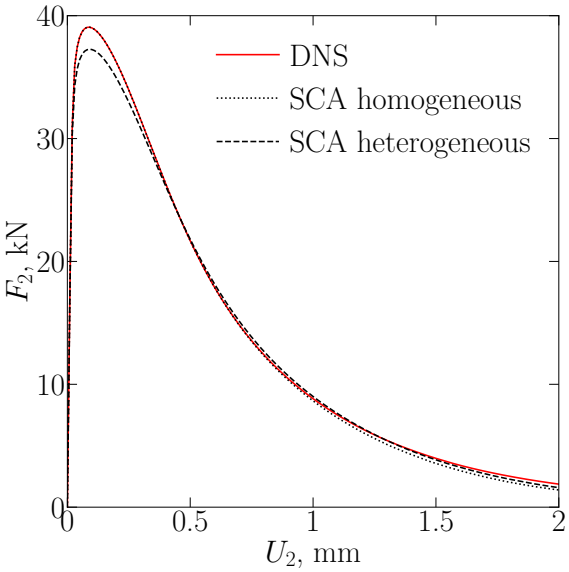

(a) Force-displacement curves

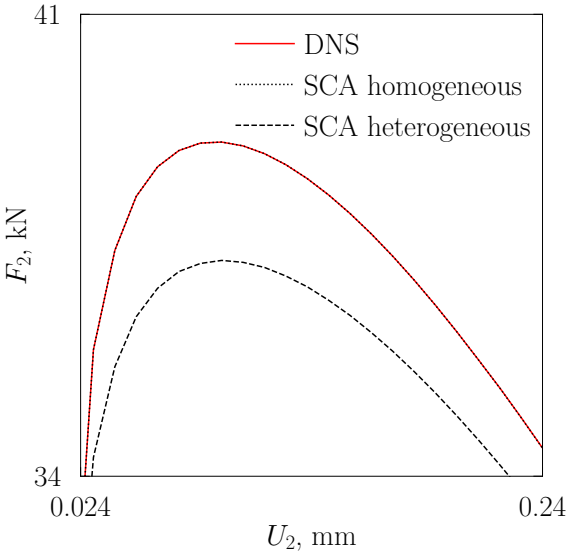

(b) Zoomed-in view

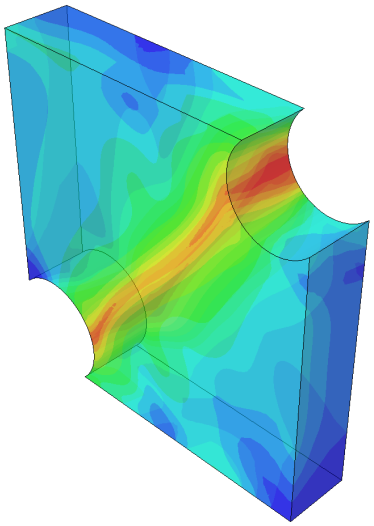

(c) Crack topology - DNS

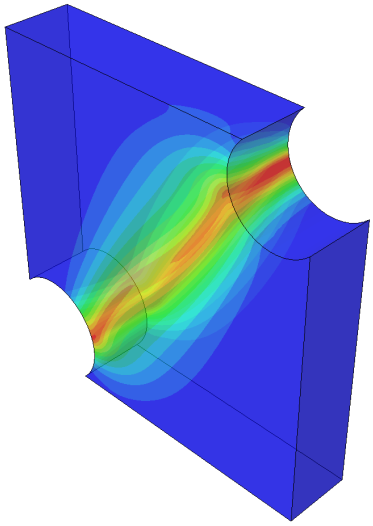

(d) Crack topology - SCA homogeneous

Figure 4.32: A 3D double-notched specimen (ductile fracture)

Table 4.19: Comparisons of the computational time for a 3D double-notched specimen (ductile fracture)

Analysis	DNS	SCA homogeneous	SCA heterogeneous
CPU time, min	261.23	1125.48	1440.85

A 3D Sandia fracture challenge specimen is the last example in this subsection. The model is discretized by 35241 fully integrated hexahedral elements. The chosen length-scale parameter is equal to 0.4 mm. The analysis is performed in 200 increments using no energy split.

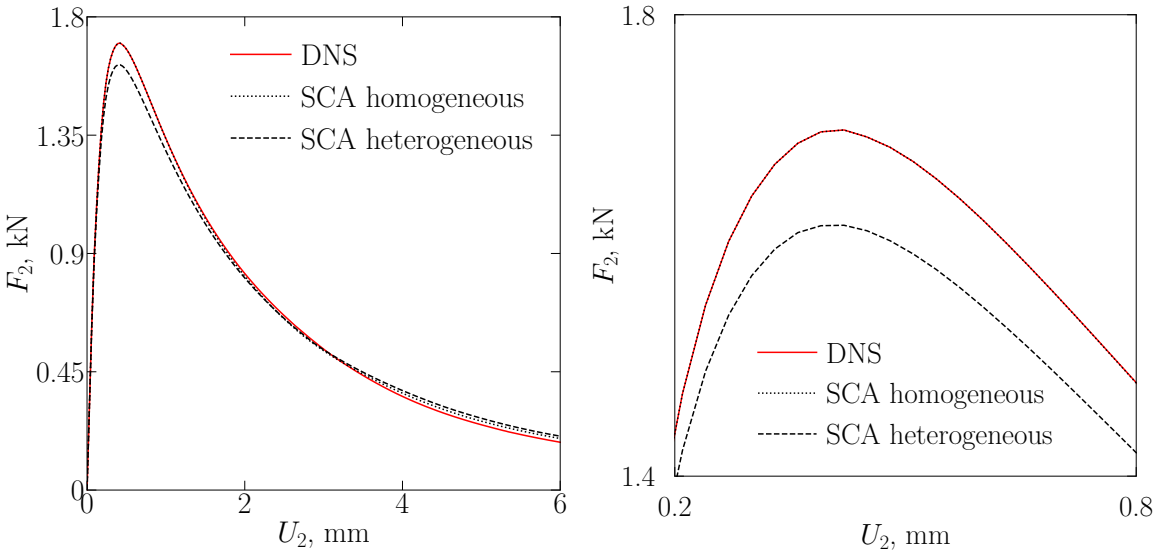

(a) Force-displacement curves

(b) Zoomed-in view

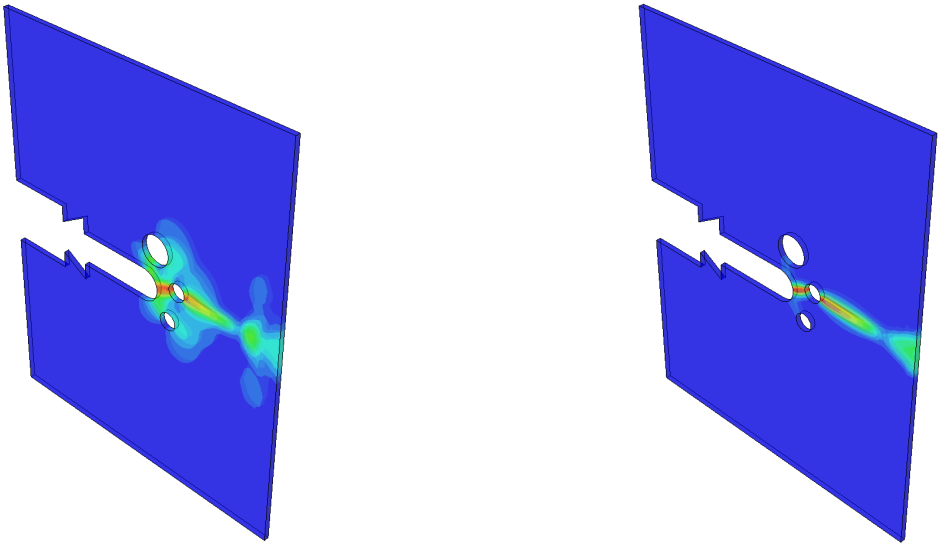

(c) Crack topology - DNS

(d) Crack topology - SCA homogeneous

Figure 4.33: A 3D Sandia fracture challenge specimen; volumetric-deviatoric split

Table 4.20: Comparisons of the computational time for a 3D Sandia fracture challenge specimen; volumetric-deviatoric split

Analysis	DNS	SCA homogeneous	SCA heterogeneous
CPU time, min	480.30	2220.15	5119.33

From the figures and tables provided in the previous pages, it can be concluded that the proposed algorithm is also able to describe ductile fracture in an accurate and computationally efficient way. As was the case in the previous subsection, the difference between force-displacement curves obtained using DNS and the concurrent approach (by means of first material configuration) is almost non-existent. However, this is not present throughout the whole loading history, since after a significant accumulation of damage the difference between the two approaches becomes visible. The point at which these discrepancies start and their magnitude varies from specimen to specimen, with their values being within the acceptable limits in all examples. A perfect correlation between the two approaches throughout the whole analysis is unrealistic, for both brittle and ductile fracture. What is important is the fact that both approaches give an almost exact match before the peak force occurs.

The results obtained by the concurrent approach using the second material configuration are in line with the expectations. Degradation of both modulus of elasticity and the initial value of yield strength yields a lower value of peak force in all examples. However, unlike in brittle fracture, this difference is clearly observed even without the zoomed-in views that are provided alongside each force-displacement diagram. This is, again, an important result, as it provides proof that the proposed concurrent procedure gives physically correct results when fracture in ductile materials is considered.

Figures that depict the crack phase-field for both DNS and "SCA homogeneous" are also in good agreement. The topologies of cracks in specimens that were also present in the analysis of brittle fracture are completely different, more precisely for the 2D notched plate with a hole and a 2D/3D double-notched specimen. A phenomenon of a more localized crack phase-field is also present in the case of ductile fracture analysis. This is especially noticeable when examining a 2D double-notched specimen, i.e. **Figure 4.16**.

In terms of computational efficiency, the factor for which the time needed to complete the concurrent analysis is higher for the case of ductile fracture. More precisely, in the 2D plane strain configuration, the average increase in computational time in regards to DNS is 6.97. This is approximately two times higher when compared to the brittle fracture. As was the case in the previous subsection, the increase for the case of 3D analysis is smaller and is equal to 6.19. Comparison with the increase in computational time for the case of 3D brittle fracture again results in an approximately two times higher value. This drop in computational efficiency is not unexpected, as the SCA algorithm at the microlevel now has to perform multiple iterations at each integration point in order to satisfy the stopping criterion.

In addition to having a higher increase in computational time when compared to DNS, the concurrent multiscale approach for the case of ductile fracture differs from the concurrent multiscale approach for the case of brittle fracture in one additional way. Namely, the increase in the computational time is higher when the modulus of elasticity E and the initial yield strength σ_y^0 of the inclusion are degraded, i.e. for "SCA heterogeneous". This is true for all test specimens; however, the ratio between times obtained with "SCA heterogeneous", i.e. "SCA homogeneous" varies. For example, this ratio for a 2D double-notched specimen is equal to 1.276, while for a 2D Sandia fracture challenge specimen its value is higher and amounts to 2.716. A 2D Sandia fracture challenge specimen represents, from the geometrical point of view, a more complex specimen and therefore is more sensitive to the changes at the microlevel. The main "driving force" behind the higher computational time of the "SCA heterogeneous" analyses is of course a higher level of heterogeneity that the unit cell/unit sphere now exhibits. In contrast to brittle fracture, where there exists no difference in the computational efficiency between the "SCA homogeneous" and "SCA heterogeneous" (as in both cases only one iteration at the microlevel is needed to satisfy the stopping criterion), the increase in the number of iterations at the microlevel is always on the side of "SCA heterogeneous" when a fracture in ductile microstructure is considered. This is because a higher level of heterogeneity, that is present in the "SCA heterogeneous", is forcing the self-consistent clustering analysis algorithm to perform a higher number of iterations than in the case of "SCA homogeneous" - where no level of material heterogeneity exists. Also, a more complex material and geometrical configuration at the microlevel can lead to slower convergence at the macrolevel, which further increases the total computational time of the analysis.

4.4. Complex RVEs analyses

The second stage of testing will focus on the algorithm's robustness and its ability to analyze more complex microstructures. The unit cell and unit sphere microstructural samples represent, from the point of geometrical and material configuration, extraordinarily simple RVEs. In contrast to them, RVEs depicted in **Figure 4.9** clearly represent more realistic microstructures, as they consist of multiple inclusions that all have specific size, shape and spatial orientation, and are randomly placed in space.

As was the case in the first stage of testing, both brittle and ductile fracture is considered; however, inclusions, in all analyses, are treated as a linear elastic material. Mechanical properties of the elastoplastic matrix correspond to those from [250] and

their values are

$$\begin{aligned} E = 228900 \text{ MPa}, \nu = 0.282, \\ \sigma_y^0 = 246.67 \text{ MPa}, k = 117.95, r = 0.208, \end{aligned} \tag{4.1}$$

while the mechanical behaviour of inclusions is modelled by means of material properties of isotropic graphite [251]

$$E = 25500 \text{ MPa}, \nu = 0.312. \tag{4.2}$$

Using values of the modulus of elasticity and the Poisson ratio that are provided in (4.1), i.e. (4.2), k-means clustering was conducted and the results of it are presented in **Figure 4.34** and **4.35**.

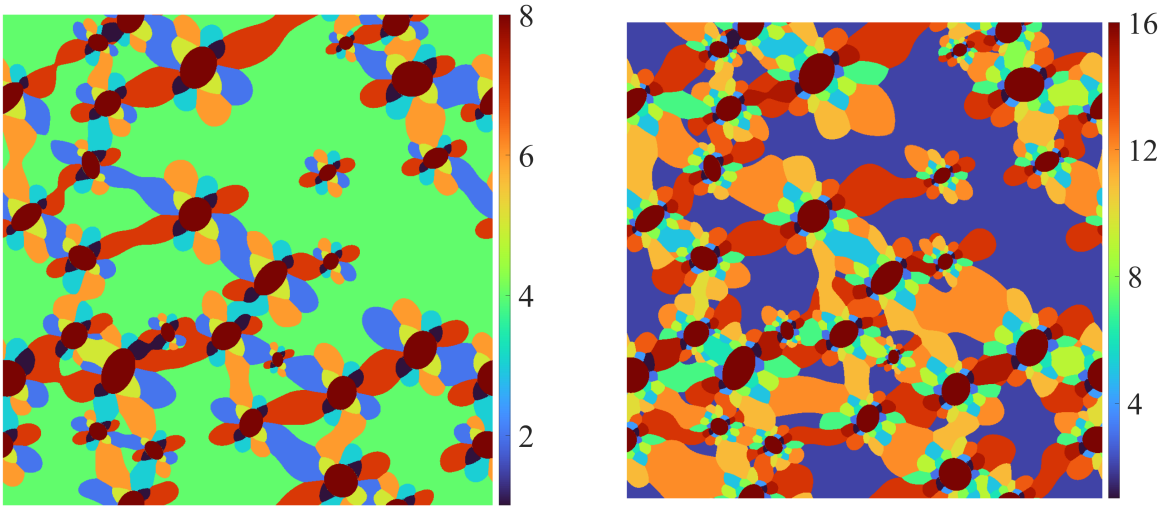

(a) $k = 8$ **(b)** $k = 16$

Figure 4.34: Results of the k-means clustering for the complex 2D RVE

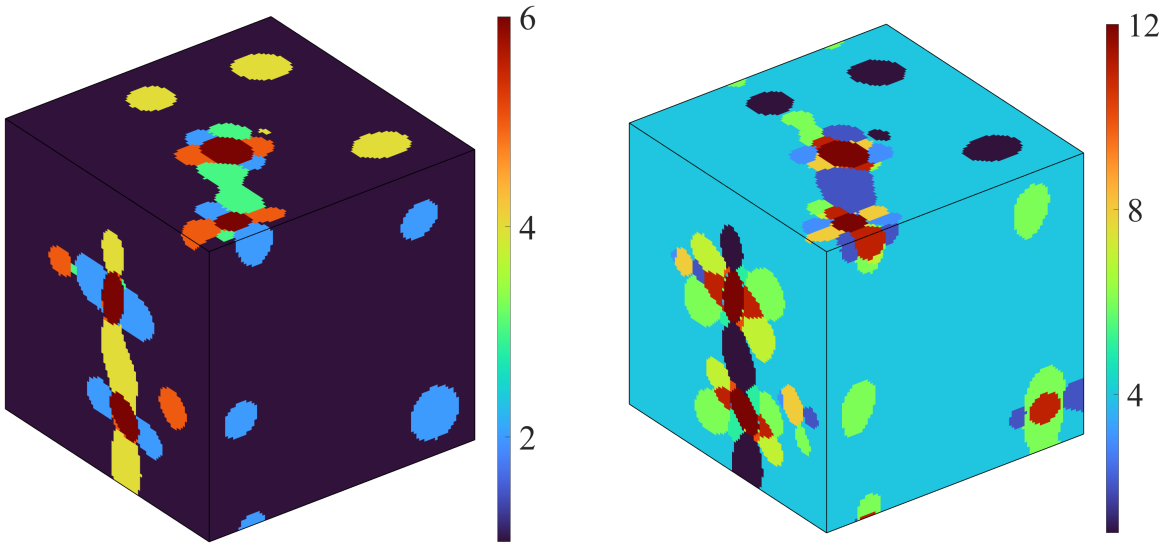

(a) $k = 6$ **(b)** $k = 12$

Figure 4.35: Results of the k-means clustering for the complex 3D RVE

As can be seen from both figures above, two discretizations will be used - with 8, i.e. 16 material clusters (for two-dimensional analyses) and 6, i.e. 12 material clusters (for three-dimensional analyses).

In order to perform phase-field simulation at the macrolevel, the critical value of strain energy release rate G_c and the length-scale parameter l are mandatory parameters. For both brittle and ductile fracture, values of critical strain energy release rate correspond to actual materials and are equal to

$$\begin{aligned} \text{brittle fracture} &\rightarrow G_c = 1.2597 \text{ N/mm}, \\ \text{ductile fracture} &\rightarrow G_c = 86.0 \text{ N/mm}. \end{aligned} \tag{4.3}$$

The first value in (4.3) corresponds to the value of G_c for the high carbon chromium alloy E52100, which was taken from the online material database MatWeb [252]. On the other hand, the value of G_c for ductile fracture analysis is related to the fracture property of the nodular cast iron obtained by the Tundish method of casting [248].

As far as the length-scale parameter l is considered, its values have not changed. More precisely, for a given test specimen and analysis (brittle or ductile fracture) the value of a length-scale parameter is already provided in **subsection 4.3.1** and **4.3.2**, i.e. in the initial phase of testing.

In addition to multiscale analysis with 8 and 16 (in 2D), i.e. 6 and 12 (in 3D) material clusters, a third analysis using DNS and the homogeneous properties of the RVEs is also conducted. Homogeneous properties of the microstructures depicted in **Figure 4.9**, and with the material properties defined through (4.1), i.e. (4.2), can be

obtained by running a uniaxial tension test with one finite element at the macrolevel. From the obtained macro stress-strain curve it is possible to calculate macro-values of: modulus of elasticity $\overline{E}$, Poisson ratio $\overline{\nu}$, initial yield strength $\overline{\sigma}_y^0$, Swift's law parameter $\overline{k}$ and Swift's law parameter $\overline{r}$. For the 2D RVE depicted in **Figure 4.9 (a)** the homogeneous parameters are

$$\begin{aligned} \overline{E} = 195.1 \text{ GPa}, \overline{\nu} = 0.2815, \\ \overline{\sigma}_y^0 = 248.9 \text{ MPa}, \overline{k} = 44.7468 \text{ MPa}, \overline{r} = 0.48836, \end{aligned} \tag{4.4}$$

while for the 3D RVE depicted in **Figure 4.9 (b)** the following macroscopic properties were obtained

$$\begin{aligned} \overline{E} = 216 \text{ GPa}, \overline{\nu} = 0.28, \\ \overline{\sigma}_y^0 = 252.8 \text{ MPa}, \overline{k} = 51.3573 \text{ MPa}, \overline{r} = 0.3865. \end{aligned} \tag{4.5}$$

Homogenized properties in (4.5) are actually mechanical properties of nodular cast iron that was obtained through Tundish mode of casting - see [248].

The results that are displayed in the following pages include force-displacement diagrams, and figures of crack topologies for the analysis conducted using DNS and proposed concurrent approach with a higher number of clusters - 16 for 2D plane strain analysis and 12 for 3D analysis. Computational efficiency here is not in the foreground and therefore computational times are not provided.

4.4.1. Brittle fracture

Both DNS and the concurrent multiscale analyses of brittle fracture include in total four test specimens: a 2D three-point bending specimen, 2D double-notched specimen, 3D three-point bending specimen and 3D double-notched specimen. Finite element meshes and values of the length-scale parameters correspond to those used in **subsection 4.3.1**, while material properties needed to run all analyses are provided by (4.1), (4.2), (4.4) and (4.5). Of course, when fracture in brittle materials is considered, only modulus of elasticity E and the Poisson ratio ν are required. The results obtained by the two approaches (DNS and concurrent multiscale) in this subsection are expected to be similar, if not the same, in the region before the fracture occurs, and to a certain degree different after the fracture had occurred, i.e. in the post-fracture region. The reason for the expected difference in the post-fracture region is due to a higher level of material nonlinearity, which should have a significant impact on the discrepancies between the results obtained by the two approaches.

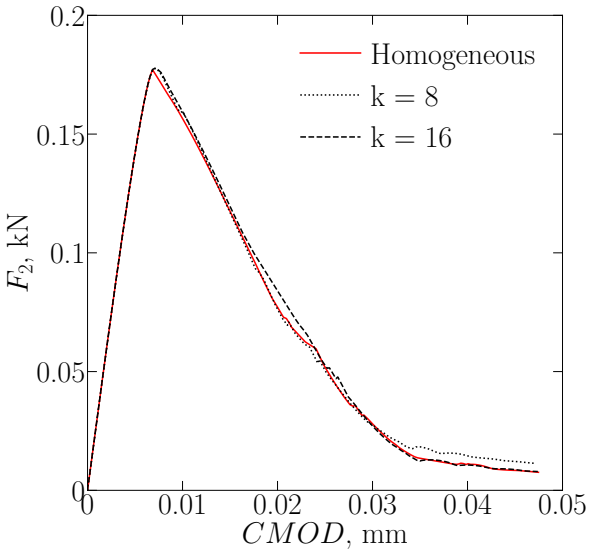

(a) Force-displacement curves

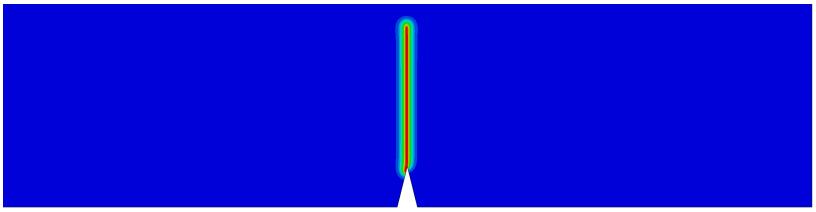

(b) Crack topology - DNS

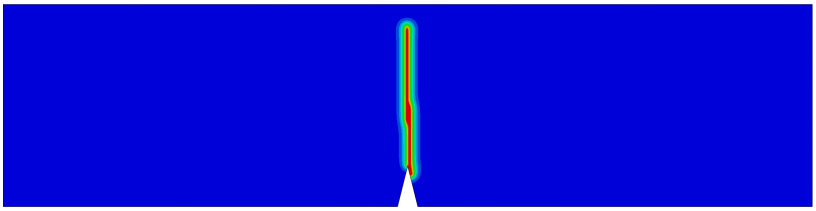

(c) Crack topology - SCA; k = 16

Figure 4.36: A 2D three-point bending specimen; spectral decomposition (complex RVE)

As evident from **Figure 4.36 (a)**, both DNS and concurrent multiscale approach give similar results in terms of force-displacement relationship. The difference between the two approaches is negligible in the pre-fracture region, i.e. before the reaction force reaches its peak value. Although not significant, the difference is noticeable in the post-fracture region, which was expected as a higher degree of material nonlinearity is included in the simulation. In terms of the crack topologies, both approaches give qualitatively the same crack paths; however, **Figure 4.36 (c)** shows a more irregular crack trajectory as material heterogeneity is now fully present in the analysis.

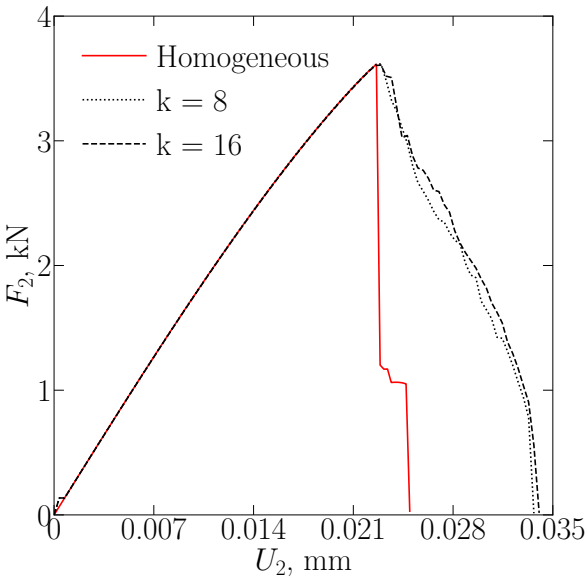

(a) Force-displacement curves

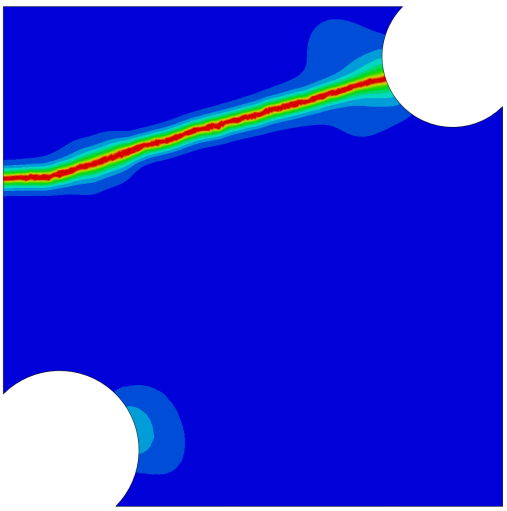

(b) Crack topology - DNS

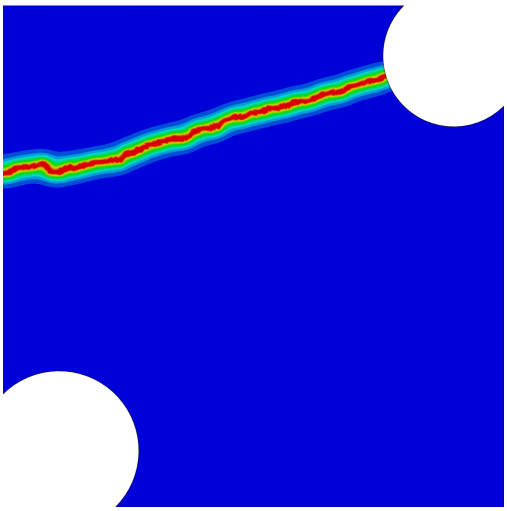

(c) Crack topology - SCA; k = 16

Figure 4.37: A 2D double-notched specimen (complex RVE)

In contrast to the previous example, where no significant difference in the force-displacement relationship was present, a 2D double-notched specimen shows noticeably different post-fracture behaviour when comparing DNS and concurrent multiscale approach. After the peak force is reached, results obtained using DNS and homogeneous material properties depict an abrupt loss in material stiffness. This is not the case in the concurrent multiscale approach, where material degradation follows a more gradual path. Before the peak force, both approaches give almost the same result. Similarly to the previous example, crack topologies are qualitatively similar, with the trajectory in **Figure 4.37 (c)** having again a more irregular path.

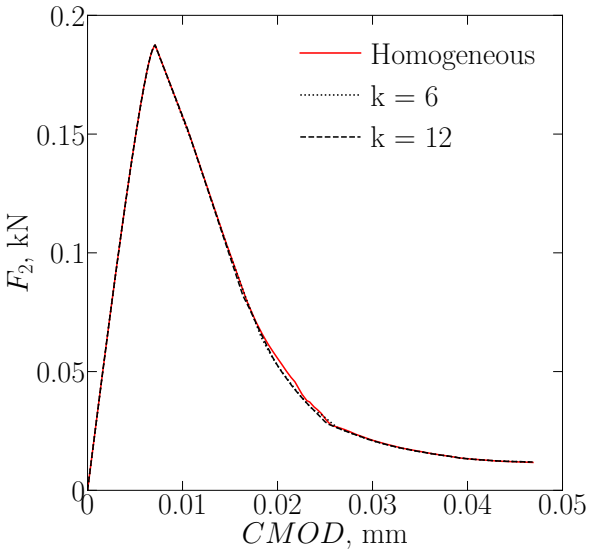

(a) Force-displacement curves

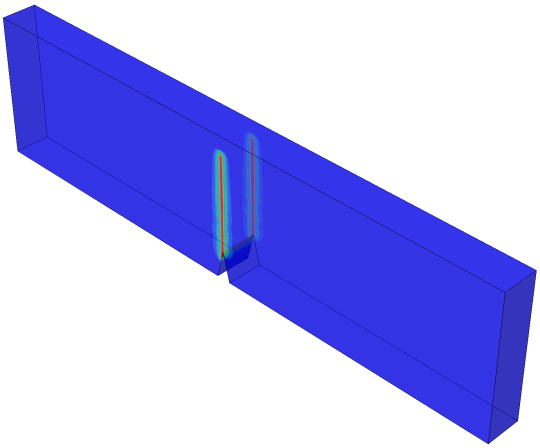

(b) Crack topology - DNS

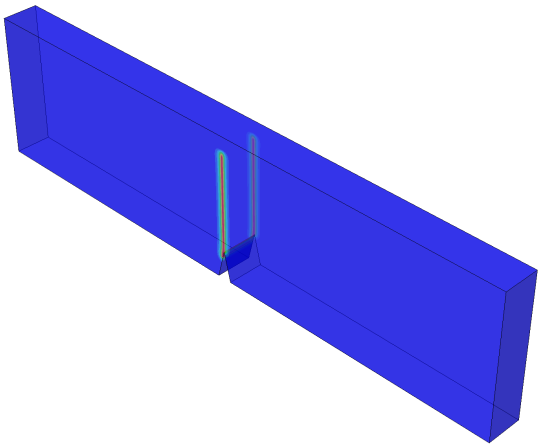

(c) Crack topology - SCA; k = 12

Figure 4.38: A 3D three-point bending specimen; spectral decomposition (complex RVE)

As was the case with a 2D three-point bending specimen (**Figure 4.36**), force-displacement curves obtained from the analyses of the 3D three-point bending specimen also show small discrepancies. However, from both **Figure 4.36 (a)** and **Figure 4.38 (a)** it is clear that the difference is even smaller if the 3D configuration is in question. When looking at **Figure 4.38 (b)** and **(c)**, it is evident that both approaches give exactly the same crack paths. Herein, crack topologie obtained using a concurrent approach exhibits no "noisy" behaviour, which was the case in the previous two examples. Notice also that the increase in the number of material clusters does not lead to major differences either in the pre- or the post-fracture behaviour. This is also observable from **Figure 4.36 (a)** and **4.37 (a)**.

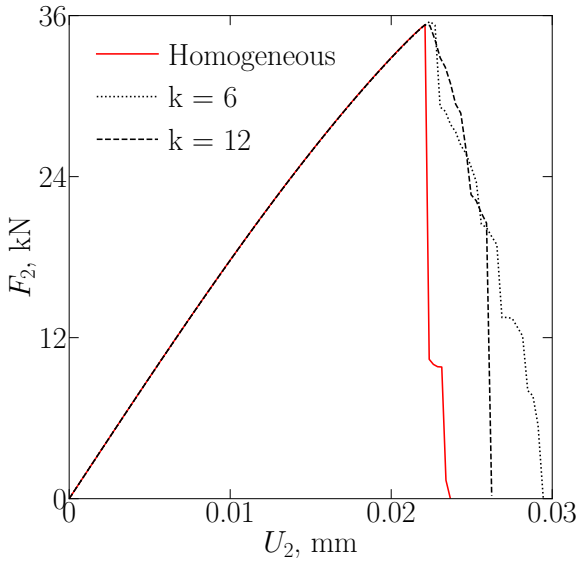

(a) Force-displacement curves

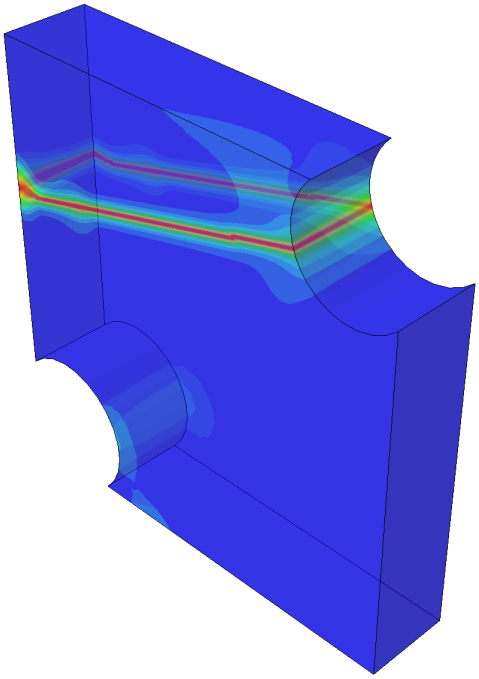

(b) Crack topology - DNS

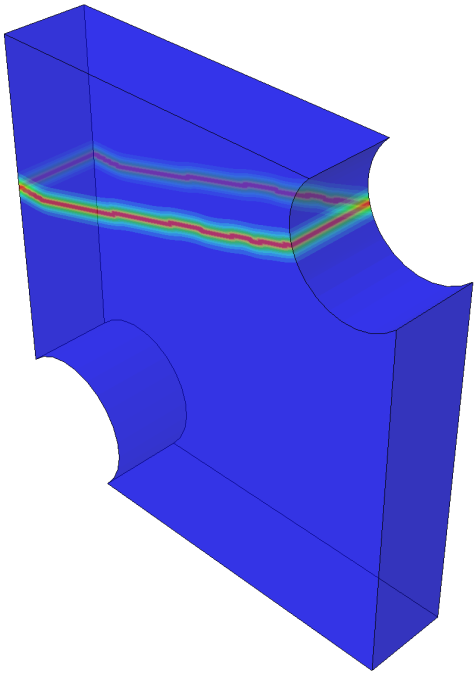

(c) Crack topology - SCA; k = 12

Figure 4.39: A 3D double notch specimen; (complex RVE)

The last example in this subsection, i.e. a 3D double-notched specimen shows similar behaviour to its 2D counterpart. In terms of force-displacement relationships, results obtained by both approaches are in excellent agreement in the pre-fracture region; however, when fracture does occur, DNS gives again a more abrupt drop in material stiffness. When looking at crack topologies, the crack phase-field obtained with the concurrent approach (using 12 material clusters) shows again a more irregular

and realistic crack propagation curve. Also, notice from **Figure 4.39 (a)** that in this example there are more noticeable differences between the analysis run with 6, i.e. 12 material clusters.

4.4.2. Ductile fracture

As was the case in the previous subsection, DNS and the concurrent multiscale analyses in this subsection will also include four test specimens in total: a 2D unnotched specimen, 2D double-notched specimen, 3D unnotched specimen and 3D double-notched specimen. Finite element mesh and values of the length-scale parameters are also already defined - see **subsection 4.3.2**. Unlike the previous subsection, in the case of ductile fracture, all five material parameters provided in (4.1), (4.4) and (4.5) are required in order the perform simulations.

Here it is important to note that unlike the homogenized (macroscopic) values of the modulus of elasticity $\overline{E}$ and the Poisson ratio $\overline{\nu}$, the homogenized parameters that describe the hardening curve ($\overline{\sigma}_{\mathrm{y}}^{0}, \overline{k}$ and $\overline{r}$) are not uniquely determined. The reason for this lies in: (1) the way in which the initial yield strength is determined, and (2) the value of the macroscopic strain at which the uniaxial tension was performed.

The first aspect directly impacts the value of the macroscopic initial yield strength $\overline{\sigma}_{\mathrm{y}}^{0}$. The conventional way of determining σ_{y}^{0}, which is used in this dissertation, comes down to evaluating the value of equivalent (von Mises) stress at the equivalent plastic deformation of 0.2 %. This means that the $\overline{\sigma}_{\mathrm{y}}^{0}$ in both (4.4) and (4.5) was obtained for $\overline{\varepsilon}_{\mathrm{eq}}^{p} = 0.002$. However, different values of the macroscopic equivalent plastic strain $\overline{\varepsilon}_{\mathrm{eq}}^{p}$ can be used and therefore different values of the initial macroscopic yield strength $\overline{\sigma}_{\mathrm{y}}^{0}$ can be obtained. In reality, at $\overline{\varepsilon}_{\mathrm{eq}}^{p} = 0.002$ the material has already entered the elastoplastic region and started to accumulate plastic deformation.

The second aspect is related to the values of $\overline{k}$ and $\overline{r}$. More precisely, these parameters are obtained by performing a non-linear curve fit of the macroscopic data that consists of homogenized equivalent plastic strain and homogenized von Mises stress. Depending on the data that is available, the non-linear curve fit will produce different values of $\overline{k}$ and $\overline{r}$. In this dissertation, the uniaxial tension on one 2D/3D finite element was performed under a total macroscopic longitudinal strain of 15 %. In other words, an element with a side length of one millimeter was loaded by the uniaxial displacement of 0.15 millimeters. As in the first aspect, herein it is also acceptable to use different values of the macroscopic displacement, i.e. deformation.

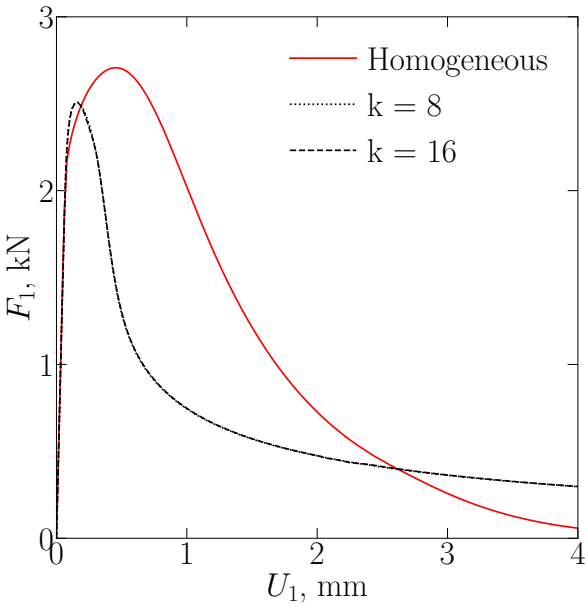

(a) Force-displacement curve

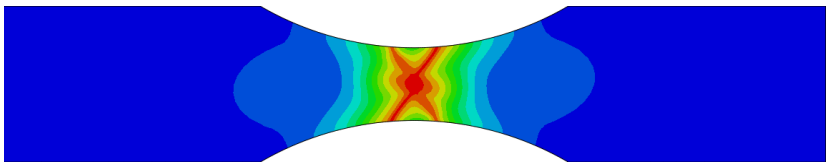

(b) Crack topology - DNS

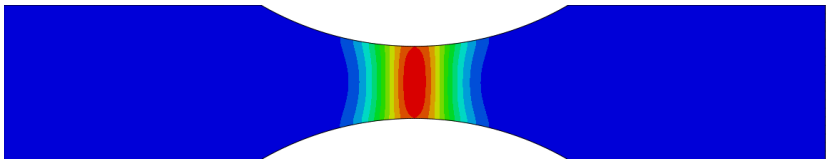

(c) Crack topology - SCA; k = 16

Figure 4.40: A 2D unnotched specimen (complex RVE)

From **Figure 4.40 (a)** it is clear that the trend of the same force-displacement relationship, before the peak force is reached, is again present in the case of fracture in ductile heterogeneous material. However, herein, there is a significant difference between the peak force obtained by DNS and the concurrent multiscale approach. From **Figure 4.40 (a)** it is also visible that the rate of material degradation is noticeably higher in the case of multiscale analysis. The main factor that influences this behaviour is the value of the macroscopic initial yield strength, which in the case of homogeneous material is determined as the value of homogenized von Mises stress at the homogenized equivalent plastic strain of 0.2 %. This means, that the homogeneous material enters the elastoplastic region only when von Mises stress exceeds the value

of 248.9 MPa, while for the heterogeneous material that transition will happen for lower values of the macroscopic von Mises stress. In terms of crack topologies, both DNS and the concurrent multiscale approach do not provide similar results - not even qualitatively. This is again a direct consequence of material parameters determination that was discussed in **subsection 4.4.2**.

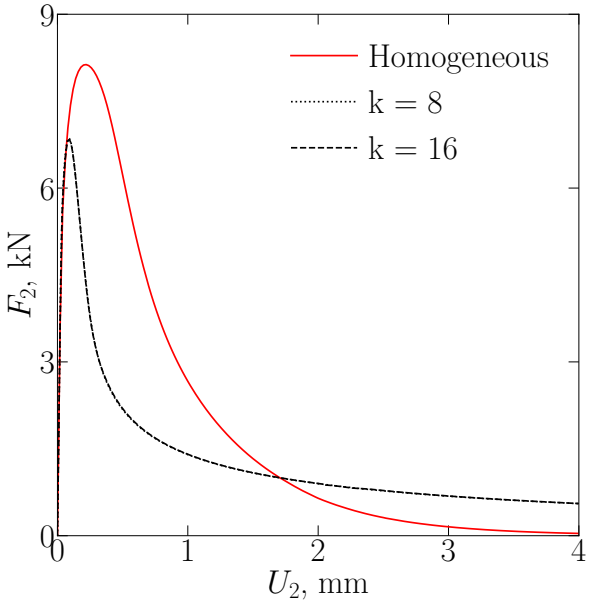

(a) Force-displacement curve

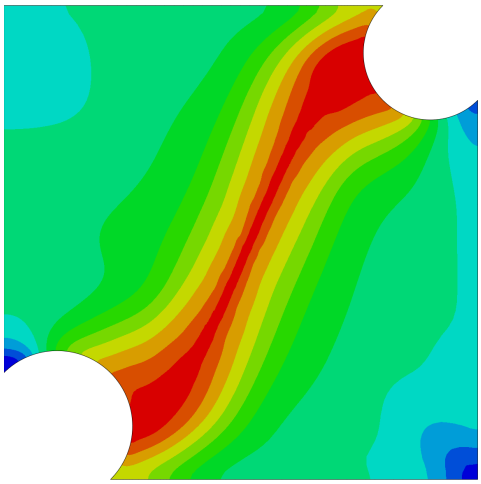

(b) Crack topology - DNS

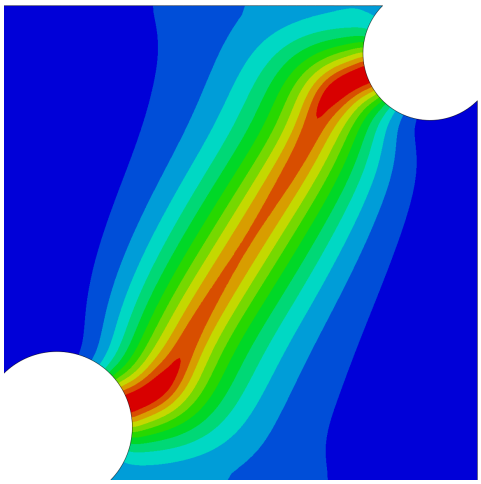

(c) Crack topology - SCA; k = 16

Figure 4.41: A 2D double-notched specimen (ductile fracture; complex RVE)

As can be seen from **Figure 4.41 (a)**, the difference in the rate of material degradation between the two approaches is even more significant for the case of a 2D double-notched specimen. When compared to the concurrent approach, the peak force obtained by the DNS sits on an 18.6 % higher value, which is more than double

when compared to the 2D unnotched specimen where the peak force for the case of DNS was 7.94 % higher - see **Figure 4.40 (a)**. On the other hand, crack topologies depicted in **Figure 4.41 (b)** and **(c)** are qualitatively similar, which wasn't the case for the 2D unnotched specimen. However, the damaged region obtained by the concurrent multiscale approach (using 16 material clusters) is more localized than the one obtained by the DNS (using homogeneous material properties).

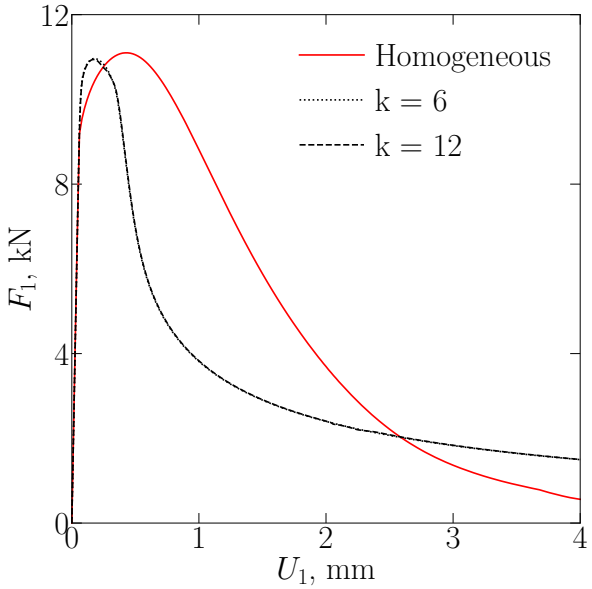

(a) Force-displacement curve

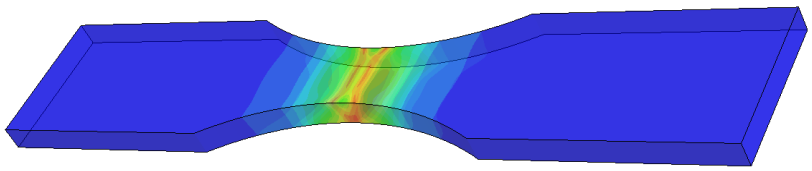

(b) Crack topology - DNS

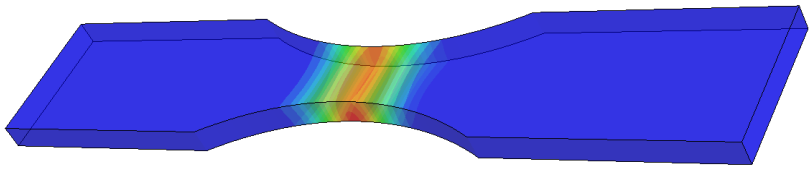

(c) Crack topology - SCA; k = 12

Figure 4.42: A 3D unnotched specimen (complex RVE)

Figure 4.42 (a) shows a negligible difference between the peak force obtained by the two approaches, with the value obtained by the DNS being only 1.4 % higher. However, a more "aggressive" rate of material degradation is again present in the case of a concurrent multiscale approach. Notice also that this faster rate of material degradation is not characteristic for the whole analysis, but rather for one portion

of it. At some point, the degradation rate for the case of a concurrent approach falls below that of a DNS. The same phenomenon is also observable in **Figure 4.40 (a)** and **Figure 4.41 (a)**. Crack topologies on the other hand are quite similar for both approaches; however, with again more localized damage zone when the concurrent approach is considered.

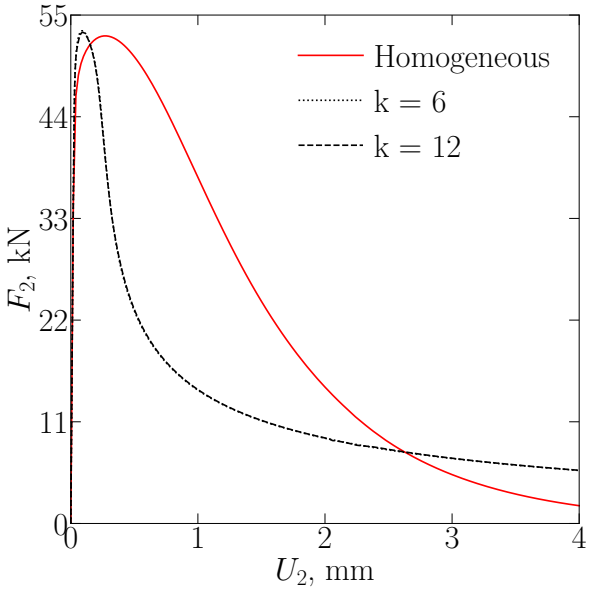

(a) Force-displacement curve

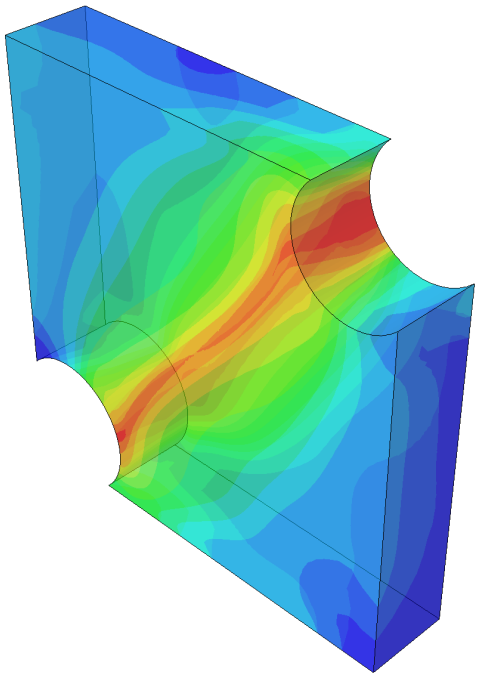

(b) Crack topology - DNS

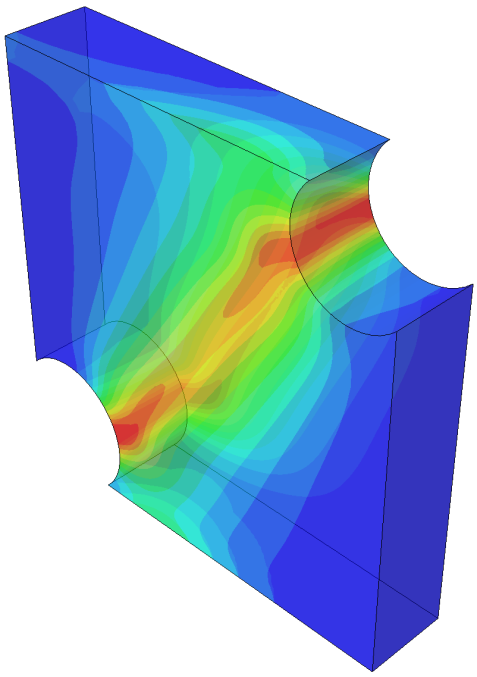

(c) Crack topology - SCA; k = 12

Figure 4.43: A 3D double-notched specimen (ductile fracture; complex RVE)

From the last figure in this dissertation, it is clear that the 3D double-notched specimen behaves similarly to the 3D unnotched specimen. **Figure 4.43 (a)** shows again a higher and faster material degradation when microstructural effects are taken into account. Although the peak force in all previous examples was higher for the DNS (homogeneous material), in this case, the opposite is true. However, the concurrent approach gives a value of the peak force that is only 1.1 % higher when compared to DNS. Last but not least, crack phase-fields depicted in **Figure 4.43 (b)** and **(c)** are in good agreement, with again more localized damage zone being present when the concurrent multiscale approach is in question. Also, notice that for all the examples shown in this subsection, no difference in the force-displacement relationship is observed when different cluster discretizations are considered.

5. Conclusions and future work

5.1. Achievements

Numerical modelling of damage and fracture in heterogeneous materials represents an ongoing challenge in the field of computational mechanics. Since fracture under any kind of loading is highly sensitive to the microstructure that forms the material, the use of classical phenomenological constitutive relations that characterize the average behaviour of the material is not an adequate solution. For a more realistic and accurate description of damage and fracture in heterogeneous materials, novel and advanced modelling techniques that include microstructural effects in the calculation are required.

Concurrent multiscale methods are one category of such techniques since they possess the ability to link the microstructure (which is characterized by the representative volume element, i.e. RVE) and the behaviour of the material at the macrolevel through the process of homogenization. If utilized exclusively using DNS, concurrent multiscale methods come at the cost of high computational resources and long computational time. Even without the inclusion of the damage calculation, concurrent multiscale methods still exhibit the previously mentioned shortcomings. However, when numerical modelling of damage comes into the equation, the number of issues increases even further. In addition to high computational costs, there are also problems related to stable convergence, non-objective results and questionable representativeness of the RVE. Resolving one problem usually creates a new one, or requires additional sacrifices and compromises in terms of computational efficiency. Also, the goal of every multiscale algorithm should be generality and robustness, i.e. the ability to model a large suite of constitutive laws and materials with complex and arbitrary microstructures. Last, but not least, the issue of mesh dependence at the macrolevel must not be neglected. The choice of either discrete (discontinuous) or diffusive (continuum) damage model at the macrolevel requires adequate treatment. If a discrete damage modelling approach is utilized at the macrolevel, mesh dependence needs to be resolved by introducing additional criteria for crack initiation and propagation as well as the

remeshing algorithm (for resolving discontinuity at the element's edge) or some kind of element enrichment (for resolving discontinuity on the element itself). In the case of a diffusive damage approach, pathological mesh dependence at the macrolevel is resolved only if a non-local approach, driven by a non-local variable, is introduced.

The main objective of the research presented in this dissertation was to develop and implement an accurate, robust, computationally efficient but also general concurrent multiscale procedure for modelling of damage and fracture in ductile heterogeneous materials. By combining the best features of the reduced order homogenization method called self-consistent clustering analysis (SCA) and the phase-field fracture method, the research attempted to satisfy all the necessary requirements of a highly efficient multiscale damage algorithm. The SCA has been given the task of resolving the RVE boundary value problem at the microlevel and determining the average (homogenized) properties for a given value of macro small strain tensor. On the other hand, the phase-field method was utilized at the macrolevel in order to determine the value of material degradation from the homogenized properties that were obtained by the SCA. The use of reduced-order homogenization method, such as the SCA, at the microlevel ensures accuracy and computational efficiency, while the presence of the non-local continuum damage model, such as phase-field, provides mesh independence and an accurate description of complex material processes that arise during the formation and propagation of crack(s). The absence of a damage algorithm at the microlevel and the separation of two methods helps to maintain a clear distinction between two scales but also provides an additional level of numerical stability.

In this dissertation, the SCA is first implemented in the commercial software Matlab. First for small, and later for finite elastoplastic strains. The implemented SCA algorithm has been thoroughly tested on several different microstructures loaded by different macro-strain constraints for both two- and three-dimensional configuration. The developed algorithm has been proven capable of accurate and computationally efficient calculation of the homogenized stress-strain relations when compared to the DNS, which was performed using commercial finite element software Abaqus. Unfortunately, the algorithm's behaviour in finite strain configuration was not satisfactory and therefore the problem of large elastoplastic strains was not considered in the concurrent procedure.

After the successful implementation of the SCA algorithm into Matlab, in order to perform concurrent analyses, the SCA was implemented into Abaqus (using user UEL and UMAT subroutines) and combined with the already tested and verified phase-field staggered algorithm. The testing of the developed concurrent approach has been performed in two stages. In the initial stage of testing, the accuracy and

computational efficiency of the proposed procedure have been thoroughly examined. The testing was performed on several geometrical specimens with simple unit cell, i.e. unit sphere microstructures at the microlevel. For every analysis, force-displacement diagram, crack phase-field and overall time needed to complete the analysis has been provided. The robustness of the proposed approach was put to the test in the second phase, where more complicated microstructures were present at the microlevel. Both the first and the second phase of testing included brittle and ductile heterogeneous materials.

The main contributions of this dissertation are made in the field of multiscale modelling of damage and fracture in brittle and ductile heterogeneous materials. The main contributions are as follows:

1. Implementation of the SCA into commercial finite element software Abaqus
    - The SCA algorithm has been initially developed and tested in commercial software Matlab. With the goal of conducting concurrent multiscale simulations, the algorithm was later implemented into commercial finite element software Abaqus.
    - Multiple tests on different 2D and 3D microstructures have shown a noticeable level of computational efficiency and overall accuracy of homogenized results, which is crucial in every multiscale procedure. In addition, it has been shown that some forms of macro-strain constraints, under certain material configurations at the microlevel, should be avoided.
    - The SCA algorithm was initially developed for the description of small elastic and elastoplastic deformations, and later on was extended to model large elastoplastic deformations. However, the algorithm in the case of finite strains shows unexpected behaviour and is not able to provide satisfactory results. For that reason, an additional and detailed mathematical investigation will be necessary in order to resolve this issue.
2. Combining the phase-field method and SCA into one unique multiscale procedure
    - The developed concurrent multiscale approach is proven to be correct and computationally efficient, which is shown by the multiscale simulations carried out on several geometrical specimens for both brittle and ductile fracture.
    - The approach is also robust, which is again evident from simulations that were carried out on different geometrical specimens, where more complex microstructure was present at the microlevel.

- Ultimately, the approach is general and adaptive. More precisely, the extension to other material types, e.g. hyperelastic materials, and other plasticity models such as the Drucker-Prager or Mohr-Columb yield criterion represents a relatively simple procedure.

5.2. Suggestions for future work

Although there are many research directions based on the work in this dissertation, three main suggestions include: (1) the improvement of the SCA accuracy, (2) resolving issues concerning finite strain analysis using SCA and (3) calculation of the phase-field fracture parameters (l, and G_c) directly from the microstructure.

Even though the data-driven SCA homogenization algorithm shows good accuracy for various heterogeneous material systems, its ability to provide highly accurate results in three-dimensional configuration is noticeably lower in contrast to two-dimensional configuration. In order to ensure higher levels of accuracy in three dimensions, the offline stage of the SCA must be improved. This improvement can be achieved in two ways: (1) discretization of the complex 3D RVE with a higher number of voxels, and (2) improvements in the material characterization of the mechanical behaviour of each voxel. The first improvement does not represent something complicated or advance and can be achieved by using either an FFT-based numerical solver or by applying an iterative method (instead of direct) for solving the FEM linear system of equations. Both approaches will allow for a significantly higher number of voxels in the data collection stage as a direct solution of the DNS problem using FEM requires a noticeably higher computational capacity in terms of RAM. The second improvement is more complex and includes the use of additional material descriptors, besides the strain concentration tensor, to characterize each material point and to improve the quality of k-means clustering. Which additional information would improve the clustering analysis remains an open question. In addition to the improvements in the offline stage, the SCA's online stage, i.e. the self-consistent scheme is a part that also needs a more thorough investigation. The self-consistent scheme has been proposed to improve the accuracy; however, the mechanism behind this procedure requires better understanding, which can be achieved only through rigorous mathematical testing.

The second suggestion is related to the situation when finite strains are present in the analysis. As was shown in **subsection 2.6.1**, the SCA algorithm is unable to provide satisfactory results when large elastoplastic deformations occur. In the

regression based scheme, the only way of conducting the analysis was to decompose the microstructure into k number of material clusters that is equal to the number of material phases. However, this discretization is not sufficient and cannot give accurate results for various types of heterogeneous material systems. The projection based scheme on the other hand did not experience any stability issues when dealing with finite strain configuration; however, its accuracy wasn't at the desired level, even with a relatively high number of material clusters. This area of the SCA obviously requires additional analysis and testing, as there should be a clear reason, i.e. explanation for why the regression based scheme performs the analysis correctly only when the number of material clusters is equal to the number of material phases. The focus should be on the derivation of the Lippmann-Schwinger equation for the case of finite strains, which, as stated in **subsection 2.3.2** is not physically justified. As a good starting point, derivation based on the second Piola-Kirchhoff stress tensor $\mathbf{S}$ and the right Cauchy–Green deformation tensor $\mathbf{C}$ should be thoroughly investigated. Also, the use of the mentioned tensors could be a better choice, in contrast to the first Piola-Kirchhoff stress tensor $\mathbf{P}$ and the deformation gradient $\mathbf{F}$, when the regression based scheme is utilized in the online stage.

The last, i.e. third suggestion is not related to the SCA but rather the phase-field fracture method itself. The length scale parameter l and the critical value of the energy release rate G_{c} are necessary parameters in every phase-field simulation and represent key factors that determine a point of crack formation and the rate of its propagation. In this research, their macroscopic values have been "directly" prescribed and were not connected, in any way, to the RVE that was analyzed. In reality, both geometrical and material configuration at the microlevel have an impact on the value of l and G_{c} at the macrolevel. Therefore, homogenized (macroscopic) values of both $\overline{l}$ and $\overline{G}_{\mathrm{c}}$ should be calculated directly from the RVE itself, as in that way all the material properties at the macrolevel would come directly from the information at a lower level. Performing a uniaxial tension FEM analysis on the RVE seems like a good starting point, as it would allow for observation of the RVE's fracture property directly using the most accurate approach.

With all the above, the utilization of neural networks would also contribute to the effectiveness of the SCA. A well trained neural network can increase the computational efficiency of the SCA even further, thus reducing the time needed for the conduction of the fully concurrent multiscale approach. The use of neural networks in the field of computational mechanics has experienced a significant upswing in recent years, which is why they should be considered as a possible upgrade to the online phase of the SCA algorithm.

Appendices

A. Inverse Fourier transform of Green's function for small strains

Originally, Green's function for the case of small strains has been derived in **subsection 2.4.1** in the Fourier space as

$$\hat{\Phi}^0_{ijkl}(\boldsymbol{\xi}) = \frac{1}{4\mu^0\xi_m\xi_m}\left(\delta_{ik}\xi_j\xi_l + \delta_{il}\xi_j\xi_k + \delta_{jl}\xi_i\xi_k + \delta_{jk}\xi_i\xi_l\right) - \frac{\lambda^0+\mu^0}{\mu^0\left(\lambda^0+2\mu^0\right)}\frac{\xi_i\xi_j\xi_k\xi_l}{\xi_m\xi_m\xi_n\xi_n}, \tag{A.1}$$

with $\boldsymbol{\xi}$, i.e. ξ_i being a coordinate vector in Fourier space. Unlike the spatial domain, the Fourier domain is defined through frequencies, which as well as spatial coordinates, take values between negative and positive infinity. For a one-dimensional scalar function y, Fourier transform $\mathscr{F}$ is defined through a definite integral

$$\mathscr{F}\left[y\left(x\right)\right] = \hat{y}\left(\xi\right) = \frac{1}{2\pi}\int_{-\infty}^{\infty} y\left(x\right)\exp\left(-i\xi x\right)\mathrm{d}x, \tag{A.2}$$

where i denotes complex number, $\hat{y}$ indicates that the function is defined in the frequency domain, while ξ is the one-dimensional coordinate in the Fourier space. On the other hand, inverse Fourier transform $\mathscr{F}^{-1}$ is also defined as a definite integral and allows for a function in the frequency domain to be transformed into a spatial domain, i.e.

$$\mathscr{F}^{-1}\left[\hat{y}\left(\xi\right)\right] = y\left(x\right) = \int_{-\infty}^{\infty}\hat{y}\left(\xi\right)\exp\left(i\xi x\right)\mathrm{d}\xi. \tag{A.3}$$

For a two-dimensional scalar function y, the Fourier transform $\mathscr{F}$ can be written as

$$\mathscr{F}\left[y\left(x_1,x_2\right)\right] = \hat{y}\left(\xi_1,\xi_2\right) = \frac{1}{2\pi}\int_{-\infty}^{\infty}\int_{-\infty}^{\infty} y\left(x_1,x_2\right)\exp\left[-i\left(\xi_1x_1+\xi_2x_2\right)\right]\mathrm{d}x_1\mathrm{d}x_2, \tag{A.4}$$

while its inverse is then

$$\begin{gathered}\mathscr{F}^{-1}\left[\hat{y}\left(\xi_1,\xi_2\right)\right]=y\left(x_1,x_2\right)= \\ \int_{-\infty}^{\infty}\int_{-\infty}^{\infty}\hat{y}\left(\xi_1,\xi_2\right)\exp\left[i\left(\xi_1x_1+\xi_2x_2\right)\right]\mathrm{d}\xi_1\mathrm{d}\xi_2.\end{gathered} \tag{A.5}$$

Since definite integrals in (A.2) and (A.4) are defined on a full spectrum, i.e. from negative to positive infinity, any function y, either one-dimensional or multi-dimensional, that undergoes Fourier transform has to obey

$$\lim_{x_i\to\ \pm\infty} y\left(x_i\right)=0. \tag{A.6}$$

If this is not the case, the definite integral will go to positive/negative infinity, making both Fourier and inverse Fourier transform undetermined. An important property of the Fourier transform, needed for this derivation, refers to a derivative of a scalar function y. More precisely, for the Fourier transform of the derivative of function y, it is valid to write

$$\mathscr{F}\left[y'\left(x\right)\right]=i\xi\mathscr{F}\left[y\left(x\right)\right]. \tag{A.7}$$

This can be proven with the use of integration by parts, i.e.

$$\begin{gathered}\frac{1}{2\pi}\int_{-\infty}^{\infty}y'\left(x\right)\exp\left(-i\xi x\right)\mathrm{d}x=\frac{1}{2\pi}\left[y\left(x\right)\exp\left(-i\xi x\right)\right]|_{-\infty}^{\infty}- \\ \frac{1}{2\pi}\int_{-\infty}^{\infty}y\left(x\right)\exp\left(-i\xi x\right)\left(-i\xi\right)\mathrm{d}x.\end{gathered} \tag{A.8}$$

Using (A.6), the first term on the right-hand side of Eq. (A.8) vanishes leaving

$$\frac{1}{2\pi}\int_{-\infty}^{\infty}y'\left(x\right)\exp\left(-i\xi x\right)\mathrm{d}x=\frac{1}{2\pi}i\xi\int_{-\infty}^{\infty}y\left(x\right)\exp\left(-i\xi x\right)\mathrm{d}x, \tag{A.9}$$

which is the identity (A.7). Following this procedure, Fourier transform for the higher-order derivative can also be derived. For a Fourier transform of a fourth-order derivative of a one-dimensional scalar function y, the rule is

$$\mathscr{F}\left[y^{(IV)}\left(x\right)\right]=\xi^4\mathscr{F}\left[y\left(x\right)\right], \tag{A.10}$$

where $y^{(IV)}$ denotes the fourth-order derivative of function y.

A direct application of the inverse Fourier transform $\mathscr{F}^{-1}$ on the (A.1) would eventually produce extremely complex integrals, whose solution would be almost impossible to obtain. Therefore, the problem of the transformation from frequency

to spatial domain will be solved gradually. From [227], the Fourier transform of the functions

$$g\left(x_1,x_2\right)=\frac{1}{16\pi}\left(x_1^2+x_2^2\right)\ln\left(x_1^2+x_2^2\right)=\frac{1}{16\pi}x_ix_i\ln\left(x_jx_j\right), \tag{A.11}$$

and

$$h\left(x_1,x_2,x_3\right)=-\frac{1}{8\pi}\sqrt{x_1^2+x_2^2+x_3^2}=-\frac{1}{8\pi}\sqrt{x_ix_i}, \tag{A.12}$$

takes the following form

$$\mathscr{F}[g\left(x_1,x_2\right)]=\frac{1}{\left(\xi_1^2+\xi_2^2\right)^2}=\frac{1}{\xi_i\xi_i\xi_j\xi_j}, \tag{A.13}$$

$$\mathscr{F}[h\left(x_1,x_2,x_3\right)]=\frac{1}{\left(\xi_1^2+\xi_2^2+\xi_3^2\right)^2}=\frac{1}{\xi_i\xi_i\xi_j\xi_j}. \tag{A.14}$$

Moreover, functions g and h are fundamental solutions to the biharmonic differential equation in 2D

$$\frac{\partial^4 g\left(x_1,x_2\right)}{\partial x_i\partial x_i\partial x_j\partial x_j}=0, \tag{A.15}$$

and 3D

$$\frac{\partial^4 h\left(x_1,x_2,x_3\right)}{\partial x_i\partial x_i\partial x_j\partial x_j}=0. \tag{A.16}$$

Using partial fractions, the initial form of Green's function, i.e. Eq. (A.1) can be rewritten as

$$\begin{aligned}\hat{\Phi}^0_{ijkl}\left(\boldsymbol{\xi}\right)=\frac{1}{\mu^0}\left[\frac{\xi_p\xi_p\left(\delta_{ik}\xi_j\xi_l+\delta_{il}\xi_j\xi_k+\delta_{jl}\xi_i\xi_k+\delta_{jk}\xi_i\xi_l\right)-4\xi_i\xi_j\xi_k\xi_l}{4\xi_m\xi_m\xi_n\xi_n}\right]+\\ \frac{1}{\lambda^0+2\mu^0}\frac{\xi_i\xi_j\xi_k\xi_l}{\xi_m\xi_m\xi_n\xi_n},\end{aligned} \tag{A.17}$$

and by applying identities in (A.10), (A.13) and (A.14) on a newly written Eq. (A.17), Green's function in the spatial domain is obtained for the case of two-dimensional analysis

$$\begin{aligned}\Phi^0_{ijkl}\left(\mathbf{x},\mathbf{x}'\right)=\frac{1}{4\mu^0}\left[\delta_{ik}g^{(ppjl)}+\delta_{il}g^{(ppjk)}+\delta_{jl}g^{(ppik)}+\delta_{jk}g^{(ppil)}-4g^{(ijkl)}\right]+\\ \frac{1}{\lambda^0+2\mu^0}g^{(ijkl)},\end{aligned} \tag{A.18}$$

as well as three-dimensional analysis

$$\Phi^0_{ijkl}\left(\mathbf{x},\mathbf{x}'\right)=\frac{1}{4\mu^0}\left[\delta_{ik}h^{(ppjl)}+\delta_{il}h^{(ppjk)}+\delta_{jl}h^{(ppik)}+\delta_{jk}h^{(ppil)}-4h^{(ijkl)}\right]+\frac{1}{\lambda^0+2\mu^0}h^{(ijkl)}. \tag{A.19}$$

In Eq. (A.18) and (A.19) indices in the superscript indicate the derivation of the function. For example, $g^{(ijkl)}$ implies

$$g^{(ijkl)}=\frac{\partial^4 g\left(x_1,x_2\right)}{\partial x_i\partial x_j\partial x_k\partial x_l}, \tag{A.20}$$

while $h^{(ppik)}$ is equal to

$$h^{(ppkl)}=\frac{\partial^4 h\left(x_1,x_2,x_3\right)}{\partial x_p\partial x_p\partial x_i\partial x_k}. \tag{A.21}$$

B. Inverse Fourier transform of Green's function for finite strains

The procedure for obtaining Green's function in the spatial domain for the case of finite strains follows the same procedure that was outlined in **Appendix A**. To begin with, Green's function derived in **subsection 2.4.2** for the case of finite strains is given by

$$\hat{\Phi}^0_{ijkl}(\boldsymbol{\Xi}) = \frac{1}{\mu^0 \Xi_m \Xi_m}\left(\delta_{ik}\Xi_j\Xi_l - \frac{\lambda^0+\mu^0}{\lambda^0+2\mu^0}\frac{\Xi_i\Xi_j\Xi_k\Xi_l}{\Xi_n\Xi_n}\right). \tag{B.1}$$

where $\boldsymbol{\Xi}$, i.e. Ξ_i is a coordinate vector in the Fourier space. Once again, it should be noted that both ξ_i and its capital Ξ_i represent the same coordinate in the frequency domain, as Fourier space does not discriminate between the current and reference configuration. The only reason for choosing Ξ_i over ξ_i is the additional clarity and the consistency with the capitalization of the position vector $\mathbf{x}$ that is present in the spatial domain.

As in the case of small strains, with the use of partial fractions, Green's function in (B.1) is rewritten in the following form

$$\hat{\Phi}^0_{ijkl}(\boldsymbol{\Xi}) = \frac{1}{\mu^0}\left(\frac{\delta_{ik}\Xi_j\Xi_l\Xi_p\Xi_p - \Xi_i\Xi_j\Xi_k\Xi_l}{\Xi_m\Xi_m\Xi_n\Xi_n}\right) + \frac{1}{\lambda^0+2\mu^0}\frac{\Xi_i\Xi_j\Xi_k\Xi_l}{\Xi_m\Xi_m\Xi_n\Xi_n}. \tag{B.2}$$

Now, using the fourth-order derivative rule of the Fourier transform of a one-dimensional scalar function Y

$$\mathscr{F}\left[Y^{(IV)}(X)\right] = \Xi^4 \mathscr{F}\left[Y(X)\right], \tag{B.3}$$

and having in mind the values of a Fourier transform for scalar functions G and H are

$$G(X_1, X_2) = \frac{1}{16\pi}(X_iX_i)\ln(X_jX_j) \rightarrow \mathscr{F}[G(X_1, X_2)] = \frac{1}{\Xi_i\Xi_i\Xi_j\Xi_j}, \tag{B.4}$$

$$H\left(X_1, X_2, X_3\right) = -\frac{1}{8\pi}\sqrt{X_i X_i} \rightarrow \mathscr{F}[H\left(X_1, X_2, X_3\right)] = \frac{1}{\Xi_i \Xi_i \Xi_j \Xi_j}, \tag{B.5}$$

Green's function in the spatial domain for finite strains is obtained for the case of two-dimensional analysis

$$\hat{\Phi}^0_{ijkl}\left(\mathbf{X}, \mathbf{X}'\right) = \frac{1}{\mu^0}\left(\delta_{ik} G^{(ppjl)} - G^{(ijkl)}\right) + \frac{1}{\lambda^0 + 2\mu^0} G^{(ijkl)}, \tag{B.6}$$

as well as three-dimensional analysis

$$\hat{\Phi}^0_{ijkl}\left(\mathbf{X}, \mathbf{X}'\right) = \frac{1}{\mu^0}\left(\delta_{ik} H^{(ppjl)} - H^{(ijkl)}\right) + \frac{1}{\lambda^0 + 2\mu^0} H^{(ijkl)}. \tag{B.7}$$

In Eq. (B.6) and (B.7) indices in the superscript indicate the derivation of the function. For example, $G^{(ijkl)}$ implies

$$G^{(ijkl)} = \frac{\partial^4 G\left(X_1, X_2\right)}{\partial X_i \partial X_j \partial X_k \partial X_l}, \tag{B.8}$$

while $H^{(ppik)}$ is equal to

$$H^{(ppik)} = \frac{\partial^4 H\left(X_1, X_2, X_3\right)}{\partial X_p \partial X_p \partial X_i \partial X_k}. \tag{B.9}$$

Životopis

Ante Jurčević rođen je u Zagrebu, 21. studenog 1994. godine. Osnovnu školu pohađao je u Zagrebu, gdje je 2009. godine upisao opću gimnaziju. Nakon mature, 2013. godine upisuje Fakultet strojarstva i brodogradnje na Sveučilištu u Zagrebu, a na drugoj godini odabire smjer Inženjersko modeliranje i računalne simulacije. Diplomirao je 2018. godine uz najvišu pohvalu (summa cum laude) uz diplomski rad pod nazivom "Mikromehaničko modeliranje vlačnog testa nodularnog lijeva" pod vodstvom prof. dr. sc. Zdenka Tonkovića. Od 2018. godine zaposlen je na Fakultetu strojarstva i brodogradnje Sveučilišta u Zagrebu na Zavodu za tehničku mehaniku kao asistent. Iste godine upisao je i postdiplomski studij - smjer Numerička mehanika. Kao istraživač sudjelovao je na 2 znanstvena projekta. Autor i koautor je ukupno 10 znanstvenih radova od kojih je jedan objavljen u CC znanstvenom časopisu.

Curriculum vitae

Ante Jurčević was born on November 21st 1994 in Zagreb. He attended primary school in Zagreb, where he enrolled in grammar school in 2009. After graduating in 2013, he enrolled Faculty of Mechanical Engineering and Naval Architecture at the University of Zagreb. He graduated in 2018 with the highest honors (summa cum laude) and with the graduation thesis on the theme "Micromechanical Modeling of Nodular Cast Iron Tensile Test" under the supervision of Prof. Zdenko Tonković. Since 2018, he has been employed as a research assistant at the Department of Technical Mechanics at the Faculty of Mechanical Engineering and Naval Architecture, University of Zagreb. In the same year, he enrolled in postgraduate studies in Numerical Mechanics. As a researcher, he participated in two scientific projects. He is the author and co-author of 10 scientific papers in total, including one contribution published in CC scientific journal.

Bibliography

[1] A.E. Jakus, E.B. Secor, A.L. Rutz, S.W. Jordan, M.C. Hersam, and R.N. Shah, Three-Dimensional Printing of High-Content Graphene Scaffolds for Electronic and Biomedical Applications, *ACS Nano* 9 (2015), 4636–4648.

[2] L.R. Meza, S. Das, and J.R. Greer, Strong, lightweight, and recoverable three-dimensional ceramic nanolattices, *Science* 345 (2014), 1322–1326.

[3] L.R. Meza, A.J. Zelhofer, N. Clarke, A.J. Mateos, D.M. Kochmann, and J.R. Greer, Resilient 3D hierarchical architected metamaterials, *PNAS* 112 (2015), 11502–11507.

[4] Z. Tomić, N. Gubeljak, T. Jarak, T. Polančec, and Z. Tonković, Micro- and macromechanical properties of sintered steel with different porosity, *Scripta Materialia* 217 (2022).

[5] T. Polančec, T. Lesičar, Z. Tonković, and S. Glodež, Modelling of rolling-contact fatigue pitting phenomena by phase field method, *Wear* 532-533 (2023).

[6] T. Polančec, T. Lesičar, and J. Rako, Constitutive Modelling of Sintered Steel by Phase-field Method, *Procedia Structural Integrity* 52 (2024), 348–355.

[7] E.A. de Souza Neto, D. Perić, and D.R.J. Owen, *Computational Methods for Plasticity: Theory and Applications,* 1st ed. Wiley, 2008.

[8] R. Bidulský, J. Bidulská, and M.A. Grande, Analysis of Densification Process and Structure of PM Al-Mg-Si-Cu-Fe and Al-Zn-Mg-Cu-Sn Alloys, *Archives of Metallurgy and Materials* 59 (2014), 17–23.

[9] S. Hampshire, Silicon nitride ceramics - review of structure, processing and properties, *Journal of Achievements in Materials and Manufacturing Engineering* 24 (2007), 43–50.

[10] URL: https://www.polcast.com.tr/en/nodular-graphite-cast-iron.

[11] J. Hu, Y. Mu, Q. Xu, N. Yao, S. Li, and X. Lei, The Effect of the Forging Process on the Microstructure and Mechanical Properties of a New Low-Cost Ti-5Al-1.5Mo-1.8Fe Alloy, *Materials* 16 (2023).

[12] E. Cosserat and F. Cosserat, Théorie des Corps déformables, *Nature* 81 (1909), 67–67.

[13] R.D. Mindlin, Micro-structure in linear elasticity, *Archive for Rational Mechanics and Analysis* 16 (1964), 51–78.

[14] R.D. Mindlin, Second gradient of strain and surface-tension in linear elasticity, *International Journal of Solids and Structures* 1 (1965), 417–438.

[15] R.D. Mindlin and H.F. Tiersten, Effects of couple-stresses in linear elasticity, *Archive for Rational Mechanics and Analysis* 11 (1962), 415–448.

[16] R.D. Mindlin, Influence of couple-stresses on stress concentrations, *Experimental Mechanics* 3 (1963), 1–7.

[17] W. Koiter, Couple Stresses in the Theory of Elasticity, I & II, *Philosophical Transactions of the Royal Society of London B* 67 (1964), 17–44.

[18] R.A. Toupin, Elastic materials with couple-stresses, *Archive for Rational Mechanics and Analysis* 11 (1962), 385–414.

[19] R.A. Toupin, Theories of elasticity with couple-stress, *Archive for Rational Mechanics and Analysis* 17 (1964), 85–112.

[20] A.C. Eringen and E.S. Suhubi, Nonlinear theory of simple micro-elastic solids—I, *International Journal of Engineering Science* 2 (1964), 189–203.

[21] R.D. Mindlin and N.N. Eshel, On first strain-gradient theories in linear elasticity, *International Journal of Solids and Structures* 4 (1968), 109–124.

[22] P. Germain, The Method of Virtual Power in Continuum Mechanics. Part 2: Microstructure, *SIAM Journal on Applied Mathematics* 25 (1973), 556–575.

[23] A. Zervos, P. Papanastasiou, and I. Vardoulakis, A finite element displacement formulation for gradient elastoplasticity, *International Journal for Numerical Methods in Engineering* 50 (2001), 1369–1388.

[24] N.A. Fleck and J.W. Hutchinson, A phenomenological theory for strain gradient effects in plasticity, *Journal of the Mechanics and Physics of Solids* 41 (1993), 1825–1857.

[25] N.A. Fleck, G.M. Muller, M.F. Ashby, and J.W. Hutchinson, Strain gradient plasticity: Theory and experiment, *Acta Metallurgica et Materialia* 42 (1994), 475–487.

[26] R.A.B. Engelen, M.G.D. Geers, and F.P.T. Baaijens, Nonlocal implicit gradient-enhanced elasto-plasticity for the modelling of softening behaviour, *International Journal of Plasticity* 19 (2003), 403–433.

[27] R. De Borst and H.-B. Mühlhaus, Gradient-dependent plasticity: Formulation and algorithmic aspects, *International Journal for Numerical Methods in Engineering* 35 (1992), 521–539.

[28] R. de Borst, J. Pamin, and M.G.D. Geers, On coupled gradient-dependent plasticity and damage theories with a view to localization analysis, *European Journal of Mechanics - A/Solids* 18 (1999), 939–962.

[29] T.-H. Tran, V. Monchiet, and G. Bonnet, A micromechanics-based approach for the derivation of constitutive elastic coefficients of strain-gradient media, *International Journal of Solids and Structures* 49 (2012), 783–792.

[30] T. Lesičar, Multiscale modeling of heterogeneous materials using second-order homogenization, PhD thesis, University of Zagreb, 2015.

[31] J.L.L. Mishnaevsky and S. Schmauder, Continuum Mesomechanical Finite Element Modeling in Materials Development: A State-of-the-Art Review, *Applied Mechanics Reviews* 54 (2001), 49–67.

[32] V.P. Nguyen, M. Stroeven, and L.J. Sluys, Multiscale continuous and discontinuous modeling of heterogeneous materials: A review on recent developments, *Journal of Multiscale Modelling* 3 (2011), 229–270.

[33] M.G.D. Geers, V.G. Kouznetsova, and W.A.M. Brekelmans, Multi-scale computational homogenization: Trends and challenges, *Journal of Computational and Applied Mathematics* 234 (2010), 2175–2182.

[34] U. Galvanetto and M.H.F. Aliabadi, *Multiscale Modeling in Solid Mechanics,* 1st ed. Imperial College Press, 2010.

[35] T. Lesičar, Z. Tonković, and J. Sorić, A second-order two-scale homogenization procedure using C^1 macrolevel discretization, *Computational Mechanics* 54 (2014), 425–441.

[36] T. Lesičar, J. Sorić, and Z. Tonković, Large strain, two-scale computational approach using C^1 continuity finite element employing a second gradient theory, *Computer Methods in Applied Mechanics and Engineering* 298 (2016), 303–324.

[37] F. Feyel and J.-L. Chaboche, FE^2 multiscale approach for modelling the elastoviscoplastic behaviour of long fibre SiC/Ti composite materials, *Computer Methods in Applied Mechanics and Engineering* 183 (2000), 309–330.

[38] V. Kouznetsova, M.G.D. Geers, and W.A.M. Brekelmans, Multi-scale constitutive modelling of heterogeneous materials with a gradient-enhanced computational homogenization scheme, *International Journal for Numerical Methods in Engineering* 54 (2002), 1235–1260.

[39] V. Kouznetsova, W.A.M. Brekelmans, and F.P.T. Baaijens, An approach to micro-macro modeling of heterogeneous materials, *Computational Mechanics* 27 (2001), 37–48.

[40] C. Miehe and A. Koch, Computational micro-to-macro transitions of discretized microstructures undergoing small strains, *Archive of Applied Mechanics* 72 (2002), 300–317.

[41] C. Miehe, J. Schröder, and J. Schotte, Computational homogenization analysis in finite plasticity Simulation of texture development in polycrystalline materials, *Computer Methods in Applied Mechanics and Engineering* 171 (1999), 387–418.

[42] C. Miehe, J. Schotte, and J. Schröder, Computational micro–macro transitions and overall moduli in the analysis of polycrystals at large strains, *Computational Materials Science* 16 (1999), 372–382.

[43] I. Temizer and T.I. Zohdi, A numerical method for homogenization in non-linear elasticity, *Computational Mechanics* 40 (2007), 281–298.

[44] Ł. Kaczmarczyk, C.J. Pearce, and N. Bićanić, Studies of microstructural size effect and higher-order deformation in second-order computational homogenization, *Computers & Structures* 88 (2010), 1383–1390.

[45] V.-D. Nguyen, G. Becker, and L. Noels, Multiscale computational homogenization methods with a gradient enhanced scheme based on the discontinuous Galerkin formulation, *Computer Methods in Applied Mechanics and Engineering* 260 (2013), 63–77.

[46] X. Bai, M.A. Bessa, A.R. Melro, P.P. Camanho, L. Guo, and W.K. Liu, High-fidelity micro-scale modeling of the thermo-visco-plastic behavior of carbon fiber polymer matrix composites, *Composite Structures* 134 (2015), 132–141.

[47] N. Vu-Bac, M.A. Bessa, T. Rabczuk, and W.K. Liu, A Multiscale Model for the Quasi-Static Thermo-Plastic Behavior of Highly Cross-Linked Glassy Polymers, *Macromolecules* 48 (2015), 6713–6723.

[48] I.M. Gitman, H. Askes, and E.C. Aifantis, The Representative Volume Size in Static and Dynamic Micro-Macro Transitions, *International Journal of Fracture* 135 (2005), L3–L9.

[49] K. Baek, W. Lee, H. Shin, and M. Cho, Multiscale study on determining representative volume elements size for mechanical behaviours of complex polymer nanocomposites with nanoparticulate agglomerations, *Composite Structures* 253 (2020).

[50] I.M. Gitman, H. Askes, and L.J. Sluys, Representative volume: Existence and size determination, *Engineering Fracture Mechanics* 74 (2007), 2518–2534.

[51] R. Hill, Elastic properties of reinforced solids: Some theoretical principles, *Journal of the Mechanics and Physics of Solids* 11 (1963), 357–372.

[52] R. Hill, A self-consistent mechanics of composite materials, *Journal of the Mechanics and Physics of Solids* 13 (1965), 213–222.

[53] O.C. Zienkiewicz, R.L. Taylor, and J.Z. Zhu, *The Finite Element Method: Its Basis and Fundamentals,* 6th ed. Elsevier, 2005.

[54] R.A. Lebensohn, A.K. Kanjarla, and P. Eisenlohr, An elasto-viscoplastic formulation based on fast Fourier transforms for the prediction of micromechanical fields in polycrystalline materials, *International Journal of Plasticity* 32-33 (2012), 59–69.

[55] H. Moulinec and P. Suquet, A numerical method for computing the overall response of nonlinear composites with complex microstructure, *Computer Methods in Applied Mechanics and Engineering* 157 (1998), 69–94.

[56] J.D. Eshelby, The Determination of the Elastic Field of an Ellipsoidal Inclusion, and Related Problems, *Proceedings of the Royal Society of London. Series A, Mathematical and Physical Sciences* 241 (1957), 376–396.

[57] Z. Hashin and S. Shtrikman, A variational approach to the theory of the elastic behaviour of multiphase materials, *Journal of the Mechanics and Physics of Solids* 11 (1963), 127–140.

[58] Z. Liu, J.A. Moore, S.M. Aldousari, H.S. Hedia, S.A. Asiri, and W.K Liu, A statistical descriptor based volume-integral micromechanics model of heterogeneous material with arbitrary inclusion shape, *Computational Mechanics* 55 (2015), 963–981.

[59] B. Budiansky, On the elastic moduli of some heterogeneous materials, *Journal of the Mechanics and Physics of Solids* 13 (1965), 223–227.

[60] S. Ghosh, K. Lee, and S. Moorthy, Two scale analysis of heterogeneous elastic-plastic materials with asymptotic homogenization and Voronoi cell finite element model, *Computer Methods in Applied Mechanics and Engineering* 132 (1996), 63–116.

[61] M. Paley and J. Aboudi, Micromechanical analysis of composites by the generalized cells model, *Mechanics of Materials* 14 (1992), 127–139.

[62] G.J. Dvorak, Transformation Field Analysis of Inelastic Composite Materials, *Proceedings: Mathematical and Physical Sciences* 437 (1992), 311–327.

[63] J.C. Michel and P. Suquet, Nonuniform transformation field analysis, *International Journal of Solids and Structures* 40 (2003), 6937–6955.

[64] J.C. Michel and P. Suquet, Computational analysis of nonlinear composite structures using the nonuniform transformation field analysis, *Computer Methods in Applied Mechanics and Engineering* 193 (2004), 5477–5502.

[65] J. Yvonnet and Q.-C. He, The reduced model multiscale method (R3M) for the non-linear homogenization of hyperelastic media at finite strains, *Journal of Computational Physics* 223 (2007), 341–368.

[66] J. Aboudi, Micromechanical Analysis of Composites by the Method of Cells, *Applied Mechanics Reviews* 42 (1989), 193–221.

[67] Z. Liu, Reduced-order Homogenization of Heterogeneous Material Systems: from Viscoelasticity to Nonlinear Elasto-plastic Softening Material, PhD thesis, Northwestern University, 2017.

[68] J. Yvonnet, D. Gonzalez, and Q.-C. He, Numerically explicit potentials for the homogenization of nonlinear elastic heterogeneous materials, *Computer Methods in Applied Mechanics and Engineering* 198 (2009), 2723–2737.

[69] C. Habermann and F. Kindermann, Multidimensional Spline Interpolation: Theory and Applications, *Computational Economics* 30 (2007), 153–169.

[70] J. Yvonnet, E. Monteiro, and Q.-C. He, Computational homogenization method and reduced database model for hyperelastic heterogeneous structures, *International Journal for Multiscale Computational Engineering* 11 (2013), 201–225.

[71] A. Clément, C. Soize, and J. Yvonnet, Computational nonlinear stochastic homogenization using a nonconcurrent multiscale approach for hyperelastic heterogeneous microstructures analysis, *International Journal for Numerical Methods in Engineering* 91 (2012), 799–824.

[72] B.A. Le, J. Yvonnet, and Q.-C. He, Computational homogenization of nonlinear elastic materials using neural networks, *International Journal for Numerical Methods in Engineering* 104 (2015), 1061–1084.

[73] T. Kirchdoerfer and M. Ortiz, Data-driven computational mechanics, *Computer Methods in Applied Mechanics and Engineering* 304 (2016), 81–101.

[74] T. Kirchdoerfer and M. Ortiz, Data Driven Computing with noisy material data sets, *Computer Methods in Applied Mechanics and Engineering* 326 (2017), 622–641.

[75] M. Flaschel, S. Kumar, and L. De Lorenzis, Unsupervised discovery of interpretable hyperelastic constitutive laws, *Computer Methods in Applied Mechanics and Engineering* 381 (2021).

[76] M. Flaschel, S. Kumar, and L. De Lorenzis, Discovering plasticity models without stress data, *Computational Materials* 8 (2022).

[77] M. Zhang, *Artificial Higher Order Neural Networks for Computer Science and Engineering: Trends for Emerging Applications,* 1st ed. Information Science Reference, 2010.

[78] Z. Liu, M.A. Bessa, and W.K. Liu, Self-consistent clustering analysis: An efficient multi-scale scheme for inelastic heterogeneous materials, *Computer Methods in Applied Mechanics and Engineering* 306 (2016), 319–341.

[79] J.B. MacQueen, Some Methods for Classification and Analysis of Multivariate Observations, *Proceedings of the 5th Berkeley Symposium on Mathematical Statistics and Probability* 1 (1967), 281–297.

[80] T. Kohenen, The self-organizing map, *Neurocomputing* 21 (1998), 1–6.

[81] B.A. Lippmann and J. Schwinger, Variational Principles for Scattering Processes. I, *Phys. Rev.* 79 (1950), 469–480.

[82] Z. Liu, M. Fleming, and W.K. Liu, Microstructural material database for self-consistent clustering analysis of elastoplastic strain softening materials, *Computer Methods in Applied Mechanics and Engineering* 330 (2018), 547–577.

[83] C. He, J. Gao, H. Li, J. Ge, Y. Chen, J. Liu, and D. Fang, A data-driven self-consistent clustering analysis for the progressive damage behavior of 3D braided composites, *Composite Structures* 249 (2020).

[84] Y. Yang, L. Zhang, and S. Tang, A comparative study of cluster-based methods at finite strain, *Acta Mechanica Sinica* 38 (2022).

[85] C. Yu, O.L. Kafka, and W.K. Liu, Self-consistent clustering analysis for multiscale modeling at finite strains, *Computer Methods in Applied Mechanics and Engineering* 349 (2019), 339–359.

[86] S. Saha, O.L. Kafka, Y. Lu, C. Yu, and W.K. Liu, Macroscale Property Prediction for Additively Manufactured IN625 from Microstructure Through Advanced Homogenization, *Integrating Materials and Manufacturing Innovation* 10 (2021), 360–372.

[87] M. Shakoor, O.L. Kafka, C. Yu, and W.K. Liu, Data science for finite strain mechanical science of ductile materials, *Computational Mechanics* 64 (2019), 33–45.

[88] T.-R. Liu, Y. Yang, O.R. Bacarreza, S. Tang, and M.H. Aliabadi, An extended full field self-consistent cluster analysis framework for woven composite, *International Journal of Solids and Structures* 281 (2023).

[89] X. Han, J. Gao, M. Fleming, C. Xu, W. Xie, S. Meng, and W.K. Liu, Efficient multiscale modeling for woven composites based on self-consistent clustering analysis, *Computer Methods in Applied Mechanics and Engineering* 364 (2020).

[90] S. Mojumder, J. Gao, and W.K Liu, Self-consistent clustering analysis for modeling of theromelastic heterogeneous materials, *AIP Conference Proceedings* 2324 (2021).

[91] Y. Nie, Z. Li, and G. Cheng, Efficient prediction of the effective nonlinear properties of porous material by FEM-Cluster based Analysis (FCA), *Computer Methods in Applied Mechanics and Engineering* 383 (2021).

[92] M.A. Bessa, R. Bostanabad, Z. Liu, A. Hu, D.W. Apley, C. Brinson, W. Chen, and W.K. Liu, A framework for data-driven analysis of materials under uncertainty: Countering the curse of dimensionality, *Computer Methods in Applied Mechanics and Engineering* 320 (2017), 633–667.

[93] S. Tang, L. Zhang, and W.K. Liu, From virtual clustering analysis to self-consistent clustering analysis: a mathematical study, *Computational Mechanics* 62 (2018), 1443–1460.

[94] M. Schneider, On the mathematical foundations of the self-consistent clustering analysis for non-linear materials at small strains, *Computer Methods in Applied Mechanics and Engineering* 354 (2019), 783–801.

[95] A.A. Griffith, The Phenomena of Rupture and Flow in Solids, *Philosophical Transactions of the Royal Society of London. Series A, Containing Papers of a Mathematical or Physical Character* 221 (1921), 163–198.

[96] T.L. Anderson, *Fracture Mechanics: Fundamentals and Applications,* 4th ed. CRC Press, 2017.

[97] G.R. Irwin, Fracture Dynamics, Fracturing of Metals, *American Society for Metals* (1948), 147–166.

[98] G.R. Irwin, Onset of fast crack propagation in high strength steel and aluminum alloys, *Sagamore Research Conference Proceedings* (1956), 289–305.

[99] P.C. Paris, M.P. Gomez, and W.E. Anderson, A rational analytic theory of fatigue, *The Trend in Engineering* 13 (1961), 9–14.

[100] G.I. Barenblatt, The Mathematical Theory of Equilibrium Cracks in Brittle Fracture, *Advances in Applied Mechanics* 7 (1962), 55–129.

[101] D.S. Dugdale, Yielding of steel sheets containing slits, *Journal of the Mechanics and Physics of Solids* 8 (1960), 100–104.

[102] J. Liu, J. Li, and L. Liu, Finite Element Analysis for Brittle and Ductile Fracture Using a Unified Cohesive Zone Model, *Advances in Mechanical Engineering* 5 (2013).

[103] M. Elices, G.V. Guinea J. Gómez, and J. Planas, The cohesive zone model: advantages, limitations and challenges, *Engineering Fracture Mechanics* 69 (2002), 137–163.

[104] S. Roychowdhury, Y. Das Arun Roy, and J.R.H. Dodds, Ductile tearing in thin aluminum panels: experiments and analyses using large-displacement, 3-D surface cohesive elements, *Engineering Fracture Mechanics* 69 (2002), 983–1002.

[105] S. Li, M.D. Thouless, A.M. Waas, J.A. Schroeder, and P.D. Zavattieri, Use of a cohesive-zone model to analyze the fracture of a fiber-reinforced polymer–matrix composite, *Composites Science and Technology* 65 (2005), 537–549.

[106] M. Ortiz and A. Pandolfi, Finite-deformation irreversible cohesive elements for three-dimensional crack-propagation analysis, *International Journal for Numerical Methods in Engineering* 44 (1999), 1267–1282.

[107] P. Gilormini and J. Diani, Testing some implementations of a cohesive-zone model at finite strain, *Engineering Fracture Mechanics* 148 (2015), 97–109.

[108] K. Park and G.H. Paulino, Cohesive Zone Models: A Critical Review of Traction-Separation Relationships Across Fracture Surfaces, *Applied Mechanics Reviews* 64 (2011).

[109] P.O. Bouchard, F. Bay, and Y. Chastel, Numerical modelling of crack propagation: automatic remeshing and comparison of different criteria, *Computer Methods in Applied Mechanics and Engineering* 192 (2003), 3887–3908.

[110] A. Trädegård, F. Nilsson, and S. Östlund, FEM-remeshing technique applied to crack growth problems, *Computer Methods in Applied Mechanics and Engineering* 160 (1998), 115–131.

[111] J. Mediavilla, R.H.J. Peerlings, and M.G.D. Geers, Discrete crack modelling of ductile fracture driven by non-local softening plasticity, *International Journal for Numerical Methods in Engineering* 66 (2006), 661–688.

[112] N. Moës, J. Dolbow, and T. Belytschko, A finite element method for crack growth without remeshing, *International Journal for Numerical Methods in Engineering* 46 (1999), 131–150.

[113] A.R. Khoei, *Extended Finite Element Method: Theory and Applications,* 1st ed. Wiley, 2014.

[114] N. Moës, A. Gravouil, and T. Belytschko, Non-planar 3D crack growth by the extended finite element and level sets—Part I: Mechanical model, *International Journal for Numerical Methods in Engineering* 53 (2002), 2549–2568.

[115] A. Gravouil, N. Moës, and T. Belytschko, Non-planar 3D crack growth by the extended finite element and level sets—Part II: Level set update, *International Journal for Numerical Methods in Engineering* 53 (2002), 2569–2586.

[116] N. Sukumar, N. Moës, B. Moran, and T. Belytschko, Extended finite element method for three-dimensional crack modelling, *International Journal for Numerical Methods in Engineering* 48 (2000), 1549–1570.

[117] I.V. Singh, B.K. Mishra, S. Bhattacharya, and R.U. Patil, The numerical simulation of fatigue crack growth using extended finite element method, *International Journal of Fatigue* 36 (2012), 109–119.

[118] R. Ghandriz, K. Hart, and J. Li, Extended finite element method (XFEM) modeling of fracture in additively manufactured polymers, *Additive Manufacturing* 31 (2020).

[119] N. Moës and T. Belytschko, Extended finite element method for cohesive crack growth, *Engineering Fracture Mechanics* 69 (2002), 813–833.

[120] F. Erdogan and G.C. Sih, On the Crack Extension in Plates Under Plane Loading and Transverse Shear, *Journal of Basic Engineering* 85 (1963), 519–525.

[121] G.C. Sih and B. Macdonald, Fracture mechanics applied to engineering problems-strain energy density fracture criterion, *Engineering Fracture Mechanics* 6 (1974), 361–386.

[122] P. Dumstorff and G. Meschke, Crack propagation criteria in the framework of X-FEM-based structural analyses, *International Journal for Numerical and Analytical Methods in Geomechanics* 31 (2007), 239–259.

[123] S. Bordas, T. Rabczuk, and G. Zi, Three-dimensional crack initiation, propagation, branching and junction in non-linear materials by an extended meshfree method without asymptotic enrichment, *Engineering Fracture Mechanics* 75 (2008), 943–960.

[124] N. Sukumar, J.E. Dolbow, and N. Möes, Extended finite element method in computational fracture mechanics: a retrospective examination, *International Journal of Fracture* 196 (2015), 189–206.

[125] J. Lemaitre and H. Lippmann, *A Course on Damage Mechanics,* 2nd ed. Springer, 1996.

[126] R. De Borst, L.J. Sluys, H.B. Muhlhaus, and J. Pamin, Fundamental issues in finite element analyses of localization of deformation, *Engineering Computations* 10 (1993), 99–121.

[127] Z.P. Bažant and T.B. Belytschko, Wave Propagation in a Strain-Softening Bar:Exact Solution, *JournalJournal of Engineering Mechanics* 111 (1985), 381–389.

[128] Z.P. Bažant and G. Pijaudier-Cabot, Nonlocal Continuum Damage, Localization Instability and Convergence, *Journal of Applied Mechanics* 55 (1988), 287–293.

[129] R.H.J. Peerlings, R. De Borst, W.A.M. Brekelmans, and J.H.P. De Vree, Gradient enhanced damage for quasi-brittle materials, *International Journal for Numerical Methods in Engineering* 39 (1996), 3391–3403.

[130] M. Frémond and B. Nedjar, Damage, gradient of damage and principle of virtual power, *International Journal of Solids and Structures* 33 (1996), 1083–1103.

[131] G.A. Francfort and J.-J. Marigo, Revisiting brittle fracture as an energy minimization problem, *Journal of the Mechanics and Physics of Solids* 46 (1998), 1319–1342.

[132] Z.P. Bažant and B.H. Oh, Crack band theory for fracture of concrete, *Matériaux et Construction* 16 (1983), 155–177.

[133] Y.-D. Li and K.Y. Lee, Fracture analysis in micropolar elasticity: mode-I crack, *International Journal of Fracture* 156 (2009), 179–184.

[134] S. Forest, Micromorphic Approach for Gradient Elasticity, Viscoplasticity, and Damage, *Journal of Engineering Mechanics* 135 (2009), 117–131.

[135] H. Amor, J.-J. Marigo, and C. Maurini, Regularized formulation of the variational brittle fracture with unilateral contact: Numerical experiments, *Journal of the Mechanics and Physics of Solids* 57 (2009), 1209–1229.

[136] T.T. Nguyen, J. Yvonnet, M. Bornert, C. Chateau, K. Sab, R. Romani, and R. Le Roy, On the choice of parameters in the phase field method for simulating crack initiation with experimental validation, *International Journal of Fracture* 197 (2016), 213–226.

[137] R.J.M Geelen, Y. Liu, J.E. Dolbow, and A. Rodríguez-Ferran, An optimization-based phase-field method for continuous-discontinuous crack propagation, *International Journal for Numerical Methods in Engineering* 116 (2018), 1–20.

[138] B. Giovanardi, A. Scotti, and L. Formaggia, A hybrid XFEM –Phase field (*Xfield*) method for crack propagation in brittle elastic materials, *Computer Methods in Applied Mechanics and Engineering* 320 (2017), 396–420.

[139] S. Cuvilliez, F. Feyel, E. Lorentz, and S. Michel-Ponnelle, A finite element approach coupling a continuous gradient damage model and a cohesive zone model within the framework of quasi-brittle failure, *Computer Methods in Applied Mechanics and Engineering* 237-240 (2012), 244–259.

[140] P. Moonen, J. Carmeliet, and L.J. Sluys, A continuous–discontinuous approach to simulate fracture processes in quasi-brittle materials, *Philosophical Magazine* 88 (2008), 3281–3298.

[141] A. Simone, H. Askes, and L.J. Sluys, Incorrect initiation and propagation of failure in non-local and gradient-enhanced media, *International Journal of Solids and Structures* 41 (2004), 351–363.

[142] M.G.D. Geers, R. de Borst, W.A.M. Brekelmans, and R.H.J. Peerlings, Strain-based transient-gradient damage model for failure analyses, *Computer Methods in Applied Mechanics and Engineering* 160 (1998), 133–153.

[143] G. Pijaudier-Cabot, K. Haidar, and J.-F. Dubé, Non-local damage model with evolving internal length, *International Journal for Numerical and Analytical Methods in Geomechanics* 28 (2004), 633–652.

[144] L.H. Poh and G. Sun, Localizing gradient damage model with decreasing interactions, *International Journal for Numerical Methods in Engineering* 110 (2016), 503–522.

[145] B. Bourdin, G.A. Francfort, and J.-J. Marigo, Numerical experiments in revisited brittle fracture, *Journal of the Mechanics and Physics of Solids* 48 (2000), 797–826.

[146] B. Bourdin, G.A. Francfort, and J.-J. Marigo, The variational approach to fracture, *Journal of Elasticity* 91 (2008), 5–148.

[147] L. Ambrosio and V.M. Tortorelli, Approximation of functional depending on jumps by elliptic functional via t-convergence, *Communications on Pure and Applied Mathematics* 43 (1990), 999–1036.

[148] D. Mumford and J. Shah, Optimal approximations by piecewise smooth functions and associated variational problems, *Communications on Pure and Applied Mathematics* 42 (1989), 577–685.

[149] G. Lancioni and G. Royer-Carfagni, The Variational Approach to Fracture Mechanics. A Practical Application to the French Panthéon in Paris, *Journal of Elasticity* 95 (2009), 1–30.

[150] C. Miehe, F. Welschinger, and M. Hofacker, Thermodynamically consistent phase-field models of fracture: Variational principles and multi-field FE implementations, *International Journal for Numerical Methods in Engineering* 83 (2010), 1273–1311.

[151] C. Miehe, M. Hofacker, and F. Welschinger, A phase field model for rate-independent crack propagation: Robust algorithmic implementation based on operator splits, *Computer Methods in Applied Mechanics and Engineering* 199 (2010), 2765–2778.

[152] K. Seleš, A. Jurčević, Z. Tonković, and J. Sorić, Crack propagation prediction in heterogeneous microstructure using an efficient phase-field algorithm, *Theoretical and Applied Fracture Mechanics* 100 (2019), 289–297.

[153] M. Ambati, T. Gerasimov, and L. De Lorenzis, A review on phase-field models of brittle fracture and a new fast hybrid formulation, *Computational Mechanics* 55 (2015), 383–405.

[154] G. Liu, Q. Li, M.A. Msekh, and Z. Zuo, Abaqus implementation of monolithic and staggered schemes for quasi-static and dynamic fracture phase-field model, *Computational Materials Science* 121 (2016), 35–47.

[155] M. Hofacker and C. Miehe, Continuum phase field modeling of dynamic fracture: variational principles and staggered FE implementation, *International Journal of Fracture* 178 (2012), 113–129.

[156] M.J. Borden, C.V. Verhoosel, M.A. Scott, T.J.R. Hughes, and C.M. Landis, A phase-field description of dynamic brittle fracture, *Computer Methods in Applied Mechanics and Engineering* 217-220 (2012), 77–95.

[157] M. Ambati, T. Gerasimov, and L. De Lorenzis, Phase-field modeling of ductile fracture, *Computational Mechanics* 55 (2015), 1017–1040.

[158] R. Alessi, J.-J. Marigo, and S. Vidoli, Gradient damage models coupled with plasticity: Variational formulation and main properties, *Mechanics of Materials* 80 (2015), 351–367.

[159] P. Rodriguez, J. Ulloa, C. Samaniego, and E. Samaniego, A variational approach to the phase field modeling of brittle and ductile fracture, *International Journal of Mechanical Sciences* 144 (2018), 502–517.

[160] M. Dittmann, F. Aldakheel, J. Schulte, P. Wriggers, and C. Hesch, Variational phase-field formulation of non-linear ductile fracture, *Computer Methods in Applied Mechanics and Engineering* 342 (2018), 71–94.

[161] M. Ambati, R. Kruse, and L. De Lorenzis, A phase-field model for ductile fracture at finite strains and its experimental verification, *Computational Mechanics* 57 (2016), 149–167.

[162] C. Miehe, F. Aldakheel, and A. Raina, Phase field modeling of ductile fracture at finite strains: A variational gradient-extended plasticity-damage theory, *International Journal of Plasticity* 84 (2016), 1–32.

[163] M.J. Borden, T.J.R. Hughes, C.M. Landis, A. Anvari, and I.J. Lee, A phase-field formulation for fracture in ductile materials: Finite deformation balance law derivation, plastic degradation, and stress triaxiality effects, *Computer Methods in Applied Mechanics and Engineering* 312 (2016), 130–166.

[164] C. Miehe, L.-M. Schänzel, and H. Ulmer, Phase field modeling of fracture in multi-physics problems. Part I. Balance of crack surface and failure criteria for brittle crack propagation in thermo-elastic solids, *Computer Methods in Applied Mechanics and Engineering* 294 (2015), 449–485.

[165] M. Dittmann, F. Aldakheel, J. Schulte, F. Schmidt, M. Krüger, P. Wriggers, and C. Hesch, Phase-field modeling of porous-ductile fracture in non-linear thermo-elasto-plastic solids, *Computer Methods in Applied Mechanics and Engineering* 361 (2020).

[166] P. Sicsic, J.-J. Marigo, and C. Maurini, Initiation of a periodic array of cracks in the thermal shock problem: A gradient damage modeling, *Journal of the Mechanics and Physics of Solids* 63 (2014), 256–284.

[167] M.F. Wheeler, T. Wick, and W. Wollner, An augmented-Lagrangian method for the phase-field approach for pressurized fractures, *Computer Methods in Applied Mechanics and Engineering* 271 (2014), 69–85.

[168] K. Li and S. Zhou, Numerical investigation of multizone hydraulic fracture propagation in porous media: New insights from a phase field method, *Journal of Natural Gas Science and Engineering* 66 (2019), 42–59.

[169] Y.-S. Lo, M.J. Borden, K. Ravi-Chandar, and C.M. Landis, A phase-field model for fatigue crack growth, *Journal of the Mechanics and Physics of Solids* 132 (2019).

[170] R. Alessi, S. Vidoli, and L. De Lorenzis, A phenomenological approach to fatigue with a variational phase-field model: The one-dimensional case, *Engineering Fracture Mechanics* 190 (2018), 53–73.

[171] P. Carrara, M. Ambati, R. Alessi, and L. De Lorenzis, A framework to model the fatigue behavior of brittle materials based on a variational phase-field approach, *Computer Methods in Applied Mechanics and Engineering* 361 (2020).

[172] K. Seleš, F. Aldakheel, Z. Tonković, J. Sorić, and P. Wriggers, A general phase-field model for fatigue failure in brittle and ductile solids, *Computational Mechanics* 67 (2021), 1431–1452.

[173] K. Jukić, M. Ambati, T. Jarak, M. Kästner, and Z. Tonković, Calibration of phase-field brittle fatigue model by purposeful design of crack driving forces, *Engineering Fracture Mechanics* 289 (2023).

[174] C. Miehe, F. Welschinger, and M. Hofacker, A phase field model of electromechanical fracture, *Journal of the Mechanics and Physics of Solids* 58 (2010), 1716–1740.

[175] J.-Y. Wu and W.-X. Chen, Phase-field modeling of electromechanical fracture in piezoelectric solids: Analytical results and numerical simulations, *Computer Methods in Applied Mechanics and Engineering* 387 (2021).

[176] T. Cajuhi, L. Sanavia, and L. De Lorenzis, Phase-field modeling of fracture in variably saturated porous media, *Computational Mechanics* 61 (2018), 299–318.

[177] T. Wu and L. De Lorenzis, A phase-field approach to fracture coupled with diffusion, *Computer Methods in Applied Mechanics and Engineering* 312 (2016), 196–223.

[178] C. Miehe, D. Kienle, F. Aldakheel, and S. Teichtmeister, Phase field modeling of fracture in porous plasticity: A variational gradient-extended Eulerian framework for the macroscopic analysis of ductile failure, *Computer Methods in Applied Mechanics and Engineering* 312 (2016), 3–50.

[179] A. Raina and C. Miehe, A phase-field model for fracture in biological tissues, *Biomechanics and Modeling in Mechanobiology* 15 (2016), 479–496.

[180] R.U. Patil, B.K. Mishra, and I.V. Singh, A multiscale framework based on phase field method and XFEM to simulate fracture in highly heterogeneous materials, *Theoretical and Applied Fracture Mechanics* 100 (2019), 390–415.

[181] R.U. Patil, B.K. Mishra, and I.V. Singh, An adaptive multiscale phase field method for brittle fracture, *Computer Methods in Applied Mechanics and Engineering* 329 (2018), 254–288.

[182] R.U. Patil, B.K. Mishra, I.V. Singh, and T.Q. Bui, A new multiscale phase field method to simulate failure in composites, *Advances in Engineering Software* 126 (2018), 9–33.

[183] T. Lesičar, T. Polančec, and Z. Tonković, Convergence Check Phase-Field Scheme for Modelling of Brittle and Ductile Fractures, *Applied Sciences* 13 (2023).

[184] S. Nagaraja, P. Carrara, and L. De Lorenzis, Experimental characterization and phase-field modeling of anisotropic brittle fracture in silicon, *Engineering Fracture Mechanics* 293 (2023).

[185] T. Gerasimov and L. De Lorenzis, A line search assisted monolithic approach for phase-field computing of brittle fracture, *Computer Methods in Applied Mechanics and Engineering* 312 (2016), 276–303.

[186] S. May, J. Vignollet, and R. de Borst, A new arc-length control method based on the rates of the internal and the dissipated energy, *Engineering Computations* 33 (2016), 100–115.

[187] T. Wick, Modified Newton methods for solving fully monolithic phase-field quasi-static brittle fracture propagation, *Computer Methods in Applied Mechanics and Engineering* 325 (2017), 577–611.

[188] P.K. Kristensen and E. Martínez-Pañeda, Phase field fracture modelling using quasi-Newton methods and a new adaptive step scheme, *Theoretical and Applied Fracture Mechanics* 107 (2020).

[189] F.P. Duda, A. Ciarbonetti, P.J. Sánchez, and A.E. Huespe, A phase-field/gradient damage model for brittle fracture in elastic–plastic solids, *International Journal of Plasticity* 65 (2015), 269–296.

[190] K. Seleš, T. Lesičar, Z. Tonković, and J. Sorić, A residual control staggered solution scheme for the phase-field modeling of brittle fracture, *Engineering Fracture Mechanics* 205 (2019), 370–386.

[191] URL: https://data.mendeley.com/datasets/p77tsyrbx2/4/.

[192] M.J. Borden, T.J.R. Hughes, C.M. Landis, and C.V. Verhoosel, A higher-order phase-field model for brittle fracture: Formulation and analysis within the isogeometric analysis framework, *Computer Methods in Applied Mechanics and Engineering* 273 (2014), 100–118.

[193] M. Klinsmann, D. Rosato, M. Kamlah, and R.M. McMeeking, An assessment of the phase field formulation for crack growth, *Computer Methods in Applied Mechanics and Engineering* 294 (2015), 313–330.

[194] T. Heister, M.F. Wheeler, and T. Wick, A primal-dual active set method and predictor-corrector mesh adaptivity for computing fracture propagation using a phase-field approach, *Computer Methods in Applied Mechanics and Engineering* 290 (2015), 466–495.

[195] K. Jukić, T. Jarak, K. Seleš, and Z. Tonković, Adaptive Phase-Field Modeling of Brittle Fracture, *Proceedings of the 2nd International Conference on Structural Damage Modelling and Assessment*. Ed. by Magd Abdel Wahab. Singapore: Springer Singapore, 2022, 145–161.

[196] M. Artina, M. Fornasier, S. Micheletti, and S. Perotto, Anisotropic Mesh Adaptation for Crack Detection In Brittle Materials, *SIAM Journal on Scientific Computing* 37 (2015), B633–B659.

[197] P. Čanžar, Z. Tonković, and J. Kodvanj, Microstructure influence on fatigue behaviour of nodular cast iron, *Materials Science and Engineering: A* 556 (2012), 88–99.

[198] F. Putar, J. Sorić, T. Lesičar, and Z. Tonković, Damage modeling employing strain gradient continuum theory, *International Journal of Solids and Structures* 120 (2017), 171–185.

[199] S. Graham and N. Yang, Representative volumes of materials based on microstructural statistics, *Scripta Materialia* 48 (2003), 269–274.

[200] T. Belytschko, S. Loehnert, and J.-H. Song, Multiscale aggregating discontinuities: A method for circumventing loss of material stability, *International Journal for Numerical Methods in Engineering* 73 (2008), 869–894.

[201] T. Hettich, A. Hund, and E. Ramm, Modeling of failure in composites by X-FEM and level sets within a multiscale framework, *Computer Methods in Applied Mechanics and Engineering* 197 (2008), 414–424.

[202] I.M. Gitman, H. Askes, and L.J. Sluys, Coupled-volume multi-scale modelling of quasi-brittle material, *European Journal of Mechanics - A/Solids* 27 (2008), 302–327.

[203] M.G. Kulkarni, P.H. Geubelle, and K. Matouš, Multi-scale modeling of heterogeneous adhesives: Effect of particle decohesion, *Mechanics of Materials* 41 (2009), 573–583.

[204] M.V. Cid Alfaro, A.S.J. Suiker, C.V. Verhoosel, and R. de Borst, Numerical homogenization of cracking processes in thin fibre-epoxy layers, *European Journal of Mechanics - A/Solids* 29 (2010), 199–131.

[205] C.V. Verhoosel, J.J.C. Remmers, and M.A. Gutiérrez, A partition of unity-based multiscale approach for modelling fracture in piezoelectric ceramics, *International Journal for Numerical Methods in Engineering* 82 (2010), 966–994.

[206] C.V. Verhoosel, J.J.C. Remmers, M.A. Gutiérrez, and R. de Borst, Computational homogenization for adhesive and cohesive failure in quasi-brittle solids, *International Journal for Numerical Methods in Engineering* 83 (2010), 1155–1179.

[207] V.P. Nguyen, O. Lloberas-Valls, M. Stroeven, and L.J. Sluys, On the existence of representative volumes for softening quasi-brittle materials – A failure zone averaging scheme, *Computer Methods in Applied Mechanics and Engineering* 199 (2010), 3028–3038.

[208] H.-W. Zhang, J.-K. Wu, J. Lü, and Z.-D. Fu, Extended multiscale finite element method for mechanical analysis of heterogeneous materials, *Acta Mechanica Sinica* 26 (2010), 899–920.

[209] H.W. Zhang, J.K. Wu, and J. Lv, A new multiscale computational method for elasto-plastic analysis of heterogeneous materials, *Computational Mechanics* 49 (2012), 149–169.

[210] A. Ibrahimbegović and D. Markovič, Strong coupling methods in multi-phase and multi-scale modeling of inelastic behavior of heterogeneous structures, *Computer Methods in Applied Mechanics and Engineering* 192 (2003), 3089–3107.

[211] A. Tchalla, W.L. Azoti, Y. Koutsawa, A. Makradi, S. Belouettar, and H. Zahrouni, Incremental mean-fields micromechanics scheme for non-linear response of ductile damaged composite materials, *Composites Part B: Engineering* 69 (2015), 169–180.

[212] T. Lesičar, J. Sorić, and Z. Tonković, Ductile damage modelling of heterogeneous materials using a two-scale computational approach, *Computer Methods in Applied Mechanics and Engineering* 355 (2019), 113–134.

[213] I. Benedetti and M.H. Aliabadi, Multiscale modeling of polycrystalline materials: A boundary element approach to material degradation and fracture, *Computer Methods in Applied Mechanics and Engineering* 289 (2015), 429–453.

[214] M. Xiang and J. Chen, Numerical simulation of ductile fracture based on mean field homogenization method: Modeling and implementation, *Engineering Fracture Mechanics* 152 (2016), 147–161.

[215] D.R. Curran, L. Seaman, and D.A. Shockey, Dynamic failure of solids, *Physics Reports* 147 (1987), 253–388.

[216] Y. Wang, H. He, and L. Wang, Critical Damage Evolution model for spall failure of ductile metals, *Mechanics of Materials* 56 (2013), 131–141.

[217] URL: https://www.3ds.com/products/simulia/abaqus.

[218] URL: https://www.polcast.com.tr/en/nodular-graphite-cast-iron.

[219] URL: https://www.mathworks.com/help/stats/kmeans.html.

[220] E. Kröner, *Statistical Continuum Mechanics,* Springer, 1972.

[221] J. Lee and A.K. Mal, A volume integral equation technique for multiple scattering problems in elastodynamics, *Applied Mathematics and Computation* 67 (1995), 135–159.

[222] T. Mura, *Micromechanics of Defects in Solids,* 2nd ed. Martinus Nijhoff Publishers, 1987.

[223] T. Mori and K Tanaka, Average stress in matrix and average elastic energy of materials with misfitting inclusions, *Acta Metallurgica* 21 (1973), 571–574.

[224] T.W.J. de Geus, J. Vondřejc, J. Zeman, R.H.J. Peerlings, and M.G.D. Geers, Finite strain FFT-based non-linear solvers made simples, *Computer Methods in Applied Mechanics and Engineering* 318 (2017), 412–430.

[225] N. Lahellec, J.C. Michel, H. Moulinec, and P. Suquet, Analysis of Inhomogeneous Materials at Large Strains using Fast Fourier Transforms, *IUTAM Symposium on Computational Mechanics of Solid Materials at Large Strains* (2003), 247–258.

[226] Z. Hashin and S. Shtrikman, A variational approach to the theory of the elastic behaviour of multiphase materials, *Journal of the Mechanics and Physics of Solids* 11 (1963), 127–140.

[227] L. Zhang, S. Tang, C. Yu, X. Zhu, and W.K. Liu, Fast calculation of interaction tensors in clustering-based homogenization, *Computational Mechanics* 64 (2019), 351–364.

[228] G. Cheng, X. Li, Y. Nie, and H. Li, FEM-Cluster based reduction method for efficient numerical prediction of effective properties of heterogeneous material in nonlinear range, *Computer Methods in Applied Mechanics and Engineering* 348 (2019), 157–184.

[229] A. Tewari and A.M. Gokhale, Nearest-neighbor distances between particles of finite size in three-dimensional uniform random microstructures1mm. *Materials Science and Engineering: A* 385 (2004), 332–341.

[230] V. Hakim and A. Karma, Laws of crack motion and phase-field models of fracture1mm. *Journal of the Mechanics and Physics of Solids* 57 (2009), 342–368.

[231] H. Henry and H. Levine, Dynamic Instabilities of Fracture under Biaxial Strain Using a Phase Field Model1mm. *Physical Review Letters* 93 (2004).

[232] 73 - On the theory of superconductivity. *Collected Papers of L.D. Landau1mm*. Ed. by D. Ter Haar. Pergamon, 1965, 546–568.

[233] K. Pham, J.-J. Marigo, and C. Maurini, Gradient Damage Models and Their Use to Approximate Brittle Fracture1mm. *Journal of the Mechanics and Physics of Solids* 20 (2011), 618–652.

[234] E. Lorentz, A nonlocal damage model for plain concrete consistent with cohesive fracture1mm. *International Journal of Fracture* 207 (2017), 123–159.

[235] J.-Y. Wu, A unified phase-field theory for the mechanics of damage and quasi-brittle failure1mm. *Journal of the Mechanics and Physics of Solids* 103 (2017), 72–99.

[236] C. Kuhn, A. Schlüter, and R. Müller, On degradation functions in phase field fracture models1mm. *Computational Materials Science* 108 (2015), 374–384.

[237] J.M. Sargado, E. Keilegavlen, I. Berre, and J.M. Nordbotten, High-accuracy phase-field models for brittle fracture based on a new family of degradation functions1mm. *Journal of the Mechanics and Physics of Solids* 111 (2018), 458–489.

[238] C. Miehe and M. Lambrecht, Algorithms for computation of stresses and elasticity moduli in terms of Seth–Hill's family of generalized strain tensors, *Communications in Numerical Methods in Engineering* 17 (2001), 337–353.

[239] C. Steinke and M. Kaliske, A phase-field crack model based on directional stress decomposition, *Computational Mechanics* 63 (2019), 1019–1046.

[240] F. Freddi and G. Royer-Carfagni, Regularized variational theories of fracture: A unified approach, *Journal of the Mechanics and Physics of Solids* 58 (2010), 1154–1174.

[241] F. Freddi and G. Royer-Carfagni, A variationally consistent phase-field anisotropic damage model for fracture, *Computer Methods in Applied Mechanics and Engineering* 358 (2020).

[242] K. Seleš, Z. Tonković, A. Jurčević, and J. Sorić, Strain Energy Decomposition Influence in the Phase Field Crack Modelling at the Microstructural Level of Heterogeneous Materials, *Key Engineering Materials* 827 (2019), 482–487.

[243] K. Seleš, Numerical phase-field modeling of damage in heterogeneous materials, PhD thesis, University of Zagreb, 2020.

[244] C. Miehe, M. Hofacker, L.-M. Schänzel, and F. Aldakheel, Phase field modeling of fracture in multi-physics problems. Part II. Coupled brittle-to-ductile failure criteria and crack propagation in thermo-elastic–plastic solids, *Computer Methods in Applied Mechanics and Engineering* 294 (2015), 486–522.

[245] R. Alesi, M. Ambati, T. Gerasimov, S. Vidoli, and L. De Lorenzis, Comparison of Phase-Field Models of Fracture Coupled with Plasticity, *Advances in Computational Plasticity: A Book in Honour of D. Roger J. Owen*. Ed. by E. Oñate, D. Peric, E. de Souza Neto, and M. Chiumenti. Springer International Publishing, 2018, 1–21.

[246] A. Mesgarnejad, B. Bourdin, and M.M. Khonsari, Validation simulations for the variational approach to fracture, *Computer Methods in Applied Mechanics and Engineering* 290 (2015), 420–437.

[247] K. Solberg and F. Berto, The effect of defects and notches in quasi-static and fatigue loading of Inconel 718 specimens produced by selective laser melting, *International Journal of Fatigue* 137 (2020).

[248] P. Čanžar, Eksperimentalno i numeričko modeliranje zamornog ponašanja nodularnog lijeva, PhD thesis, Sveučilište u Zagrebu, 2012.

[249] URL: https://imagej.net/ij.

[250] L. Plavšić, Mikrostrukturno modeliranje elastoplastičnog ponašanja nodularnog lijeva primjenom homogenizacije s reduciranim brojem stupnjeva slobode, (2023). Graduation thesis, University of Zagreb.

[251] J.R. Cost, K.R. Janowski, and R.C. Rossi, Elastic properties of isotropic graphite, *The Philosophical Magazine: A Journal of Theoretical Experimental and Applied Physics* 17 (1968), 851–854.

[252] URL: https://www.matweb.com/search/DataSheet.aspx?MatGUID=d0b0a51bff894778a97f5b72e7317d85&ckck=1.